Modeling aquatic constraints

Its application from rehabilitation to competitive swimming

Jessy Lauer

Porto, 2017

Doctoral thesis under co-supervision submitted in partial fulfillment of the requirements for obtaining a doctoral degree in sport sciences under the terms of the decree-law nº74/2006 of March 24th.

Abstract

The load on the musculoskeletal system has been estimated during terrestrial activities through inverse dynamics for about 80 years, providing invaluable insight into animal and human movement mechanics. In water, such knowledge remains inaccessible. This is mainly due to the great challenge of measuring hydrodynamic forces and their point of application acting on largely deforming bodies. Here we report a novel approach coupling numerical fluid flow simulations, computer graphics algorithms and inverse dynamics to explore aquatic movement mechanics from a joint-level perspective.

New dynamic mesh methods were implemented to realistically animate body virtual models, and ultimately model fluid flow and external forces under unsteady conditions. We then answered fundamental questions regarding the way the human musculoskeletal system accommodated increasing mechanical demands in water. Since understanding how power is produced at a joint level does not offer a complete kinetic picture, we further explored the complex energy flow between the water and one's arm, and challenged the longstanding idea that internal and external works were two independent mechanical costs in water. Last, motivated by requests from healthcare professionals, we chose to shed light onto shoulder joint function and task mechanical requirements of scapular plane aquatic exercises performed at various speeds and in different body positions.

Errors <2% between the simulation and the experiment gave confidence in the results. No proximal redistribution of work was observed across a threefold increase in load, supporting the idea that movements are controlled modularly. Internal work was found to be an integral part of the work imparted to the water through a mechanism of energy transfer likely analogous that in cycling; a revisited energy cascade of aquatic locomotion was proposed. Simple predictive equations of the load on the shoulder musculature were provided, together with updated clinical guidelines to inform rehabilitation protocol design.

This thesis paves the way towards musculoskeletal modeling of aquatic activities to elucidate the fundamental principles of muscle coordination and evaluate the loading of individual anatomical structures. Much effort will be dedicated in the near future to turn the present methodology free to a wide audience through an open source package of computational fluid dynamics.

KEYWORDS: AQUATIC LOCOMOTION; COMPUTATION FLUID DYNAMICS; INVERSE DYNAMICS; JOINT KINETICS; POWER.

Resumo

A carga sobre o sistema músculo-esquelético tem sido avaliada durante atividades terrestres através da dinâmica inversa desde há cerca de 80 anos, proporcionando descobertas consideráveis sobre a mecânica do movimento humano e animal. Contudo, em relação ao movimento aquático, este conhecimento continua a ser inacessível. Isso é devido em grande parte à extrema dificuldade em quantificar as forças hidrodinâmicas e os pontos de aplicação das mesmas em corpos largamente deformáveis. Na presente tese mostra-se a implementação de uma abordagem inovadora juntando dinâmica computacional de fluidos, algorítmos de animação computacional e dinâmica inversa, a fim de investigar a mecânica do movimento submerso a partir do cálculo dos esforços a que são sujeitas as articulações.

Novos métodos de malha dinâmica foram implementados para animar um modelo virtual do corpo de forma realística e medir as forças hidrodinâmicas instantâneas exercidas na mão, braço e antebraço durante o deslocamento. Respondemos depois a questões fundamentais relativas à forma como o sistema músculo-esquelético humano responde a um aumento da carga mecânica dentro de água. Uma vez que uma melhor compreensão da estratégia de modulação de potência não fornece a imagem cinética mais completa possível, exploramos mais em detalhe: o fluxo de energia mecânica entre a água e o membro superior. Questionámos a ideia segundo a qual o trabalho mecânica interno é independente do trabalho externo realizado contra a resistência da água. Finalmente, decidimos de esclarecer a função do ombro e a carga mecânica de exercícios terapêuticos efetuados no plano da escápula em várias velocidades e diferentes posições do corpo.

Erros <2% entre as simulações e os resultados experimentais deram crédito aos resultados. Apesar da carga triplicar, não foi observada uma redistribuição proximal da potência articular, corroborando a hipótese de que movimentos complexos são controladas de forma modular. Descobriu-se que o trabalho interno era uma parte integrante do trabalho externo através de um mecanismo de transferência de energia provavelmente semelhante com o encontrado durante ciclismo. Nessa decorrência, uma nova cascata de energia da locomoção aquática foi sugerida. Foram ainda criadas equações simples para prever a carga mecânica sobre os grupos musculares do ombro, tal como orientações clínicas atualizadas para ajudar na tomada de decisão e no estabelecimento de protocolos de reabilitação.

Esta tese abre o caminho para o uso de modelos músculo-esqueléticos mais avançados a fim de esclarecer os princípios fundamentais da coordenação motora e avaliar a carga individual exercida sobre cada estrutura anatómica. No futuro, os nossos esforços serão dirigidos à partilha livre dessa metodologia inovadora para o público através de software de modelação de escoamento de fluidos gratuito.

PALAVRAS-CHAVES: LOCOMOÇÃO AQUÁTICA; DINÂMICA DE FLUIDOS COMPUTACIONAL; DINÂMICA INVERSA; CINÉTICA ARTICULAR; POTÊNCIA.

Résumé

La charge mécanique sur le système musculo-squelettique lors d'activités terrestres est estimée grâce à la dynamique inverse depuis presque 80 ans, apportant un éclairage sans précèdent sur la mécanique du mouvement humain et animal. Ces connaissances restent cependant inaccessibles lors de mouvements aquatiques, l'énorme difficulté résidant principalement dans la mesure des forces hydrodynamiques s'exerçant sur un corps subissant de grandes déformations. Nous décrivons ici une approche innovante mêlant simulations numériques d'écoulement des fluides, algorithmes d'infographie et dynamique inverse dans le but d'explorer la mécanique du mouvement dans l'eau par le calcul des efforts aux articulations du membre supérieur.

De nouvelles méthodes de maillage dynamique ont été implémentées, permettant d'animer de manière réaliste un corps virtuel et d'estimer les forces agissant dessus. Nous avons ensuite répondu à des questions fondamentales relatives à la manière dont le système musculo-squelettiques réagit, dans l'eau, à une demande mécanique croissante. Pour améliorer notre compréhension des mécanismes de production de puissance, nous avons explorer plus en détail les transferts d'énergie mécanique entre le membre supérieur et l'eau, contestant l'idée communément admise selon laquelle le travail interne serait indépendant du travail externe. Enfin, nous avons choisi d'examiner la fonction de l'articulation de l'épaule ainsi que les besoins mécaniques à remplir lors d'exercices thérapeutiques dans l'eau effectués dans le plan de la scapula à différentes vitesses et dans diverses positions du corps.

L'erreur moyenne entre les forces hydrodynamiques théoriquement attendues et celles calculées par simulation était inferieure à 2%. Aucune redistribution du travail mécanique n'a été observée au sein du membre supérieur alors que la charge était triplée, renforçant la possibilité que les mouvements complexes soient contrôlés de manière modulaire. Le travail interne faisait partie intégrante du travail fourni à l'eau par un mécanisme de transfert d'énergie semblable à celui observé en cyclisme ; la cascade d'énergie de la locomotion aquatique est revisitée. Des équations simples de prédiction de la charge mécanique sur la musculature de l'épaule sont données, ainsi que des conseils cliniques aidant à la prise de décision et à l'établissement de protocoles de rééducation.

Ce travail de thèse ouvre la voie à l'utilisation de modèles musculo-squelettiques avancés afin de découvrir les principes fondamentaux de coordination musculaires et d'évaluer la charge mécanique sur chacune des structures anatomiques. Nos efforts seront tournés, dans un futur proche, vers le partage pour tous de cette nouvelle méthodologie via un programme de simulations d'écoulement des fluides gratuit et libre d'accès.

MOTS-CLÉS : LOCOMOTION AQUATIQUE ; MÉCANIQUE DES FLUIDES NUMÉRIQUE ; DYNAMIQUE INVERSE ; CINÉTIQUE ARTICULAIRE ; PUISSANCE.

Table of Contents

1 General introduction

1.1. Problem and justification

One of the defining features of (most) animals is that they are motile. They move through air, land, or water, exhibiting locomotor modes each as sophisticated and diverse as the other. Kangaroos routinely hop over 10 meters, golden wheel spiders roll down sand dunes, scallops jet water backwards to swim, gibbons brachiate from branch to branch, swifts flying for no less than ten months straight. Some travel within two different physical environments (e.g., water vs land), such as some frogs, ducks, rodents, and lizards. Humans fall in that category, as they continuously strive to improve their performance in media with strikingly different physical properties, though for other than ecological purposes. Yet, to operate optimally in both environments poses a great challenge. In semi-aquatic animals, natural selection has favored a compromise between form and function, providing only reasonable performance in both environments. Humans however evolved a natural propensity for terrestrial locomotion, whereas they prove highly uneconomical swimmers.

Powering oneself is achieved through producing force on the external environment. Be it from pushing against the ground or on masses of water, forces are typically produced by the musculoskeletal machinery according to an efferent cascade of events. A simple intentional drive excites the muscular system, which leads to the production of muscle force dependent on muscle–tendon dynamics, hence torques at the joints. The interaction between the body and the environment ultimately determines changes in skeletal system configuration over time, and forces transmitted to the environment.

Examining how the musculoskeletal system is loaded[1] is therefore the lowest level of observation of system dynamics from which to understand system mechanical performance and its interaction with the environment.

On land, the calculation of the mechanical demands of a task is a very common procedure, regardless of the approach used. The interaction with the environment (between the feet and the ground) and the work done against it are fairly easy to quantify, which drastically simplifies the analysis. It is a real challenge in water though, mainly because of the difficulty in evaluating hydrodynamic forces acting on the moving limbs. This in turn severely impedes our capacity to understand further aquatic movement mechanics, as the bridge between kinematics and physiological or electromyographical measures is lacking. This thesis sought to investigate human mechanical performance when moving in water from the unprecedented angle of joint load computation.

1.2. Organization

The thesis is articulated around seven main parts: a review of the literature, followed by a methodological section and five chapters associated with this thesis' contributions in scientific journals. The first part of the review of literature thoroughly describes how assessing load is traditionally done when moving on land. The second emphasizes the insights that can be gained through such analyses, and their relevance to the field of biomechanics. The last will illustrate the difficulties associated with applying these procedures in water, notably from the point of view of external forces computation, and what are the expected steps required to eventually take up this challenge. The content of the remaining chapters, although largely mirroring published papers, is enriched with supplementary information.

[1] Mechanical load through the remainder of the current work does not refer to stress or strain of anatomical structures as in rheology. It rather designates the mechanical demands or requirements of a particular task that have to be met by the musculoskeletal system. These terms will here be used interchangeably.

2 Noninvasive estimates of mechanical load on the musculoskeletal system

The knowledge of musculoskeletal system loading during motion is essential for the understanding of movement mechanics. That load associated with many different locomotion tasks in terrestrial conditions have been evaluated essentially through two methods that will be discussed hereafter. Invasive methods (such as in vivo muscle–tendon unit work measurements through sonomicrometry and force buckles or optical fibers), the use of which is restricted to animal studies, will not be addressed here.

2.1. External and internal mechanical work

Non-invasively estimating the total mechanical work (W_{TOT}) of locomotion can be done through separating total mechanical work into external (W_{EXT}) and internal work (W_{INT}). The first quantity corresponds to the work performed by external forces (mainly from the ground) to lift and accelerate the body center of mass. It has been traditionally determined from the potential and kinetic energy traces (E_p and E_k, respectively) of the body center of mass, as follows:

$$E_{COM} = \underbrace{MgH}_{E_p} + \underbrace{\frac{1}{2}MV_{COM}^2}_{E_k}, \tag{2.1}$$

$$W_{EXT} = \Delta E_{COM}, \tag{2.2}$$

where M is the body mass; g, the standard acceleration due to gravity; H and V_{COM}, the height and velocity of the body center of mass (relative to the surroundings), respectively. However, this is based on differentiating noisy kinematics data and approximation of inertial parameters, necessary to assess the relative mass of each body segment (Willems et al., 1995). Alternatively, W_{EXT} can be readily computed from the ground reaction forces alone, according to an easy-to-implement, noise-free force platform analysis (Cavagna, 1975). Most importantly, W_{EXT} measurements have revealed two universal mechanisms of terrestrial locomotion. Walking is characterized by continuous transfer between potential and kinetic energies as in an inverted pendulum, with an optimum recovery at (or near) the most economical speed. This feature is already apparent in 3 year-old children walking (Schepens et al., 2004), and conserved even in parkinsonian patients at advanced stages of the disease (Dipaola et al., 2016). By contrast, no such energy exchange occurs during running, trotting, hopping, although energy is stored in elastic structures and recovered through a bouncing mechanism. Galloping, skipping, and some forms of locomotion on snow do constitute a third locomotion paradigm, as a combination of both mechanisms is used (Cavagna et al., 1977; Minetti, 1998; Pellegrini et al., 2014). None of these mechanisms could have been evidenced with any other analysis. Remarkably, energy fluctuations of the center of mass (hence W_{EXT}) could explain why African women could carry head-supported loads substantially more cheaply than even army recruits: they were simply better pendulums, conserving a higher fraction of energy (occasionally over 80%) and thus diminishing work input requirements (Heglund et al., 1995). Penguins recover high energy levels too, among the highest ever observed; they waddle side-to-side, increasing the kinetic energy available to convert into gravitational potential energy and also causing these energies to fluctuate more completely out of phase. In fact, excluding lateral kinetic energy (i.e., waddling) would have resulted in the recovery of less mechanical energy and more work being required from the muscles (Griffin and Kram, 2000). Therefore, center of mass energy patterns and W_{EXT} can be used to identify functionally different gaits (more reliably than from kinematic measurements), as well as to gain insight into how body mechanics operate to reduce muscle work and metabolic energy use (Biewener, 2006).

The second quantity, W_{INT}, is associated with the acceleration of body segments relative to the body center of mass. The concept was introduced by Fenn (Fenn, 1930), and later refined by Cavagna and Kaneko (Cavagna and Kaneko, 1977) based on the König's

theorem of physics to account for kinetic energy changes of segments whose movements do not affect the position of the body center of mass (e.g., the reciprocal motion of the arms during walking). To be calculated, W_{INT} requires measures of body segment inertial parameters and a parameterization of their 3D attitude in space, which is sensibly harder than ground reaction force measurements. Mechanical energy profiles of n body segments are then summed (allowing or not possible between- or within-segment transfer; Willems et al., 1995), and W_{INT} follows from energy increments in the resulting curve, according to the classical equations:

$$E_{\mathrm{INT}} = \sum_{i=1}^{n} \left(\underbrace{\frac{1}{2} m_i V_i^2}_{E_{k,t}} + \underbrace{\frac{1}{2} I_i \omega_i^2}_{E_{k,r}} \right), \tag{2.3}$$

$$W_{\mathrm{INT}} = \Delta E_{\mathrm{INT}}, \tag{2.4}$$

with m, the mass of a segment; I, its moment of inertia tensor: V, its linear velocity relative to the body center of mass; and ω, its angular velocity about the principal axes. Physiologists and biomechanists are familiar with this procedure. W_{INT} can account for effort perception associated with limb movement (Minetti et al., 1994a), but also allows an in-depth examination of the efficiency cascade of locomotion and the limit of the musculoskeletal system. For instance, remarkably deep insights have been gained into terrestrial gaits, unveiling the mechanical determinants of step frequency (Cavagna and Franzetti, 1986), cost of transport (Formenti et al., 2005; Minetti et al., 1994b; 1993), and gait control (Minetti et al., 1994a). It also proved clinically useful in the study of pathological gait, providing a new understanding of the role of segmental impairments in the resulting decreased economy (Detrembleur et al., 2003), and offering treatment directives in rehabilitation programs (McGibbon et al., 2001).

In swimming…

Despite its scientific relevance on land, this approach remains poorly explored in human aquatic locomotion. The internal power (i.e., the rate at which W_{INT} is done) while kicking the leg and swimming the front crawl was calculated by Zamparo and coworkers (Zamparo et al., 2005; 2006; 2002). They found out that arm stroke internal power was rather small, contrary to the leg that asked for a great fraction (80–85%) of the total internal power. The resulting suboptimal hydraulic efficiency of front crawl swimming provides a quantitative mechanical explanation of the general understanding that it is

better to use the leg kick as little as possible (in non-sprint races where efficiency rather than absolute power output is to be maximized) (Zamparo et al., 2005). In breaststroke, modeling the swimmer as two piston mechanisms not only accurately predicted the actual W_{INT}, but also revealed a decline in a parameter reflecting limb geometry and inertial properties (Lauer et al., 2015). It is as if swimmers were able, through some unknown form of sensing, to actively control and reduce the moment needed to rotate their limbs through motor reorganization at the highest swimming frequencies in order to mitigate increases in W_{INT}.

Unlike on land, W_{EXT} in water is not a quantity readily accessible. There is no such thing as force plates to provide 3D force vectors acting at the upper limb, and it cannot alternatively be taken solely from potential and kinetic energy levels of the body center of mass. Whereas air resistance and skidding can confidently be neglected, work done against the water must be accounted for—just like the work done in deforming the environment when walking on sand (Lejeune et al., 1998). As a matter of fact, neglecting the latter would result in the paradox that swimming at constant speed (i.e., with constant center of mass energy level) would require no mechanical work. W_{EXT} has generally been partitioned into: (1) the work to overcome active drag on the swimmer's body W_D, and (2) an extra quantity W_K reflecting the fact that part of W_{EXT} does not result in forward propulsion and is thus not accounted for in W_D.

- Four different methods were reported to assess W_D. (i) The first, developed in the 70s (di Prampero et al., 1974; Pendergast et al., 1977), involves adding or subtracting to the swimmer horizontal forces of various known intensities while measuring oxygen consumption during constant, submaximal swimming. At constant speed, this is equivalent to an increase or decrease of the body drag by the same amount. The actual drag is then obtained from the linear relationship between added drag and energy expenditure: extrapolating to resting oxygen consumption value yields the desired force. Calculation of W_D naturally follows. (ii) The MAD-system directly measures hand forces on paddles mounted underwater on a force transducer over a wide range of constant swimming speeds in arm-only front crawl (Hollander et al., 1986). At steady speed, these forces match the active drag the swimmer faces. (iii) The third, named the velocity perturbation method, determines the work to overcome drag from maximal

effort trials towing a known additional resistance (Kolmogorov and Duplishcheva, 1992); drag derives from a simple equation containing the maximal speeds reached when swimming with and without the resistance. However, these different methods are limited. They return a mean active drag value, therefore ignoring force fluctuations within a stroke. Furthermore, high variability in their results come either from the lack of validity (i.e., measurement of dissimilar phenomenon) or systematic errors introduced due to different equipment and testing protocol being used (Havriluk, 2007; Toussaint et al., 2004; Zamparo et al., 2009). (iv) Last, instantaneous force can be obtained through a motorized towing device mounted on a force plate and attached to the swimmer's waist (Formosa et al., 2010). Power expended against body drag can be similarly computed from semi-tethered swimming, during which swimming speed and load are simultaneously measured, and can further be integrated over time to compute W_D (Dominguez-Castells et al., 2013).

- W_K is indirectly determined either from approximate Froude efficiency (specifically, from the ratio between forward speed and stroke frequency (Zamparo et al., 2005)) or extrapolation from MAD-system swimming (Toussaint et al., 1988). In the first case, calculations are derived from a simplistic model assuming a rigid upper limb of fixed length rotating at constant speed. In the second, additional measurements of oxygen consumption while evaluating active drag were required to determine the relationship between metabolic and mechanical power (P_{MET} and P_{MECH}). Total power output during free swimming could then be predicted from VO_2 measurement. Knowing the actual power done against drag only (P_D) from trials on the MAD-system at the same speed (since no power is transmitted to the water while pushing on fixed pads), P_K (hence W_K), directly follows form the difference $P_{MECH} - P_D$.

- Alternatively, external work (the sum of W_D and W_K) can be measured through dry-land ergometry as if the swimmer was swimming suspended in the air, directly integrating the power generated at the arms and legs (Zamparo and Swaine, 2012).

As done on land, the total mechanical work that muscles supposedly produce is taken from the sum of internal and external work. Yet, mechanical energy analyses and subsequent work calculations have two important limitations. First, the possible independence between internal and external work may prevent the total mechanical work from being estimated as a simple sum of the two measures. Studies in walking, running (Aleshinsky, 1986a; Zatsiorsky, 1998), and cycling (Kautz et al., 1994; Kautz and Neptune, 2002; Neptune and van den Bogert, 1998; van Ingen Schenau et al., 1990) indeed pointed out that internal work was actually an integral part of external work, so that they are not independent mechanical quantities as usually treated. The concept of internal work as an additional cost of moving segments might therefore be flawed, an idea further supported by Minetti (Minetti, 2011) for whom internal work is almost meaningless as limb rotation in cycling can, in theory, be achieved passively.

The same issue is suspected to occur in swimming (Kautz and Neptune, 2002), although this hypothesis has never been tested. This is critical, as most of the works attempting to relate swimming mechanics with energetics are based on that assumption of independent mechanical costs. Therefore, one of the central works of the present thesis will be to evaluate whether this analysis is mechanically meaningful in water. Second, a value of total mechanical work does not tell us where this work is actually produced. Whereas it does offer a global kinetic picture taken at the scale of the entire body, it provides only little insight into which muscle groups control the movement and how they individually contribute to the mechanical requirements of the locomotor task of interest (Robertson and Winter, 1980). Rather, such level of analysis would be best approached from inverse dynamics.

2.2. Inverse dynamics

A mechanical system consisting of rigid links is driven by internal and/or external forces (including gravity) plus inertial effects. Finding those internal forces knowing the kinematics, inertial properties, and other forces (if any) is equivalent to solving the inverse problem of dynamics, traditionally called *inverse dynamics*. The first solution to this inverse problem in human dates back to 1939 (Elftman, 1939). Herbert Elftman—who had pioneered one year earlier an ingenious apparatus to give the precise point of

application as well as the magnitude along the three components of space of the ground reaction force (Elftman, 1938)—documented sagittal human leg dynamics during stance through a procedure that has since then become the most widely used for estimating internal load (van den Bogert, 1994).

Inverse dynamics relies upon the Newton–Euler formulation. The elements of a connected system are regarded as free bodies. Two sets of three equations (in 3D) per element (one for the linear accelerations, the Newton equations; another for the rotational accelerations, the Euler equations) are required to solve the inverse dynamics problem:

$$\begin{aligned} \sum \mathbf{F} &= m\mathbf{a} \\ \sum \mathbf{M} &= I\boldsymbol{\alpha} \end{aligned} \tag{2.5}$$

Consider now the right upper limb in terrestrial conditions, broken down into three rigid segments (hand, forearm, and upper arm) linked by ideal, frictionless joints[2]. The corresponding free-body diagrams are pictured below (note that vectors are arbitrarily represented).

[2] Although inverse dynamics modeling treats joints as being frictionless, cartilage–cartilage (i.e., intact joint) or cortical bone–cortical bone (e.g., joint with osteoarthritis) contacts do cause friction in vivo. In the first case, coefficients of friction of 0.001–0.003 were found (Büchler et al., 2002; Poitout, 2016), which contributes only 1–3 thousandths of the joint reaction force; inverse dynamics therefore provides very reasonable musculoskeletal loading estimates in healthy subjects. In the latter case though, coefficients of up to 0.9 (corresponding to cortical bone–spongious bone contact; Zhang et al., 1999) can be expected, thus adding considerable load that is not accounted for via traditional inverse dynamics analysis. Engineers have however long recognized the difficulties associated with modeling friction in mechanical systems, introducing complicated, discontinuous equations (Dupont, 1990). Although inverse dynamics is expected to perform very well in healthy subjects, it may yield unreliable mechanical loading estimates of pathological joints.

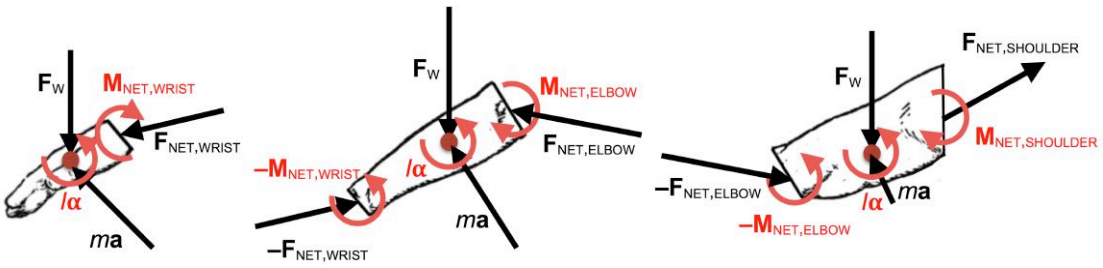

Figure 2-1 Free-body diagrams of the upper limb segments and relevant forces and moments

For illustration purposes, we substitute all variables in Equation 2.5 in 2D, which yields:

$$\begin{aligned} F_{\text{NET,WRIST}X} &= ma_X \\ F_w + F_{\text{NET,WRIST}Y} &= ma_Y \\ M_{\mathbf{F}_{\text{NET,WRIST}}} + M_{\text{NET,WRIST}Z} &= I\alpha_Z \end{aligned} \tag{2.6}$$

and rearranging:

$$\begin{aligned} F_{\text{NET,WRIST}X} &= ma_X \\ F_{\text{NET,WRIST}Y} &= ma_Y - F_w \\ M_{\text{NET,WRIST}Z} &= I\alpha_Z - M_{\mathbf{F}_{\text{NET,WRIST}}} \end{aligned} \tag{2.7}$$

Iterating the procedure moving proximally gives new systems of equations:

$$\begin{aligned} F_{\text{NET,ELBOW}X} &= ma_X + F_{\text{NET,WRIST}X} \\ F_{\text{NET,ELBOW}Y} &= ma_Y + F_{\text{NET,WRIST}Y} - F_w \\ M_{\text{NET,ELBOW}Z} &= I\alpha_Z - M_{-\mathbf{F}_{\text{NET,WRIST}}} - M_{\mathbf{F}_{\text{NET,ELBOW}}} + M_{\text{NET,WRIST}Z} \\ F_{\text{NET,SHOULDER}X} &= ma_X + F_{\text{NET,ELBOW}X} \\ F_{\text{NET,SHOULDER}Y} &= ma_Y + F_{\text{NET,ELBOW}Y} - F_w \\ M_{\text{NET,SHOULDER}Z} &= I\alpha_Z - M_{-\mathbf{F}_{\text{NET,ELBOW}}} - M_{\mathbf{F}_{\text{NET,SHOULDER}}} + M_{\text{NET,ELBOW}Z} \end{aligned} \tag{2.8}$$

Forces and moments in 3D are deduced following the same recursive procedure. It will be thoroughly described in Chapter 5 using a numerical formulation more suited to computer programming than the vector notation above.

2.2.1. Inverse dynamics: what outcomes?

It is already apparent that inverse dynamics provides kinetic data at a much deeper level than the previous method based on segmental mechanical energy. These outcomes should be defined unambiguously in the first place before understanding how they contributed to enhance our understanding of movement mechanics.

Joint force

It is interesting that the way joint forces are predicted by modern researchers has been shaped by four concepts that developed prior to the twentieth century (Crowninshield and Brand, 1981). The first is the realization that human body functions in many ways as an inanimate machine. Although the origins of this idea cannot be dated precisely, muscles were depicted as wires as early as the fifteenth century by Leonardo da Vinci, already recognizing the mechanics of body movement. The second is that anatomical elements may be modeled as simple elements for the purpose of understanding their function. The third, that of static equilibrium to make the first calculations of muscle forces, is due to Borelli. He recognized that small muscles and other structures (such as ligaments and joint capsules) could be ignored in order to estimate forces in large muscles. Although simplistic, his extensive collection of drawings De Motu Animalium (Borelli, 1680) showed quantitative description of muscle function, and revealed an understanding of external loading, equilibrium, muscle synergism and antagonism, and biarticular muscles. The last concept was developed by Braune and Fischer (Braune and Fischer, 1895), who the first proposed that a moving man could be modeled as a series of connected rigid bodies, each subject to the laws of three-dimensional rigid body mechanics. Using such a model, the resultant forces between segments could be calculated from Newtonian equations and described at either end of each segment.

In clinical frameworks, knee joint forces decomposed along compressive and shear components were used as predictors of the risk of anterior cruciate ligament injury, as resultant forces were believed to indirectly reflect stress on the corresponding anatomical structures (Sell et al., 2007). Ergonomics and more industrial applications include the evaluation of occupational performance. For example, Nagura et al. computed knee joint forces during single- and double-leg kneeling to document knee dynamic loading during

deep flexion exercises (Nagura et al., 2002). They found out that the net posterior force acting on the tibia (~60% of subject's body weight) would substantially strain any structure providing knee joint posterior stability. Reasoning that the contact area of the knee joint is significantly reduced in deep flexion, they argued that high joint forces would accelerate the rate of degenerative changes to the knee over time in individuals routinely performing deep flexion activities. Joint forces were also calculated during sit-to-stand tasks performed at various speeds (Hutchinson et al., 1994). Their preliminary results indicated that joint load was mainly dominated by static load, with segmental dynamics being only relevant at the highest speeds and when moving rostrally (e.g., back and neck joints). Axial forces of up to 60% body weight at the ankle propagated proximally at the hip up the neck, where their magnitude was still ~10% body weight. Joint forces are also useful for a general understanding of the constraints under which prosthetic devices must operate, hence to guide engineers in the design stage. Joint forces provided reasonably accurate estimates of the contact force on the prosthetic knee of a transfemoral amputee, with errors of at most 56 N (~9% of the peak value) (Dumas et al., 2009). Yet, the authors explained that more accurate estimations could only be reached by taking into account the dynamics of the absorption and friction of the prosthesis components.

Admittedly, one must bear in mind that joint forces are only net estimates of the actual load at a joint, and by no means do they represent joint contact force. This is the reason why the title of this section had been intentionally left vague. Forces acting at a given joint have received a lot of different names in the literature, and although the issue has been considerably debated back in 1993 in the Biomch-L forum (de Leva, 1993), it still is confusing to many. David Winter, who largely contributed to the popularity of inverse dynamics in human biomechanics, refers to *joint reaction* and *bone-on-bone forces* (Winter, 2005). Winter's *joint reaction force* arises from the very nature of inverse dynamics analysis. Segments are examined one at a time, and the reaction between them must be calculated. This requires a free-body diagram, where the original link-segment model is broken into its segmental parts to compute all unknown joint reaction forces. Winter's *bone-on-bone force* is the contact force across the surface of the joint. If muscles were true torque motors, *bone-on-bone* and *joint reaction forces* would be equal. However, this is not the case: muscles are linear motors that induce additional forces at a joint. Consider a simple situation where an upper limb with weight 40 N is hanging passively. Shoulder muscles

are not contracting but are, assisted by ligaments, pulling upward with an equal and opposite force of 40 N. Neither compression nor distraction is experienced at the joint, hence a null *bone-on-bone force*. Let us imagine now that muscles contract, actively pulling the articular surfaces together with an upward force of 100 N. From static equilibrium equations, one calculates a compressive *bone-on-bone force* of 60 N. Winter's *bone-on-bone force* is thus the vector sum of the *joint reaction force* and the muscle force.

Forces remain inconsistently named in the literature. For example, Nordin and Frankel's textbook on skeletal biomechanics (Nordin and Frankel, 2012) actually refers to Winter's *bone-on-bone force* when writing *joint reaction force*. Paolo de Leva argued against this denomination for the following reasons (de Leva, 1993). According to Newton's third law, no force exists alone: a reaction is associated with an action. In a joint though, as during a tug of war competition, one cannot simply tell what structures generate the action, or react to it. Joint forces can be considered reaction when they arise from muscle action. Yet, they might as well be considered action when they naturally result from external forces; e.g., the force exerted by the femur on the tibial plate, resulting from the weight of the segments above the knee, can intuitively be considered action, just like the force of the foot on the ground. Thus, in his view, use of the terminology *joint reaction force* is improper to refer to either force. Some authors prefer joint intersegmental force (Zajac et al., 2002), or joint resultant force (Crowninshield and Brand, 1981), which is more tightly coupled to its mechanical definition; i.e., the vector sum of all the forces in structures crossing the joint (articular surfaces, ligamentous tissue, and muscles and tendons; Paul, 1976). Therefore, the prediction of joint forces via inverse dynamics has limited applications, and should be interpreted with caution. For that reason, joint forces will see only very little use in the present thesis.

Joint moment

A moment represents the tendency to cause rotation, which is performed about axes. The topic of interest is classically to examine moments relative to predefined rotation axes, preferentially anatomical ones. The muscles of the body operate by pulling on segments they attach to, thus producing moments of force about the joint they cross. This has been recognized early 19th century (although only for static tasks), representing joints as levers with a fulcrum at the joint center (Weber and Weber, 1992). Additional

moments come from ligaments and tendons (although more passively), as well as from bone and cartilage contact between segments (Farley and Ferris, 1998), although these are believed to be much lower than the moments produced by muscles (Winter, 2005). Net joint moments thus provide reliable estimates of the loading of the musculature crossing the joint (Biewener et al., 1988; Fukashiro et al., 1993; Prilutsky et al., 1996).

The interpretation of net joint moments is uniquely determined by the choice of the reference frame into which these kinetic vectors are described. Four reference frames are traditionally adopted (Schache and Baker, 2007). Three of them are orthogonal coordinate systems: the laboratory (or global) frame, as well as the proximal and distal segment anatomical frames. The last possibility is to express the joint moments in a non-orthogonal frame or joint coordinate system.

The choice of one over another is open to the researchers and is often guided by the research questions and/or personal preferences. Joint moments expressed relative to a laboratory axis, for example, represent this joint's contribution to movement in the plane perpendicular to that axis. This is particularly helpful during terrestrial gait, since lower limb segments do not follow trajectories in a local frame but rather move forward in the plane of progression (Winter and Ishac, 1994). When interpreted locally however, joint moments more closely correspond to the underlying anatomical structures. The International Society of Biomechanics recommends the description of joint kinetics in the joint coordinate system (Wu et al., 2002; 2005). Joint moments can be similarly described, providing a sounder understanding of joint dynamics (Schache and Baker, 2007), a less ambiguous and more anatomically relevant representation of joint moments, and a clearer demonstration of muscle activity (Morrow et al., 2009). Two further procedures can be employed in the joint coordinate systems, each serving a different purpose. With non-orthogonal projections, joint moments represent the net mechanical action about each joint axis (Desroches et al., 2010a), and it is then known for certain that a net flexion moment, for example, causes pure flexion. With orthogonal projections though, joint moments are more representative of muscle force production and ligament loading (Kristianslund et al., 2014b).

Joint power

Joint power is an important, net kinetic quantity that is closely related to the muscular sources of energy (Aleshinsky, 1986a; 1986b). The net power output at a joint is calculated from the dot product of joint moment and joint angular velocity vectors. When both are in the same direction, joint power is positive. Conversely, when they are opposite in sign, joint power is negative. Physically, positive joint power indicates that mechanical energy flows from the muscles to the segment, and vice versa (Robertson and Winter, 1980). In the case of negative power, the joint structures—muscles and connective tissues—absorb mechanical energy and either store it as elastic deformation energy or dissipate it into heat (Zatsiorsky and Prilutsky, 2012).

Most importantly, joint power allows the identification of the type of muscle contraction occurring during movements (Robertson and Winter, 1980; Winter, 1978). Robertson and Winter (Robertson and Winter, 1980) envisaged all eight possible work functions that can occur between two segments connected by an active muscle. The rule of thumb is simple. Whenever a joint rotates in the same direction as the net moment acting at that joint, power is produced and is associated with concentric muscle action. Whenever a joint rotates in the opposite direction, power is absorbed and is associated with eccentric contraction.

This association between net joint power and muscle contraction type has been debated extensively, and it has been suggested that the analysis might be flawed for several reasons. First, net joint power does not necessarily equal the total power of all muscles crossing the joint due to the presence of multi-joint muscles that can redistribute mechanical energy from the segments connected by that joint to others in the limb. In fact, biarticular muscle behavior depends on neighboring joint movements and thus cannot be predicted from single joint behavior. It is entirely possible that a biarticular muscle acts concentrically in spite of power being negative (Zatsiorsky and Prilutsky, 2012). Second, joint power analysis does not refer to actual anatomically defined muscles, but rather to equivalent monoarticular muscle–tendon unit (Robertson and Winter, 1980). Yet, muscle–tendon unit mechanics is uncoupled from fascicle mechanics because of the compliance of series elastic elements (Sawicki et al., 2015). Therefore, net joint power might not correctly capture the power generated by muscle contractile tissue *stricto*

sensu. The only statement that can be made therefore is that positive joint power has to originate from the contractile and/or the elastic elements of contracting muscles (van Ingen Schenau et al., 1990). Recently, Cronin et al. (Cronin et al., 2013) addressed this question by comparing directly joint power with muscle fascicle length changes during walking in humans and cats. Pattern of joint power at the soleus and medial gastrocnemius were computed through inverse dynamics, while length changes at the muscle–tendon unit and fascicle level were recorded using ultrasonography and sonomicrometry. In both cats and humans, they found that ankle joint power was a reasonable estimate of muscle–tendon unit mechanics. However, ankle joint power was a better predictor of muscle fascicle contraction type in cats, concluding that joint power may be more strongly coupled with fascicle behavior in muscle–tendon units with shorter tendons (such as the elbow and shoulder).

The total joint power of a body system naturally equals the time rate of change of body's mechanical energy minus (when external forces—such as friction—are large) the time rate of energy losses to the environment. The first to deduce such an unambiguous relationship, also called power equation, was Aleshinsky (Aleshinsky, 1986b; 1986a). This equality is invalid for the entire human body, due to the simple fact that power can be generated from metabolic power or absorbed and degraded into heat by the deformable human body. The equation is in balance in rigid mechanical systems though, since mechanical energy can neither be created nor absorbed by a rigid body (van Ingen Schenau et al., 1990).

The power equation proved fairly valid during walking (Robertson and Winter, 1980). There was very good correspondence between total joint power and the rate of change of total mechanical energy during stance (correlation coefficient [0.82–0.98]), except at the foot during heel contact and push-off (correlation coefficient <0.49). The authors attributed this large discrepancy to the inability to accurately locate the instantaneous ankle joint center, which is not fixed as assumed but moves relative to the bones. Van Ingen Schenau provided an additional element of discussion, invoking the fact that the foot deforms significantly during these periods due to joints that are not accounted for in the analysis (van Ingen Schenau et al., 1990). This provided indirect evidence of the inadequacy of treating the foot as a rigid body. In cycling, both measures of instantaneous power were almost identical, although a significant difference existed

during the mid-stroke (van Ingen Schenau et al., 1990). The work done at the joints was 4.4% lower than that done on the pedal, an error likely introduced experimentally by the placement of the markers indicating joint axes. The main advantage of this approach is that the equation unambiguously relates the inflow of energy from the joint moments to the segments and the outflow from the segments to the environment. It is thus convenient to distinguish between different forms of power and their possible transfer (which may be crucial to the understanding of aquatic movement mechanics).

Joint work

Muscle work—muscle force times muscle length changes—can hardly be obtained in human subjects. Procedures are invasive and are better performed in animals. Muscle work must therefore be estimated from the work done by the net moment at a given joint. Net joint mechanical work is taken from the integral of the power trace with respect to time. Positive and negative works are better computed separately over discrete periods of positive and negative power. Otherwise positive and negative works can cancel out and may not realistically represent the actual work done at the joint (Farris and Sawicki, 2012). They represent measures of the amount of mechanical energy generated and absorbed at the joint level (Zatsiorsky and Prilutsky, 2012).

Joint work has generally been regarded as the most accurate estimate of the work performed by muscles (Neptune et al., 2009). Now that complex musculoskeletal models have become an integral part of studying the mechanics of terrestrial locomotion, relationships between different measures of work could be precisely tested. Simulations of human walking allow the computation of every possible sources of work, and critically examine the extent to which joint work reflect musculotendon work (Sasaki et al., 2009). The sum of the net musculotendon work and net passive joint work was equal to the net joint work. Therefore, the authors concluded that net joint work could estimate net musculotendon work in locomotor tasks or subjects where net passive joint work is negligible (i.e., negligible contribution from joint capsule and connective tissues). Furthermore, since net elastic energy was null over a gait cycle, net joint work was also reliably representative of the net work performed by muscle fascicles. However, net mechanical quantities are not much useful to estimate overall mechanical work, metabolic cost or efficiency; total (absolute) work measures bear more physiological

relevance (Sawicki et al., 2009). Total joint work was found to underestimate total musculotendon work by ~7%. The underestimation was due to the combined contributions of antagonist–agonist muscle cocontraction, biarticular muscle work and passive (ligaments and connective tissues) work to the total joint work. Muscle cocontraction acted to increase the underestimation of total musculotendon work, while biarticular muscle work and passive work acted to decrease the underestimation. Inverse dynamics and joint-level work thus give a reasonably accurate access to in vivo, muscle-level quantities.

2.2.2. Inverse dynamics: what do we learn from it?

Now that the definitions of joint forces, moments, power and work have been clarified, we have identified three questions that inverse dynamics can specifically address. They represent, in our view, fundamental and/or novel knowledge that substantially enhanced our understanding of terrestrial locomotion mechanics, and thus are likely relevant to the study of aquatic movements.

Neuromuscular strategy of power production

To move in their environment, humans' and animals' musculoskeletal system must meet mechanical requirements by modulating muscle groups work performance. This can be accomplished in two ways. (i) All muscle groups of a limb contribute equally to the apportionment of mechanical work and power; or (ii) some muscle groups are better suited to that role and are recruited preferentially, therefore producing disproportionately high amount of work and power. Interestingly, the way this is accomplished is tightly linked to task mechanical demands; i.e., whether tasks require net positive work or not. Of the activities demanding on average no net work, steady level locomotion come directly to mind. Indeed, limb muscles are required to do negligible work because the net work on the body center of mass associated with potential and kinetic energy fluctuations is zero when averaged over a series of strides (e.g., Roberts and Belliveau, 2005). Moreover, very little work is dissipated against the environment to overcome friction at the interface between the ground and the shoes, or wind resistance. The first analysis of that sort was carried out by Winter (Winter, 1983). Through standard, sagittal inverse dynamics, he computed instantaneous lower limb joint power output in healthy adults

walking. The shape of power patterns was conserved across slow, natural, and fast cadences. Only peak magnitude was significantly affected. Notably, ankle power burst was closely related to the acceleration of the recovery leg, and in turn shortened stride periods. He concluded that increased cadence was a result of higher amount of energy produced/absorbed and not from an increase in the 'clock rate' of gait. Cadence increase appeared to be an effect of increased power, not the cause. Moreover, the tightness of power pattern timing with speed was, in his view, ample evidence of closed-loop control through afferent feedback, possibly from spindle receptors and/or Golgi tendon organs. Chen et al. (Chen et al., 1997) extended Winter's earlier analysis by computing joint work in walking children. Relative contribution of hip and knee work showed significant increases with increasing speed, while that of ankle work substantially decreased. The ankle, knee, and hip joint respectively contributed ~60, 20, and 20% at the lowest speed, and ~20, 50, 30% at the highest. They discussed that this redistribution indicated a shift in ankle joint function from propulsion at slower speeds to stability at faster speeds. Furthermore, it marked a transfer of work to larger muscle groups, which eventually permits the muscles to work at a lower percentage of their maximum capacity and therefore optimize energy consumption during gait. Data from Teixeira-Salmela et al. (Teixeira-Salmela et al., 2008) lend further support from a proximal redistribution of joint work (for a range of speeds [0.7–1.4 m s^{-1}]). However, no modulation at all of lower limb joint relative contributions to total work were noted while exploring a larger spectrum of walking speeds up to 2 m s^{-1} (Farris and Sawicki, 2012; Schache et al., 2015), contradicting previous experiments.

In running, Belli et al. (Belli et al., 2002) found that relatively little negative work was done at the knee and ankle regardless of running speed. This indicated only short periods of stretching, and the authors assumed for that reason that it might be due to high muscle cocontraction preventing the body to collapse during stance. The hip behaved much differently, being the main motor powering the contact phase. Bursts of negative and positive power followed, very much indicative of the storage of energy as the leg was vigorously brought forward and its release during leg traction. Joint work was not computed though, so that the relative contribution of lower limb muscle groups to total task demand was not discussed. In a study by Schache et al. (Schache et al., 2011), ankle work during stance was found to increase by 30% between 3 and 5 m s^{-1} then plateau, while knee work remained constant and hip work during swing increased by 300%. This

led the authors to think that increases in running speed were unlikely to be caused by proportional increases in joint work. Relative joint contributions were calculated more recently (Farris and Sawicki, 2012). No statistical differences were observed from 2 to 3.25 m s^{-1}, a result later supported by Schache et al. (Schache et al., 2015) for a wider range of speeds (up to 7 m s^{-1}), whether during stance or swing.

Overall, increased mechanical demands (e.g., increased locomotion speed) are achieved through proportional increases in work simultaneously at all joints when the task requires no net work input. This agrees with forward dynamics simulations of human gait. Human walking could indeed be successfully simulated at various speeds with unvarying apportionment of work at the lower limb joints to achieve trunk support, forward propulsion or leg swing (Neptune et al., 2008). In other words, muscle function was invariant. Moreover, experimental results do lend support to the idea that complex movements are controlled modularly. Accordingly, the central nervous system adopts a simple control scheme in which muscles assuring a similar function are grouped together, forming a few set of invariant muscle synergies or 'modules'. These motor modules act at the spinal cord triggering selected central pattern generators that evoke specific motor behavior, hence simplifying motor coordination and the accomplishment of complex motor tasks (Lacquaniti et al., 2012). For example, walking mechanics under different mechanical demands could be robustly reproduced through tuning module recruitment intensity alone (McGowan et al., 2010).

Tasks requiring a net work input show a fundamentally different power modulation strategy. When running uphill, net positive work is required to increase body's potential energy over each step. As incline got steeper, net work at the hip dramatically rose, whereas ankle and knee work remained unchanged (Roberts and Belliveau, 2005). A fairly different observation was more recently made in the hindlimb of goats as they ran on inclined terrain, as all lower limb joints contributed significant work (Arnold et al., 2013). This is likely a functional difference between bipedal and quadrupedal locomotion. The hindlimb not only provides propulsion but also improved support, which may consequently redistribute ground reaction force to a much larger extent than in bipeds. When accelerating on level terrain, there is a need for positive work input to increase body's kinetic energy over time. Accelerations in wild turkeys were performed primarily through almost equal and linear increases in work at the hip and ankle joints with higher

accelerations (Roberts and Scales, 2004). Humans accelerating also displayed an identical strategy, with the hip and ankle increasing their motor-like function (Qiao and Jindrich, 2016). Joint function was assessed through the calculation of an index taking into account the positive work done during stance minus the fraction that could potentially be stored and returned (i.e., minus the minimum of negative work during compression and positive work during push-off).

Increased mechanical demands (e.g., increased incline) are achieved through disproportionate increases in work at the proximal joints when the task requires net work input. This is consistent with the morphology of proximal muscles. They are generally large and composed of long, parallel fibers with little or no free tendon, allowing them to strain over long distances and favoring a role in work production. It is thus logical to see that proximal muscles become predominant to accommodate net work requirements of the environment.

The work performed by a muscle during its contraction is the product of the force developed and the distance shortened. Increased mechanical work output can thus be achieved through either producing higher forces or shortening more, which would be apparent in increases in joint moments or joint excursions. During level acceleration, changes in joint moment the orientation of the ground reaction force vector were small (Roberts and Scales, 2004). Turkeys rather relied on a more than threefold increase in hip extension, and ankle excursion increased from a net flexion to a net extension. Assuming that muscle shortening is proportional to net joint excursion and muscles force are proportional to joint moments, the authors concluded that the primary mechanism for increasing mechanical output during level acceleration was from an increase in muscle shortening, rather than higher muscle force. In the study of Roberts and Belliveau (Roberts and Belliveau, 2005) though, increased hip work output with incline was primarily achieved through alterations in joint moment, rather than joint excursion. This mechanism resulted, in turn, from a change in mechanical advantage with which muscles produced force against the ground. Specifically, the ground reaction force vector was oriented more forward of the hip during incline compared to level running, and, as a result, moment arm was larger. This increased the work to be produced to balance the external joint moment, and muscles operated at poorer mechanical advantage (the ratio of the average of the muscle moment arms acting at a joint and the effective moment

arm of the resultant ground reaction force (Biewener, 1990). The authors hypothesized that such a change in mechanical advantage may provide a mechanism for selectively utilizing different muscles for different locomotor tasks. This analysis of mechanical advantage therefore shows great relevance to our understanding of movement energetics and muscle function.

As far as tasks requiring net work input are concerned, there is a subtle nuance to introduce with respect to non-steady tasks. In effect, those require only transient changes in mechanical work over the course of a few cycles (or strides), ecologically closer to an animal's behavior in its natural environment. This mechanical distinction is important, and relevant to the understanding of motor control with altered interaction between the limb and the ground. Daley et al. investigated how a running guinea fowl negotiated a sudden unexpected pothole in terrain (camouflaged by paper to remove visual cues) from the viewpoint of limb and joint mechanics (Daley et al., 2007). This perturbation resulted in a significant loss of potential energy (~40% of the bird's hip height), which must have been accommodated by the animal's muscles as it fell and make contact with the force platform below. Interestingly, they observed two modes for stabilizing the perturbed vertical motion of the body. Essentially, the distal joints acted as dampers when the limb touched the ground with an extended knee, resulting in net energy absorption. In contrast, when the limb contacted the ground with a flexed knee, the distal joints acted as springs, associated with net positive limb work. Work performance at the hip was however maintained. Such a posture-dependent work performance of the distal joints at the time of ground contact suggests that intrinsic mechanical factors also mediate increases in work output, in addition to feedforward-controlled demand at more proximal joints. Higher proprioceptive feedback gain and greater sensitivity to limb loading distally supported a proximo-distal gradient in joint neuromuscular control, shedding a new light on the complex interplay between the environment, neural and intrinsic mechanical factors.

Aquatic movements naturally combine both specificities described above. They require net positive work input to replace the energy inevitably lost against the dissipative, unstable load of the water as body parts continuously interact with it. This is an unusual interplay of properties that is unseen on land. It can therefore be anticipated that movements in water have the potential to unveil new motor strategies, or, at the very

least, to provide new insights into the mechanics of human movement. This fundamental question will be purposely addressed in the present thesis.

Joint function/dynamics

In 2D, negative/positive power is traditionally associated with eccentric/concentric muscle actions, whereas a null power is due to a null joint moment or a null joint angular velocity; the latter indicating an energy transfer associated with an isometric muscle action (Robertson and Winter, 1980). In 3D though, power analysis is more controversial (Dumas and Chèze, 2008). A null power can alternatively be due to the joint moment and joint angular velocity vectors being orthogonal to each other, which warrants further investigation. Moreover, unlike joint moment, joint power cannot simply be decomposed into three components along the three axes of a coordinate system, as power is a scalar quantity. Last, mechanical power does not readily inform about joint dynamics, nor does it indicate the proportion of the joint moment contributing to the movement (Samson et al., 2009).

For ease of interpretation, Dumas and Cheze (Dumas and Chèze, 2008) proposed the computation of the 3D angle $\alpha_{\mathbf{M}\boldsymbol{\omega}}$ between the joint moment $\mathbf{M}$ and the joint angular velocity $\boldsymbol{\omega}$ according to:

$$\alpha_{\mathbf{M}\boldsymbol{\omega}} = \tan^{-1}\left(\frac{||\mathbf{M}\times\boldsymbol{\omega}||}{\mathbf{M}\cdot\boldsymbol{\omega}}\right). \tag{2.9}$$

Equation 1 returns an angle positive in the range [0–180°]. Recalling that joint power P equals:

$$P = ||\mathbf{M}||\,||\boldsymbol{\omega}||\cos\alpha_{\mathbf{M}\boldsymbol{\omega}}, \tag{2.10}$$

Dumas and Cheze (Dumas and Chèze, 2008) identified three intervals of interest. When $\alpha_{\mathbf{M}\boldsymbol{\omega}}$ is in the interval 0–60° (i.e., $\cos\alpha_{\mathbf{M}\boldsymbol{\omega}}>0.5$), it follows from Equation 2 that more than 50% of the joint moment contributes to positive joint power: the joint is said to be in a propulsion configuration. When $\alpha_{\mathbf{M}\boldsymbol{\omega}}$ is in the interval 60–120° (i.e., $|\cos\alpha_{\mathbf{M}\boldsymbol{\omega}}|<0.5$), less than 50% of the joint moment contributes to either positive or negative power: the joint is in a stabilization configuration. Finally, when $\alpha_{\mathbf{M}\boldsymbol{\omega}}$ is in the interval 120–180° (i.e., $\cos\alpha_{\mathbf{M}\boldsymbol{\omega}}<-0.5$), more than 50% of the joint moment contributes to negative joint power: the joint is in a resistance configuration. It can be noted that for a given set of $\mathbf{M}$ and $\boldsymbol{\omega}$,

P is maximal only when both vectors are aligned ($\alpha_{\mathbf{M}\boldsymbol{\omega}}$ = 0 or 180°); i.e., when 100% of the mechanical action at the joint translates into movement. Reciprocally, this angle is independent of the norm of both vectors and can always be computed, however small the vector magnitude is. Thus, an angle of 0 or 180° does not necessarily imply a peak of power. Such computation is therefore essential since it is the only way to gain insight into the fraction of the joint moment that contributes to power (that is, the observed movement). For example, it might very well be that joint moment and joint angular velocity peak simultaneously, but by virtue of the 3D nature of the movement, they might only result in small power output because of how vectors are oriented in space.

Using this measure, Dumas and Cheze (Dumas and Chèze, 2008) investigated instantaneous lower limb joint function in healthy subjects walking. The hip was in a stabilization configuration throughout the stance, with notable changes at pre-swing to propulsion and early swing to resistance. The knee was in the same configuration during stance with the exception of resistance at weight acceptance, whereas it turned to propulsion during early swing and resistance during late swing. The ankle was found to be predominantly stabilized during swing, showing resistance configuration during stance and propulsion at pre-swing (at push-off). Importantly, none of these joints were fully driven; i.e., the 3D angle $\alpha_{\mathbf{M}\boldsymbol{\omega}}$ never reached either 0 or 180°. The fact that they were, however, in pure stabilization ($\alpha_{\mathbf{M}\boldsymbol{\omega}}$=90°) at different instants of the stride and for varying durations likely reflected anatomical differences in joint type, which requires different amount of stabilization. A hinge (the knee), for instance, naturally requires much less stabilization than a ball-and-socket joint (the hip). Combined with the analysis of joint moments, stabilization was observed to be achieved through abduction actions, consistent with previous EMG recordings. A traditional power analysis could not have provided such insightful conclusions as to the role of these joint moments.

The same procedure can be used to investigate possible differences in motor strategies between populations. In children vs adults, computation of the 3D angle $\alpha_{\mathbf{M}\boldsymbol{\omega}}$ successfully helped in characterizing and understanding level of gait maturation (Samson et al., 2009). Significant differences were observed at the ankle joint. During the loading phase of walking, children showed a resistance configuration vs stabilization in adults. Distinct ankle function was attributed to different flexion/extension moments, likely because of flat foot contact in children vs heel strike in adults. At mid-stance, children

showed a stabilization configuration while adults were in a resistance configuration. Although both showed an extension moment at the ankle, it resulted in negative power only in adults to slow down their more important anterior mass transfer. Likewise, at pre-swing, children and adults both revealed extension moment, although it only produced minimal energy in children (stabilization configuration) whereas adults showed a propulsion configuration. Overall, children never exhibited a propulsion configuration at the ankle, which is consistent with the fact that mature ankle function (its propulsive role during gait) is only acquired later on (~6–9 years old, against 3 in their experiment). No differences were noted at the knee. At the hip, children were in a propulsion configuration for about 80% of the stride, against only 56% for adults whose hips were mostly stabilized. However, only a small fraction of hip joint moment produced the calculated power in children (~60%), indicating important wastage at that level. Motor strategies are adequately unveiled through the calculation of this 3D angle—with children mainly stabilizing the ankle and propelling the hip whereas adults stabilize and propel the ankle while stabilizing the hip—and provide valuable, complementary evidence for inter-individual differences in gait dynamics.

More broadly, the calculation of the 3D angle can provide an additional tool to better identify the risk of developing pathologies. In the case of level manual wheelchair locomotion, for example, the rationale is that analyzing further the contribution of individual joint moments to joint dynamics may allow a better understanding of propulsion mechanics, and yield potential mechanistic causes of injury (Desroches et al., 2010b). Upper limb joints were all found to operate mainly in a stabilization configuration, with only a short period of propulsion at the shoulder during the push phase (~30% of total cycle duration). The authors argued that, from a mechanical point of view, such a system requiring strong stabilization to achieve movement is surely sub-optimal. The fact that an important fraction of upper limb joint moments did not produce energy partly explained the low mechanical efficiency of this particular locomotion. However, from an anatomical standpoint, stabilization can be seen as essential to maintain joint integrity. At the wrist, stabilization while the forces generated by the upper limb were transmitted to move the wheel forward was achieved by either an extension moment or an ulnar deviation moment, or a combination of both. This placed the wrist in an awkward position, possibly explaining, in part, the high incidence of repetitive strain injuries at the wrist. At the shoulder, although the joint was driven in

propulsion during the push phase, only slightly more than 50% was allocated to that task. In other words, shoulder remained largely stabilized, consistent with its ball-and-socket nature and the need to provide active stabilization. This simultaneous need of stabilization and propulsion is assumed to relate to increased muscle fatigue (particularly of the rotator cuff muscles), and possibly shoulder injury. The interesting matter that must be investigated is this balance between both functions, and whether a trade-off exists in particular populations. Stabilization at the elbow was done thanks to high abduction moment. Since muscles crossing the elbow possess only short abduction/adduction moment arms, the authors advanced that these moments were likely the result of passive structures such as articular surfaces and ligaments. By analogy with the knee, passive vs active stabilization is mechanically advantageous since passive structures can sustain high loads, hence clarifying why elbow is the joint least prone to overuse injuries among manual wheelchair users.

In aquatic movements, large forces are produced through fast elbow and shoulder rotations (since hydrodynamic forces are proportional to the square of velocity), which requires joint compliance (Gottlieb, 1994); force transmission across the joint towards the trunk, by contrast, asks for stiffness (Fornalski et al., 2003). Thus, for example, the more compliant the elbow joint, the faster the elbow movement and the greater the force production at the expense of a weakened force transmission capability. There should therefore exist an optimal neuromuscular balance between upper limb joint stiffness and compliance to efficiently generate thrust power and ultimately propel the human body in water. Acknowledging that higher joint stiffness is accompanied by an increase in joint stability (Baratta et al., 1988), there must be a compromise between the joints being simultaneously driven and stabilized throughout the movement. Addressing this question would shed a new light onto the mechanics of aquatic force generation, and elucidate the decline in Froude efficiency with fatigue. Yet, investigating the balance between these two functions is a hard task. Thoroughman and Shadmehr (Thoroughman and Shadmehr, 1999) had introduced an elegant approach based on EMG measurements where signals were partitioned into portions responsible for increased stiffness (muscle cocontraction) and another for setting segments in motion. Cocontraction during the movement was estimated using a measure termed "wasted contraction", computed as the minimum normalized EMG value of an antagonistic muscle pair. This yielded a time series representing the magnitude of normalized EMG that was cancelled by the larger,

opposing activation (i.e., EMG in opposing muscles that increases joint impedance (Gribble et al., 2003), and contributes to force transmission). Second, subtracting this smaller trace from the larger gave a second time series of "effective contraction" (believed to contribute to movement). Nonetheless, EMG–stiffness and EMG–force relationships in dynamic conditions are inherently complex (and quantitatively different from those during isometric contractions) because of nonlinear muscle mechanical properties (Osu et al., 2002). Therefore, equal EMG levels in antagonist muscles may possibly yield unequal opposing torques. In other words, the "wasted contraction" might still contribute to joint movement to a small extent, and, reciprocally, the "effective contraction" to increased joint impedance. Inverse dynamics and the analysis of the 3D angle between the joint moment and joint angular velocity vectors may offer a new and promising avenue for addressing this issue.

Joint loading evaluation

Improving our knowledge about joint function, and, more practically, understanding how injuries may develop, are two important themes for clinical applications. On land joint loading patterns serves a fundamental role in injury causation model, particularly in the description of the inciting event leading to injury (Bahr and Krosshaug, 2005). Thanks to inverse dynamics, ankle joint moment patterns could be very precisely documented during ankle sprain in a laboratory setting. The ankle was loaded to unphysiological levels about the axes of inversion and internal rotation compared to control trials, likely exceeding ligament limits and causing the injury (Kristianslund et al., 2011).

Identifying the determinant factors of joint loading also allows the researchers to optimize preventive interventions and training protocols by targeting specific variables. Knee joint loading during sidestep cutting, for example, was best predicted by technical factors (e.g., knee valgus angle, approach speed, cutting angle, cut width, toe landing), accounting for 62% of the variance in peak knee abduction moment (Kristianslund et al., 2014a). Clarifying relationships between easily observable kinematic features and hidden joint kinetics provides valuable guidance to coaches or physiotherapists to prescribe safer exercises. The effectiveness of a program can then be objectively evaluated through comparing pre- and post-intervention limb loading. Risberg et al. (Risberg et al., 2009) investigated potential changes in lower limb joint moments while walking and hopping

after a 20-session strength training following anterior cruciate ligament surgery. Knee extension moment was completely restored during walking, whereas it was still impaired (compared to the non-injured side) during hop landing. On that basis, the authors encouraged a reevaluation of the traditional rehabilitation program duration and exercise type, in particular prior to returning to sport activities including jumping tasks.

These examples are some of many ways that can hardly be explored in water precisely because internal load cannot be adequately evaluated. This is particularly harmful for aquatic rehabilitation. Therapeutic exercises in water have become a very popular modality to provide pain relief and improve muscle strength and overall fitness for a wide variety of neurological and musculoskeletal conditions (e.g., (Hall et al., 2008)). Thanks to buoyancy, the upward thrust that counteracts the action of gravity, water offers near-weightlessness exercise conditions. This unique physical property was found to significantly accelerate the restoration of shoulder flexion range of motion as early as three weeks post surgery (Brady et al., 2008). Furthermore, water is very viscous and thus highly dampening. Resistance rapidly decays upon cessation of movement, which is believed to dramatically reduce the risk of reinjury (Prins and Cutner, 1999).

However, there is a mismatch between the popularity of these interventions and the paucity of evaluations of their efficacy (Pittler et al., 2006). This issue, accompanied by the lack of treatment guidelines and best practices, prevents therapists from prescribing accurate rehabilitation program (in terms of volumes/intensities and types of exercises) and predicting patient dose responses. Such lack of knowledge also hinders the development of specific rehabilitation equipment. That uncertainty in the prescription (but also in diagnosis) is critical since it conditions the success of an intervention, and hence costs for healthcare systems and the economy. In Portugal, for instance, the total indirect cost of chronic joint pain was estimated at approximately €740 million in 2008, with a considerable productivity loss of 0.5% of the gross domestic product (Gouveia and Augusto, 2011). In just two years, total costs rocketed to €4,600 million (with 57% indirect costs), corresponding to 2.7% of Portuguese 2010 GDP (Azevedo et al., 2016). On top of that, the financial crisis has led to the desire to reduce healthcare expenditure, and placed greater focus on cost-effectiveness, in line with the authors' recommendations to improve the quality of pain management and associated research should be a priority (Azevedo et al., 2016).

As emphasized by Biscarini and Cerulli (Biscarini and Cerulli, 2007), critically examining therapeutic protocols might be achieved by assessing joint forces when moving in water, a step that will prove crucial to plan effective therapeutic exercises and understand all the clinical implications. There is a real need to rely on scientific evidence (Daly and Lambeck, 2007). Without the tools for a strict evaluation of joint load, researchers have resorted to alternative, indirect measures from which to infer joint loading levels. Consider the shoulder, for example, which is the third joint most affected by musculoskeletal disorders (Urwin et al., 1998). The latest American Society of Shoulder and Elbow Therapists' consensus promotes the use of slow (30°/s) aquatic scapular plane movements to initiate aquatic therapy (Thigpen et al., 2016). The guideline is based on a key observation of electromyographical (EMG) studies of muscles crossing the shoulder (Castillo-Lozano et al., 2014; Kelly et al., 2000). At 30°/s, activity of the deltoid and rotator cuff muscles was on average ~2–5× lower in water than on land. Assuming load was proportional to muscle activity, the authors concluded that slow underwater shoulder exercises were safe enough for early active mobilization.

Continua of exercises for progressive aquatic rehabilitation have been designed following the same logic. Optimal, gradual planning of aquatic exercises is a difficult task (Colado et al., 2008; Pöyhönen et al., 2001a). Shoulder musculature loading should be tailored so as not to exceed biomechanical limits of healing tissues, which might cause pain and tendon repair failure (R. J. Neviaser and T. J. Neviaser, 1992). Sufficient solicitation should be guaranteed though, not to deteriorate joint mobility (Schollmeier et al., 1994) and gradually restore joint function before transitioning to dry-land exercises. Kelly et al. (Kelly et al., 2000) consistently measured lower normalized integrated EMG when performing slow to medium speed (<45°/s) underwater scaption in the range 0–90° vs on land. By contrast, Castillo-Lozano et al. (Castillo-Lozano et al., 2014) observed similar activation levels between media at 45°/s, leading them to hypothesize that this speed actually constitutes a threshold at which aquatic exercises turn from assisted to resisted. They proposed a protocol whereby shoulder exercises are implemented first in the water at slow speeds (30°/s), then indifferently in water or on land at medium speeds (45°/s) prior to land-based routines (90°/s). However, EMG recordings only offer insight into individual muscle activation level and are poor indicators of joint mechanical load (Winby et al., 2013; Zajac et al., 2002).

Rather, an aquatic exercise's intensity would be best monitored through a noninvasive estimation of its actual mechanical demands on the musculoskeletal system. Inverse dynamics analysis has the potential to provide an in-depth evaluation of the loading of a joint and its musculature, as well as to inform aquatic rehabilitation protocol design. This is essential to understand all clinical implications and optimize treatment effectiveness. One final goal of the present thesis will therefore be to explore this opportunity to provide clinicians and health professionals with nonempirical knowledge of joint mechanics in water and straightforward equations to evaluate exercise intensity and plan progressive rehabilitation protocols.

We have identified in this chapter three central issues relevant to our understanding of aquatic movement mechanics. The neuromotor strategy of power production and the corresponding joint dynamics, as well as the loading of the musculoskeletal system during aquatic exercises of all sort collectively highlight the richness of the knowledge that can be brought by inverse dynamics. Such knowledge however remains out of reach because of the difficulty in measuring external forces and locating the points at which they act. These concerns are addressed in the following chapter.

3 Measurement of external forces in the water

The key input to inverse dynamics analysis is an accurate measure of the external forces and their points of application. External forces are hard to measure in water though, unlike on land where they are easily measured via force platforms during support on the ground. This limitation has significantly slowed down the way towards the estimation of internal load during aquatic movements. Scientists came up with ingenious solutions to estimate hydrodynamic forces though, presented in the following sections together with notable contribution to research progress.

3.1. Analytical force calculations

The forces acting on an immersed object (drag D, the component that is parallel to the flow direction; lift L, acting perpendicular to the flow direction) are commonly described as a function of fluid density (ρ, kg·m^{-3}), object surface area (S, m^2), and its velocity relative to the fluid (u, m·s^{-1}) according to the standard formulae:

$$D = \frac{1}{2}\rho C_D S u^2, \tag{3.1}$$

$$L = \frac{1}{2}\rho C_L S u^2, \tag{3.2}$$

where C_L and C_D are the lift and drag coefficients. These are dimensionless parameters dependent on object orientation, defined at the hand in terms of angle of attack (or pitch angle; i.e., between the plane of the hand and its velocity vector) and the sweepback angle (i.e., the projection of the hand velocity vector onto its plane). Once they are determined

experimentally in a multitude of hand position, the analysis is rather straightforward: hand kinematics is recorded during actual swimming motion, and injected in the above-mentioned equations in combination with the corresponding coefficients to separately estimate lift and drag.

Although the hydrodynamics of swimming force propulsion were first envisaged empirically by James Counsilman (Counsilman, 1970) and Charles Silvia (Silvia, 1970), Schleihauf (Schleihauf, 1979) was the first to tackle the problem experimentally. Plastic resin hand models were sunk in an open-water channel in 19 pitch angles in the range 0–90° and eight sweepback angles in the range 0–360° while two-dimensional forces were measured by a strain-gauge apparatus. No indication was given regarding the flow conditions. Schleihauf so obtained (after rearranging the two equations) the very first hand lift and drag coefficient profiles as a function of its position relative to flow. Interestingly, he also confirmed the striking resemblance between a hand and an airfoil on the basis of their lift production capabilities[3]. The study was partially replicated about 15 years later by Berger et al. (Berger et al., 1995) towing two different hand and forearm models in a tank, this time measuring three-dimensional forces. They extended Schleihauf's seminal work by examining further the effect of speed (0.3–3.0 $m \cdot s^{-1}$) and possible interaction between hand and forearm by varying the immersion depth. Crucial observations were made that improved our understanding of force production in water. Most of the hydrodynamic forces (lift, mainly) were produced at the hand, whereas the forearm contributed very little. Drag and lift coefficients were relatively constant at speeds >1 $m \cdot s^{-1}$. Last, models similar in shape but different in size showed substantial deviations in hydrodynamic profile at low pitch angle, hence widely different capabilities to generate forces. Subsequent studies focused on improving the accuracy of hand position reconstruction (Gourgoulis et al., 2008a; Lauder et al., 2001), to popularize the use of this procedure to estimate fluid forces in various conditions (Gourgoulis et al., 2008b; 2015).

[3] Anecdotally, experiments in wind tunnel by Wood challenged this view of lift being the predominant force. Rather, "swimming propulsion is the result of subtle and changing combinations of lift and drag forces. The opportunities for either one or the other to be solely responsible for swimming propulsion are very limited, and roles are seen to change." (Wood, 1979)

The analysis is known as *quasi-steady*, that is, based on the assumption that the actual forces produced while swimming under unsteady flow conditions are equal to the forces exerted on immersed bodies in water tank under steady conditions (constant speed and hand orientation). Yet, despite its appealing simplicity, the accuracy of the approach has been seriously questioned. When compared to the average body drag obtained from the MAD system (which theoretically must equal the average propulsive force at the hand and forearm), forces were overestimated by 17% (Berger et al., 1999). Displacing the point at which hand+forearm speed is computed from the tip to the midpoint of the middle finger improves the prediction down to a 5% overestimation, whereas forces were underestimated by 21% when computed from the fifth metacarpophalangeal joint (Berger et al., 1999). Such sensitivity to the location of an imaginary point makes the reliability of hydrodynamic forces calculated analytically highly hazardous. Ideally, the center of pressure should be determined from the integration of the full hydrodynamic picture around a given segment.

The fact remains that the calculated force does not entirely capture all mechanisms of force production. Indeed, a quasi-steady analysis implicitly ignores unsteady mechanisms of force production (vortex shedding, added-mass effects (Dickinson, 1996)), particularly present in accelerating segments. Pai and Hay (Pai and Hay, 1988) were aware of this issue as early as 1988. They aimed at evaluating the validity of the quasi-steady assumption through comparing analytical and experimental hydrodynamic profiles of a cylinder oscillating at various frequencies. Differences were very small (<0.1) at low frequency (0.3 Hz), whereas dynamic, experimental coefficients were 2–4 higher than those computed according to the quasi-steady assumption at 1.3 and 2.4 Hz. They warned that the approach must not be used at high frequency/large accelerations given how inaccurate it is. For swimming motions under similar conditions, the authors urged the need to take unsteady mechanisms into account to reach satisfactory accuracy.

With that in mind, Sanders computed two additional coefficients proportional to hand acceleration to account for inertial force and added mass to total force (Sanders, 1999). These effects could contribute up to ~60% of the total drag in stroke phases of large acceleration and reduced velocity, such as after the catch. Furthermore, he reported hydrodynamic coefficients ~2× lower than those computed until then. Surprisingly, he

suggested that Schleihauf's and Berger's data might have been significantly overestimated because of free-surface effects when towing the models near the surface.

Further evidence was brought forward by Lauder and Dabnichki in support of the inadequacy of the quasi-steady assumption (Lauder and Dabnichki, 2005). In a study design similar to that of Pai and Hay (Pai and Hay, 1988), they compared shoulder torque profiles derived from forces calculated analytically and forces measured directly via an instrumented robotic arm. Arm movement was simply described by a cosine wave, and elbow angle could be varied from 110 to 180°. Clear differences in profiles were found, particularly in the early phases of the movement (where, as observed by Sanders (Sanders, 1999), the neglected force related to inertia and added mass likely contributed significantly to the total force). Average and peak torques estimated using the quasi-steady approach deviated by as much as ~50% from the measured ones. The authors concluded that the quasi-static assumption was unreliable. Moreover, since hand relative contribution to total force strongly depended on elbow configuration, they challenged the widely shared idea that the hand is the major contributor to hydrodynamic force propulsion; the forearm is likely just as important.

Importantly, the quasi-steady assumption disregards the pumped-up effect unveiled by Toussaint and colleagues whenever movements are largely rotational (Toussaint et al., 2002). As the upper limb rotates, a velocity gradient along the arm builds up (the tangential velocity being higher distally), which is accompanied by a corresponding pressure gradient where the local pressure in the vicinity of the arm drops in direction of the fingertips. This induces, in turn, an axial fluid flow along the arm towards the extremity, as seen in rotating wings of hovering insects or around wind turbine blades. As a result, the pressure on the dorsal side of the hand strongly decreases, which contributes to increase the pressure difference over the hand and, ultimately, propulsion.

3.2. Blade element or strip theory

A direct extension of the quasi-steady analysis described above is the blade element or strip theory. The propulsive surface of interest is treated as a simple geometrical shape, and partitioned into a finite number of slices that are assumed to individually contribute

to propulsion. This approach was originally developed in the field of ship hydrodynamics to estimate the load acting on the hull and predict ship motion (Newman, 1977). It was first reported in biology back in 1979 to calculate the thrust, work and power produced by a fish pectoral fin from pressure drag and added mass integrated over all elements (Blake, 1979). The same methodology was later used to estimate the thrust on frog feet during the kick (Gal and Blake, 1988), and more recently to thoroughly explore frog kicking performance (Richards, 2008). Translational and rotational components of foot velocity were considered, which allowed the authors to dissect the components of thrust. Furthermore, the blade element model was coupled with a forward dynamic approach to create a generalized model of frog swimming. The time varying thrust due to foot kinematics was solved, and further used to predict time-varying acceleration and velocity of the frog body. Therefore, the effects of manipulating hind limb kinematic patterns on the overall kick performance could be directly observed and quantified. Rotational motion produced significantly more impulse than translational motion, and was sufficient to counteract the retarding thrust related to foot translational deceleration. To verify the model, simulated center of mass kinematics output from the model were compared to actual frog swimming. The numerical model was found to reliably predict the temporal pattern of the swimming velocity profiles, although velocity magnitude was slightly underestimated (within 15% of the observed data).

Blade-element theory provided a framework to examine the hydromechanics and energetics of bottom feeding in ducks (Ribak et al., 2010). The model accurately predicted both the direction and magnitude of the propulsive force during the first 80% of the paddling cycle, yet failed at the transition between power and recovery stroke due to the predominance of unsteady flow phenomena during this period (likely, vortices shed in the wake as feet quickly rotate). Moreover, the mass-specific power output reported by Ribak and colleagues was more than twice as large as values reported until then. This large discrepancy stems from the fact that they reported total mechanical power exerted in paddling whereas the earlier values referred to the power needed to move the body. Power output would theoretically be the same only if the feet were 100% efficient in converting all the momentum from the water moved into thrust that is directed in the direction of swimming. Since some of the energy spent on producing the propulsive force is always lost during swimming, power calculated from the observed body motion is always lower than total power.

In humans, this analytical approach has successfully been applied to address clinical questions related to the estimation of joint load. Biscarini and Cerulli employed the strip theory coupled with a simple biomechanical model of the knee to derive the patellar tendon force as well as shear and axial components of the tibiofemoral joint load during underwater knee extension exercises (Biscarini and Cerulli, 2007). Hydrodynamic forces on a resistive device placed on the shank were calculated by treating individually parallel slices onto which drag, added mass and buoyancy acted. This information was then injected in the biomechanical model that is dependent on the properties of the system (dimensions and mass of the device, kinematical parameters and drag and added mass coefficients). As a result, kinetic parameters could be solved for varying system configuration, which allowed for the identification of regions of the total range of motion where the anterior cruciate ligament was not solicited. Region boundaries were found to be independent of muscular activation level (maximum angular velocity in the range 100–500° s^{-1}), but shifted to the right (i.e., favoring a protective role of the aquatic exercise on the ligamentous structures) as the surface of the device increased. The strength of the approach is that the hypothetical joint loading space can be explored by mapping a single output (e.g., patellar tendon force) against two independently varied inputs (e.g., knee angle and resistive device properties). Results are plotted in the form of maps (possibly color-coded) that ease reading and detection of favorable combinations of inputs. Biscarini and Cerulli provided a framework from which to knowingly select specific device characteristics to target desired level of muscle activity while maintaining peak load below certain thresholds (Biscarini and Cerulli, 2007).

Strip theory was later used to calculate the hydrodynamic forces exerted on the lower limbs when humans walk (<0.5 m s^{-1}) in shallow water, and ultimately compute internal joint kinetics (Orselli and Duarte, 2011). Lower limb joint forces and moments were overall significantly lower in water than on land. Compressive force peaks in water were ~2–3× inferior, whereas differences in shear forces between media attenuated towards the hip (from ~4–5× less at the ankle and knee to ~2–3× less at the hip). Extensor moments at the ankle and knee were drastically reduced, whereas they were unchanged at the hip, paralleling the changes in water depth: the closer the joint is to the surface, the lesser the reduction in load. Expectedly, decreases in mechanical power in water were important, consistent with the severe reduction in movement speed under the water.

These results gave interesting insight into joint function. The authors discussed that significant work and power reductions at the ankle *extensors* were consistent with its role in providing support to body weight—severely diminished in water due to buoyancy. However, as originally discussed by Sutherland et al. (Sutherland et al., 1980) that the authors cited, this is the main feature of the ankle *flexors*, where no differences were noted between water and land. We believe that reduced, yet still present, ankle power at push-off is rather indicative of a different mechanism, evidenced three years after the paper was published. This seems in line with the understanding that the major role of the ankle extensors is to power leg swing rather than to restore the mechanical energy lost during foot collision (which was found to be null in water) (Lipfert et al., 2014). The accuracy in determining drag was assessed by comparing the change in whole body momentum along the anterior-posterior direction due to the estimated drag with that due to the ground reaction force. Values were generally in good agreement, although the trend indicated a slight, systematic overestimation. This procedure provides a criterion to validate total drag computation over the support phase of walking in water, but by no means reflects the accuracy of the calculations on a segment-by-segment basis.

In 2007, Japanese researchers introduced a swimming human model (SWUM) aimed at exploring whole body dynamics in swimming and providing a tool to analyze various mechanical problems in water (Nakashima et al., 2007). Rigid body dynamics and strip theory were applied to a human body model made of 21 body segments represented as truncated elliptic cones whose dimensions match subject morphology. Normal and tangential drag, inertial force due to added mass and buoyancy were computed on each cone at thin elliptic slices and then solved for body center of mass motion. Hydrodynamic coefficients were determined through optimization procedure minimizing the errors between numerical and experimental values of moment at various angles of attack; errors associated with fluid force modeling were thought to be ~10%. Simulated front crawl compared favorably with the observed motion, the predicted stroke length being 7.5% smaller than the actual one. The coefficient of active drag was however more than twice as large as those previously reported in the literature (Nakashima, 2007). The discrepancy was attributed to errors in estimating fluid forces and joint motion. Short duration of computation is appealing for parametric studies, and the simulation of the effects of slight alterations in kinematics or joint moment capabilities. The model of Nakashima et al. was capable of predicting the curved and straight pull paths during front

crawl (as well as the high elbow catch feature) only on the basis of maximizing swimming speed or propelling efficiency at discrete stroke durations (Nakashima et al., 2012). Simulated swimming speeds agreed with those measured during top-level swimming events, although swimmer strength seemed to be somewhat overestimated (stroke cycle duration was underestimated at top speed, whereas swimming speed was exaggerated at maximum efficiency).

The main prowess achieved by the team was to couple their software with musculoskeletal modeling in order to estimate the forces develop by individual muscles (Nakashima and Motegi, 2007). After comparing simulated muscle forces to muscle activation levels recorded in vivo, the authors concluded that patterns exhibited "a certain validity". More objectively, temporality was not quite preserved (particularly at the anterior deltoid and latissimus dorsi). This was a rather artificial validation though, since EMG was collected in a former experiment on a different subject. An additional validation stage was later conducted through the simultaneous comparison of both measures in a single subject during the same trial in breaststroke (Nakashima et al., 2013). However, satisfactory agreement (relative to peak timing and overall pattern shape) between predicted and measured EMG was only found at the triceps brachii and pectoralis major; significant deviations were noted at the biceps brachii, latissimus dorsi, deltoid, rectus femoris, biceps femoris, and tibialis anterior. While this level of accuracy might be sufficient for a rapid evaluation of swimming technique, it seems below average from a clinical perspective. This indicates that much effort must be devoted to the improvement of hydrodynamic force calculations.

Blade element theory therefore provides a very useful modeling tool for resolving the complex interactions by which animals propel themselves through water. Forces are calculated at the moving appendages rather than at the body, which is important whenever work has to be computed while the animal's body is hold still. Indeed, in the case where a body is holding position against buoyancy for example, the net work done on the body is zero according to the mechanical definition of work, although it is evident that work is done to keep the body in place. Studies used indirect estimates of work based on the estimated distance that the body would have moved had the animal stopped paddling (e.g., (Stephenson, 1994)). Additionally, the source of the propulsive force, its magnitude and direction, can be identified. The approach fits very well in parametric

studies aimed at evaluating the subtle effects of alterations in certain parameters on the overall performance, although it explicitly ignores important flow phenomena. Accuracy is satisfactory, yet likely insufficient to predict internal load with high fidelity.

3.3. Pressure sensors

The hydrodynamic resultant force exerted at the hand can alternatively be derived from the pressure distribution on its surface. This approach emerged in the mid-80s, initially with a single pressure sensor to provide instantaneous biofeedback to the swimmer (Chollet et al., 1988; Svec, 1982). Hand forces were first reported by Loetz et al. (Loetz et al., 1988) using what the authors called the difference-pressure method. Pressure fluctuations were recorded through piezo-resistive pressure sensors attached to the palm and the back of the hand, calibrated electronically. The rest of the method is vague. The authors did not describe the number of sensors used, their exact locations, the calibration procedure, or the validity of the calculations. Later, Thayer discredited analyses conducted with a very limited number of sensors (Thayer, 1994). Using a mechanically driven hand model instrumented with 127 pressure sensors, she had found that no single sensor was able to predict hydrodynamic force with acceptable accuracy. A minimum of eight sensors was necessary to estimate the resultant force at the hand, and three more in order to accurately predict the propulsive force. Takagi and Wilson reached the same conclusions when replicating the experiment with 88 sensors (Takagi and Wilson, 1999). However, hand forces did not fully account for the forces required to maintain the body vertically still while sculling with known ballasts, suggesting that the forearm likely contributes significantly to force production. Predictions were recently enhanced (Kudo et al., 2008) using a set of 12 sensors under realistic accelerated angular conditions (N = 1044 trials). Second and third order polynomial predictive equations were devised; they yielded RMS differences <6 N (~20% of the actual hydrodynamic force) equivalent to the measurement error associated with the mechanical system. The resultant force was decomposed into drag and lift components once the direction of the flow relative to the hand was approximated[4]. Pressure sensors thus provide a convenient and reliable way to

[4] It must be noted that in unsteady flow analysis, it is incorrect to view drag and lift as originating from two separable phenomena; i.e., lift resulting from circulation bound to

evaluate the resultant fluid force acting on the hand, and drag and lift components whenever hand kinematics can be recorded simultaneously. The same methodology has recently been used to estimate the forces at the feet during the breaststroke kick using four pressure sensors only (Tsunokawa et al., 2015), with mitigated success (underestimation of the actual fluid force; Pearson's correlation coefficient between maximum predicted and measured force of 0.77).

Nonetheless, in practice, there are four minor drawbacks that might impede a proper inverse dynamics analysis. First, drag is assumed to be made up of only pressure drag. However, viscous drag can account for ~25% of total drag while gliding at 2.25 m s^{-1}, and occupies an even greater fraction of total drag at slower speeds (Bixler et al., 2007)[5]. Second, inter-individual variability in morphology is explicitly ignored. Whereas this is unlikely to be an issue at the hand, this might be more critical in the event of recording pressure over the whole arm in heterogeneous populations. Third, the point of force

---

the biofoil, and drag resulting from flow separation. Under this condition, as discussed by Dickinson (Dickinson, 1996), the under pressure created by an attached vortex produces a force that acts roughly perpendicular to the plane of the biofoil (rather than the direction of motion). Thus, the attached vortex will contribute almost equally to lift and drag, which are therefore the manifestation of a single fluid mechanics phenomenon.

[5] In active (human swimming) conditions, no consensus is reached as for the magnitude of skin friction drag. Yet, for swimming dolphins, Bone and Lighthill predicted that friction drag could increase up to a factor of five (Lighthill, 1971). This is due to appendage movements transverse to the boundary flow thinning the boundary layer, resulting in higher shear stress and friction drag. Strong evidence in favor of this argument were provided by numerical fluid flow simulations of undulating swimming (Liu et al., 1997), with the contribution of friction drag to total drag increasing by a factor of 1.8 in active swimming conditions compared to passive towing. Experimental data on fish boundary layers further substantiated this hypothesis, and revealed a second, independent mechanism whereby streamwise acceleration of the near-field flow could increase friction drag regardless of transverse motion (Anderson et al., 2001).

application can only be grossly approximated, complicating the calculation of moments of force.

3.4. Digital particle image velocimetry

So far, forces have been predicted directly on the surfaces onto which they act. Nonetheless, acknowledging that force production is accompanied by a transfer of momentum to the water (as dictated by Newton's second and third laws), fluid forces can also be predicted from the geometry of the wake and the dynamics of vortex formation. Digital particle image velocimetry (DPIV) is a video-based flow visualization technique introduced by Willert and Gharib (Willert and Gharib, 1991) that is the digital counterpart of PIV, a film-based technique developed about two decades earlier (Vogel and Feder, 1966). Flow patterns and the corresponding velocity and vorticity fields are directly measured by tracking the displacement of neutrally buoyant particles that are small enough to follow fluid motion, yet large enough to be identified on image recordings. These are illuminated by a laser light sheet, and statistically processed frame-by-frame through cross-correlation algorithms. This yields a matrix of velocity vectors that provides a snapshot of wake structure and strength. The main advantage of DPIV over PIV is that images are recorded and computationally processed without delay since it does not rely on time-consuming manual photographic methods to obtain velocity data (Willert and Gharib, 1991).

DPIV became a valuable tool for the understanding of animal-generated flows and the calculation of locomotive forces after the pioneering studies on the fluid dynamics of fish swimming (Drucker and Lauder, 1999; Liao et al., 2003). Propulsive forces on the moving appendages are then inferred from circulation of vortices in the wake (that is, a measure of vortex strength, determined from integrating tangential velocity along a contour enclosing the vortex (Lauder and Drucker, 2002)). Thrust can be estimated according to the Kutta–Joukowski theorem, which states that the generated force is proportional to the circulation of the vortex shed in the wake, the length of the appendage, and the speed at which it moves (Dickinson, 1996). In other words, forces are calculated as the reaction to the momentum of vortex loops injected in the wake usually at the instant when the vortex ring has just detached from the appendage. The

time-averaged propulsive force over the stroke cycle is then determined by dividing the momentum of the shed vortex by the time duration of the stroke cycle (Peng et al., 2007). Average lift and thrust calculated in the wake of a fish did not differ significantly from fish weight and resistive forces, respectively. This force balance indicated that DPIV successfully detected the major vortical structures and allowed accurate estimates of aquatic force production (Drucker and Lauder, 1999). Likewise, propulsive force were calculated in swimming frogs from the vortex rings shed at the feet during the kick (Stamhuis and Nauwelaerts, 2005). The forces calculated through two-dimensional DPIV were, on average, 20% lower than those estimated from the impulse given to the masses of water accelerated along the webbed feet. This is a clear illustration that deriving 3D forces from planar flow information is not satisfactory.

This approach of force calculation based on vortex morphology implicitly assumes that the flow is steady so that the vortex momentum can be determined from distribution vorticity alone. The method was thus refined to quantify instantaneous forces at discrete time points during a stroke cycle by taking into account the additional linear momentum of the vortex added mass (Peng et al., 2007). This required a great deal of fluid dynamics theory in order to properly identify the boundary of a vortex and the mass of water surrounding it and moving with it. Their key findings can be summarized as follows.

- Fish fins were observed to be embedded within the vortex structure.
- The dynamical effect of the vortex is similar to replacing the real animal fin with a virtual "effective appendage".
- Forces are not only produced by accelerating and decelerating the fin, but also by altering vortex shape via fin morphology.
- Although a demonstration that the estimated instantaneous forces agree with the time-averaged force is necessary, it is an insufficient measure of validity. A true validation of force measurements requires a comparison of the animal body trajectory predicted by the force measurements with the body trajectory measured empirically.

Although the three first points are more relevant to the way we understand human force production in water, the last one emphasizes the need for mutual methodologies to gain confidence in the computations.

There is a famous and longstanding paradox in marine biology: the Gray paradox—from Sir James Gray, a famous British zoologist—whereby, according to his observations and calculations, dolphins would need muscles approximately seven times more powerful than those of other mammals to attain their extraordinary speeds (Gray, 1936). Recently, Fish et al. (Fish et al., 2014) resolved it by calculating for the first time hydrodynamic force on dolphin's fluke as they swim through a curtain of illuminated bubbles. Following the procedure described above, flow fields could be resolved, and hydrodynamic forces subsequently estimated. They corresponded to very high mechanical power outputs (~45–100 $W \cdot kg^{-1}$), yet falling within the theoretical capacities of skeletal vertebrate muscles. Gray's calculations based on the quasi-steady assumption were actually flawed, reinforcing how misleading it is to disregard unsteady phenomena.

The brilliant resort to bubble DPIV (due mainly to the size of the animal, its protected status and the volume of water required to allow continuous swimming) was not unprecedented, as it had been already used in human swimmers back in 2004 (Wei et al., 2014)[6]. Traditional (suspended reflective particles) DPIV was more recently employed to examine vortex dynamics in front crawl (Matsuuchi et al., 2009) and ventral dolphin kick (Hochstein and Blickhan, 2011), although it served more as a tool to visualize fluid flow rather than to purposely compute external forces. Matsuuchi et al. did anecdotally estimate the propulsive force from the change in momentum imparted past the swimmer's hand. They came up with an instantaneous peak force (expressed per unit

[6] Although Wei and colleagues were the first to strictly apply the procedure of (bubble) DPIV in humans, Colwin already used bubbles as a means to investigate swimming propulsion mechanisms back in 1985 (Colwin, 1985). Fifteen years later, Arellano (Arellano, 1999) built on past studies and thoroughly described his ideas to deepen our understanding of the fluid dynamics of human swimming through three flow visualization techniques: air bubbles injected close at the toes during undulatory swimming and breaststroke kick; reflective particles in water to see hand short movements; and a "bubble wall" in the pool, making it possible for the swimmer to swim through. Colored dye had also been used for visualization purposes, although this procedure does not allow the computation of the velocity and vorticity fields because of the absence of individual "particles".

depth in a plane) of 407 N m^{-1} at the transition from insweep to outsweep, and an associated lift coefficient of 2.6 (Matsuuchi et al., 2009). This seems excessively high! It is 1.67× higher than the maximal lift coefficient of a cambered airfoil (NACA 6409, angle of attack = 15°, Re = 10^6). However, it must be noted that drag was inevitably part of the change in momentum. Furthermore, forces were calculated from the momentum in the whole measurement window (area = 2116 cm^2), rather than in a control volume closer to the vortices past the hand. Calculating forces from the rate at which the fluid momentum of a control volume changes indeed suffers important limitations (Dabiri, 2005). Using this method, fluid velocity field is not sufficient by itself to determine the forces generated by swimming; pressure field is also required, which was not explicitly reported by the authors. Furthermore, whenever an animal exhibits linear or angular accelerations, defining a proper control volume is a hard task since the measured forces will change in an accelerating frame of reference (Dabiri, 2005). These constraints might have exaggerated the momentum truly imparted by the hand into the fluid, hence the overestimation of the propulsive forces.

These theoretical constraints are associated with additional experimental difficulties (Stamhuis et al., 2002), which hinder the implementation of DPIV in human subjects. If asked to swim in a flume, swimmers' coordination might be affected and might not ecologically represent the actual force production mechanisms experienced in a traditional pool. Moreover, too small of a flow tank would produce undesired wall or ground effects. In a pool though, a much higher volume of water must be seeded homogeneously with small particles, whose density must satisfy recordings requirements without interfering with the swimmer. Because of the illumination provided by the laser, swimmers must wear special protective goggles subtracting the particular wavelength of the laser. However, this also removes any visual clues of swimmer's orientation relative to the exact location of the laser sheet. Preliminary testing sessions are therefore necessary, since hands must cut through the illuminated plane in very specific locations. Overall, DPIV offers formidable insight into fluid dynamics and unsteady force production mechanisms, but requires very complex setups that are unimaginable for measurements in small pools.

Collectively, the four methods presented above appeared better suited to strictly study the hydrodynamics of swimming propulsion rather than to envisage an inverse dynamics

analysis. Several weaknesses were identified and must be addressed prior to conducting inverse dynamics analysis in an effort to achieve increased accuracy. Analytical calculations consider the hand only most of the time, and are based on biased hydrodynamic assumptions. The blade element approach reaches only satisfactory accuracy as it neglects important unsteady flow phenomena, and are best suited for planar movements. Pressure sensors do not consider viscous drag nor axial pressure gradients, and only provide approximate the center of pressure regardless of limb morphology. Last, digital particle image velocimetry requires complex setups and serves mainly as a flow visualization technique. To perform inverse dynamics analysis necessarily requires:

- to measure forces on the whole upper limb;
- to accurately locate the points at which forces act;
- to account for unsteady phenomena at high movement speeds;
- to consider complex time history of force development.

3.5. Computational fluid dynamics

Incompressible fluid flows and related phenomena are governed by the 3D Navier–Stokes equations[7], which are partial differential equations that can hardly be solved analytically. Computational fluid dynamics (CFD) is the branch of fluid mechanics that resorts to computer and a set of numerical tools to obtain approximate solutions. These non-linear equations are discretized in space and time to transform them into a system of algebraic equations that can then directly be solved.

Numerical fluid dynamics emerged back in 1953 at the Los Alamos National Laboratory with the arrival of the first large computers (Harlow, 2004). Their research was essentially

[7] This sentence is historically inaccurate. As a matter of fact, Navier–Stokes equations originally referred to the momentum equations only, named after Claude-Louis Navier and George Gabriel Stokes who independently obtained the equations in the first half of the nineteenth century. However, in its more modern definition, this terminology includes the entire system of flow equations—continuity, momentum, and energy (Anderson, 2009).

centered on aerodynamics and supersonic flows at first, before turning to the modeling of turbulent flows in the late 60s. This period coincided with the spread of CFD around the world, despite a climate of global suspicion relative to these new techniques. The need to make contact with a wide array of agencies and develop sources of funding initiated the diversification of CFD applications. For that purpose, Harlow explains that they had extended their activities to the analysis of pollution transport by winds through urban areas with streets and tall buildings, the behavior of tornadoes or wildfire propagating through a forest, or the dynamics of biological cell (Harlow, 2004). The same impulsion has likely touched all laboratories, and contributed largely to applying CFD at the service of problems of all kinds. It is important to realize how CFD has shaped the world we live in. Many aircraft parts are designed and tested numerically, contributing immensely to their modern performance. In the automotive industry, the time required for the design and production of a new car model has been reduced from 6–8 years in the 70s to roughly 36 months in 2005 (Hirsch, 2007). CFD has become interdisciplinary. It now occupies a dominant place in virtual prototyping, and allows researchers and engineers to explore and refine more and more complex configurations. A word must be given about an area where CFD is surely expected the least, just as an additional glance to its innumerable potential applications. Simulations have recently been carried out to examine and model the dynamics of effervescence and bubble nucleation in champagne (Beaumont et al., 2014). While this may seem intriguing, the rationale behind this work is that bubbles act as active transporters of champagne aromas to the surface and their release in the air. Understanding this random process is key to learn how to control it (e.g., through varying glass shape) and get maximum 'olfactive return' from champagne.

Nowadays, CFD capabilities have widely spread to the study of living biological systems. Simulations of internal flows—flows confined by walls as diverse as in food processing, hemodynamics, or nasal cavity airflow dynamics—have direct and sound applications to the fields of physiology and medicine. For example, Hoi et al. (Hoi et al., 2004) investigated the role that arterial geometry plays in the growth of intracranial aneurysms. They were able to simulate complex blood flow and quantify the relationship between hemodynamic stresses and arterial curvature, which is essential to understand aneurysm pathogenesis and predict treatment success. CFD shows tremendous strength in such parametric studies that cannot be conducted in vivo.

By contrast, studies of external flows around bluff bodies are more relevant to understand the energetics and mechanical demands of physical activities where resistance to forward progression matters a lot. CFD has unsurprisingly taken roots in cycling, ski jumping, bobsleighing, and swimming. The question of the effect of body position on the experienced resistance was central to all the commencing works (Dabnichki and Avital, 2006; Defraeye et al., 2010a; Meile et al., 2006; Zaïdi et al., 2008). Collectively, these studies emphasize the major advantage of CFD over experimental measurements—that is, simulations offer very detailed flow field information. This, in turn, provides deep insight into the mechanisms causing drag reduction and informed guidance towards further improvements.

Where numerical studies of swimming significantly depart from other activities is in the need to evaluate forces acting on a swimmer's arm. Water indeed provides both resistance and support against which to produce forces, and the issue of force production determinants has quickly become a major interest. Bixler and Riewald (Bixler and Riewald, 2002) initiated this trend. They computed hand–forearm drag and lift coefficients at various speeds and angle of attack, with satisfactory agreement with experimental flume measurements. Massive flow separation from the skin on the downstream side of the hand and arm was observed through unprecedented flow visualization. Importantly, they invalidated the use of Bernoulli's principle to explain lift production by a swimmer, as this principle only applies to steady flows. Rouboa et al. (Rouboa et al., 2006) built on that momentum, and examined the hydrodynamic characteristics of a realistic hand–forearm 2D model under steady and linearly accelerated flow regimes for the very first time. Plots of pressure distribution along the entire surface revealed the expected pressure differential between the anterior and posterior part of the limb, as well as boundary layer separation and vortex shedding. Furthermore, drag coefficients were ~23% higher over the whole range of simulated speeds in accelerated vs steady flow conditions. The authors were careful to avoid boundary singularity at the base of the forearm that would have inflated the hydrodynamic coefficients, thus confidently providing strong evidence against the quasi-steady assumption. Later on, body roll dynamics and intra-cyclic fluctuations in arm rotation speed were found to significantly affect upper arm propulsive forces (Lecrivain et al., 2010). The first increased the mean hydrodynamic force by up to 73%, whereas reducing pull duration by

20% (~0.6 s) doubled the peak propulsive force to ~18 N. The upper arm thus produces high levels of force and likely contributes substantially to propulsion during a regular stroke, an issue largely overlooked in the literature. Moreover, the history of force development was complex and unpredictable, as it did not simply match the bell-shaped arm angular velocity profile but rather displayed two maxima and a local minimum towards the middle of the stroke.

Ongoing works mostly abandoned the simulation of unsteady motion to inspect how subtle morphological hand changes affect force generation. There is a strong evolutionary argument supporting such research. Humans have not evolved a body shape favorable to swimming. For that reason, the room for performance improvement is likely larger than with terrestrial locomotion. Spreading one's fingers as seen in elite swimmers might be such a strategy. Studies by Minetti et al. (Minetti et al., 2009), Marinho et al. (Marinho et al., 2010), and Bilinauskaite et al. (Bilinauskaite et al., 2013) are unanimous on the matter, and all agreed that a small finger spread (~13° or 0.32 cm inter-fingertip distance) enhances drag coefficient by up to 5–8.8% and maximum local pressure by about 9%. Interestingly, lift coefficient was independent of finger spread (Marinho et al., 2010). This advantage had been theoretically predicted to occur when finger spread does not exceed the thickness of the laminar boundary layer surrounding each finger (about a fifth of finger diameter in transitional flows), and further validated through CFD simulations (Lorente et al., 2012). Recently, Vilas-Boas and coworkers demonstrated that the benefit provided by finger spread could be modulated through small changes in thumb adduction and hand attack angle (Vilas-Boas et al., 2015). In spite of the tiny amplitude of the changes, numerical simulations exhibited great discriminant capability, and were able to accurately capture and render these microscopic phenomena.

In light of the above strengths, CFD appropriately addresses the weaknesses identified in the previous section. Simulations are transient; forces can be measured at any element of the computational domain; centers of pressure can accurately be located through integration of the pressure field over a surface. Yet, the advantages of CFD are conditional on the accuracy with which Navier–Stokes equations are solved, which is a very difficult task. Unlike experiments, numerical simulations and the underlying codes are more opaque to the users, and one must be aware of the inevitable approximations that are disseminated throughout the flow of numerical procedures. In the context of

confidence in CFD modeling, the American Institute of Aeronautics and Astronautics (AIAA, 1998) distinguishes error—a *recognizable* deficiency in a CFD model that is *not due to lack of knowledge*—and uncertainty—a *potential* deficiency *caused by lack of knowledge*. The main causes of potential inaccuracies must be identified to gain awareness of the expected precision of joint kinetics calculation. This is also necessary to delineate the framework in which these calculations can reasonably be done, without the fear to yield flawed outcomes.

3.5.1. Differential equations contained approximations

The mass, momentum, and energy equations are complex non-linear coupled equations. Intriguingly, despite their wide range of applications, it has not yet been proven that solutions systematically exist, and, if they do, that they are smooth (i.e., free from mathematical singularities). This is one of the seven Millennium problems—judged the deepest and most difficult problems—whose solutions are awarded a $1,000,000 prize by the Clay Mathematics Institute. Although analytical solutions can be obtained in a restrained number of cases (such as fully developed flows in pipes or between parallel plates), simplifying assumptions are very often seen otherwise, which introduces errors in the calculations. This process is a major source of errors in the results (Zikanov, 2010). This is clearly illustrated when considering the modeling of: (i) complex flow phenomena, e.g., turbulences, naturally occurring in human movement in water due to the shape of the upper limb; and, (ii) the boundary layer.

Turbulence modeling

The challenge of numerically analyzing turbulence can be approached in the three ways summarized below, the two first being thoroughly documented in (Pope, 2000). The first way involves the direct numerical simulation (DNS) of all scales of motion contained in the flow, without averaging or approximation. Conceptually, this is the simplest yet most accurate approach, which is now permitted thanks to growing computational power. It remains that, despite the performance of massively parallel processing infrastructures,

DNS is restricted in use to very particular fundamental research purposes, notably for the understanding of turbulent structures and laminar–turbulent transitions. Computational demands grow so steeply with the Reynolds number Re—the number of grid points needed for sufficient spatial resolution scales as $Re^{9/4}$ and the CPU-time as Re^3—that DNS is inapplicable to applications at high Re as encountered in human aquatic movement. In typical conditions of human swimming, for example, the Kolmogorov scale (Landahl and Mollo-Christensen, 1992) yields a crude estimate for the smallest eddy length of the order of 10 μm. A grid this fine is simply unimaginable.

An alternate, less expensive approach to take into account the effects of turbulence is the large-eddy simulation (LES). Its development is founded on the observation that larger-scale eddies are affected by flow geometry and are by far the most effective transporters of energy, unlike smaller-scale eddies that are weaker and possess more of a universal character (Pope, 2000). A simulation treating more accurately the first than the second is intuitively sound, and is precisely what LES does: larger-scale motions are computed explicitly, whereas the influence of the smaller scales is modeled. Thus, compared to DNS, the computational cost of resolving the small-scale motions is avoided. However, because of its three-dimensional and unsteady nature, LES still remains computationally expensive. Moreover, in wall-bounded flows, near-wall motions are substantial and must be either fully resolved (although this implies a greater computational cost $\propto Re^{1.8}$, unfeasible at high Re flows over aircrafts' wings, ships' hull and, supposedly, humans' upper limbs) or modeled (at no additional cost, but introducing further uncertainties in the simulations). The issue of boundary layer and near-wall region modeling is a serious one and will be discussed in the next section.

The last approach is based on the Reynolds-averaged Navier–Stokes equations, named after Osborne Reynolds who introduced the concept back in 1895. Flow variables are decomposed into a time-averaged value and a fluctuation about that value (Ferziger and Peric, 2002). Upon averaging, the regular Navier–Stokes equations are obtained for the mean variables with the exception of two additional terms: the Reynolds stresses, which represent the transport of mean momentum due to turbulent fluctuations, and the turbulent scalar flux. Nonetheless, the presence of the two terms prevents the closure of the conservation equations (i.e., they contain more variables than there are equations); modeling approximations in the forms of turbulence models are required.

The complexity of turbulence makes it unlikely that, in spite of the variety of models developed, any single one can accurately represent all the phenomena contained in the flow. These models should therefore be regarded as engineering approximations rather than scientific laws. However, they are entirely suitable whenever just a few quantitative fluid properties are of interest, such as the average forces on a body (Ferziger and Peric, 2002). That being said, attention should be paid to the models most commonly found in the literature of human swimming and critically examine their constituents. According to Takagi et al. (Takagi et al., 2016), about two thirds of the works published since Bixler and Schloder (Bixler and Schloder, 1996) resorted to the k–ε model introduced by Launder and Spalding (Launder and Spalding, 1974), whereas the use k–ω model popularized by Wilcox (Wilcox, 1988) was reported ~15% of the time. These are first-order closures employing two transport equations to model the convection and diffusion of turbulence; hence history effects are considered. The two models belong to the class of eddy-viscosity models; i.e., the stress tensor is modeled as proportional to the mean strain-rate tensor (similar to laminar flow) according to the Boussinesq hypothesis, introducing the eddy viscosity as the factor of proportionality[8] (Bardina et al., 1997). The first assumed that the flow is fully turbulent in the whole domain and viscosity is negligible. For wall-bounded flows, the k–ε model gives good agreement with

[8] By contrast, second-order closures (embodied in the family of Reynolds stress models) are the most elaborate type of Reynolds-averaged Navier–Stokes turbulence model. The Boussinesq hypothesis is abandoned; equations are closed by solving the transport equations for each of the terms in the Reynolds stress tensor, plus an equation for the dissipation rate, for a total of seven additional equations in 3D. Second-order closures more rigorously account for history effects than one- or two-equation models, and capture the influence of streamline curvature or system rotation on the turbulent flow (Blazek, 2005). This gives them more potential to solve complex flows (e.g., highly swirling flows). However, second-order closures are still limited by the various modeling assumptions required to close the equations, which are considered to compromise seriously prediction accuracy. As a result, they are not clearly superior to the first-order closures in all classes of flow to justify the extra computational effort (ANSYS, Inc, 2012). For this reason, first-order closures remain more popular in practice.

experimental results for zero and small mean pressure gradients, but is much less accurate (with errors up to 72% between measured and computed skin friction) for strong adverse pressure gradients. Moreover, the k–ε model fails to predict any flow separation (Wilcox, 2006), which is massive around the human hand and forearm (Marinho et al., 2011; Minetti et al., 2009). Further complications occur at the wall when specifying the dissipation rate ε. On the other hand, the standard k–ω model is superior in numerical stability to the k–ε model primarily in the viscous sublayer near the wall thanks to the introduction of the specific dissipation rate ω (Wilcox, 2006). This model had been found to outperform the k–ε model in the calculation of body drag and the visualization of vortices in streamlined position, with numerical results very closely agreeing with experimental measurements (Zaïdi et al., 2010). This is in contradiction with the findings from Defraeye et al. (Defraeye et al., 2010b) who found that the standard k–ω model had the weakest performance of all when simulating the air flow past a cyclist. For this particular flow problem, the wake is large (unlike a streamlined swimmer), and the accurate prediction of the flow turbulent core region is more important than the boundary layer separation. This exemplifies the great sensitivity of k–ω model solutions to values of k and ω outside the shear layer—also known as the freestream sensitivity (ANSYS, Inc, 2012). It should be noted that another formulation exists— the Menter's shear-stress transport (SST) k–ω model (Menter, 1992)—that has the serious advantage to conjugate the robust and accurate formulation of the k–ω model in the near-wall region with the free-stream independence of the k–ε model in the far field (Wilcox, 2006). These features make the SST k–ω model more accurate and reliable for a wider class of flows (such as strong adverse pressure gradient flows, and flows past airfoils) than the standard k–ω model (ANSYS, Inc, 2012). However, this model's effectiveness is only fully exploited when the boundary layer is entirely resolved. This requires a very fine mesh resolution at the wall, which is very demanding in terms of computational power and surely explains why this model has received poor consideration in human aquatic biomechanics (to the best of our knowledge, only Minetti et al. used it to better capture flow separation around the hand (Minetti et al., 2009)).

Boundary layer

In wall-bounded flows, the only correct boundary condition at the surface is the no-slip condition (Versteeg and Malalasekra, 2007a). However, turbulent flows develop very small structures near walls that play an important role in the production of vorticity and turbulence. Furthermore, these are regions where flow variables exhibit steep gradients (Kline et al., 1967). Ludwig Prandtl—the father of modern aerodynamics and the boundary layer concept—recognized that the boundary layer was very thin (of the order of a few mm at high Reynolds number). Hence, fluid velocity (among other quantities) changes enormously over a very short distance normal to the immersed body. This in turn causes important skin friction, by virtue of Newton's shear-stress law (Anderson, 2005). An accurate representation of the flow in near-wall regions is therefore mandatory to guarantee accurate solutions.

The near-wall region can be essentially divided into four layers (Sreenivasan, 1989). These are rather hypothetical in the sense that they are not clearly separated by interfaces: (i) the region closest to the wall in which the viscous shear stress is dominant is called the viscous sublayer. It is known from empirical data that the height of the viscous sublayer is about $y^+=5$ (a dimensionless distance to the wall, normalized using the friction velocity; this can also be viewed as a ratio between turbulent and laminar influences in a cell); (ii) the viscous sublayer extends into the buffer layer up to $y^+=30$. Peak production and dissipation of turbulent energy occur in the middle of this interim region ($y^+\approx12$), and viscous and turbulent stresses are nearly equal. (i) and (ii) form the viscous layer, which is responsible for the production of a third of the total turbulent energy; (iii) the viscous layer then smoothly merges with the so-called log-law layer until approximately $y^+=500$. The name is after the existence of a logarithmic region in the velocity profile of the layer. The turbulent stress is many times greater than the viscous stress. In other words, the momentum flux across layers of fluid is accomplished almost entirely by turbulence; (iv) the outer, or defect, layer is encountered for $y^+>500$, a region where large-scale turbulent eddy shear dominates.

At high Re, the viscous sublayer is so thin that it is difficult (and computationally expensive) to use a grid fine enough to resolve the entire boundary layer accurately (Rodi et al., 1997). This issue can be resolved by applying an artificial boundary condition at

some distance from the wall (ideally, the first cell should lie in the log-law region). These *wall functions* link the viscosity-affected region between the wall and the log-law region without requiring changes in turbulence models. A simple expression connecting the velocity at the first grid point above the wall and the wall shear stress can then be derived (Ferziger and Peric, 2002). There is however a couple of limitations associated with the use of wall functions, beyond the errors introduced by extrapolating variables in the viscous layer. Numerical results rapidly deteriorate under refinement of the grid: too small of a y^+ value (i.e., the first cell in the direction normal to the wall lies in the viscous layer rather than the log-law region) and the assumption underlying wall functions cease to be valid. Although much effort has been dedicated to the development of y^+-insensitive wall treatments including the effects of pressure gradient, these solutions become less and less reliable as the fluid flow depart from these ideal conditions (e.g., in the presence of severe pressure gradients leading to boundary layer separation) and suffer from important numerical drawbacks (ANSYS, Inc, 2012). Therefore, no single approach proves satisfactory in a wide range of flows, particularly whenever massive flow separation occurs, and the introduction of errors when resolving the boundary layer is inevitable in high Re simulations.

3.5.2. Discretization process

Errors can be reduced by using higher order discretization scheme p, or restraining the approximations to small regions of the computational domain. The general rule of thumb is that errors reduce by approximately m^p times when mesh element size is reduced m-fold (Zikanov, 2010). Two schemes of the same order or two differently designed grids used with the same scheme likely result in significantly different discretization errors. Comparing solutions on two grids with different steps is the only way to obtain reliable quantitative measure of the amplitude of the discretization error. This method, known as the Richardson extrapolation, is not easy to implement since it requires computation on increasingly fine grids. As the refinement must be significant (a factor 2 is usually taken), this implies that, in 3D, the second grid must be 8 times denser than the first. However, this procedure is necessary whenever a new analysis (or a new scheme or type of grid) is used. The main purpose is not much to estimate the discretization error, but rather to determine the level of refinement beyond which the solution changes very little; i.e., the solution is said grid-independent (Zikanov, 2010).

3.5.3. Iterative nature of the solvers

One component of the inaccuracy of numerical solutions arises from round-off error of computer operations. Fortunately, these are in magnitude several orders lower than the magnitude of errors of other types (e.g., discretization errors). Much more relevant are the errors appearing because of solving a system of equations iteratively. Indeed, unless they are run for a very long time, exact solutions are never produced. Iterations are traditionally stopped when the norm of the residuals becomes smaller than a certain non-zero tolerance level (about 10^{-4}–10^{-6}). However, as discussed in (Zikanov, 2010), a very low tolerance level does not guarantee small iteration errors as the residuals do not represent the actual error magnitude. Both decrease at approximately the same rate during the convergence process though, so that the norm of the iteration error relative to the amplitude of the solution (i.e., scaled residuals) is approximately equal to the observed total reduction of the norm of the residuals (Versteeg and Malalasekra, 2007b). Therefore, if residuals fall by four orders of magnitude, the norm of the iteration error can be reasonably expected to be around 10^{-4}, and definitely smaller than 10^{-3}.

Although popular, the approach based on normalized residuals is not appropriate to judge convergence in some cases. For example, if a very good initial guess of the solution is provided, or if certain nonlinear terms begin at zero and build up slowly during the computation, residuals may not drop this much. Conversely, if the initial guess is very bad, the initial residuals are so large that a huge drop by no means guarantees convergence. Monitoring an integrated physical quantity over time should generally be preferred (ANSYS, Inc, 2012).

3.5.4. Programming errors

These are virtually inevitable, and can be made while settling the problem or writing user-defined routines. Intriguingly, even commercially available codes contain algorithmic errors. An analysis dating back to the late 90s revealed an average 10 faulty lines per 1,000 lines of code in more than 100 engineering codes reviewed (Hatton, 1997), leading the author to conclude at that time that calculations relying heavily on numerical

procedures should be taken with "several large pinches of salt". Whether these insidious errors are still present in the same proportion nowadays is unknown, and there are no systematic ways to estimate and control their effects.

3.5.5. Model imperfection

Last but not least, one must bear in mind that a CFD analysis is merely an approximate description of the behavior of a model, rather than of a real physical system. Inaccuracies are introduced at two different levels: during the scanning procedure, and the collection of body kinematics to animate the body's virtual model.

3D body scan

A first source of errors occurs when creating a numerical replica of the real physical participant's body to be analyzed. Such a virtual object has been traditionally obtained through 3D body scanners. However, the extent to which errors propagate in that very first step is hard to quantify. Here, distinction is made between laser and photonic scanning. The first is made of scanning units mounted on towers projecting a laser beam towards the body and screening it from head to toes to obtain the model in one pass. In the second, light stripes are projected on the body surface, and distortion of these patterns are recorded by cameras; 3D body surface topography is then automatically reconstructed with built-in software algorithms (e.g., Douros et al., 1999).

Scanning procedure has become very common in many domains (principally the apparel industry) to capture specific anthropometric measurements, hence an abundant literature about body scanners' accuracy. Laser scanners were found to yield a total reconstruction error of geometrical shape dimensions of ~1 mm (~1%). Errors in body surface area calculations were higher (<10%), suggesting that the highest error was associated with software computations rather than actual measurement error in the 3D scanner (Yu et al., 2003). Unlike inanimate objects, living subjects are however swaying and breathing, although this latter issue is likely more critical when using laser rather than photonic scanner because of exposure duration. This inevitably introduces artifacts (of the order of several centimeters) in the scan data (Daanen et al., 1997). These authors reported that holding one's breath at mid-level inspiration, and using a pointer on the head,

considerably reduced body sway magnitude and eliminated about 50% of the artifacts (Daanen et al., 1997). In a study of upper body measurements, laser scanner was found to accurately (within <20-mm non-significant differences) represent the main tailor measures, besides slight overestimation of neck-base girth and underestimation of body height (Lee and Ashdoon, 2005). Photonic scanners measurements of volume also has shown strong agreement with measurements by water displacement, with differences of no more than 0.02 L (<5%) for the arms, and 0.25 L (1%) for the entire body (J. Wang et al., 2006). Besides, measurements of thigh length and body joint circumferences displayed very high accuracy (~1–3%). Collectively, these studies seem to indicate that: (i) there is no marked difference between laser and photonic scanners, and (ii) macroscopic body features are well rendered numerically.

In water though, smaller features (such as at the fingers or the head) might be just as important as they have a crucial role in shaping fluid flow and thus hydrodynamic forces. Measurements of craniofacial landmarks through photonic scanning were consistently more accurate than through direct anthropometry. In more than half the cases, mean differences were at the submillimeter level (Weinberg et al., 2004). The validation procedure of a full-body laser scanner described by Tikuisis et al. is instructive as it used a human hand as a model (Tikuisis et al., 2001). Hand volume computed from the scan compared reasonably well (i.e., within one standard error, or 0.5%) with the mean value calculated from three measurements by the water displacement method. We can therefore safely assume that (i) buoyancy can be accurately predicted from body scans, and (ii) minor details are appropriately rendered so as to give confidence in this initial step of converting the real model under study to its virtual counterpart.

Kinematics

Errors associated with the capture of human body kinematics (from reflective markers location, passing by inaccuracies in kinematic reconstruction, to data filtering techniques) are common to the entire field of biomechanics. For that reason, they present very little interest to document our particular concern regarding CFD modeling.

The study of a motile biological system through engineering software mainly coded for inanimate systems raises the question of the prescription of the motion. It requires no

particular engineering knowledge to realize that animating a virtual body swimming to match what pool observations is more intricate than to make the air flow past an non-deformable car. This issue is not recent. Back in 2006, Rouboa et al. (Rouboa et al., 2006) had already identified the difficulty in analyzing force production under real unsteady conditions (i.e., with the inclusion of multi-axis rotation, acceleration and deceleration, deformation of the whole mesh). Commercial software frequently comes with rigid body kinematics tools, so that an entire rigid model can be animated in translation and rotation around its center of gravity. However, human limbs are made of several segments connected by joints that deform. The geometry of these flexible regions is severely constrained by the motion of the adjacent surfaces, and therefore requires a special treatment to guarantee a realistic, smooth transition between segments.

A very limited number of research groups have succeeded in properly animating a virtual body or arm model within flow simulations. Most of those groups are engineers addressing biological questions with in-house solvers purposely built. The great advantage here is that they designed the entire computational workflow to suit their needs and significantly ease the process. American and Australian scientists independently simulated human dolphin kick (Cohen et al., 2012; Loebbecke et al., 2009a; 2009b) and front crawl arm pull (Cohen et al., 2015; Loebbecke and Mittal, 2012) using solvers based on fundamentally different CFD methods.

- The American team's solver relies on the immersed boundary method (Mittal and Iaccarino, 2005), originally developed by Peskin (Peskin, 1982) to investigate cardiac mechanics and associated blood flow. The very characteristic feature of this formulation is that the simulation is carried out on a stationary, non-body-conformal Cartesian grid. The method offers several important benefits. Although its size requirements increase faster than a body-conformal grid as the Reynolds number grows, this does not necessarily imply a corresponding increase in computational cost. Indeed, a substantial fraction of the grid points may actually lie inside the solid body where the fluid flow equations need not be solved; this fraction is proportional to body volume and orientation. Furthermore, a fixed grid relaxes the need for complex grid dynamic adaptations, hence a drastic reduction in per-grid-point operation. The task of grid generation is obviously made simpler, which is highly relevant in the case of moving boundaries (Mittal and Iaccarino, 2005).

- The Australian team's solver is based on Smoothed Particle Hydrodynamics (SPH)—a mesh-free approach originally developed for astrophysical applications. Unlike traditional Eulerian, finite-volume approaches, SPH follows a Lagrangian specification of the flow field. It is well suited to the modeling of complex free-surface effects and geometries undergoing large deformations (Monaghan, 2012). The fluid is replaced by a set of particles that move around as a result of stresses produced by particles interaction.

- Besides the advantages relative to the way hydrodynamics is approached, both solvers dealt with geometry deformation in the same way. Body scans were imported into Maya (Autodesk Inc., San Rafael, CA; one of the most renown 3D animation software), and rigged to a virtual skeleton to manipulate joint orientations, easily and smoothly deform the surface mesh, and create body poses to match video footages. About 20–40 key frames were inserted in the solver, and interpolated spatially and temporally to produce thousands of instances for a cycle. In a sense, model deformations are externally computed, and input in the solvers for flow resolution.

The situation is much different in Fluent. The Immersed Boundary module is no longer available or supported by their developers (Cascade Technologies Inc., Mountain View, CA). Body-conforming grids are the only provided solutions, which are inevitably accompanied by a whole lot of difficulties in the meshing process and the way to prescribe boundary motion. Fluent comes with built-in dynamic mesh macros to aid in that task. The DEFINE_GRID_MOTION macro circumvents the automatic mesh motion based on rigid-body kinematics (i.e., implying that there is no relative motion between the vertices of the moving region) by providing the possibility to independently prescribe the motion of each individual vertex. Lecrivain et al. were the first to simulate in Fluent the rotation of the arm about the shoulder (Lecrivain et al., 2008). This was done in a lower-arm amputee swimmer, which advantageously reduces the number of deformable regions to take into account. Very little information was provided, besides that "user-defined functions (UDF) were implemented using the C-programming language to describe the motion of the three distinct parts of the swimmer." This methodological prowess was later renewed by Keys (Keys, 2010) at all body joints,

though UDFs had been written in collaboration with a private company and thus could not be divulgated. The solution to the long-standing problem of large, realistic 3D deformation in CFD applications remains obscure.

Summary

Turbulences cannot be fully resolved at high Reynolds number over a human upper limb; the required computational power would exceed that of modern supercomputers. Less expensive approaches employ turbulence models, which are engineering approximations suitable whenever rather simple quantities (such as the average forces acting on a body) are of interest. Nonetheless, in the case of wall-bounded flows with massive separation (as in the vicinity of the upper limb surface), no single model proves entirely satisfactory. Errors introduced at that stage are unavoidable. The main challenge remains to integrate dynamic numerical fluid flow simulations with inverse dynamics and obtain the first insight into movement mechanics and instantaneous loading of the musculoskeletal system. Although some very rare teams have managed to simulate a full stroke in the past using proprietary solvers, prescribing a participant's kinematics is still an unsolved problem in Fluent commercial software solution. No guidance in the literature can direct our quest.

4 Summary and objectives

The main objective of this thesis is to evaluate aquatic movement mechanics from a joint level perspective. With respect of the current state of science advances in aquatic locomotion, joint level is the one offering the more realistic and non-invasive estimates of the mechanical work that must be apportioned to perform the task. However, it is only attainable through inverse dynamics analysis, which requires the accurate measurement of external forces and their points of force application. This poses a veritable challenge in water—as the hydrodynamic forces and centers of pressure are very difficult to estimate under dynamic conditions—that must be faced in order to expand the field further. Up to now, the mechanical load on the musculoskeletal system during movements performed in water is unknown. Novel numerical tools must be developed to perform inverse dynamics in water. The review of literature suggests that this has to be achieved through significant advances in computational fluid dynamics, although 'how' this can be done in commercial software remains mysterious. Once the solution to this long-lasting problem is found, fundamental questions related to motor control strategies and joint dynamics can be approached. These are at the interface between fundamental biomechanical knowledge and applied clinical research. It is expected that human musculoskeletal system will resolve the dilemma of operating in an unstable fluid medium (partly) deprived of gravity by sensibly new mechanical behavior.

4.1. Thesis structure

The thesis is organized around five core studies, according to the fundamental points highlighted in the literature review. They are preceded by a chapter on the methodological developments that made possible the subsequent studies. **The first reports the methodological developments and algorithms for unsteady fluid flow**

simulation with bodies undergoing large deformations, and their novel integration with inverse dynamics. Currently, there is no existing software solution allowing one to undertake the whole analysis and reach a new depth into our understanding of aquatic movement mechanics (Section 3.5). We integrate works from computer graphics and robotics, and test the validity of the whole interface. This primary study constitutes the *sine qua non* condition before establishing a strong basis onto which to build the subsequent works. **The second study deals with the way the musculoskeletal system modulates work and power output in response to substantial changes in task mechanical demands in water.** It is aimed at answering for the first time questions such as: "Where in the upper limb is work and power developed?" or "Is mechanical output modulated similarly at all joints, or are certain muscle groups favored?" On land, the theory predicts that work and power will be redistributed proximally to large muscles to accommodate increased mechanical demands, but this has never been tested at the upper limbs in an environment where net work must be done against a dissipative load (Section 2.2.2). **The third study thoroughly examines the transfers of energy between the water and the moving limbs.** A recurrent issue in the biomechanics and energetics of aquatic locomotion is whether the work of accelerating the limbs relative to the body center of mass and another done against the water should be treated independently (Section 2.1). This conceptual controversy must be addressed, as it is paramount to the calculation of total mechanical work, as well as to compute locomotor efficiencies and identify the levels at which energy wastage occurs. **The two last studies are oriented towards applied, clinical knowledge to provide guidance in the design of shoulder rehabilitation protocols. Specifically, the fourth one is intended to evaluate joint kinetics during aquatic scapular plane exercises performed in different positions.** It is argued in the literature that slow aquatic exercises represent no risk for the injured shoulder, yet present recommendations are only based on muscle activity recordings that are poor predictors of joint mechanical load. Moreover, varying body position might influence power output requirements, hence how muscles work (Section 2.2.2). Since therapy success may be compromised, this is clinically relevant and must be thoroughly analyzed. **The last one examines changes in shoulder joint function and dynamics as exercise speed is manipulated.** Mainly based on the calculation of the 3D angle between joint moment and angular velocity vectors, we seek to reveal a possible trade-off between joint stability and propulsion. From estimates of mechanical work, predictive

equations of shoulder loading are devised in order to provide clinicians with a practical, objective criterion of exercise intensity.

4.2. Diagram

The diagram below illustrates how each concept and mechanical quantity articulate with each other. Jagged borders denote the methods (in orange) or quantities (in green) that are readily accessible based on the present state of knowledge. Round borders are for methods/quantities requiring significant methodological improvements. These combined to form the basis for the five core studies of this thesis.

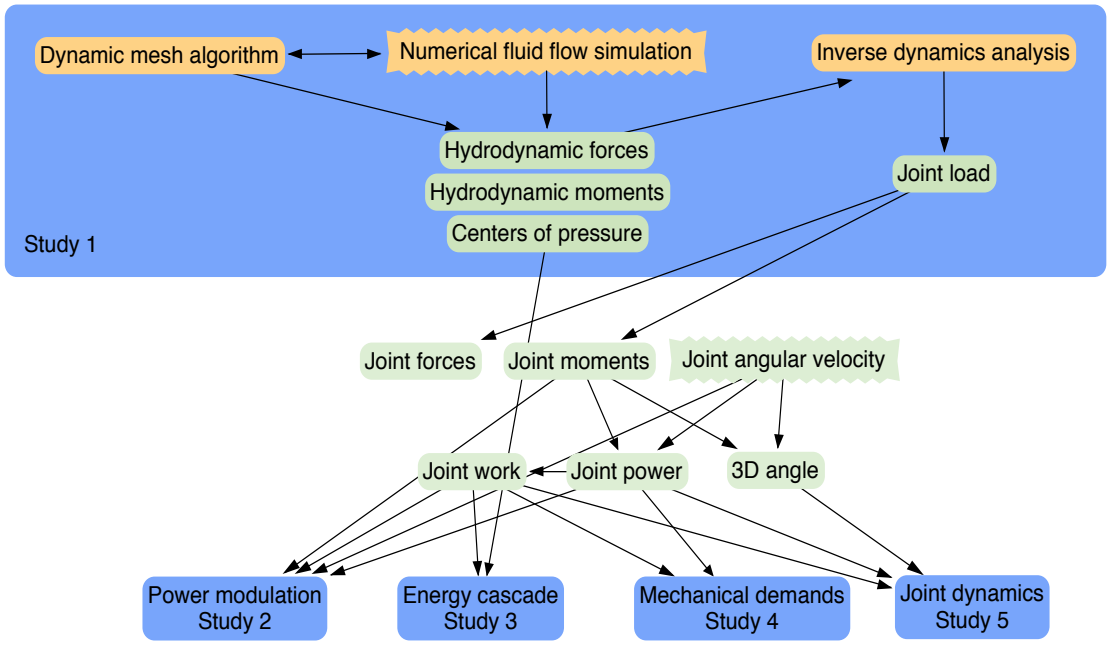

5 Methodological developments

A thorough evaluation of the load on the musculoskeletal system during movements performed in water has never been reported. In order to do so, two major challenges must be tackled: i) the development of new dynamic mesh algorithms to realistically animate a numerical model according to kinematics captured in a pool, and ii) the modeling of the upper limb via a robust formulation of the inverse dynamics problem. Both issues were solved in this thesis. The basis for the associated methodological developments we implemented is reported below.

5.1. Overview of dynamic mesh implementation

Dynamic mesh capabilities are essential to tackle problems involving deforming boundaries. These are now very common, ranging from prescribed motion of valves or wing actuators (both in the aerospatial industry and in biology, to simulate flapping appendage motion of swimming and flying species; e.g., Young et al., 2009) to physical problems of contact stress analysis and fluid–structure interaction (as in the simulation of hemodynamics and heart valve motion (Dumont et al., 2004)).

In Fluent, three powerful dynamic mesh update schemes are used to automatically handle smooth motion of the mesh in the interior of the computational domain; namely, smoothing, layering, and remeshing (ANSYS, Inc, 2012). Smoothing displaces the interior nodes while preserving their connectivity, as if they were simply absorbing the deformation. This is based upon either modeling the mesh as an idealized network of

interconnected springs where the displacement of a node generates a proportional force that is transmitted to all its neighbors until equilibrium, a Laplace equation describing how boundary motion smoothly diffuses through the interior mesh, or regarding the mesh as a linearly elastic solid whose motion is governed by a set of rheological properties. By contrast, dynamic layering applies to prismatic zone and can automatically add or remove layers of cell adjacent to a moving boundary. Last, remeshing methods deal with large boundary displacement relative to local cell size. Cell quality can rapidly deteriorate, ultimately yielding degenerate meshes and convergence problems (and simulation abortion in the worst case). Using remeshing methods, too distorted cells are agglomerated and remeshed to meet a skewness criterion; old cells are then discarded, resulting in mesh topological changes. However, none of these tools address the need to deal with very large deformations of the boundary itself, which is clearly needed to animate a body moving in water. Fluent does not allow for motion to be prescribed at several body joint, with realistic and smooth deformation being achieved at bending body parts. This has severely hindered the investigation of human movement mechanics in water.

The key steps taken by our algorithms are detailed below. The code builds on works from computer graphics. References to the relevant literature are made in order to provide the necessary scientific foundations and ease the reading. Obviously some loops are performed only once at compilation, but here the whole process is broken down into pseudocodes for clarity purposes. First, partition-of-unity weights are computed for each single vertex of the mesh. These describe the amount of influence that each joint (or bone) has on that particular vertex. The local transformation matrices are then converted into equivalent dual quaternion, linearly blended, and converted back into a matrix to obtain the transformed position of each vertex.

5.1.1. Weight computation

The computation of weights attributed to every single vertex in the mesh is far from being a trivial operation. Weights should be independent of mesh resolution, vary smoothly over the surface and handle the transition between joints to avoid deformation artifacts (Baran and Popovic, 2007). In traditional computer graphics software (e.g., Autodesk® Maya®, Blender, etc.), weights can be manually painted on the mesh by the

user. This is very often performed by professional artists in the animation movie and video game industries, at the expense of a great amount of time and effort. It is therefore unsurprising that researchers have strived to supply automatic solutions. These computerized solutions are fortunate since Fluent—which is designed to numerically solve flow problems—does not possess features to interact with geometries.

The simplest weights are said 'rigid'. Such weight functions take the value of 1 whenever a vertex is closer to the corresponding joint than to any other, and 0 otherwise. This is clearly unsatisfactory as such weights are not smooth. Rather, weights should progressively decay from 1 to 0 along the bone controlled by that joint. Such a problem falls within the scope of scattered data interpolation. A very common scheme is based on the inverse Euclidean distance between the joint and a vertex, in a similar fashion to Shepard's method (Shepard, 1968). Very often, weights are taken as inversely proportional to the distance squared (e.g., (Yang and Zhang, 2006)), although this results in smooth but uneven interpolation, the derivative of the function being 0 at the data points (Anjyo et al., 2014). An alternative approach relies on the calculation of an influence ratio that measures how close a vertex is to its bone. Weights were nonlinear, polynomial functions of that influence ratio, which eliminates discontinuities of the surface (Yang and Zhang, 2005). Weights must then be normalized to partition unity, a mandatory property of skinning weights ensuring affine invariance (i.e., applying a transformation to each joint yields the same result as if that transformation is applied to the whole shape). However, as discussed in Jacobson et al. (Jacobson et al., 2014), doing so allows for unintuitive behavior since the notion of 'farther' becomes relative to the other joints. Furthermore, methods dependent on Euclidean metric are not shape-aware. Shape-awareness has been achieved by some authors by explicitly computing geodesic distances; that is, the shortest path along a surface (in conjunction, for example, with radial basis functions (Levi and Levin, 2014)), or through a volume (e.g., (Dionne and de Lasa, 2014)). Alternatively, most recent techniques implicitly integrate the shape of the input model by solving energy minimization partial different equations. An energy function is determined solely by the metric on the shape rather in terms of differential quantities, and measures the smoothness of a shape and its behavior with respect to user-defined constraints (Jacobson, 2013). Those belong to variational modeling techniques. Perhaps the two most iconic works in that category are the bone heat weighting of Baran and Popovic (Baran and Popovic, 2007) and the bounded biharmonic weights of

Jacobson et al. (Jacobson et al., 2011). The first relates smooth weight computation to solving thermal equilibrium over a surface treating the underlying bones as heat sources for the vertices attached to them. Colloquially, an initial set of 'raw' weights are computed based upon a vertex nearest bone, then blurred through the heat diffusion step. The problem is discretized on the mesh using finite element method, yielding a linear system of very large sparse matrices hardly handled in Fluent. The second minimizes the Laplacian energy (resulting in functions "as harmonic as possible", in contrast to the Dirichlet energy that results in functions "as constant as possible") together with a set of constraints that enforce, for the first time, all the desirable weight properties at once (i.e., smoothness, non-negativity, shape-awareness, partition of unity, locality and sparsity, and the absence of local maxima). This scheme provides intuitive and high-quality deformations, although these are not deformation-aware. Very recent improvements were made in that direction by seeking the minimizer of a nonlinear elastic energy (Kavan and Sorkine, 2012). The deformation energy is not minimized over a single mesh pose, but rather simultaneously for various sample rotations (±90 degrees of rotation along each dimension, hence six different poses per joint). Furthermore, these two last techniques require the discretization of the volume into voxels. Those are huge drawbacks in the context of a workflow implemented in a CFD solver. We therefore had to resort to simpler weight functions, with very satisfactory results.

Algorithm 1: Automatic weight computation

Input: joint indices $j_1,\ldots,j_n$, mesh in rest pose (vertices **v,** bones **b**)
Output: joint weight w_j and endpoint weight e_j at each vertex for each joint/bone

---

// Define the limit angle α, which indicates the influence that each vertex must
// receive from the neighboring joints (Yang and Zhang, 2005)
for each joint *j* **do**
    // denote **d** the vector between the vertex and the joint *j*
    // denote $\mathbf{b_1}$ and $\mathbf{b_2}$ the distal and proximal bones, respectively
    // denote α_{b1} and α_{b2} the angles formed between **d** and $\mathbf{b_1}$ and $\mathbf{b_2}$, respectively
    // compute the influence ratio *r*

$$r = \frac{\alpha_{b_2} - \alpha}{\alpha_{b_2} + \alpha_{b_1} - \alpha}$$

// refine with a higher-order function

$w_j = -6.4r^5 + 16r^4 - 14.8r^3 + 6.2r^2$

end for

// Compute endpoint weights according to (Jacobson and Sorkine, 2011)

// let proj(**v**) be the projection of **v** onto the nearest bone **b,** and **a** be the distal joint

$$e_j = \frac{||\text{proj}(\mathbf{v}) - \mathbf{a}||}{||\mathbf{b}||}$$

5.1.2. Diffusion step

Smoothing operations are common in computer graphics and geometry processing. They are based upon the discrete Laplace-Beltrami operator. A discrete Laplacian is a fundamental geometric object defined as the divergence of a gradient that can notably be used as a smoothness penalty to choose functions varying smoothly along a surface. The result of applying the discrete Laplace operator to the absolute vertex coordinates $\mathbf{v}_i$ is the Laplacian δ_i (Nealen et al., 2006):

$$\delta_i = \sum_{j \in N_i} w_{ij}\left(\mathbf{v}_i - \mathbf{v}_j\right) = \mathbf{v}_i - \left[\sum_{j \in N_i} w_{ij}\mathbf{v}_j\right],$$

where N_i denotes the first-ring neighbors of the vertex i.

Several Laplacians for an arbitrary mesh have been used in computer graphics (Wardetzky et al., 2007). There are purely combinatorial Laplacians, such as the umbrella operator (w_{ij} = 1 if i and j share an edge) and the Tutte Laplacian ($w_{ij} = 1/d_i$, with d_i the degree of vertex i), although these fail to be geometric (i.e., they do not depend on vertex position, and thus are not intrinsic surface representation). Conversely, Laplacians based on cotangent weights are probably the most popular discretization because they are uniquely determined by the geometry of the underlying mesh (cotangents of each triangle corner angle and triangle area (Desbrun et al., 1999; Meyer et al., 2003); see Algorithm 2). However, the cotangent scheme was found to show weak convergence for irregular triangulation (Wardetzky, 2008; Xu, 2004). Belkin and colleagues' algorithm addresses this issue for an arbitrary triangular mesh (Belkin et al., 2008), where the Laplacian Lf of a function f is approximated with the heat kernel as follows:

$$\mathrm{L}f(i) = \frac{1}{4\pi h^2} \sum_{t \in K} \frac{\mathrm{Area}(t)}{3} \sum_{j \in V(t)} e^{-\frac{\|j-i\|^2}{4h}} \left(f(j) - f(i) \right).$$

K denotes the mesh, *t* is a face ∈ *K*, and V(*t*) is the set of vertices of *t*. It requires an input *h*, which is a positive quantity corresponding to the size of the neighborhood considered at each vertex and may be allowed to vary to allow the algorithm to adapt to local mesh size. To favor algorithms independent of user parameters, the cotangent Laplacian is implemented here to smooth vertex weights.

Algorithm 2: Optional diffusion smoothing of vertex weights

Input: mesh in rest pose, weights w_j

Output: smoothed weights w_j

---

for each vertex *i* **do**

identify its one-ring neighbors $j \in N_i$ and incident faces

// denote A_{ring} the area covered by all faces incident to *i*

// compute the entries of the lumped mass matrix *M* with barycentric area

$$M(i,j) = \begin{cases} 0 & \text{if i} \neq j \\ A_{ring}/3 & \text{if i} = j \end{cases}$$

// denote α_{ij} and β_{ij} the angles opposite the edge *ij*

// compute the entries of the weight matrix *W*

$$W(i,j) = \begin{cases} 0.5\left(\cot\alpha_{ij} + \cot\beta_{ij}\right) & \text{if } i \neq j \text{ and } j \in N_i \\ 0 & \text{if } i \neq j \text{ and } j \notin N_i \\ -\sum_{j \in N_i} W_{i,j} & \text{if } i = j \end{cases}$$

end for

// compute the Laplacian matrix

$L = M^{-1}W$

// evaluate the smoothed weights after a duration *h*

$w_j += hLw_j$

5.1.3. Smooth skinning

The most popular skin deformation technique for virtual characters is linear blend skinning (Kavan et al., 2009). The algorithm builds on ideas first appearing in the 80s (Badler and Morris, 1982; Magnenat-Thalmann et al., 1988), and was formally described mathematically by Levis et al. (Lewis et al., 2000). Linear skinning computes the deformed vertex position $\mathbf{v}'_i$ according to the following formula:

$$\mathbf{v}'_i = \sum_{j=1}^{m} w_{i,j} T_j \mathbf{v}_i = \left(\sum_{j=1}^{m} w_{i,j} T_j \right) \mathbf{v}_i ,$$

where $w_{i,j}$ is the weight describing the amount of influence of bone j on vertex i, as in Algorithm 1; T_j, a 4×4 matrix defining the rigid transformation (rotation and translation) associated with the bone j; and $\mathbf{v}_i$, a 4×1 vector storing the global coordinates of v in rest pose (with the last coordinates equal to one according to homogeneous coordinates convention). T_j is actually the concatenation of two matrices $T_{j,c} T_{j,r}^{-1}$, which, reading right to left, transforms the vertex position from the world coordinate system to the local coordinate system of bone j in rest pose, then transforms it in the world coordinate system of bone j in the current pose. The previous equation underlines the fact that a rest-pose vertex is deformed according to a weighted linear combination (blend) of transformation matrices, hence the name of the skinning method. These matrices are the deformation primitives of linear blend skinning; i.e., they are the elementary building blocks of deformations (Jacobson et al., 2014). The algorithm is simple to implement, fast at runtime, and works very well when blended transformations are not very different. Whenever transformations differ a lot in their rotational components though, serious failings occur. Because a linear combination of rotations is no longer a rotation (Alexa, 2002), linear blend skinning results in volume loss at the joint (see Fig. 5–1a). This is problematic as upper limb joints exhibit large range of motion. This issue is even more flagrant when dealing with bone twist (joint longitudinal rotation), and goes by the notorious name of "candy-wrapper artifact". In the case of a 180-degree rotation, the blended transformation is a rank-one matrix, projecting the 3D space onto the longitudinal axis and resulting in extreme shape collapse.

The above drawbacks cannot be avoided by changing weights, since their cause has deep geometrical roots. However, adding more weights does correct them to some extent. These techniques, called multi-linear, require the computation of a great number of extra parameters (theoretically 36, but 4 (Merry et al., 2006) and 12 (X. C. Wang and Phillips, 2002) are found in the literature) that are learned from a set of example poses, a task infeasible in Fluent. Even then, shape shrinking can still be visible. A more satisfactory and practical approach is to blend transformations in a nonlinear fashion using unit dual quaternions (Fig. 5–1b) (Kavan et al., 2008). Geometrically, the singularity apparent in the special orthogonal group $SO(3)$ is avoided because the space of unit quaternions is "less curved". In other words, dual quaternion blending is closer to a perfect manifold-intrinsic averaging (Jacobson et al., 2014). One issue, although minor for our application but worth mentioning, is that dual quaternions represent strictly rigid transformations; i.e., they are unable to parameterize non-uniform scale and shear. Jacobson and Sorkine (Jacobson and Sorkine, 2011) modified the standard dual quaternion blending formula to properly handle stretch and twist distributed along the length of a bone. They inserted additional scaling and rotation terms that are function of a new set of weights, successfully extending the original deformation space (Fig. 5–1c,d).

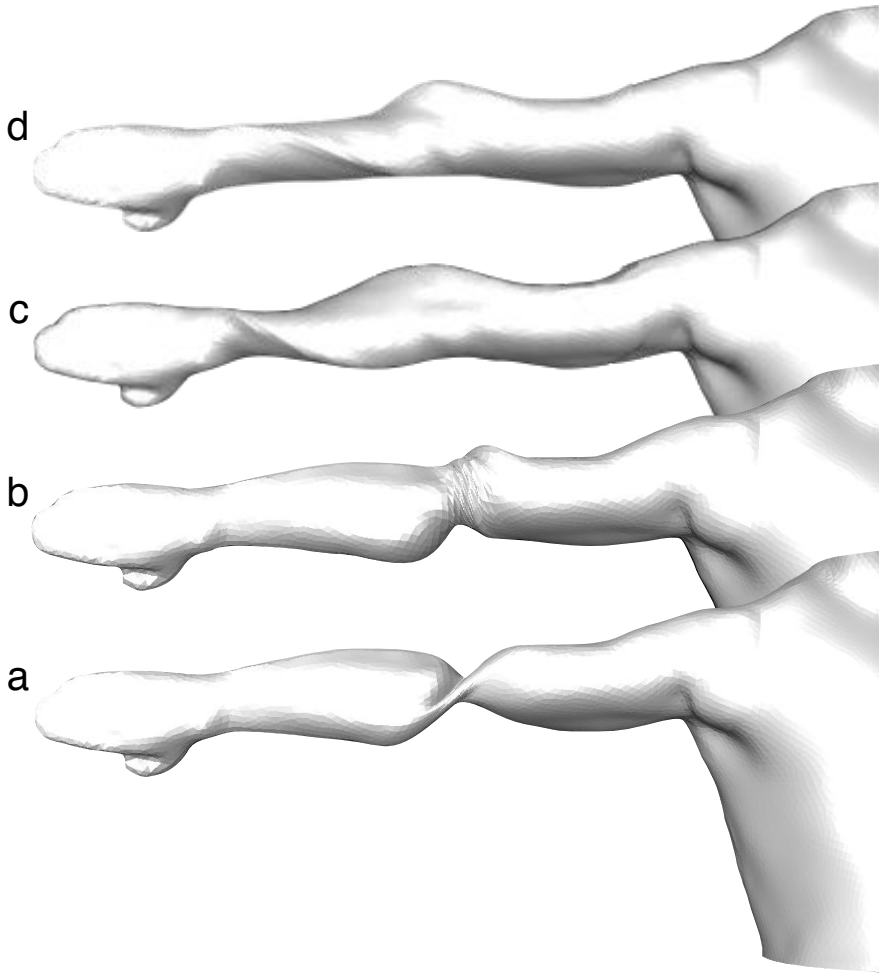

Figure 5–1. The forearm bone is given a 180-degree twist. Resulting deformation with linear blend skinning (a), dual quaternion skinning (b), and two different endpoint weights (c,d).

Conventional geometric skinning techniques have recently been enhanced to handle bulge artifact, contact modeling and volume preservation thanks to implicit skinning (Vaillant et al., 2013; 2014). A single scalar field (whose 0.5 iso-surface approximates the shape of the skin, hence the name "implicit skin") is computed in rest pose and rigidly transformed by the skeleton at each animation frame. Vertices are then projected back onto their respective iso-value within the scalar field to preserve the details of the mesh and adequately deal with surface self-intersection. Although this method results in visually realistic skin elastic deformation and collision, it would certainly fail within the CFD environment. As a matter of fact, unlike applications in computer graphics, fluid flow simulations require not only the character, but also the entire domain to be discretized. Squeezing the exterior mesh to produce skin fold would result in negative volume and simulations stopping before completion in the worst-case scenario. In that

sense, slight volume loss at the joint and the "artifacts' of dual quaternion skinning might actually reduce the risk of too distorted elements and ensure better simulation convergence.

Algorithm 3: Conversion from transformation matrix to dual quaternion

Input: joint indices $j_1,\ldots,j_n$, local transformation matrices M_j

Output: dual quaternion $\hat{\mathbf{q}}_j$

---

for each joint *j* **do**

// Let *R* and ***t*** be the 3×3 rotation matrix and 3×1 translation vector, respectively

// *I* denotes the identity matrix

$$B = (R - I)(R + I)^{-1}$$

s[0] = B[2][1]

s[1] = B[0][2]

s[2] = B[1][0]

mag = norm(s); s /= mag; z = atan(mag); sz = sin(z); cz = cos(z);

// Build the rotation part of the dual quaternion

$\hat{\mathbf{r}}_j$ = [cz;sz*s[0];sz*s[1];sz*s[2];0;0;0;0]

// Build the translation part of the dual quaternion

$\hat{\mathbf{t}}_j$ = [1;0;0;0;0;t[0]/2;t[1]/2; t[2]/2]

// Build the dual quaternion form of the combined transformation

$$\hat{\mathbf{q}}_j = \hat{\mathbf{t}}_j \hat{\mathbf{r}}_j$$

end

// Correct for quaternion antipodal property

for j = 2 : n **do**

if $\langle \hat{\mathbf{q}}_{j_1}, \hat{\mathbf{q}}_{j_n} \rangle < 0$ **then**

$$\hat{\mathbf{q}}_{j_n} = -\hat{\mathbf{q}}_{j_n}$$

end if

end for

Algorithm 4: Update vertex position

Input: joint indices $j_1,\ldots,j_n$, dual quaternions $\hat{\mathbf{q}}_j$, convex weights $w_1,\ldots,w_n$, vertex position in rest pose **v**

Output: transformed vertex position **v'**

// Dual quaternion linear blending based on (Kavan et al., 2007)

$$\hat{\mathbf{b}} = w_1\hat{\mathbf{q}}j_1 + \ldots + w_n\hat{\mathbf{q}}j_n$$

// Normalize to a unit dual quaternion $\hat{\mathbf{b}}'$

// Let $\mathbf{b}_0$ be the non-dual part of $\hat{\mathbf{b}}$, and $\mathbf{b}_\varepsilon$ the dual one

$$\mathbf{b}'_0 = \mathbf{b}_0 / \|\mathbf{b}_0\|$$
$$\mathbf{b}'_\varepsilon = \mathbf{b}_\varepsilon / \|\mathbf{b}_0\|$$

// Let the components of $\mathbf{b}'_0$ be w_0, x_0, y_0, z_0

// Let the components of $\mathbf{b}'_\varepsilon$ be $w_\varepsilon, x_\varepsilon, y_\varepsilon, z_\varepsilon$

// Build the translation vector

// Multiply by 2 to account for the fact that dual quaternions work with half

// of the translation vector

$$t_0 = 2(-w_\varepsilon x_0 + x_\varepsilon w_0 - y_\varepsilon z_0 + z_\varepsilon y_0)$$
$$t_1 = 2(-w_\varepsilon y_0 + x_\varepsilon z_0 + y_\varepsilon w_0 - z_\varepsilon x_0)$$
$$t_2 = 2(-w_\varepsilon z_0 - x_\varepsilon y_0 + y_\varepsilon x_0 + z_\varepsilon w_0)$$

// Convert back into a transformation matrix

$$M = \begin{pmatrix} 1-2y_0^2-2z_0^2 & 2x_0y_0-2w_0z_0 & 2x_0z_0+2w_0y_0 & t0 \\ 2x_0y_0+2w_0z_0 & 1-2x_0^2-2z_0^2 & 2y_0z_0-2w_0x_0 & t1 \\ 2x_0z_0-2w_0y_0 & 2y_0z_0+2w_0x_0 & 1-2x_0^2-2y_0^2 & t2 \\ 0 & 0 & 0 & 1 \end{pmatrix}$$

// Compute the blended position **v'** of vertex **v**

v' = M

5.2. Inverse dynamics analysis, a variety of formulations

The classical approach to inverse dynamics uses the vectorial form of the Newton–Euler equations. However, more methods have been developed, each devised to facilitate a particular analysis and supposedly equivalent from a theoretical point of view.

5.2.1. Vectors and Euler angles

This is the conventional formulation, which involves three steps concisely described in (Dumas et al., 2004): (i) according to the first Newton–Euler law, the force vector at the proximal end of a body segment is computed in an inertial reference frame provided that force vector at the distal end, the linear acceleration vector of the center of mass, and any external force vector are known; (ii) according to the second Newton–Euler law, the moment vector at the proximal end is computed in the segment coordinate system knowing the moment vector at the distal end and all (external, proximal and distal) force vectors. The latter, as well as angular velocity and acceleration vectors and the segment inertia tensor, must be known in the segment coordinate system and therefore require appropriate transformation; (iii) according to the action–reaction principle (Newton's third law of motion), the force and moment vectors acting at the distal end of the adjacent segment are equal in magnitude and opposite in sign to the force and moment vectors are the proximal end of the current segment. The moment vector must thus be transformed from the current segment coordinate system to the adjacent one. This three-step procedure therefore yields successive coordinate transformations and the manipulation of many attitude matrices. Besides the fact that these multiple operations add errors in the inverse dynamics solutions (Dumas et al., 2007b), attitude matrices are generally computed through a pre-determined sequence of Euler angles.

Euler angles singularity: gimbal lock

According to the Cardan/Euler angles convention, the 3D attitude of a body in space is parameterized in terms of three independent angles, resulting from an ordered sequence of rotations about either the global or local axes of a Cartesian coordinate system.

Although this is a popular approach in biomechanics because rotations are chosen so that they correspond to anatomical components of joint orientation and movement (Cappozzo et al., 2005; Wu et al., 2005), Cardan/Euler angles suffer from two main drawbacks. First, results are sequence-dependent (Karduna et al., 2000; Phadke et al., 2011; Senk and Chèze, 2006), and cannot therefore be reliably evaluated. Second, and most importantly, angles are sensitive to gimbal lock, early spotted in biomechanics by Woltring (Woltring, 1994). In mathematics, gimbal lock manifests itself as a singularity; i.e., a point at which an object is undefined (Diebel, 2006). This phenomenon occurs when the rotation over the second axis is 90° plus or minus multiples of 180°. In this event, the third coordinate axis becomes aligned with the first axis; both axes therefore become undistinguishable and one rotational freedom is locked, hence "gimbal lock"[9] and discontinuity in kinematic patterns that make impossible the description of the body attitude. Remarkably, this problem is far more frequent at the upper limb, and solving it is challenging since no single sequence proves simultaneously accurate, free from singularity, and anatomically meaningful (Senk and Chèze, 2006).

[9] A famous gimbal lock accident happened during the Apollo 11 Moon mission (the first to land humans on the Moon back in 1969). On this spacecraft, a set of only three gimbals—a support that can pivot and allow rotation about one axis—was used. Although the engineers were aware of the gimbal lock problem, they had declined to use a fourth gimbal, whose redundancy and added security did not make the cut to keep the equipment small and simple. It is said that engineers worried they would miss the Kennedy deadline to land a man on the Moon before the end of the decade if they waited to perfect a four-gimbal system. Alternatively, they chose to use a warning light that would flash when the lunar module approaches gimbal lock position. Motors could then theoretically be commanded to flip the gimbal 180 degrees instantaneously. Instead, the system froze the inertial measurement unit, asking for Mike Collins aboard the command module to manually realign it (Jones and Fjeld, 2011). Curiously, a similar warning is still in use in today's biomechanical algorithms, automatically switching to another angle sequence as a body gets close to singularity to reset gimbals. That is not a practical solution though, since gimbal lock might very well appear later on once again. One can simply avoid gimbals and resort to a method based on a different kinematical formalism.

5.2.2. Wrenches and quaternions

This alternative formalism, first proposed by Dumas et al. (Dumas et al., 2004), solves issues associated with the traditional, vectorial approach to inverse dynamics. Wrench notation is used to describe all forces and moments in the inertial reference frame alone, relaxing the need for multiple coordinate transformations, whereas quaternions efficiently parameterize body kinematics without adverse gimbal lock effects. Unlike the previous method, wrenches and quaternions allow a single-step computation of joint kinetics. One advantageous property of wrench is that they can be conveniently transformed from one point location to another (e.g., to displace the weight wrench from the center of mass to the proximal end). This way, the non-trivial transformation (via parallel axis theorem) of the inertia tensor can be avoided. Furthermore, this method was found to be poorly sensitive to noisy inputs (Dumas et al., 2006).

5.2.3. Generalized coordinates and forces

The methods presented so far require the definition of orthonormal segment coordinate system to encode segment position and orientation. Yet, the criterion of orthogonal axes is hardly compatible with anatomical, functional, and inertial requirements the axes should meet (Dumas and Chèze, 2007). Inverse dynamics based on generalized coordinates and forces, introduced by (Silva et al., 1997), frees itself from the need for orthonormal segment coordinate systems: the position and orientation of a segment is simply defined by a set of basic points and unitary vectors. Dumas and Chèze (Dumas and Chèze, 2007) proposed a segment definition that complies with anatomical and functional coherence, which also allows for ease of construction of joint coordinate system. This description is convenient to express joint forces along and moments about axes that are clinically sound. However, since several inverse dynamics calculations must be performed in an orthonormal coordinate system (e.g., joint power, work, 3D angle between joint angular velocity and moment vectors), this method is only appropriate for a very specific, clinically oriented analysis. Furthermore, generalized coordinates necessitate 12 parameters and 6 explicit constraints for the 6 (linear and angular) degrees of freedom of a segment. As a result, sensitivity to noise is increased as the explicit

constraints of the dynamic computation become violated with perturbed gait data (Dumas et al., 2006).

5.2.4. Homogeneous matrices

This fourth and last method, presented by Legnani et al. (Legnani et al., 1996) to extend its use in robotics to rigid body kinematics and dynamics, relies on homogeneous matrix algebra. A homogeneous matrix indicated by **M** is a 4×4 matrix containing a 3×3 submatrix **R** describing the orientation of the body and a 3×1 vector **t** representing the position. The pose of a body with respect to a global reference frame (0) is therefore represented by the matrix $\mathbf{M}_{0,1}$:

$$\mathbf{M}_{0,1} = \begin{bmatrix} \mathbf{R}_{0,1} & \mathbf{t}_{0,1} \\ 0 & 1 \end{bmatrix} = \begin{bmatrix} x_x & y_x & z_x & t_x \\ x_y & y_y & z_y & t_y \\ x_z & y_z & z_z & t_z \\ 0 & 0 & 0 & 1 \end{bmatrix}, \tag{5.1}$$

where the vector $\mathbf{t}_{0,1}$ is the position of the origin of the local, body-fixed reference frame in (0), and $\mathbf{R}_{0,1}$ is a rotation matrix describing the orientation of the frame (1) in (0). The three first columns of $\mathbf{M}_{0,1}$ correspond to the three unit vectors of the frame (1) expressed in (0). Thus, this matrix (also commonly named 'transformation matrix') can be readily built from motion capture system output. Given a third frame (2) (say, the segment proximal to (1)), transformation matrices can be combined as follows to obtain the pose of the distal frame (2) into its parent (1):

$$\mathbf{M}_{1,2} = \mathbf{M}_{1,0}\mathbf{M}_{0,2} = \mathbf{M}_{0,1}^{-1}\mathbf{M}_{0,2}, \tag{5.2}$$

with $\mathbf{M}_{0,1}^{-1}$ being the inverse of $\mathbf{M}_{0,1}$. The inverse of a homogeneous matrix is simply:

$$\mathbf{M}_{0,1}^{-1} = \begin{bmatrix} \mathbf{R}_{0,1}^{\mathrm{T}} & -\mathbf{R}_{0,1}^{\mathrm{T}}\mathbf{t}_{0,1} \\ 0 & 1 \end{bmatrix}, \tag{5.3}$$

$^{\mathrm{T}}$ being the transpose operation.

To fully parameterize body kinematics, the matrices **W** and **H**, which respectively contain the linear and angular velocities and accelerations, are introduced. The velocity matrix W is calculated as follows:

$$\mathbf{W} = \dot{\mathbf{M}}_{0,1}\mathbf{M}_{0,1}^{-1}, \tag{5.4}$$

Recalling that $\mathbf{M}_{0,1}$ encodes the global positions of the three axes of frame (1), time derivatives are obtained through traditional differentiation schemes (Doriot and Chèze, 2004; Legnani et al., 1996). Since $\mathbf{W}$ is also defined as:

$$\mathbf{W} = \begin{bmatrix} \omega & \mathbf{v}_0 \\ 0 & 0 \end{bmatrix} = \begin{bmatrix} 0 & -\omega_z & \omega_y & v_x \\ \omega_z & 0 & -\omega_x & v_y \\ -\omega_y & \omega_x & 0 & v_z \\ 0 & 0 & 0 & 0 \end{bmatrix}, \tag{5.5}$$

it is easy to extract the body angular velocity $\boldsymbol{\omega} = \begin{bmatrix} \omega_x, \omega_y, \omega_z \end{bmatrix}$ and the linear velocity $\mathbf{v}_0$ of the point (called the pole) that belongs to the segment and passes, at every instant, through the origin of the reference frame. Likewise, the acceleration matrix $\mathbf{H}$ is computed according to the following equation:

$$\mathbf{H} = \ddot{\mathbf{M}}_{0,1}\mathbf{M}_{0,1}^{-1}, \tag{5.6}$$

and is defined as:

$$\mathbf{H} = \begin{bmatrix} \alpha & \mathbf{a} \\ 0 & 0 \end{bmatrix}, \tag{5.7}$$

with α, just as ω, being a skew-symmetric matrix storing 3D body angular accelerations; and $\mathbf{a}_0$, the linear acceleration of the pole with respect to the global reference frame.

To recursively solve the dynamic equilibrium of each body segment, new matrices must be introduced to generalize the homogeneous operator in dynamics (Legnani et al., 1996). (i) Traditional body segment moments of inertia I and segment mass m allow constructing the inertial tensor $\mathbf{I}$, then displaced to the origin of the segment coordinate system according to the parallel axis theorem:

$$\mathbf{I} = \begin{bmatrix} I_{xx} & I_{xy} & I_{xz} \\ I_{yx} & I_{yy} & I_{yz} \\ I_{zx} & I_{zy} & I_{zz} \end{bmatrix} + m\left[(\mathbf{R}\cdot\mathbf{R})\mathbf{E}_3 - \mathbf{R}\otimes\mathbf{R}\right] = \begin{bmatrix} A & -F & -E \\ -F & B & -D \\ -E & -D & C \end{bmatrix}, \tag{5.8}$$

where $\mathbf{E}_3$ is the 3×3 identity matrix; $\mathbf{R}$, the displacement vector from the segment center of mass to the origin of the local reference frame; and $\otimes$, the outer product of two vectors. This new matrix is ultimately used to build the pseudo-inertial matrix $\mathbf{J}$:

$$\mathbf{J}=\begin{bmatrix} \frac{\mathrm{tr}(\mathbf{I})}{2}-A & F & E & m\mathrm{X}_{\mathrm{COM}} \\ F & \frac{\mathrm{tr}(\mathbf{I})}{2}-B & D & m\mathrm{Y}_{\mathrm{COM}} \\ E & D & \frac{\mathrm{tr}(\mathbf{I})}{2}-C & m\mathrm{Z}_{\mathrm{COM}} \\ m\mathrm{X}_{\mathrm{COM}} & m\mathrm{Y}_{\mathrm{COM}} & m\mathrm{Z}_{\mathrm{COM}} & m \end{bmatrix} \tag{5.9}$$

where $\mathrm{tr}(\mathbf{I})$ denotes the trace of the inertial matrix (i.e., the sum of its diagonal elements), and $[\mathrm{X}_{\mathrm{COM}},\mathrm{Y}_{\mathrm{COM}},\mathrm{Z}_{\mathrm{COM}}]$ the center of mass position. (ii) An external force $\mathbf{f}$ and its moment (or torque) $\mathbf{m}$ acting on a body are stored in an "action" (skew-symmetric) matrix ϕ as follows:

$$\phi=\begin{bmatrix} \mathbf{m}_s & \mathbf{f}_s \\ -\mathbf{f}_s^{'} & 0 \end{bmatrix}=\begin{bmatrix} 0 & -\mathbf{m}_z & \mathbf{m}_y & \mathbf{f}_x \\ \mathbf{m}_z & 0 & -\mathbf{m}_x & \mathbf{f}_y \\ -\mathbf{m}_y & \mathbf{m}_x & 0 & \mathbf{f}_z \\ -\mathbf{f}_x & -\mathbf{f}_y & -\mathbf{f}_z & 0 \end{bmatrix}. \tag{5.10}$$

Consider, for example, the previous dynamic matrix expressed in the global frame (0). Quantities can be readily projected on the frame (k) using the expression (Legnani et al., 1996):

$$\boldsymbol{\phi}_{(k)}=\mathbf{M}_{0,k}\boldsymbol{\phi}_{(0)}\mathbf{M}_{0,k}^{\mathrm{T}}. \tag{5.11}$$

Evaluation of internal load readily follows from Newtonian mechanics, and is performed iteratively in a distal to proximal fashion. Because of its compact and efficient nature, matrix notation is very well suited to computer applications. Linear and rotational components are treated simultaneously. No assumption regarding the type of joint being modeled is required, which is convenient for complex joints, and the kinematic formulation shows low sensitivity to noisy data (Dumas et al., 2006). Surprisingly, despite its numerous advantages, inverse dynamics modeling based on homogeneous matrices is rarely seen in the literature; this is the approach we retained throughout this thesis. Its mathematical formulation is explicitly detailed in the next chapter.

6 Upper limb joint forces and moments during underwater cyclical movements

Sound inverse dynamics modeling is lacking in aquatic locomotion research because of the difficulty in measuring hydrodynamic forces in dynamic conditions. Here we report the successful implementation and validation of an innovative methodology crossing new computational fluid dynamics and inverse dynamics techniques to quantify upper limb joint forces and moments while moving in water. Upper limb kinematics of seven male swimmers sculling while ballasted with 4 kg was recorded through underwater motion capture. Together with body scans, segment inertial properties, and hydrodynamic resistances computed from a unique dynamic mesh algorithm capable to handle large body deformations, these data were fed into an inverse dynamics model to solve for joint kinetics. Simulation validity was assessed by comparing the impulse produced by the arms, calculated by integrating vertical forces over a stroke period, to the net theoretical impulse of buoyancy and ballast forces. A resulting gap of 1.2 ± 3.5% provided confidence in the results. Upper limb joint load was within 5% of swimmer's body weight, which tends to supports the use of low-load aquatic exercises to reduce joint stress. We expect this significant methodological improvement to pave the way towards deeper insights into the mechanics of aquatic movement and the establishment of practice guidelines in rehabilitation, fitness or swimming performance.

6.1. Introduction

Inverse dynamics provides kinetic quantities such as net joint moments, compressive and shear joint forces, or power flow across segments, from differentiated kinematics and external forces acting upon the body (Hatze, 2002). This approach has proved crucial to answer fundamental questions common to biomechanics and physiology, unveiling, among others, the mechanical determinants of overground locomotion metabolic cost and efficiency (Sawicki and Ferris, 2009; 2008), how joints modulate net power output (Farris and Sawicki, 2012; Roberts and Belliveau, 2005), how muscles work (Winter, 1983), strategies to reduce joint loading in the prevention and treatment of running-related injuries (Heiderscheit et al., 2011), or the mechanical bases to design biomimetic prostheses (Collins et al., 2015; Hansen et al., 2004).

These key questions have received considerable attention in terrestrial locomotion; yet, they remain unanswered in water-based activities, impeding our understanding of human aquatic 'performance'. Unlike on land where external forces are easily measured via force platforms, they are very hard to estimate in water. The prediction of fluid forces on a swimmer's hand has been achieved through pressure measurements (Kudo et al., 2008), sensors however only provide pressure at specific hand locations and thus do not offer a complete hydrodynamics picture, nor do they precisely reflect the actual instantaneous point of force application. Furthermore, external forces at the hand are insufficient to solve the inverse dynamics problem, and those at the forearm and upper arm are simultaneously needed. This method is therefore poorly suited to inverse dynamics modeling. The strip theory approach, which is a different one that consists in partitioning a system made of geometrical shapes into many thin strips on which fluid forces are computed, has also been carried out (Biscarini and Cerulli, 2007; Orselli and Duarte, 2011), though lift was ignored and the analysis was restricted to the lower limb in the sagittal plane. In the case of 3D motions, or upper limb movements where lift likely takes a more prominent place as forces are generated from cambered body surfaces (Takagi et al., 2013), such an approach would introduce complicated mathematical expressions to account for all forces acting on the moving segments and, thus, is not satisfactory for the purpose of estimating the joint load.

Over the last decade, the use of computational fluid dynamics (CFD) has emerged in aquatic locomotion research as a promising alternative to those issues. It has the advantage of providing enhanced hydrodynamic force calculations, yet mostly limited to the investigation of swimmer's gliding positions (Costa et al., 2015; Zaïdi et al., 2008) or rigid arm models in various configurations (Marinho et al., 2011; Rouboa et al., 2006). Rouboa et al. (Rouboa et al., 2006) recognized the difficulty in prescribing true kinematics with acceleration/deceleration, multiaxial rotations, limb deformation at the joints, and mesh motion. This is because commercial CFD software solutions lack features to deal with complex 3D deformations, which in turn does not allow the quantification of resistive forces acting upon a whole limb in dynamic conditions. As of today, this problem poses one of the major challenge of aquatic movement research (Biscarini and Cerulli, 2007), and by extension, hydrotherapy, competitive swimming, and aquatic fitness.

In view of the above-mentioned issues, we developed two innovative integrated techniques to assess upper limb joint load in water: a dynamic mesh CFD algorithm to smoothly handle large body deformations and compute instantaneous hydrodynamic forces at the hand, forearm and upper arm in dynamic conditions, coupled with an inverse dynamics model specifically designed for complex joints. We first tested the methodological hypothesis that CFD, when integrated with inverse dynamics, could reliably be used to assess upper limb joint load in water. Second, given the growing popularity of aquatic therapy but the lack of mechanical evidence for its benefits, we computed upper limb joint forces and moments to check whether joint load would be low and supportive of the implementation of upper limb aquatic exercises for rehabilitation.

6.2. Material and methods

6.2.1. Kinematic data collection and pre-processing

Seven experienced, right-handed male swimmers (25.3 ± 2.6 years, 1.80 ± 0.06 m, 73.5 ± 6.8 kg) provided written informed consent to participate in the study. Approval for all

experimental procedures was granted by the University of Porto ethics committee. Participants were sculling at the middle of a 25-m long, 2-m deep indoor swimming pool, while ballasted with 4 kg (effective underwater weight: 34 N) tied at the waist. They were instructed to remain stationary head above the water surface for about 10 s. Such an ∞-shaped sculling motion (divided into down and upstroke; see Fig. 6–1) was chosen since it naturally incorporates flow phenomena that are responsible for high force production in regular competitive strokes (Takagi et al., 2014), and is an exercise frequently used in fitness and rehabilitation programs.

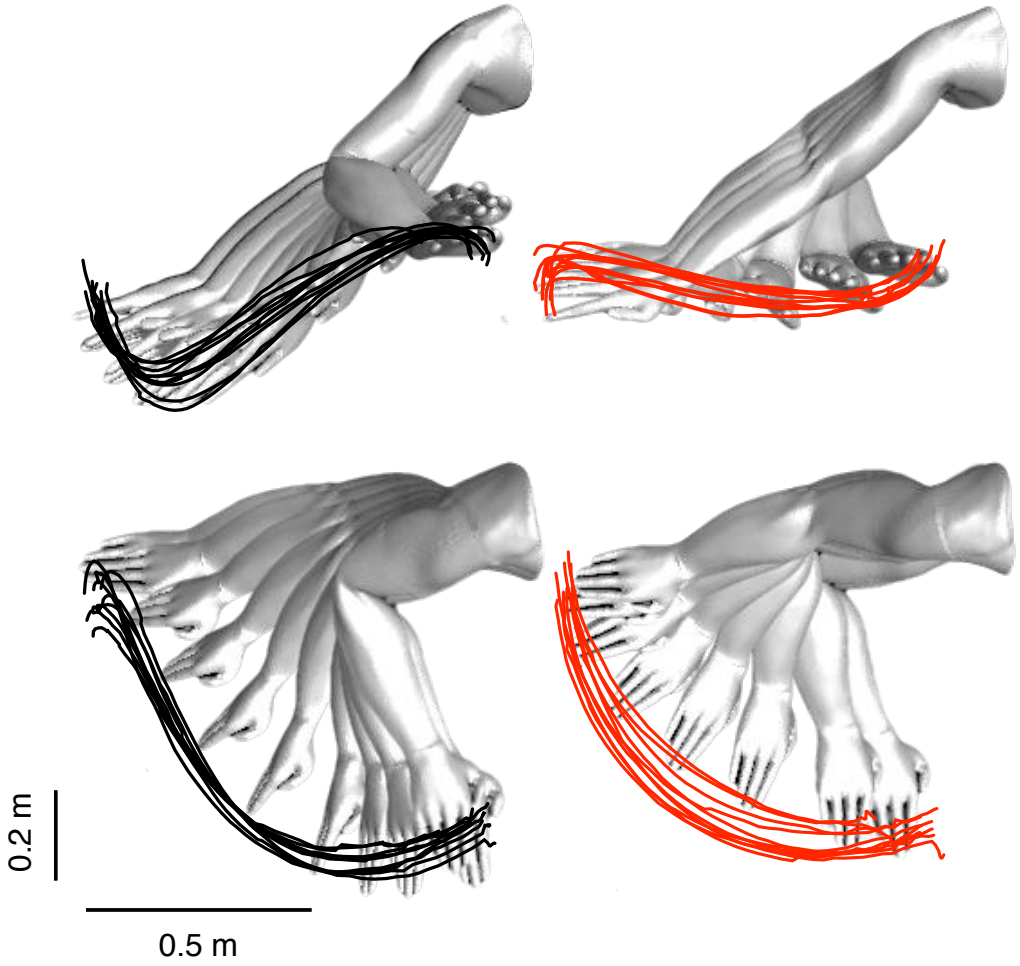

Figure 6–1. Middle finger tip trajectories in the frontal (top) and transverse (bottom) planes captured from Qualisys cameras superimposed on the upper limb geometry numerically deformed every 0.05 s (19 frames). Black traces are downstroke (when the arms are horizontally adducted); red traces, upstroke (when the arms are horizontally abducted after stroke reversal). Note how virtual upper limb motion matches experimental kinematics.

3D kinematics data were captured in the inertial coordinate system (ICS) by automatically tracking 12 reflective markers positioned along the right upper limb and thorax (see Fig. 6–2) using a 12-camera underwater motion capture set-up (Qualisys, Gothenburg, Sweden). Ten cameras were mounted along two opposite sides of the pool, just below the water surface, and the two others at the bottom of the pool facing upwards. A volume of approximately 9 m^3 (3 m long, 2 m wide, 1.5 m deep) was calibrated using an L-shaped reference structure and moving a wand with two markers (inter-point distance: 0.7495 m) according to manufacturer's recommendations. Marker reconstruction accuracy reached 99.8%.

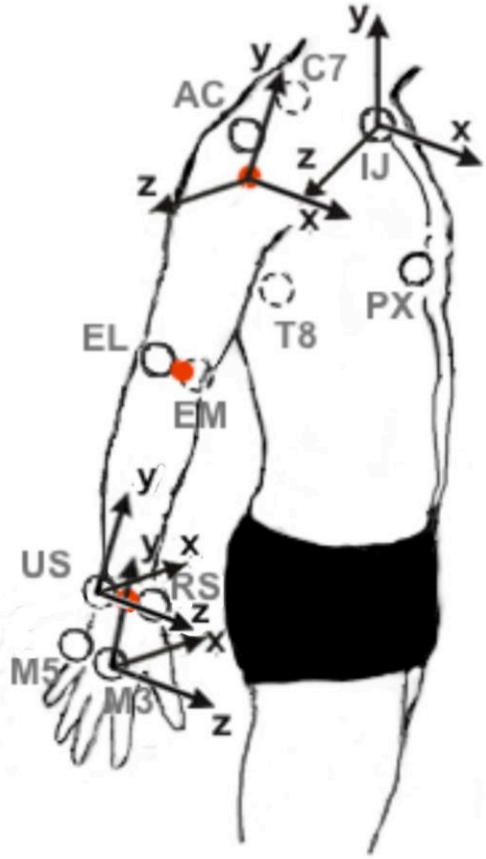

Figure 6–2. Right upper limb kinematic model. Markers are shown as open circles and joint centers as red dots. Right-handed segment coordinate systems follow ISB recommandations (Wu et al., 2005), the *X*-, *Y*- and *Z*-axes respectively pointing anteriorly, superiorly and laterally to the right. PX: xiphoid process; IJ: suprasternal notch; C7: spinous process at C7; T8: spinous process at T8; AC: acromion process; EL: lateral epicondyle; EM: medial epicondyle: US: ulnar styloid; RS: radial styloid; M3: third metacarpal; M5: fifth metacarpal; and an additional piece of reflective tape at the tip of the middle finger (not represented here).

Of the 10 s of data collection, we retained for processing four sculling strokes per subject satisfying the task instruction to move as little as possible, selected on the basis of the stability of xiphoid process marker vertical displacement. Markers trajectories were low-pass filtered (4^{th} order Butterworth filter, cutoff frequency of 6 Hz). Segment coordinate systems (SCS; thorax, upper arm, forearm and hand) were constructed according to the right-hand rule with the *X*-axis directed anteriorly (abduction/adduction axis), the *Y*-axis superiorly (internal/external rotation axis) and the *Z*-axis laterally to the right (flexion/extension axis), and embedded respectively at the suprasternal notch,

glenohumeral joint center (estimated from the calculation diagram provided by Reed et al. (Reed et al., 1999)), ulnar styloid and third metacarpal (Table 6–1 and Fig. 6–2). Joint angle time series—later on required into the dynamic mesh algorithm to realistically deform the body—were computed from the relative motion between two adjacent SCS through the *Z*–*X*–*Y* Euler angles sequence. These procedures agreed with the International Society of Biomechanics (ISB) convention (Wu et al., 2005), and were carried out in MATLAB® R2014a (The MathWorks, Inc., Natick, MA, USA).

Segment	*X*-axis	*Y*-axis	*Z*-axis
Thorax	$\overline{t}_x = \overline{t}_y \times \overline{t}_z$	$\overline{t}_y = \frac{(\overline{m}_{IJ} + \overline{m}_{C7})/2 - (\overline{m}_{PX} + \overline{m}_{T8})/2}{\left\lvert (\overline{m}_{IJ} + \overline{m}_{C7})/2 - (\overline{m}_{PX} + \overline{m}_{T8})/2 \right\rvert}$	$\overline{t}_z = \frac{\overline{m}_{IJ} - \overline{m}_{C7}}{\left\lvert \overline{m}_{IJ} - \overline{m}_{C7} \right\rvert} \times \overline{t}_y$
Upper arm	$\overline{ua}_x = \overline{ua}_y \times \overline{ua}_z$	$\overline{ua}_y = \frac{\overline{gh} - (\overline{m}_{EL} + \overline{m}_{EM})/2}{\left\lvert \overline{gh} - (\overline{m}_{EL} + \overline{m}_{EM})/2 \right\rvert}$	$\overline{ua}_z = \frac{\overline{m}_{US} - (\overline{m}_{EL} + \overline{m}_{EM})/2}{\left\lvert \overline{m}_{US} - (\overline{m}_{EL} + \overline{m}_{EM})/2 \right\rvert} \times \overline{ua}_y$
Forearm	$\overline{fa}_x = \frac{\overline{m}_{US} - \overline{m}_{RS}}{\left\lvert \overline{m}_{US} - \overline{m}_{RS} \right\rvert} \times \overline{fa}_y$	$\overline{fa}_y = \frac{(\overline{m}_{EL} + \overline{m}_{EM})/2 - \overline{m}_{US}}{\left\lvert (\overline{m}_{EL} + \overline{m}_{EM})/2 - \overline{m}_{US} \right\rvert}$	$\overline{fa}_z = \overline{fa}_x \times \overline{fa}_y$
Hand	$\overline{h}_x = \frac{\overline{m}_{US} - \overline{m}_{RS}}{\left\lvert \overline{m}_{US} - \overline{m}_{RS} \right\rvert} \times \overline{h}_y$	$\overline{h}_y = \frac{(\overline{m}_{RS} + \overline{m}_{US})/2 - \overline{m}_{M3}}{\left\lvert (\overline{m}_{RS} + \overline{m}_{US})/2 - \overline{m}_{M3} \right\rvert}$	$\overline{h}_z = \overline{h}_x \times \overline{h}_y$

Table 6-1. Definitions of the segment coordinate systems for the right-hand side. $\overline{m}_{SUBSCRIPT}$ stands for marker locations, and $\overline{gh}$, the glenohumeral joint center location estimated as in (Reed, 1999).

6.2.2. Numerical method

Body geometries were obtained from a Mephisto 3D scanner (4DDynamics, Antwerp, Belgium), further edited and converted into a 3D computer-aided design model prior to import into ANSYS® Fluent® Release 14.5 software (ANSYS, Inc., Canonsburg, PA, USA). The computational domain was a cube of 3-m edges, single phase with no air-water interface, and discretized into unstructured tetrahedral cells. Domain size independence was checked with domain boundaries gradually moved further away from the geometry until no change in hydrodynamic forces occurs to guarantee that the results are not affected. A virtual rectangular body of influence was created to refine the mesh around the moving segments, where high velocity and pressure gradients are expected.

No velocity was imposed at the inlet, all gradients were null at the outlet, and the no-slip condition enforced at the body surface. The numerical flow simulation rests on the finite volume approach. The 3D incompressible, unsteady Navier–Stokes equations are discretized at the level of the body-conforming grid via the Fluent pressure-based segregated solver (Patankar, 1980), leading to the following system of nonlinear second-order partial differential (continuity and momentum) equations:

$$\nabla \cdot \mathbf{u} = 0, \tag{6.1}$$

and

$$\rho\left(\frac{\partial \mathbf{u}}{\partial t} + (\mathbf{u}\cdot\nabla)\mathbf{u}\right) = \rho\mathbf{g} - \nabla p + \mu\Delta\mathbf{u}, \tag{6.2}$$

where u is the velocity vector, g the body force per unit mass, p the pressure, and ρ and μ the density and dynamic viscosity of the fluid, respectively. The first-order implicit formulation was used for time discretization. No turbulence model was used in this study for the following reasons: (i) for a maximum stroke speed of 2.5 m s^{-1} and a characteristic arm–forearm length (the dimension along which the boundary layer develops) of either 0.08 m (thickness) or 0.10 m (width), this yielded a Reynolds number of 2.9×10^5, indicative of a transitional flow; and (ii) for flow with massive separation at edges, the separation point location is theoretically insensitive to the Reynolds number (Hoerner, 1965)—numerically confirmed by Marinho et al. (Marinho et al., 2011) who found constant drag coefficient regardless of water flow speed—hence a very low effect of turbulences on hydrodynamic forces. For complex flow crossing the mesh lines obliquely, the second-order discretization was adopted to limit numerical diffusion. The

PISO algorithm with skewness correction (uncoupled from neighbor correction) was used to deal with distorted meshes (ANSYS, Inc, 2012). The convergence criterion was set at 10^{-3}.

6.2.3. Dynamic mesh algorithm

Most difficulties arise when numerically controlling joint deformation; the geometry is highly constrained. Joints must connect smoothly to the adjacent rigid surfaces to prevent negative cell volumes and the simulation to stop before completion. Triangle aspect ratios also require to be preserved for the solution to converge. These requirements must absolutely be respected to simulate full aquatic upper limb movements, and to compute the external forces necessary for inverse dynamics modeling. Yet, at present, no solutions are available in commercial CFD software. To achieve this, we built upon previous works in computer graphics (Kavan et al., 2008) and implemented a dual quaternion blending algorithm in C programming language within Fluent. Briefly, each 4×4 transformation matrix T_j that defines the instantaneous configuration of an upper limb joint j was computed and converted to its dual quaternion form $\hat{\mathbf{q}}_j$. These dual quaternions were linearly blended into a new, unit (normalized) dual quaternion $\hat{\mathbf{b}}' = \sum_{j=1}^{n} \frac{w_j \hat{\mathbf{q}}_j}{\left\| w_j \hat{\mathbf{q}}_j \right\|}$ where n is 3, the number of upper limb joints; and w_j are the weights computed based on the distance from a vertex $\mathbf{v}$ in neutral pose to its neighboring joints. The transformed vertex $\mathbf{v}_c$ in the current pose then readily derived from the following relation: $\mathbf{v}_c = \hat{\mathbf{b}}'\mathbf{v}\hat{\mathbf{b}}'^{*}$, where $\hat{\mathbf{b}}'^{*}$ is the conjugate of $\hat{\mathbf{b}}'$. The resulting blended transformation does not contain shear or scale factors, which results in a smooth, skin-like animation free from skin-collapsing artifacts.

6.2.4. Inverse dynamics model

Since no existent interface readily links the external forces computed through CFD to the measurement of the joint load, we coded and implemented an inverse dynamics model of the upper limb through the homogeneous matrix approach, a compact notation derived

from robotics that treats concomitantly linear and rotational components (Legnani et al., 1996). There are sound reasons for the choice of this approach over the classical Newton–Euler vectorial equations: (i) the notation is convenient for computer applications; (ii) the method is poorly sensitive to kinematics measurement errors; (iii) importantly, no assumption about the type of joint being modeled is required, which makes the model suitable for complex joints (Doriot and Chèze, 2004).

Model inputs were the acceleration, pseudo-inertial, and action (drag, weight and buoyancy) matrices at every time step of the simulation. From the homogeneous transformation matrix $\mathbf{M}_{0,s}$ representing the attitude of the segment *s* with respect to the ICS, the acceleration matrix is obtained by:

$$\mathbf{H}_{s(0)} = \ddot{\mathbf{M}}_{0,s}\mathbf{M}_{0,s}^{-1}, \tag{6.3}$$

with $\ddot{\mathbf{M}}_{0,s}$ the second order derivative of the transformation matrix $\mathbf{M}_{0,s}$ and $\mathbf{M}_{0,s}^{-1}$ its inverse. Segment masses *m* and center of mass positions $\mathbf{r}_{COM}$ in the SCS were estimated from scaling equations based on subject anthropometry (Dumas et al., 2007a), and used to build the inertial matrix $\mathbf{I}_{s(COM)}$. This matrix was displaced from the segment center of mass to the origin of the SCS according to the parallel axis theorem:

$$\mathbf{I}_{s(SCS)} = \mathbf{I}_{s(COM)} + m\left[(\mathbf{R}\cdot\mathbf{R})\mathbf{E}_3 - \mathbf{R}\otimes\mathbf{R}\right] = \begin{bmatrix} \mathrm{I}_{xx} & \mathrm{I}_{xy} & \mathrm{I}_{xz} \\ \mathrm{I}_{yx} & \mathrm{I}_{yy} & \mathrm{I}_{yz} \\ \mathrm{I}_{zx} & \mathrm{I}_{zy} & \mathrm{I}_{zz} \end{bmatrix}, \tag{6.4}$$

where $\mathbf{I}_{s(SCS)}$ is the new inertia matrix, $\mathbf{R}$ the displacement vector, and $\mathbf{E}_3$ the 3×3 identity matrix. The pseudo-inertial matrix $\mathbf{J}$ of the segment *s* was finally derived as follows:

$$\mathbf{J}_{s(SCS)} = \begin{bmatrix} \frac{\mathrm{tr}\left(\mathbf{I}_{s(SCS)}\right)}{2} - \mathrm{I}_{xx} & -\mathrm{I}_{xy} & -\mathrm{I}_{xz} & q_x \\ -\mathrm{I}_{yx} & \frac{\mathrm{tr}\left(\mathbf{I}_{s(SCS)}\right)}{2} - \mathrm{I}_{yy} & -\mathrm{I}_{yz} & q_y \\ -\mathrm{I}_{zx} & -\mathrm{I}_{zy} & \frac{\mathrm{tr}\left(\mathbf{I}_{s(SCS)}\right)}{2} - \mathrm{I}_{zz} & q_z \\ q_x & q_y & q_z & m \end{bmatrix}, \tag{6.5}$$

where $\mathrm{tr}\left(\mathbf{I}_{s(SCS)}\right)$ denotes the trace of the inertial matrix, and $\mathbf{q} = m\mathbf{r}_{COM}{}^{\mathrm{T}}$ the product of the segment mass by the center of mass position. Fluid forces and moments were calculated in the SCS from the action of the fluid on each face of the segment. Net fluid force $\mathbf{f}_s$ on the segment *s* was computed as follows:

$$\mathbf{f}_s = \sum_{i=1}^{n} \mathbf{f}_i, \tag{6.6}$$

where $\mathbf{f}_i$ is the sum of pressure and friction drag acting on the face *i* expressed in the SCS, and *n* the number of faces composing the segment surface. The resulting moment $\mathbf{m}_s$ was given by:

$$\mathbf{m}_s = \sum_{i=1}^{n} \mathbf{r}_i \times \mathbf{f}_i, \tag{6.7}$$

where $\mathbf{r}_i$ is the position vector of the centroid of face *i* in the SCS. Fluid forces and moments acting on the segment *s* were stored in the skew-symmetric action matrix $\phi_{F,s}$:

$$\phi_{F,s(SCS)} = \begin{bmatrix} \mathbf{m}_s & \mathbf{f}_s \\ -\mathbf{f}_s{}' & 0 \end{bmatrix} = \begin{bmatrix} 0 & -\mathbf{m}_z & \mathbf{m}_y & \mathbf{f}_x \\ \mathbf{m}_z & 0 & -\mathbf{m}_x & \mathbf{f}_y \\ -\mathbf{m}_y & \mathbf{m}_x & 0 & \mathbf{f}_z \\ -\mathbf{f}_x & -\mathbf{f}_y & -\mathbf{f}_z & 0 \end{bmatrix}. \tag{6.8}$$

Weight and buoyancy action matrices ($\phi_{W,s}$ and $\phi_{B,s}$) were evaluated in the ICS. Volume of upper limb segments and centers of buoyancy were determined from participants' upper limb scan models, which allowed for the computation of moments of buoyancy. Both action matrices were converted back in the SCS as follows:

$$\phi_{W,s(SCS)} = \mathbf{M}_{s,0}\phi_{W,s(0)}\mathbf{M}_{s,0}^{-1}, \tag{6.9}$$

$$\phi_{B,s(SCS)} = \mathbf{M}_{s,0}\phi_{B,s(0)}\mathbf{M}_{s,0}^{-1}. \tag{6.10}$$

Inverse dynamics calculations were then performed iteratively to solve for upper limb net joint forces and moments. The acceleration matrix $\mathbf{H}_{s(0)}$ was similarly converted in the SCS, and further multiplied by $\mathbf{J}_{s(SCS)}$ to yield the matrix $\mathbf{A}$ containing the forces and moments producing the linear and angular acceleration of the segment *s*:

$$\mathbf{A}_{s(SCS)} = \mathbf{H}_{s(SCS)}\mathbf{J}_{s(SCS)} - \mathbf{J}_{s(SCS)}\mathbf{H}_{s(SCS)}^{\mathrm{T}}. \tag{6.11}$$

The net forces and moments acting on a segment were stored in the following matrix:

$$\mathbf{\Phi}_{s(SCS)} = \phi_{F,s(SCS)} + \phi_{W,s(SCS)} + \phi_{B,s(SCS)} + \mathbf{A}_{s(SCS)}, \tag{6.12}$$

and those acting at the proximal joint *j* of segment *s* were ultimately derived from:

$$\mathbf{\Phi}_{j(SCS)} = \mathbf{\Phi}_{s(SCS)} + \mathbf{M}_{s,s-1}\mathbf{\Phi}_{j-1(SCS)}\mathbf{M}_{s,s-1}^{-1}, \quad (6.13)$$

with $\mathbf{\Phi}_{j-1(SCS)}$, the action matrix describing net forces and moments at the joint *j*–1 distal to *j* in the distal SCS; $\mathbf{M}_{s,s-1}$, the transformation matrix of the distal SCS expressed in the proximal one; and $\mathbf{M}_{s,s-1}^{-1}$, its inverse.

6.2.5. Data processing

To get a more coherent anatomical and clinical understanding of joint dynamics, joint forces and moments were described in non-orthogonal joint coordinate systems (JCS; (Schache and Baker, 2007; Wu et al., 2005)) according to formulas in (Desroches et al., 2010a) with the first axis (the above-mentioned *Z*) fixed in the proximal segment, the third axis (*Y*) fixed in the distal one, and the second (floating) axis defined as the cross product of the two others. Positive joint forces were compression, lateral and anterior shears; positive joint moments were flexion, adduction and internal rotation. Joint forces and moments were respectively normalized to body weight and body weight times arm length (Hof, 1996). To evaluate time series intra-individual variability (for each joint and about each axis), the mean deviation was computed across the four strokes of a single participant (Hanlon et al., 2012).

6.2.6. Preliminary validation

In order to stay vertically still at the surface, the momentum imparted to the body should equate to zero over a stroke, hence a null net impulse. In other words, according to Eqn 6.14, the impulse delivered by the action of both arms should balance the impulse of the 34-N ballast and the net buoyancy (13.7 ± 3.5 N, measured via the extra load necessary to immerse the body just below the surface after maximal inspiration):

$$2\int_0^t \mathbf{f}_y\, dt = \left(\mathrm{f_{BALLAST}} + \underbrace{\mathrm{f_{WEIGHT}} - \mathrm{f_{BUOYANCY}}}_{\text{net buoyancy}} \right) \bullet t, \quad (6.14)$$

where the left term is the integral over a stroke period *t* of the external forces acting on the upper limb segments, of which solely the vertical components $\mathbf{f}_y$ were retained, multiplied by two to account for both arms (assuming symmetry). This impulse

supposedly capable of supporting the ballasted swimmer computed from CFD was compared to the right term in Eqn 6.14 to assess the validity of the present simulations.

6.3. Results

The first necessary step was to evaluate simulation validity. The net impulse applied to the body over a stroke was 16.7 ± 4.4 N s, while that produced by the arms and computed from the present numerical simulations was 16.4 ± 4.2 N s, resulting in a gap of 1.2 ± 3.5%.

Wrist, elbow and shoulder reaction forces and moments time series are plotted in Figs. 6–3 and 6–4. On an stroke-by-stroke basis, they were identical in profile, with mean deviation scores across four strokes < 0.06%BW and 0.11%BW·AL for joint forces and moments, respectively. Joint load was within 5%BW, with notable exceptions for shear forces along the posterior direction at the elbow (8.1 ± 0.6%BW), and anterior (7.1 ± 2.1%BW) and lateral (7.0 ± 1.3%BW) directions at the shoulder. Moment curves displayed two local extrema, with peaks occurring about 30 and 70% of stroke duration at the elbow, and about 20 and 80% at the shoulder; peaks were largely indiscernible at the wrist. The greatest moments were observed at the shoulder joint, with extension (6.0 ± 0.6%BW·AL), external rotation (4.9 ± 0.4%BW·AL), and adduction (4.1 ± 1.5%BW·AL) in a descending order of magnitude, whereas they were flexion (3.6 ± 0.5%BW·AL), internal rotation (3.1 ± 0.4%BW·AL) and adduction (3.0 ± 0.6%BW·AL) at the elbow, and adduction (0.7 ± 0.1%BW·AL), flexion (0.5 ± 0.1%BW·AL) and external rotation (0.06 ± 0.01%BW·AL) at the wrist.

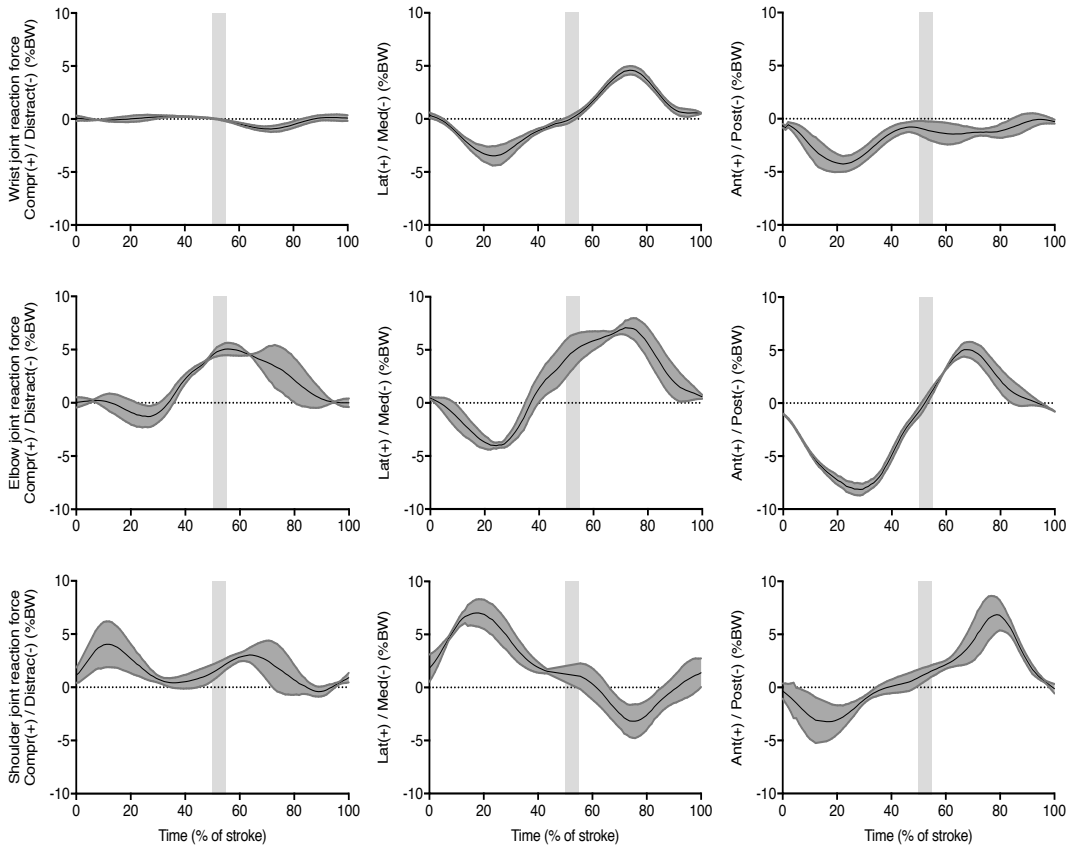

Figure 6–3. Wrist, elbow and shoulder joint reaction (compression/distraction, lateral/medial and anterior/posterior shear) forces. The black solid line and dark grey area are group means and standard deviations (N = 28 strokes), whereas the light vertical grey line represents the instant of stroke reversal; i.e., the transition between the downstroke and the upstroke.

6.4. Discussion

We presented the first thorough picture of 3D upper limb joint kinetics during underwater cyclical movements, taken from the integrated use of numerical fluid flow simulation and inverse dynamics modeling. The first featured a novel dynamic mesh algorithm capable to smoothly deform body geometries from actual kinematics and compute instantaneous hydrodynamic forces at the upper limb in dynamic conditions. The latter was approached through the homogeneous matrix formulation, well adapted to Fluent programming language and suitable for modeling complex joints. The impulse calculated from the present simulations agreed (1.2% gap on average) with that theoretically determined from the impulse of net buoyancy and ballast forces, therefore

validating our first hypothesis that this approach would be feasible and yield accurate results. In comparison to pressure sensors and strip theory approaches, our new methodology has the added benefits of providing a dual level of 3D kinetic evaluation, either at the surface of the segments through CFD or at the joint through inverse dynamics. Moreover, simulation spatial and temporal resolutions are respectively of the order of few millimeters and milliseconds, which lead to potent and ecological modeling, and discrimination of thin differences in morphology or kinematics, for example.

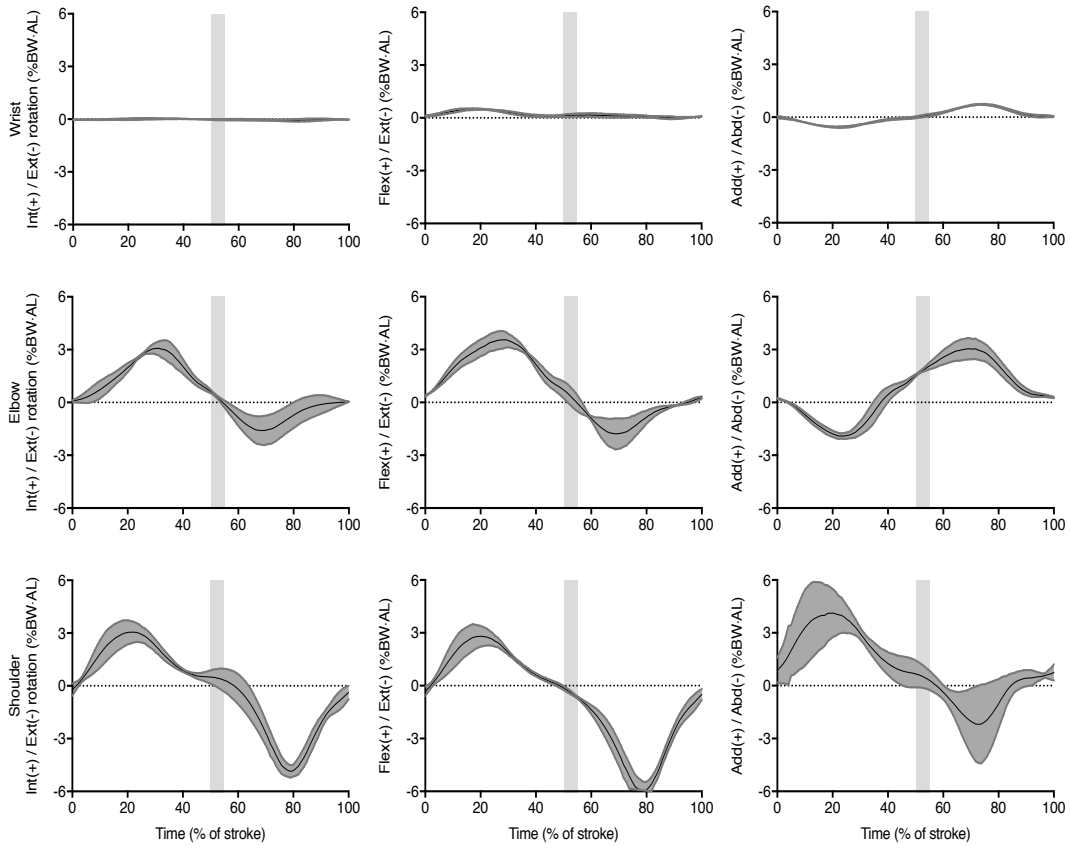

Figure 6–4. Upper limb 3D joint moments about internal/external rotation, flexion/extension, and adduction/abduction axes. See Figure 6–3 for color legend.

More practically, we predicted that upper limb joint load would be low enough to support the benefits of water on the body structure. Upper limb 3D joint forces were grossly within 5%BW, which is similar in magnitude to the joint load during walking in shallow water (Orselli and Duarte, 2011). On land, values of up to 35%BW were observed at the shoulder joint of disabled patients walking at <1 m s^{-1} with crutches (Slavens et al., 2011), and approximately within 10%BW during manual wheelchair propulsion at 3 km h^{-1} (Gil-Agudo et al., 2010). Altogether, this supports the use of low-load upper limb aquatic exercises in males to prevent joint stress and confirms our second hypothesis. However, despite performing at low intensity, our approach

highlights the fact that certain dimensions at certain joints (shoulder anterior and elbow lateral shears) might in some instances reach much higher stress of nearly 10%BW. These results question empirical rehabilitation protocols, and open the way to the scientific establishment of aquatic therapy.

Joint moments were similar in magnitude, revealing the balanced contribution of all muscle groups in this complex aquatic 3D motion. Surprisingly though, shoulder moments peaked earlier than at the elbow during the downstroke and vice versa during the upstroke, regardless of the axis of rotation. In other words, two loading patterns of the upper limb musculature were observed within the same movement. A proximo-distal sequencing of peak net joint moments has been identified since long as a fundamental motor control strategy of healthy biological systems to redistribute mechanical energy among segments and transmit power to the extremity (e.g., Marshall and Elliott, 2000; Putnam, 1993; Winters and Woo, 2012). Nonetheless, a disto-proximal organization is intriguing since it has never been discovered before at the upper limb. It may function as a strategy of stiffness regulation during on-land locomotion, essentially to provide a distal, compliant interface with the environment, and facilitate energy absorption by larger proximal muscles (Nichols et al., 2016). By analogy, perhaps aquatic environment instability is sensed distally at the hand and forearm, and the disto-proximal sequencing of peak net joint moments seen during the downstroke is a natural yet highly dynamic response to damp the perturbations.

It is important to recognize that net moment at a joint does not only affect the adjacent segments (Zajac et al., 2002). In dynamics, joint moments propagate either according to a proximal–distal or distal–proximal gradient. One intriguing example is given in (Latash and Zatsiorsky, 2015). When one is talking, the moments to accelerate and decelerate one's chin do propagate to the feet, which can in turn be sensed by sensitive force plates. This propagation of moments is most often seen during upper limb tasks on land (Putnam, 1993). Specifically, and in addition to the effects of anatomical structures net wrist, elbow, and shoulder moments were recognized to arise from gravity and dynamic interaction between segments. The latter are named interactive or interaction moments: they are passive and result from angular accelerations at a joint, and centripetal and Coriolis forces—thus dependent on upper limb motion (Topka et al., 1998). Interactive moments play important roles in determining trajectories and coordination of vigorous

movement, and failing to consider them may weaken the interpretations of data (Ketcham et al., 2004). In aquatic movements though, it is not a priori necessary that these moments are important, as they are likely dominated by moments against friction (Hollerbach and Flash, 1982). Furthermore, calculations get rapidly intricate even for a simple movement including only internal/external rotation at the shoulder (Hirashima et al., 2007). How to achieve the computation of interaction moments during more complex movements involving all upper limb joint degrees of freedom is obscure.

The integrated use of CFD and inverse dynamics is a significant methodological improvement towards unique, fundamental insights into aquatic movement biomechanics. This is crucial to more applied forms of research on aquatic rehabilitation and other popular exercises in water (e.g., competitive swimming, fitness), for example, to document how to perform faster, or to provide clinicians with best practice guidelines. Future works are directed towards the examination of joint power modulation and muscle function with emphasis on injury etiology and hydrotherapy implications.

6.5. Appendix: 3DOF vs 6DOF inverse dynamics

Regardless of the selected method, all inverse dynamics analyses presented so far have only considered rotational joint power (i.e., the mechanical quantity arising from angular changes at a joint), hence 3 (rotational) degrees of freedom. Yet, one should be aware that a full 6DOF (accounting for joint translation) inverse dynamics analysis, although extremely rare (Buczek et al., 1994; Duncan et al., 1997; Takahashi et al., 2015; Zelik et al., 2015), can be computed and may provide better joint work estimates. Indeed, 3DOF analysis ignores joint translation and power associated with joint reaction force; in other words, part of the energy flow profile for a given muscle group might be disregarded (Buczek et al., 1994). This additional term is taken as the dot product of the joint reaction force and the difference between joint center velocity estimates based on distal and proximal segment motions. When comparing 3DOF and 6DOF analysis of biological joints, differences in work done at the ankle was found to be of the order of 2–3 J (~5–7% of the positive work done; (Buczek et al., 1994; Takahashi et al., 2015; Zelik et al., 2015)). Duncan et al. (Duncan et al., 1997) found larger differences between both approaches when summing across all lower limb joints during stair ascent/descent. Specifically, 6DOF inverse dynamics provided joint work estimates more consistent with

the work required to raise/lower body center of mass. This mechanical work was fully accounted for by 6DOF inverse dynamics when modeling foot deformation and adding its contribution to total power (Zelik et al., 2015). Thus, 6DOF inverse dynamics seems to only prove strictly superior when modeling all joint deformations. Moreover, despite the more rigorous and complete picture that is gained through the analysis, 6DOF inverse dynamics suffers from one major issue relative to the interpretation of the translational power terms. When net joint moments and muscle groups are to be interpreted together, translational power terms lose significance in 3D (Buczek et al., 1994). As a matter of fact, while in 2D the rotational term around a given axis might be combined with two translational terms in the plane perpendicular to that axis, translational terms are over-represented in 3D (since each term is now included in two planes of movement). This further implies that translational terms do not represent true joint translation (Buczek et al., 1994). In addition, possible sources of work (e.g., compression of joint cartilage, inaccurate rigid-body assumptions, rotational dynamics missed as a result of joint center mislocation that then appear in the translational work term) are hard to identify and distinguish (Zelik et al., 2015). Since these issues are not resolved for aquatic movement, it is not felt that a 6DOF inverse dynamics analysis would have provided a clearer kinetic picture.

6.6. Appendix: Bottom-up vs top-down calculations

With increasingly complex and high-performance laboratory setups that allow ground reaction force data collection for the study of gait, classical "bottom-up" inverse dynamics analysis has become the norm. The analysis starts at the foot, whose contact with the surrounding (during stance) is of known (measured) magnitude, and recursively goes up the links towards the hip on a segment-by-segment manner. However, there exists a fundamental mismatch between the measurements obtained from the real biosystem and the mathematical model used for analysis (Hatze, 2002). When analyzing full-body models, the system of equations of motion becomes overdetermined (van den Bogert and Su, 2008). If we consider a body model with N degrees of freedom, and all external forces are known or measured, there are N equations of motion and only N–6 unknown internal loads. This provides more equilibrium conditions than can be satisfied.

The conventional method effectively solves this overdeterminacy by discarding six of the equations, and the results will then depend on which six equations are eliminated. Sadly, all kinematic and force measurements that entered in those six equations remain unused, even if they contain potentially useful information. Alternatively, dynamic consistency can be improved by not measuring ground reaction forces and moments, but rather by predicting them from model kinematics and segment dynamical properties only, which is known as the "top-down" inverse dynamics approach. Although much less employed than the traditional bottom-up analysis, top-down inverse dynamics has notably been used to estimate the load at the upper limb during throwing-like motion (e.g., Aguinaldo and Chambers, 2009; Reid et al., 2007), and at the pelvis particularly during lifting tasks when it can be compared to the bottom-up analysis. RMS errors of pelvic moment on average <10 N m (~5–10% of peak values) were found between bottom-up and top-down analyses (Iino and Kojima, 2012; Kingma et al., 1996; Larivière and Gagnon, 1998; Plamondon et al., 1996), yet with substantial inter-individual variability (up to about 30 N m in some participants (Iino and Kojima, 2012)). Range of application of top-down analysis was however limited, as the inverse dynamics problem becomes underdetermined whenever the system forms a closed kinetic chain (Audu et al., 2007) (e.g., during bipedal stance or double contact phase in walking). Recently, a solution based on optimization techniques applicable to daily living activities (Fluit et al., 2014) and sports-related tasks (Skals et al., 2016) accurately predicted ground reaction forces and lower limb net joint moments, proving similar to traditional bottom-up inverse dynamics while reducing dynamic inconsistency and obviating the need for force platform measurements.

In water though, the interaction with the surroundings is not uniquely represented at the upper limb extremity at a single contact point. Pressure is distributed all over the limb. And unlike throwing-like movements where external (aerodynamic) forces can be neglected, they are substantial in water and must be calculated. Therefore, the system cannot be considered an open kinetic chain, and traditional bottom-up inverse dynamics is preferable. Note that, here, "bottom-up" refers more to the methodological procedure of starting from an extremity where the external forces and moments are known towards the proximal joint, rather than the actual direction of the analysis (which is done from the hand to the shoulder).

7 Modulation of upper limb joint work and power during sculling while ballasted with varying loads

Human musculoskeletal system must modulate work and power output in response to substantial alterations in mechanical demands associated with different tasks. In water, particularly, upper limb muscles must perform net positive work to replace the energy lost against the dissipative fluid load. Where in the upper limb is work and power developed? Is mechanical output modulated similarly at all joints, or are certain muscle groups favored? For the first time, this study examined how work and power per stroke were distributed at the upper limb joints in seven male participants sculling while ballasted with 4, 6, 8, 10, and 12 kg. Upper limb kinematics was captured, and used to animate body virtual geometry. Net wrist, elbow and shoulder joint work and power were subsequently computed through a novel approach integrating unsteady numerical fluid flow simulations and inverse dynamics modeling. Across a threefold increase in load, total work and power significantly increased from 0.38±0.09 to 0.67±0.13 J kg^{-1}, and 0.47±0.06 to 1.14±0.16 W kg^{-1}, respectively. Shoulder and elbow equally supplied >97% of the upper limb total work and power, coherent with the proximo-distal gradient of work performance in the limbs of terrestrial animals. Individual joint relative contributions remained constant, as observed on land during tasks necessitating no net work. The apportionment of higher work and power simultaneously at all joints in water suggests a general motor strategy of power modulation consistent across physical environments, limbs and tasks, regardless of whether or not they demand positive net work.

7.1. Introduction

Humans move in water sometimes undulating ventrally and ricocheting at the surface swimming the butterfly, sometimes paddling dorsally in a windmill-like fashion swimming the backstroke. Not to mention unusual yet utilitarian forms of locomotion used by lifeguards or combat swimmers, lying on a side and recovering arms under the water. Regardless of the style adopted, arms are swept through the water to generate thrust. This requires that substantial net mechanical work be performed by upper limb muscles to replace the energy lost against the dissipative load of the water. As load gets higher (for example by increasing steady swimming speed, or artificially by using ballast as in (di Prampero et al., 1974)), task mechanical requirements must be met by proportional increases in mechanical work and power per stroke. How does the musculoskeletal system adapt to accommodate the changing mechanical demands of the environment? Where does the increased power come from? Is the mechanical work output modulated similarly at the shoulder, elbow and wrist or are certain muscle groups favored? This study sought to provide the answers to such questions by comparing net joint work and power during sculling performed under varying mechanical loads. Sculling is the action of sweeping the arms back and forth, typically describing the shape of a ∞. This is an integral part of swimming strokes that incorporates flow phenomena responsible for high force production (Takagi et al., 2014), and an exercise frequently used in fitness and rehabilitation programs. Sculling is thus an upper limb movement well suited to the broad study of work and power modulation in water.

Mechanical power output has been previously calculated through ingenious methods (semi-tethered swimming (Dominguez-Castells et al., 2013); MAD system (Toussaint et al., 1990); dry-land ergometry (Swaine, 2000)), yet none capture the instantaneous power directly apportioned by the upper limb musculature nor explain work and power production within the limb itself. We recently developed a novel approach integrating inverse dynamics and unsteady fluid flow simulations to examine upper limb aquatic movement kinetics for the first time at a joint-level perspective (Lauer et al., 2016). This approach nicely complements the more macroscopic, above-mentioned approaches, as it provides further insight into how muscle groups are recruited to meet the demands of the environment.

Certain muscle groups may function differently than others, and contribute unevenly to overall mechanical requirements. Such a 'division of labor' in terms of work performance mainly reflects the distribution of muscle mass within a limb (Biewener, 2016). High work output is generally observed in large muscles distributed proximally, whereas low work output is seen distally in smaller muscles. Studies of avian muscle function during flight support this regional specialization in the functional role of muscle groups. Just as humans move their arms for hydrodynamic propulsion, birds generate aerodynamic lift to power flight by moving their wings through large excursions. Rapid wing flap is achieved by large proximal muscles shortening over a significant fraction of their resting fiber length, producing considerable work (Biewener, 2011). Small muscles located at the elbow operate over shorter strains to control wing shape and orientation, yet showing both work production and absorption (Robertson and Biewener, 2012). In the human upper extremity, muscle mass is also concentrated proximally (Holzbaur et al., 2007) and can be expected to provide the majority of work. Experimental studies are however needed since no data for upper limb joint work when moving in water are available.

Human musculoskeletal system must durably alter its performance to accommodate changing mechanical demands associated with different steady tasks. These require steady work input, as opposed to non-steady tasks that require transient changes in muscle work for just one or a few strides, such as during stabilization (Daley et al., 2007). Although how this challenge is accomplished in the water remains obscure, it is, on land, relatively well understood. During level walking and running up to ~7 m s^{-1}, demands for increased positive work per stride are achieved by increasing in parallel the work done by all lower limb muscle groups (Farris and Sawicki, 2012; Schache et al., 2015). By contrast, sprinting, accelerating and incline running do necessitate a different control strategy, as they involve a redistribution of work and power output proximally to the hip (Qiao and Jindrich, 2016; Roberts and Belliveau, 2005; Schache et al., 2015). However, unlike level steady-speed locomotion, these tasks have the peculiarity that they are associated with a net positive work requirement and/or a change in limb posture that requires hip muscles to do greater work (Roberts and Belliveau, 2005); hence the suggestion that task net work requirement might be an important indicator of how humans will meet the overall mechanical demands (Farris and Sawicki, 2012).

This study aimed to test, for the first time, two fundamental hypotheses relative to upper limb aquatic movement mechanics. Based upon muscle mass relative distribution within the human upper limb, it was first predicted that the majority of the work and power would be produced proximally at the shoulder and elbow. Second, since aquatic movements naturally require that net positive work be done against the dissipative load of the water, it was expected that higher mechanical demands would be met by redistributing upper limb work output proximally to shoulder muscles.

7.2. Material and methods

7.2.1. Participants and experimental procedure

Experiments were carried out on seven male participants (27.7±5.8 years, 1.82±0.05 m, 77.8±6.5 kg). Ethical approval was granted by the University of Porto review board, and all participants provided written informed consent prior to testing. They performed sculling motion at the middle of a 25-m long, 2-m deep indoor swimming pool so as to remain vertically still and head above the water for about 10 s. Use of the legs was not allowed. To manipulate the demand for mechanical work per stroke, participants were randomly ballasted with 4, 6, 8, 10 and 12 kg tied around the waist (see Fig. 7–1 for illustration of the task). While ballasted with 14 kg, two participants only managed to stay head above the water. However, they did so for less than 5 s. These trials were discarded, as they were not deemed representative of a task requiring steady work input. 12 kg was therefore regarded as the maximum load participants could sustain. Rest periods of three minutes were observed between each condition.

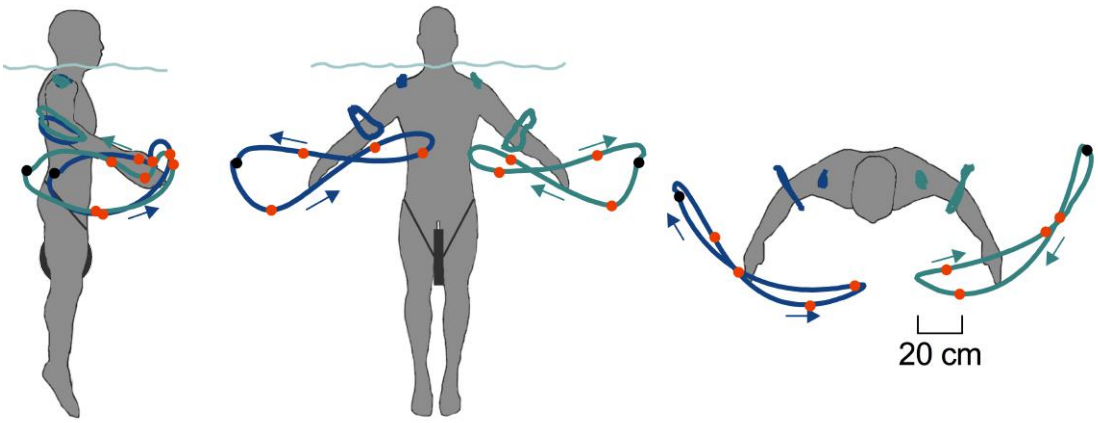

Figure 7–1. Kinematic traces of the tip of the middle finger, elbow joint center and acromion during sculling. These were averaged over four cycles from one participant sculling to maintain his head above the water surface while ballasted with 4 (blue) and 12 kg (green). Recordings are from the right arm only, but are represented on both sides for illustration purposes from lateral, front and top perspectives. Black dots indicate where the movement starts, with red dots spaced every 20% of stroke duration.

7.2.2. Fluid flow simulations and inverse dynamics analysis

The quantification of joint kinetics during underwater movements rests on a new approach integrating computational fluid dynamics (CFD) and inverse dynamics modeling. The methodology involved four steps. 3D upper limb joint kinematics was first recorded by automatically tracking the trajectories of 12 markers positioned along the upper limb and thorax (xiphoid process, suprasternal notch, C7, T8, acromion, lateral and medial epicondyles, ulnar and radial styloids, third and fifth metacarpals, and an additional piece of reflective tape at the tip of the middle finger) with a 12-camera underwater motion capture set-up sampling at 100 Hz (Oqus 3 and 4 series, Qualisys, Gothenburg, Sweden). Markers at C7, acromion, and medial epicondyle were temporarily invisible because of proximity with the water surface or occlusion by the chest when bringing the arms forwards. Missing information represented up to ~75 frames (at most 6.7% of the trial duration), distributed in short individual gaps of ~10 frames (~100 ms). These were filled with Qualisys Track Manager software built-in spline interpolation. Kinematic data were digitally filtered using a zero-lag fourth-order Butterworth filter with a cut-off frequency of 6 Hz. Four strokes, selected on the basis of minimal xiphoid process vertical displacement, were retained for processing. Segment coordinate systems (thorax, upper arm, forearm and hand) were subsequently constructed in agreement with

the International Society of Biomechanics convention (Wu et al., 2005). Body virtual geometries were then obtained from a Mephisto 3D scanner (4DDynamics, Antwerp, Belgium), edited and converted into a CAD model prior to import into ANSYS® Fluent® Release 14.5 CFD software (ANSYS, Inc., Canonsburg, PA, USA). The third step consisted in setting the numerical simulation and animating the virtual model. Difficulties arise when numerically controlling joint deformation since the geometry is highly constrained. Joints must connect smoothly to the adjacent rigid surfaces throughout the motion to prevent negative cell volumes and the simulation to stop before completion. We implemented a dual quaternion smooth skinning algorithm in C programming language to handle complex 3D deformations, a task that is otherwise unfeasible in Fluent. Each of the vertices forming the ~40000 upper limb facets was individually displaced based on kinematic data input and an additional weighted transformation ensuring skin-like animation of flexible body parts. This in turn allowed the quantification of hydrodynamic forces acting upon the entire upper limb in dynamic conditions. Ultimately, external forces and body segment inertial properties (estimated from scaling equations based on subject anthropometry; (Dumas et al., 2007a) were fed into an inverse dynamics model of the upper limb to compute net joint moments. The model was implemented through the homogeneous matrix approach (Legnani et al., 1996), a mathematical notation derived from robotics that is convenient for computer applications, poorly sensitive to kinematics measurement errors and suitable for the modeling of complex joints (Doriot and Chèze, 2004).

7.2.3. Joint power and work computation

Joint angular velocity was obtained by subtracting the angular velocity of the proximal segment from that of the distal one. Instantaneous 3D joint power was readily calculated as the dot product of the net joint moment and joint angular velocity vectors, and normalized to body mass. Shoulder, elbow and wrist power time series were integrated with respect to time over discrete periods of positive and negative power, yielding the positive W^+ and negative work W^- done per stroke at each upper limb joint. W^+_{tot} and W^-_{tot} were calculated as the sum of W^+ and W^- done at each joint, respectively. W^+ and W^- were further divided by stroke duration to give the average positive $\overline{P}^+$ and negative

joint power $\overline{P}^{-}$. $\overline{P}^{+}_{tot}$ and $\overline{P}^{-}_{tot}$ were calculated in the same manner as W^{+}_{tot} and W^{-}_{tot}. In order to determine whether or not a change in mechanical demand influenced individual joint relative contributions to $\overline{P}^{+}_{tot}$ and $\overline{P}^{-}_{tot}$, $\overline{P}^{+}$ and $\overline{P}^{-}$ at each joint were respectively expressed as a percentage of $\overline{P}^{+}_{tot}$ and $\overline{P}^{-}_{tot}$. Furthermore, joint angular excursions (i.e., the difference between the minimum and maximum angles of a given joint over a stroke) and peak joint moments were measured to indirectly evaluate the mechanisms by which joint mechanical work was altered (Arnold et al., 2013; Roberts and Scales, 2004).

7.2.4. Statistical analysis

Statistical tests were run in R 3.3.2 (R Core Team, n.d.), with a significance level of 0.05. Four cycles per participant and condition were analyzed. Data were time-normalized as a percentage (0–100%) of a single stroke. Simulation accuracy was tested with a major axis regression, comparing the impulse delivered by the arms (calculated through CFD from integrating external force vertical components) with the net ballast impulse. The simulations were considered accurate if the 95% confidence interval of the slope of the major axis included 1 (Rayner, 1985). Distribution normality was checked with the Shapiro–Wilk test. Mixed-effects models (via the R package lme4 (Bates et al., 2015)) were used to detect any main effect of the magnitude of the mechanical demand on the work and power generated, individual joint relative contributions, joint angular excursions, and peak moments. Load condition was treated as fixed effect and individual as random effect. Provided that a significant effect was found, post hoc Tukey pairwise contrasts with Bonferroni adjustment for multiple comparisons were conducted to identify which conditions were significantly different from each other.

7.3. Results

The slope of the major axis regression between numerically- and experimentally-calculated vertical impulse was β=1.00 (Fig. 7–2), with a 95% confidence interval [0.97–1.03].

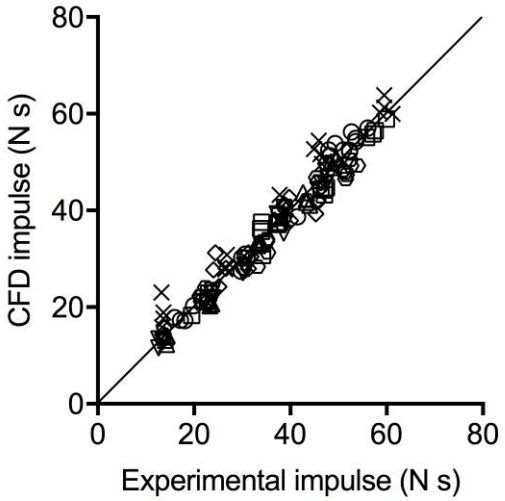

Figure 7–2. Impulse generated by the arms plotted against the net ballast impulse. Simulation accuracy was tested by regressing the impulse calculated from integrating over a cycle external force vertical components computed through CFD onto the net ballast impulse. Numerical output fell on the identity line (slope of the major axis regression β=1.00, 95% CI [0.97–1.03]), giving confidence in the results. Symbols identify different participants.

As the mechanical demand increased, so did the magnitudes of the instantaneous power at all joints (Fig. 7–3), with a measured peak power output of 2.7±0.4 W kg^{-1} at the highest load. This was reflected in W^+ and $\overline{P}^+$ done at the upper limb joints (Fig. 7–4). Specifically, a significantly higher amount of W^+ and $\overline{P}^+$ was being generated at the shoulder and elbow, whereas no change was observed at the wrist. As a result, W^+_{tot} and $\overline{P}^+_{tot}$ increased markedly from 0.38±0.09 to 0.67±0.13 J kg^{-1} ($F_{4,6}$=57.46, P<0.001), and 0.47±0.06 to 1.14±0.16 W kg^{-1} ($F_{4,6}$=140.24, P<0.001), respectively. Levels of W^-_{tot} and $\overline{P}^-_{tot}$ were negligible (on average <0.02±0.01 J kg^{-1} and 0.04±0.02 W kg^{-1}), representing less than 3.5% of the total upper limb work and power. The wrist contributed 1.8–2.4% to W^+_{tot} and $\overline{P}^+_{tot}$ (Fig. 7–5). In contrast, the shoulder and elbow were the main contributors, equally supplying on average 22 times more work and power (respectively, 47.5–52.5% and 45.6–50.0%). Mixed-effects models revealed no significant effect of mechanical loading on individual joint relative contributions (Fig. 7–5). Representative joint angular kinematics and joint moments are shown in Fig. 7–6. During sculling, shoulder and elbow angular excursions were much greater than at the wrist, remarkably about the axes of flexion/extension and adduction/abduction, though with no visible changes with load (Fig. 7–6A). Conversely, increasingly high joint moments were produced, peaking at ~25 and 75% of the stroke (Fig. 7–6B). Angular excursion remained unchanged about all joint degrees of freedom, whereas peak moments showed significant increases in magnitude at all joints as the mechanical demand rises (Fig. 7–7).

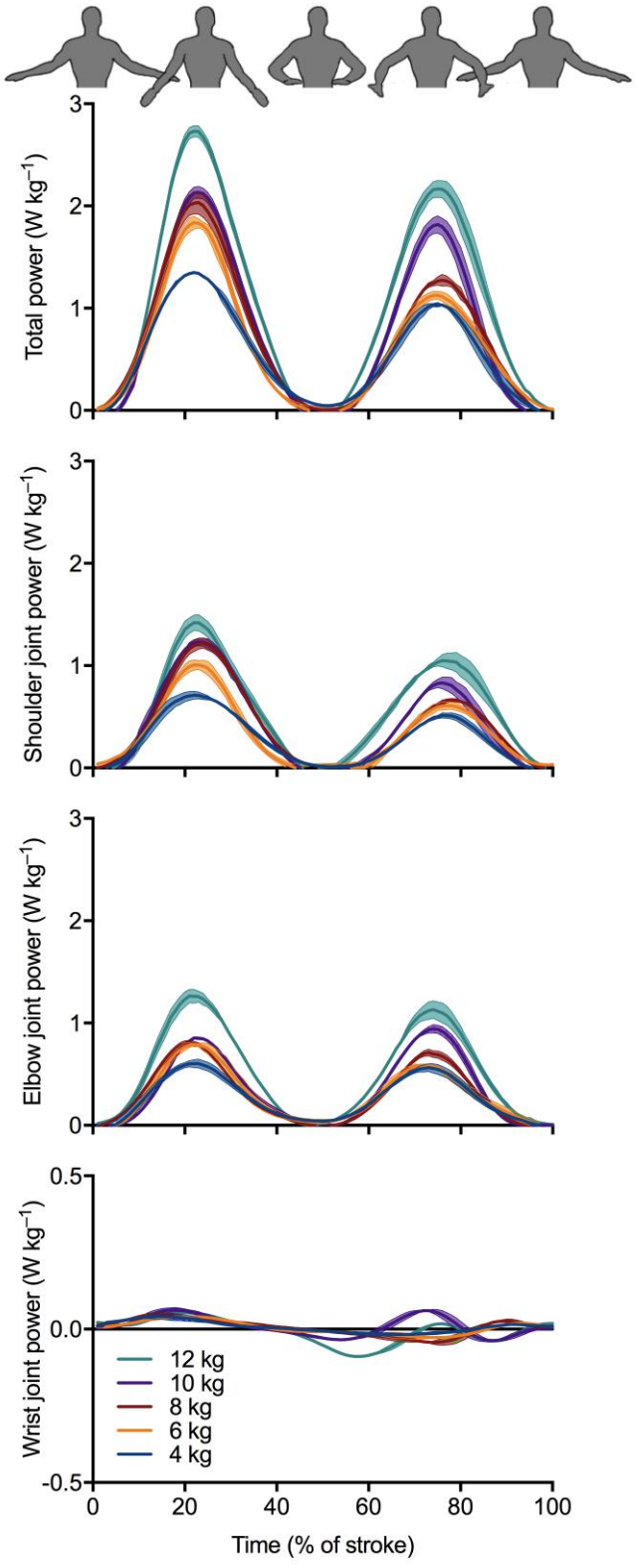

Figure 7–3. Representative instantaneous total, shoulder, elbow, and wrist joint powers normalized to a single stroke for each of the five loading conditions. Results are means ± s.d (filled bands) obtained from four strokes in each condition from participant 3. Note the different wrist plot *y*-axis scale. At the top, silhouettes show one sculling cycle, with maximum power generation when arms are moved side-to-side and null power at stroke reversal.

7.4. Discussion

7.4.1. Upper limb joint work and power distribution

We sought to analyze through a novel integrative approach how joint work and power are modulated during upper limb aquatic movements in response to substantial changes in mechanical demands. Simulations were accurate, judging by the slope of the major axis, thus giving confidence in the results. We tested two hypotheses. First, we hypothesized that the majority of the work and power would be produced at the shoulder and elbow given the proximal concentration of large muscles. This hypothesis was confirmed. We found that muscle groups crossing the shoulder and elbow supplied >97% of work and power. This is coherent with the proximo-distal gradient of work performance apparent in the limbs of many terrestrial vertebrate animals, for which evolutionary pressures have favored work modulation by proximal muscles (Biewener and Daley, 2007). Here, we report that such a gradient also exists within the human upper limb when moving in a complex, fluid physical environment. Moreover, muscle groups at the shoulder and elbow contributed mechanical demands equally, and are therefore of equal importance in the underwater production of force.

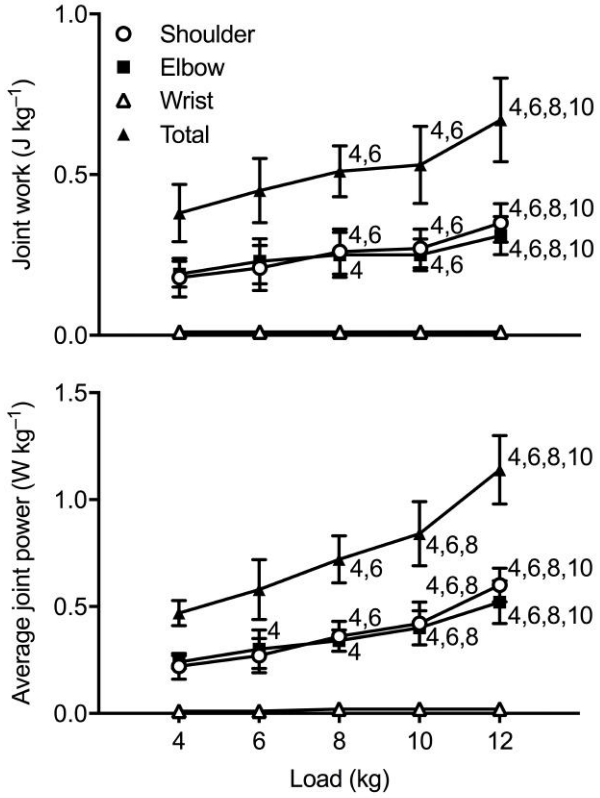

Figure 7–4. Mechanical work (top) and average power (bottom) at the shoulder, elbow and wrist as the mechanical load increases. Elbow and shoulder joints exhibited parallel, significant increases in work and power by ~75 and 150%, respectively. Error bars represent 1 s.d. ^{4,6,8,10} Significantly different from the 4-, 6-, 8- and 10-kg load conditions ($P<0.05$).

The second hypothesis was that increasing mechanical demands would be met by redistributing upper limb work output proximally to shoulder muscles since net positive work must be done against the dissipative load of the water. This hypothesis was rejected, as individual joint relative contributions were observed to remain constant when mechanical demands were substantially altered. Across a threefold increase in load (4–12 kg), elbow and shoulder joints exhibited parallel increases in work and power by ~75 and 150%, respectively. Curiously, this behavior is also observed during steady, level terrestrial locomotion (Farris and Sawicki, 2012; Schache et al., 2015), whose net mechanical work requirement is negligible. Our results therefore suggest a transversal motor strategy of power modulation across physical environments, limbs and tasks, regardless of whether or not they demand net positive work. Previous findings of proximal redistribution of work and power output that occurred when accelerating (Qiao and Jindrich, 2016), sprinting (Schache et al., 2015), and incline running (Roberts and

Belliveau, 2005), might thus be due more to postural constraints altering muscle effective mechanical advantage than to an actual neuromuscular response.

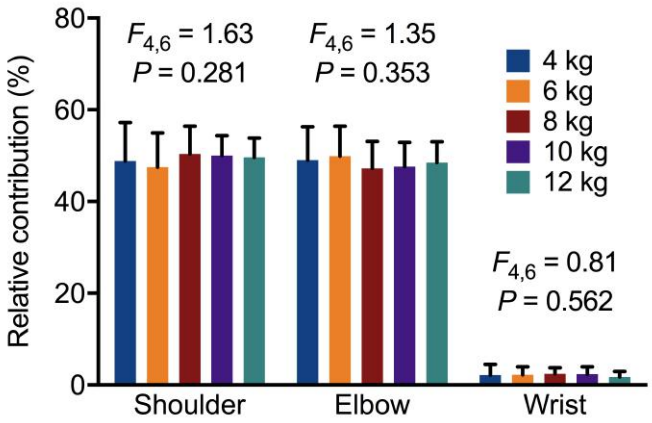

Figure 7–5. Individual joint relative contributions to the total average power and work produced by the upper limb. Across a threefold increase in load, no power redistribution occurred within the upper limb. Error bars represent 1 s.d.

Invariant joint relative contributions to total work and power do lend support to the idea that complex movements are controlled modularly; i.e., the central nervous system adopts a simple control scheme in which a few set of invariant muscle synergies or 'modules' act as building blocks to simplify motor coordination and accomplish complex motor tasks (e.g., d'Avella et al., 2003). For example, walking mechanics under different mechanical demands can be robustly reproduced through tuning module recruitment intensity alone (McGowan et al., 2010). Although muscle activity was not recorded here, we can speculate that complex aquatic movements are similarly governed. To respond to the increase demand for mechanical work, it may be that modules get simply more activated, with the result that work output proportionately increases at all joints. Further investigations are needed to test this assumption.

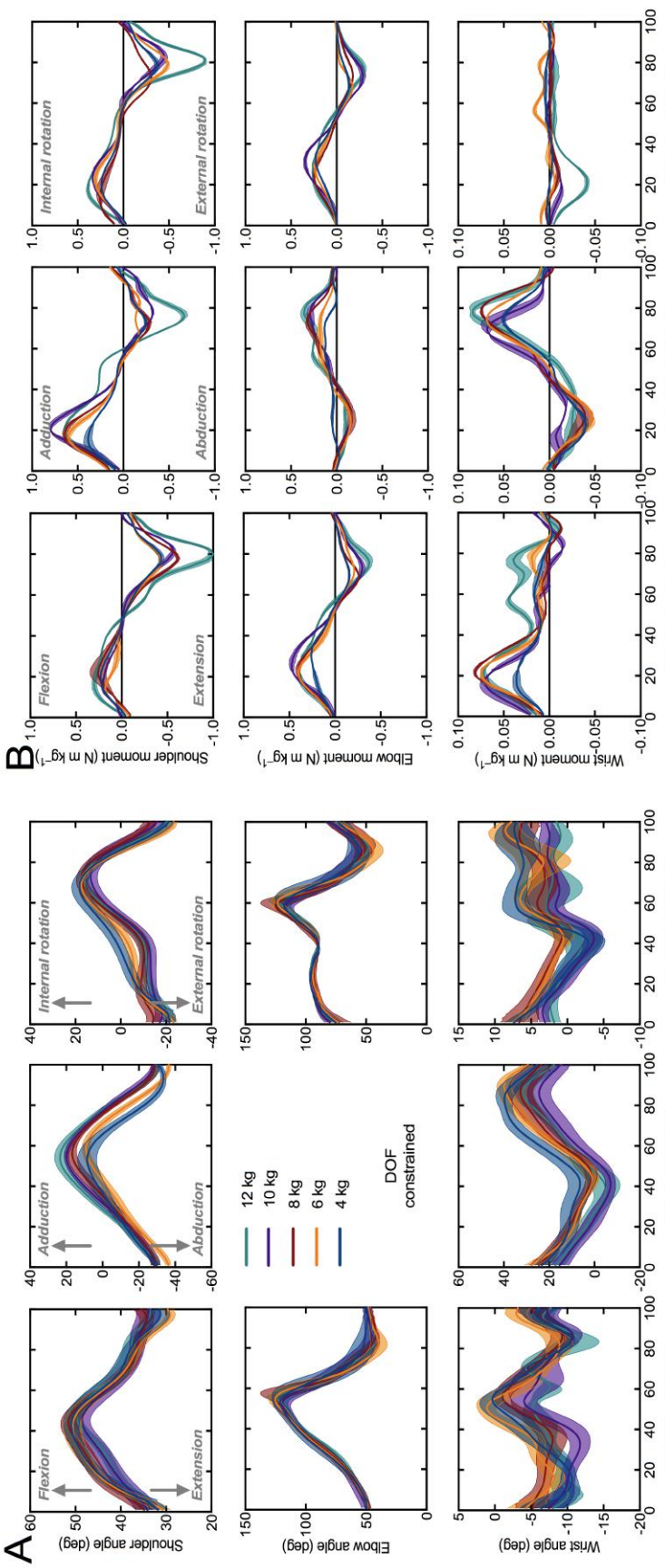

Figure 7–6. Average 3D upper limb joint kinematics (A) and joint moments (B) plotted over a stroke. Shoulder (top), elbow (middle) and wrist (bottom) joint kinematics and kinetics were projected onto non-orthogonal coordinate systems so that individual components reflected mechanical actions about the axes of flexion/extension (left column), adduction/abduction (center), and internal/external rotation (right). Elbow adduction–abduction was left blank since this degree of freedom was constrained. Means ± s.d are shown for participant 3 from four strokes in each condition, illustrating typical stroke-to-stroke variability.

The work performed by a muscle during its contraction is the product of the force developed and the distance shortened. Increased mechanical work output can thus be achieved through either producing higher forces or shortening more, which would be apparent in increases in joint moments or joint excursions (Arnold et al., 2013; Roberts and Scales, 2004). Increasing the mechanical work output of the upper limb musculature to accommodate increasing mechanical demands in water was primarily done through twofold increases in moments at all joints, rather than sweeping the arms over greater joint excursions: angular excursions remained unchanged with load. Assuming that muscle shortening and muscle force output are respectively proportional to joint angular excursion and peak joint moment, our results suggest that increased work was likely done by muscles producing higher forces.

7.4.2. Constraints to human upper limb performance in water

An insignificant amount of power was being absorbed over a stroke (<3.5% of the total generated power) regardless of the load, indicating a negligible dissipation or storage of energy in anatomical structures. This is unlike flying animals, for example, that store and release wing inertial energy in the tendon of pectoralis (amounting to 18% of the positive work the muscle performs) to aid the upstroke to downstroke transition (Biewener, 2011). The existence of springs in swimming vertebrates is much more controversial. While skin deformation and axial skeleton bending were found to provide such mechanical advantages (Pabst, 1996), there is only little, indirect evidence in whales and dolphins that tendons might serve energy-saving roles (Alexander, 2002). Furthermore, a modeling study of paddling ducks revealed that they do not operate in a resonance-like mode, concluding that drag-based swimmers' musculoskeletal system does not behave like a spring (Clark and Fish, 1994). Likewise, in humans moving in water, the nature of the medium itself—which is highly dampening and entails a substantial loss of energy to overcome drag on the appendages—likely limits the usefulness of elastic mechanisms in powering cyclical aquatic movements. Thus, performance is likely directly determined by the maximal work and power theoretically available from muscle mass.

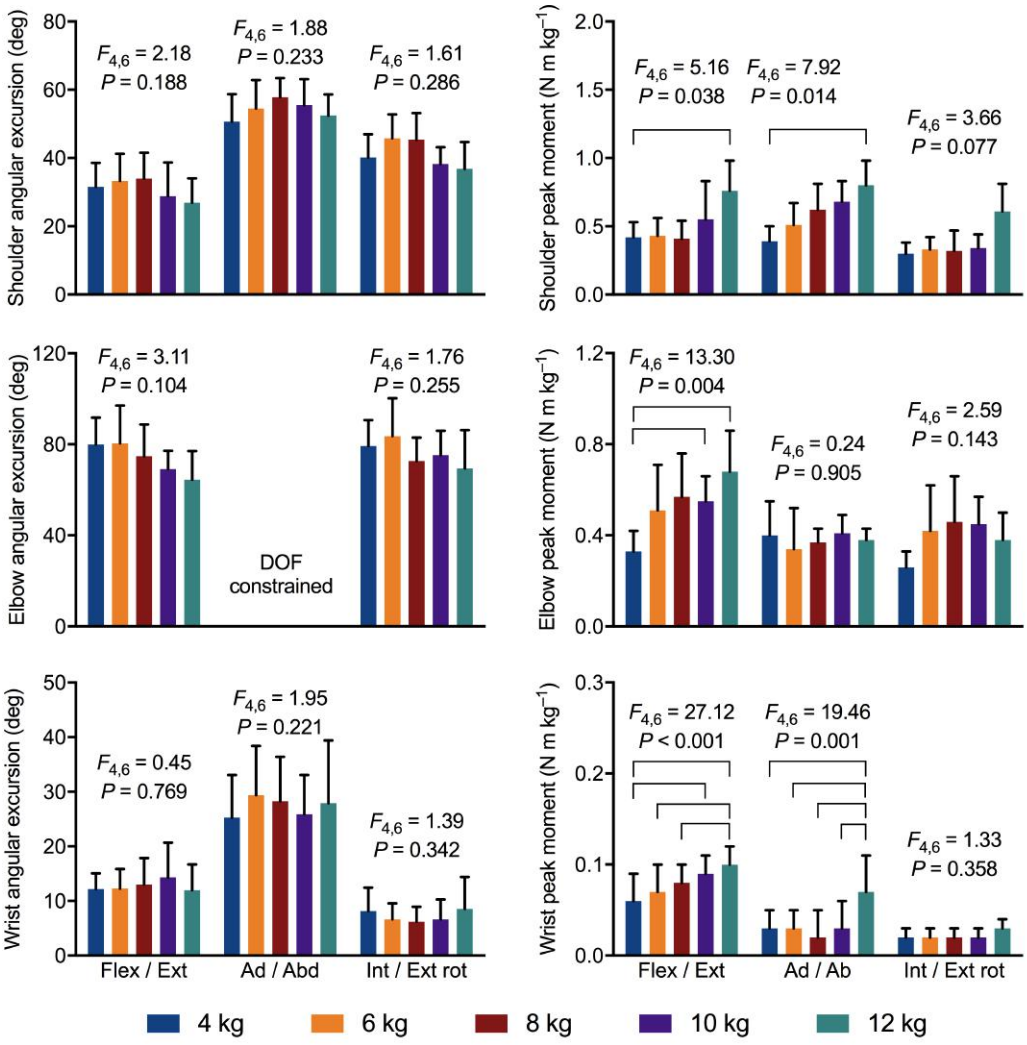

Figure 7–7. Upper limb joint angular excursion and peak moment as a function of mechanical load. Data are presented as means ± s.d about each degree of freedom at the shoulder (top), elbow (middle) and wrist (bottom). Elbow adduction–abduction was left blank since this degree of freedom was constrained. Thin horizontal lines indicate significant pairwise differences (P<0.05). Joint work output was increased primarily by increasing joint moment rather than joint excursion.

We can ask whether work and power production measured here fall within the theoretical capacities of vertebrate skeletal muscles. Participants were performing at maximum effort, as increasing load beyond 12 kg could not be steadily supported. Considering an average mass of shoulder and elbow muscles of 3 kg (Holzbaur et al., 2007), we can extrapolate to a total muscle-mass-specific work and average power of ~17 J and 30 W kg^{-1} muscle, respectively. Under optimal conditions of shortening range and speed, those values are respectively 4 and 2.5–8 times less than the estimated maximum capacity for work and power production of rapidly contracting striated muscle (Biewener et al., 1998; Peplowski and Marsh, 1997; Weis-Fogh and Alexander, 1977). This suggests

a constraint to overall human upper limb mechanical performance in water, most likely as a result of upper body morphology specialized for overhead throwing (Roach et al., 2013).

7.4.3. Summary

We investigated through a novel integrative approach coupling CFD and inverse dynamics how the human musculoskeletal system adapted to substantial changes in mechanical demands when performing in water. Shoulder and elbow muscle groups equally contributed to >97% of the total work and power. As observed on land, increasing mechanical requirements were met by the apportionment of higher work and power simultaneously at all joints, suggesting a general motor strategy of power modulation consistent across physical environments, limbs and tasks, regardless of whether or not they demand positive net work. Higher mechanical work output was achieved through increasing net joint moments rather than joint angular excursion. Total upper limb work and power were found to be well below the theoretical limit of striated muscle work and power production, likely because of an anatomical constraint to overall human upper limb mechanical performance in water. This study offers the first insight into the modulation of upper limb work and power at a joint level in water, and stimulates muscle-driven forwards dynamics modeling studies to examine further the limiting factors of underwater power production.

7.5. Appendix: Limitations and future ways of research

The present study suffers limitations that ought to be acknowledged. The analysis of joint work and power through inverse dynamics only provides an indirect measure of muscle–tendon function as these variables represent the net effect of all the muscles, tendons, ligaments, and contact forces at that joint (Farley and Ferris, 1998). Work and power estimates can be flawed due to: (i) energy storage in elastic structures that allows negative work in one phase to be recovered as positive work in a subsequent phase; (ii) muscle co-contraction causing the net moment at a joint to be less than the sum of flexor

and extensor moments; and (iii) intercompensation of joint power by biarticular muscles (Sasaki et al., 2009).

7.5.1. Inability to assess elastic energy storage and release

An exchange between mechanical energy stored in elastic anatomical structures and recovered as both kinetic and potential energy is a basic yet important mechanism for minimizing energy expenditure of terrestrial locomotion (Cavagna et al., 1977), and oscillatory movements in animals to a larger extent (Alexander, 1997). Elastic energy storage is also a major source of power amplification in many high-powered movements (e.g., Astley and Roberts, 2012; Roach et al., 2013; Zack et al., 2009). Standard rigid body inverse dynamics analysis however fails to capture such mechanisms, as non-rigid body parts are not modeled. Furthermore, negative joint work is typically interpreted as the dissipation (or absorption) of energy in anatomical structures through eccentric muscle contraction; nonetheless, it is not known whether this energy is recovered as positive work in a subsequent phase of the movement, and if so, in which proportion. An elegant approach to circumvent this limitation was developed by Zelik and Kuo (Zelik and Kuo, 2010). By computing the difference between the total mechanical work at the lower limb joints (obtained from inverse dynamics under rigid body assumptions) and the total mechanical work performed on and about the center of mass (obtained from force plate recordings without rigid body assumptions), the authors were able to estimate soft tissue work. For example, soft tissues contribute significantly to the dynamics of running in terms of energy dissipation, storage, and return, and ignoring their energetics is equivalent to disregarding the knee joint contribution to total power (Riddick and Kuo, 2016). In water, the issue is very complex since elastic energy release does not systematically result in power amplification (Richards and Sawicki, 2012). Nonetheless, we found negative work (hence potential elastic energy storage) to be insignificant. Energy storage and release was thus very unlikely to constitute a relevant source of error.

7.5.2. Inability to resolve co-contraction of antagonist muscle groups

To ascertain whether muscle co-contraction affects the current findings would require muscular activity recordings. It remains that an uncertainty bound can still be obtained by revisiting results from the literature. Inverse dynamics analysis does not refer to actual anatomically defined muscles, but rather to a single equivalent one-joint muscle (Robertson and Winter, 1980). This is why joint moments are net values. For example, if one activates his biceps, generating a flexion moment of 10 N m, and simultaneously activates his triceps, generating an extension moment of 15 N m, a perfectly accurate inverse dynamics modeling would yield a net elbow extension moment of 5 N m, although the action of the extensors was three times greater. Thus, because of the inability of inverse dynamics to account for cocontraction, the net moment is less than the sum of the individual muscle flexor and extensor moments. Cocontraction is inevitable in most human movement tasks because of the need for joint stability, movement control complexity, synergistic muscle activity and the influence of activation and deactivation dynamics. However, while this might be critical if one is willing to estimate muscle forces, this issue only causes slight underestimation of the actual musculo-tendon positive work. During normal walking, which involves substantial cocontraction at the knee and ankle joints (Falconer and Winter, 1985; Hortobágyi et al., 2009), a discrepancy of only 7% was found between joint work as computed from inverse dynamics and the actual positive work done by muscle–tendon unit (Sasaki et al., 2009). Aquatic exercise, conversely, seems much less demanding in terms of muscle cocontraction. During underwater therapeutic knee flexion–extension exercises, quadriceps and hamstrings had clear alternating activation patterns with low to quiet antagonist activity (Pöyhönen et al., 2001b). When swimming the front crawl, cocontraction of 30–50% is momentarily seen at the wrist and elbow during the insweep, when the arm is getting loaded by pushing against still masses of water (Caty et al., 2007; Lauer et al., 2013; Rouard and Clarys, 1995). Therefore, it is reasonable to expect <10% uncertainty in inverse dynamics solutions for forceful aquatic movements whenever the absolute amount of mechanical work done is of interest; this would not have altered our main conclusions.

7.5.3. Inability to account for the action of biarticular muscles

Because of its iterative nature, inverse dynamics cannot model the action of biarticular muscles. As a matter of fact, the moment at the proximal joint of a body segment is uniquely determined by the moment at its distal end, together with its motion and the knowledge of external and inter-segmental forces. This is appropriate for a series of link actuated by monoarticular muscle function. Nonetheless, this ignores the potential role of biarticular muscles. According to this iterative procedure, it is assumed that the moment at the proximal end of a segment is counteracted by a moment of equal magnitude at the distal end of the adjacent segment. However, biarticular muscles may redistribute joint moments so that part of the proximal moment is ultimately opposed at a non-adjacent segment. In other words, a net inter-segmental moment can be non-zero (Cleather et al., 2011). From a joint power viewpoint, power can appear to be absorbed at one joint and concomitantly generated at another (Zajac et al., 2002). To resolve this issue, Kautz et al. (Kautz et al., 1994) had proposed a measure allowing work savings due to intercompensation between moments at joints spanned by biarticular muscles. Based on the net joint moments at each joint, their algorithm evaluated total joint power assuming complete transfer due to the hamstrings group, the sartorius and the rectus femoris (between the hip and knee), due to the gastrocnemius (between the ankle and knee). Luckily, not considering biarticular intercompensation was found to yield more realistic estimates of total musculotendon and total muscle fiber work during simulations of cycling (Neptune and van den Bogert, 1998) and walking (Sasaki et al., 2009). However, mono and biarticular muscle roles in swimming has received poor attention (Martens et al., 2015), and the extent to which this fortuitous finding holds true in aquatic movements further warrants the use of muscle-actuated forwards dynamics simulations.

8 Upper limb internal–external power interaction in aquatic movements

Are the external work against the environment and the internal work to accelerate appendages two independent mechanical costs in water? To address this recurrent issue, we derived the power equation for aquatic movements and experimentally validated it through a novel approach integrating unsteady numerical fluid flow simulations with inverse dynamics analysis. Power time series associated with joint rotation, upper limb mechanical energy, and energy flow to the water, were computed for seven male subjects treading water with arms only. Mechanical energy decreases were coincident with power generated at the joints and power transferred from the upper limb to the water. Internal work was not correlated with the work done in excess of the external work. We conclude that internal work is an integral part of external work in water, such that calculating total mechanical work as their sum is conceptually erroneous. A revisited energy cascade of aquatic locomotion is proposed.

8.1. Introduction

Total mechanical work (W_{TOT}) is a fundamental quantity in biomechanics and physiology because it determines the economy and efficiency of locomotion, and is associated with the mechanical demands that muscles must accommodate. In aquatic locomotion, W_{TOT} is traditionally taken as the sum of the external work (W_{EXT}) done on the water, and the internal work (W_{INT}) to accelerate and decelerate the appendages with respect to the body center of mass (e.g., Blake, 1979; Fish, 1984; Pendergast et al., 2003; Zamparo and Swaine, 2012)). This is assuming that these two components are independent. However, biomechanical studies have questioned this appealing concept of two additive mechanical costs as a valid measure of W_{TOT} in walking, running (Aleshinsky, 1986b; Zatsiorsky, 1998), and cycling (Kautz et al., 1994; Kautz and Neptune, 2002; Neptune and van den Bogert, 1998; van Ingen Schenau et al., 1990). In his theoretical analysis from classical mechanics of a multi-link system, Aleshinsky (Aleshinsky, 1986b) demonstrated that there are external forces inside the mathematical expressions for W_{INT}, such that W_{INT} and W_{EXT} are not independent as usually treated. Experimental pedaling studies found that decreases in lower limb total mechanical energy were not coincident with equal amounts of negative work at the joints as predicted by Winter's internal work hypothesis (Winter, 1979), but rather with W_{EXT} done at the crank (Kautz et al., 1994; van Ingen Schenau et al., 1990). Furthermore, W_{INT} did not correlate with the work done at the joints in excess of W_{EXT} (Kautz et al., 1994), implying that W_{INT} incorrectly reflects an independent cost of moving the legs, and W_{TOT} cannot be evaluated as the sum of W_{EXT} and W_{INT}.

In swimming, their possible interaction has only rarely been disputed. Kautz and Neptune (Kautz and Neptune, 2002) suggested that, just as in cycling, W_{INT} measures might be flawed since deceleration of body segments might also cause W_{EXT}. This is a thoughtful suggestion since both activities do show the striking similarity that the support against which limbs are pushing (either the pedal or the water) is not fixed but gets continuously displaced under the applied force. More recently, a simple predictive model of breaststroke internal work revealed that the mechanical cost of moving the limbs was intriguingly mitigated at high frequencies, possibly because of a complex coupling between W_{INT} and W_{EXT} (Lauer et al., 2015). Yet, no studies have strictly tested this idea. W_{EXT} has generally been calculated as the sum of two quantities at the body: (i) the active drag on the swimmer's body W_D (di Prampero et al., 1974; Toussaint et al.,

1988); and (ii) an extra quantity W_K indirectly determined either from approximate Froude efficiency (Zamparo et al., 2002) or extrapolation from swimming on fixed pads mounted in the pool (Toussaint et al., 1988), reflecting the fact that part of W_{EXT} does not result in forward propulsion and is thus not accounted for in W_D. However, W_{EXT} directly done by the upper limbs in water is very hard to compute because of the difficulty in measuring hydrodynamic forces and their points of application. In addition, upper limb W_{TOT} as calculated from the integral of upper limb joint power has never been reported since inverse dynamics analysis of aquatic movements is lacking.

Here we tested the hypothesis that, in water, W_{EXT} and W_{INT} are tightly linked. Specifically, we assessed whether an independent mechanical cost of moving the arms truly exists by exploring the energy flow between the upper limb and the water. We derived the power equation for arm movements performed in the water and experimentally validated it for the first time through a novel approach integrating unsteady numerical fluid flow simulations with inverse dynamics analysis.

8.2. Material and methods

8.2.1. General power equation for aquatic movements

The work–energy theorem states that the work W done by non-conservative forces on a rigid body is equal to the changes in its mechanical (kinetic and potential) energy E:

$$W = \Delta E. \tag{7.1}$$

Since power is the rate of doing work, the time derivative of Eqn 1 yields the following expression for power:

$$P = \lim_{\Delta t \to 0} \frac{\Delta W}{\Delta t} = \frac{dW}{dt} = \frac{dE}{dt}, \tag{7.2}$$

with P, the instantaneous power supplied to or absorbed from a rigid body by joint moments and all external forces but weight and buoyancy, whose effects are accounted for in E (van Ingen Schenau and Cavanagh, 1990); and $\frac{dE}{dt}$, the time rate of change of mechanical energy.

Consider the free body diagram in Fig. 8–1. The upper limb was divided into rigid hand, forearm, and upper arm links, to identify forces and moments contributing to power for aquatic movements (dubbed F- and M-sources; Aleshinsky, 1986a). Forces of individual segments acting onto the water and joint moments were incorporated. Only the reaction force at the shoulder was considered, since joint forces otherwise cancel out in adjacent segments due to opposite signs. This additional source of power is present because our power analysis does not model all body segments, and the most proximal one is left with an intersegmental force that is not counteracted by the opposite one in the adjacent segment (van Ingen Schenau et al., 1990).

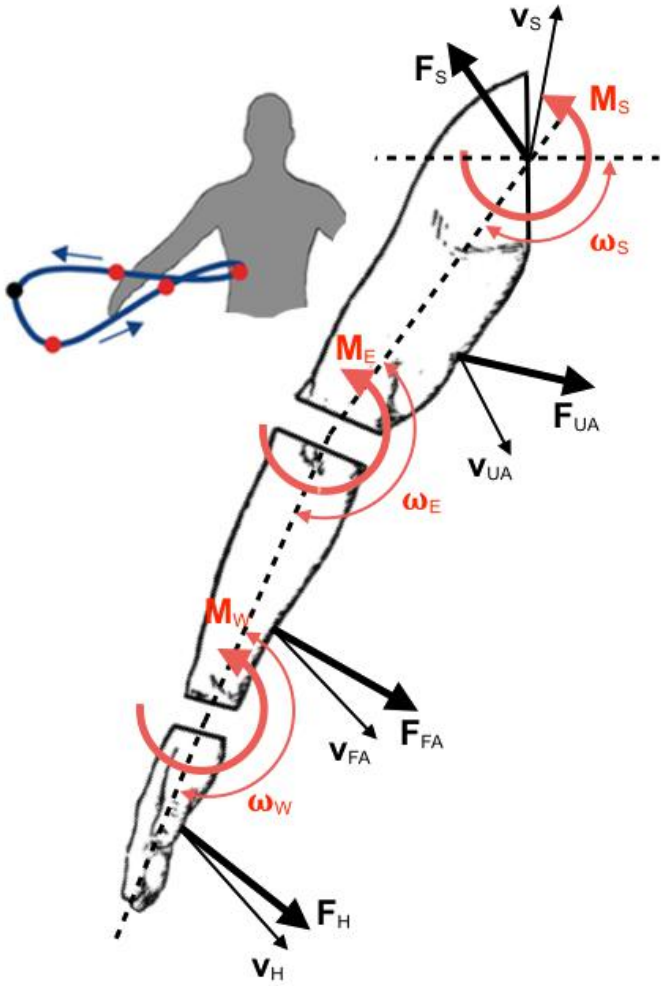

Figure 8–1. Diagram of the upper limb mechanical energy sources. Shoulder joint reaction force (F_s), forces of the upper arm, forearm and hand onto the water (F_{ua}, F_{fa}, F_h) and shoulder, elbow and wrist joint moments (M_s, M_e, M_w) are sources contributing to power during aquatic movements (F- and M-sources are represented in bold black and red, respectively). Joint angular velocities and point of force application linear velocities are respectively denoted as ω and v. Although the diagram is drawn in the transverse plane (superior view), the actual analysis is entirely three-dimensional. A representative finger trajectory is also shown: the black dot marks where movement starts, with red dots spaced every 20% of stroke duration.

The interpretation of linear power (i.e., arising from joint forces) sensibly differs from the above-mentioned rotational power (from joint moments). A positive power indicates the rate of flow of energy into the segment, whereas a negative power shows the rate of outflow of energy. However, as noted by Robertson and Winter (Robertson and Winter, 1980), the other segment connected to the one under analysis has the same joint velocity vector but its joint resultant force vector is equal in magnitude and opposite in direction. Consequently, the adjacent segment will always have a joint power equal in magnitude but opposite in sign. Thus, a flow of energy to segment 1 implies an equal outflow of energy from segment 2. Linear powers therefore show only rates of transfer of energy between segments. Besides, van Ingen Schenau et al. (van Ingen Schenau et al., 1990) noted that, in many applications, such energy flow can be considerable. During overhand throwing, for example, the power associated with pushing or pulling actions of the trunk on the arm can be as large or even larger than the summed joint power liberated by rotations of the wrist, elbow and shoulder joint.

We can then derive the general power equation for aquatic movements by replacing the components of *P*:

$$P_S + \sum P_J + \sum P_{EXT} = \frac{dE}{dt}. \tag{7.3}$$

The first term reflects the power associated with pulling or pushing actions of the trunk on the arm. The second term is the sum of joint powers done by joint moments on upper limb segments. The last term in the left-hand side of the equation equals the energy that flows from the upper limb segments to the water. This equation unambiguously relates the sum of the powers from the upper limb joints and the environment to the rate of change of segmental energies. Following the mechanical definition of power, Eqn 8–3 can be expanded as follows:

$$\underbrace{\mathbf{F}_S \cdot \mathbf{v}_S}_{P_S} + \underbrace{\mathbf{M}_S \cdot \boldsymbol{\omega}_S + \mathbf{M}_E \cdot \boldsymbol{\omega}_E + \mathbf{M}_W \cdot \boldsymbol{\omega}_W}_{P_J} - \underbrace{\mathbf{F}_{UA} \cdot \mathbf{v}_{UA} - \mathbf{F}_{FA} \cdot \mathbf{v}_{FA} - \mathbf{F}_H \cdot \mathbf{v}_H}_{P_{EXT}} = \frac{dE}{dt}, \tag{7.4}$$

where $\mathbf{F}_s$ is the shoulder joint reaction force; $\mathbf{F}_{ua}$, $\mathbf{F}_{fa}$ and $\mathbf{F}_h$, the forces of the upper arm, forearm and hand onto the water (in opposition to the reaction force of the water on the segments, hence the minus sign); $\mathbf{M}_s$, $\mathbf{M}_e$, $\mathbf{M}_w$, the shoulder, elbow and wrist joint moments; $\mathbf{v}_s$, $\mathbf{v}_{ua}$, $\mathbf{v}_{fa}$ and $\mathbf{v}_h$, the velocities of the respective points of force application; and $\boldsymbol{\omega}_s$, $\boldsymbol{\omega}_e$ and $\boldsymbol{\omega}_w$, the angular velocities of the shoulder, elbow and wrist joints.

8.2.2. Data collection and analysis

To feed all the unknown variables and validate Eqn 4, data were collected from seven male subjects (27.7±5.8 years, 1.82±0.05 m, 77.8±6.5 kg) asked to tread water with arms only for ~10 s. They were ballasted at the waist with 6 kg to ensure vigorous side-to-side arm sweep. Unlike more 'competitive' arm movement where the arm essentially accelerates throughout the stroke, this sculling task was found in a pilot study to be better suited at exploring internal–external power because of strong velocity (hence mechanical energy) fluctuations (see Results and Discussion). Experimental procedures were approved by the University of Porto review board.

Twelve reflective markers (xiphoid process, suprasternal notch, C7, T8, acromion, lateral and medial epicondyles, ulnar and radial styloids, third and fifth metacarpals, tip of the middle finger) were tracked at 100 Hz using a 12-camera underwater motion capture set-up (Oqus 3 and 4 series, Qualisys, Gothenburg, Sweden) to reconstruct 3D thorax and upper limb kinematics. Four strokes per subject were analyzed. Total mechanical energy E was computed in MATLAB® 2014a (The Mathworks, Inc., Natick, MA, USA) as the sum of hand, forearm, and upper arm kinetic and potential energies:

$$E = \sum_{i=1}^{3}\left(\frac{1}{2}m_i v_i^2 + \frac{1}{2}I_i\omega_i^2 + \left(m_i z_i - \rho V_i z_i'\right)g\right), \tag{7.5}$$

with m, the segment mass; I, the moments of inertia; v, the segment center of mass linear velocity; ω, the segment angular velocity; ρV, the product of water density and segment volume; g, the standard acceleration due to gravity; z and z', the vertical position of the segment center of mass and center of buoyancy, respectively. Segment masses, centers of mass and moments of inertia were calculated from scaling equations provided in (Dumas et al., 2007a). Segment volumes and centers of buoyancy were calculated from subjects' body scans (Mephisto 3D, 4DDynamics, Antwerp, Belgium). E was differentiated with respect to time to obtain the rate of change of total mechanical energy (i.e., the internal power, $\frac{dE}{dt}$ in Eqn 8–4).

Body scans were converted to CAD models and imported into ANSYS® Fluent® Release 14.5 computational fluid dynamics (CFD) software (ANSYS, Inc., Canonsburg, PA, USA) for unsteady fluid flow simulations, and animated via an in-house dynamic

mesh algorithm (Lauer et al., 2016). $\mathbf{F}_{ua}$, $\mathbf{F}_{fa}$ and $\mathbf{F}_{h}$ and their respective centers of pressure were evaluated from integrating the pressure and shear stress distribution over each segment surface. Shoulder joint center was estimated from the diagram in (Reed et al., 1999). $\mathbf{F}_{s}$, $\mathbf{M}_{s}$, $\mathbf{M}_{e}$, and $\mathbf{M}_{w}$ were subsequently computed through inverse dynamics analysis. Differentiating the position of points of force application with respect to time yielded $\mathbf{v}_{s}$, $\mathbf{v}_{ua}$, $\mathbf{v}_{fa}$ and $\mathbf{v}_{h}$, eventually permitting the calculation of all terms in Eqn 8–4.

As did (Kautz et al., 1994), we further assessed whether W_{int} measures were correlated with the muscular mechanical energy expenditure (MMEE) in excess of the external work. W_{int} was taken as the sum of the absolute changes in E:

$$W_{\mathrm{INT}} = \sum_{i=2}^{100} \left| E_i - E_{i-1} \right|, \tag{7.6}$$

and MMEE computed according to (Aleshinsky, 1986b):

$$\mathrm{MMEE} = \int_{1}^{100} \sum \left| P_{\mathrm{J}} \right| dt + W_{\mathrm{S}}, \tag{7.7}$$

where MMEE is the sum of the integral of the absolute joint powers over a stroke (time-normalized from 1 to 100%) and the work done by the shoulder reaction force. The work done beyond the external work W_{extra} (to be tested for correlation with W_{int}) was ultimately calculated as:

$$W_{\mathrm{EXTRA}} = \mathrm{MMEE} - W_{\mathrm{EXT}}. \tag{7.8}$$

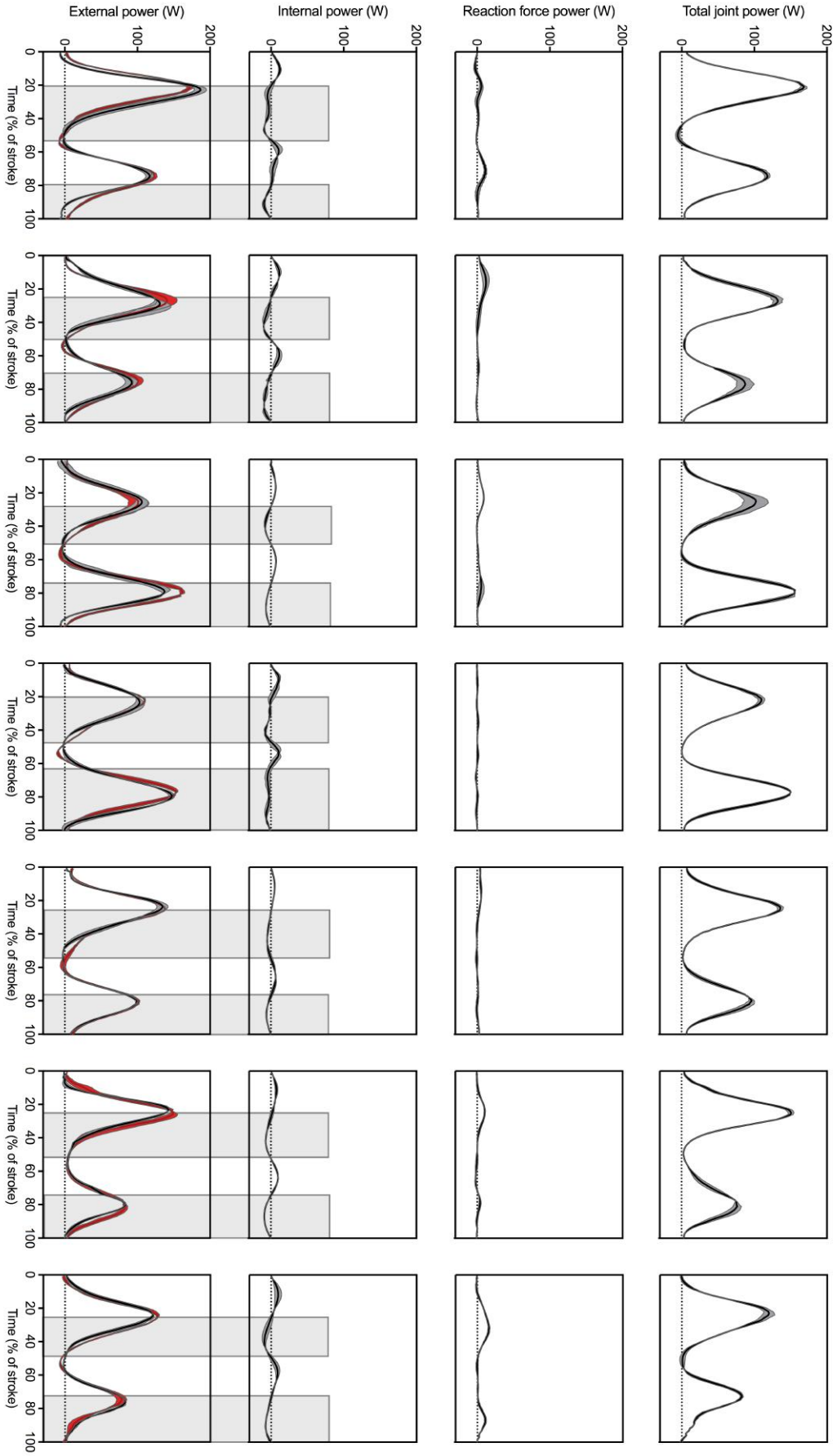
External power (W)
Internal power (W)
Reaction force power (W)
Total joint power (W)
0
100
200
Time (% of stroke)
0
20
40
60
80
100

Figure 8–2. Instantaneous powers plotted against normalized stroke duration. The top row is the total mechanical power of the upper limb (i.e., the sum of shoulder, elbow and wrist joint power) computed from inverse dynamics; the second row depicts the power associated with the joint reaction force at the shoulder, accounting for the action of the trunk on the arm; the third row reflects the internal power, calculated as the rate of change of the upper limb mechanical energy (third row); the bottom row shows the external power transferred to the water (gray) compared to the sum of the other power sources (red; calculated according to Eqn 4 as the upper limb mechanical power plus the power from the shoulder reaction force minus the rate of change of segmental energies). Shaded areas indicate periods of negative upper limb internal power. One subject is plotted per column. Data are presented as means (thick lines) ± standard deviations (filled area) across four strokes.

8.3. Results and discussion

Internal work W_{INT}, external work W_{EXT}, and the excess work W_{EXTRA} were respectively 4.8±1.9, 37.3±8.9 and 3.5±2.2 J. Statistical test revealed no correlation between W_{INT} and W_{EXTRA} (r=0.03, p=0.95), which indicates that W_{INT} does not reflect an independent mechanical cost of moving the arms in water. W_{INT} is thus an integral part of W_{EXT} and cannot be uncoupled from it, such that calculating W_{TOT} as their sum is erroneous.

To gain further insight into the dependence between W_{INT} and W_{EXT}, we derived the general power equation for aquatic movements and examined the energy flow between the upper limb and the water. The power equation proved to be fairly valid, as it yielded an overestimation of W_{EXT} of 6.5% compared to the net work input to the upper limb by all individual power sources (39.9±7.9 vs 37.3±8.9 J). Great agreement between the curves of external power and the sum of the other power sources (Fig. 8–2, bottom row) supports the assumption of inverse dynamics analysis that limbs can reasonably be considered rigid and do not undergo substantial deformations in water. This is in contrast to walking, for example, where the power equation could not be entirely validated during heel strike and late push off since feet likely deformed at joints that were disregarded (Robertson and Winter, 1980; van Ingen Schenau et al., 1990).

The power associated with the shoulder reaction force P_s was positive, albeit relatively small in magnitude (<20 W; Fig. 8–2, second row), which indicates a net power delivery from the trunk to the upper limb. Moreover, we found that periods of negative internal power $\frac{dE}{dt}$ were coincident with power transferred from the upper limb to the water

(periods of positive P_{EXT}). These decreases were the result of concentric muscle action (positive total joint power; Fig. 8–2, first row) with no remarkable energy dissipation through eccentric contraction (negative joint power), unlike Winter's W_{INT} hypothesis (Winter, 1979) that attributes decreases in E to power absorbed by the joint moments. Thus, P_{EXT} production is not just achieved by accelerating the upper limb, since kinetic energy from active deceleration as well was reconverted into significant amount of work imparted to the water.

This is analogous to cycling in many aspects. Forward dynamics simulations revealed that mechanical energy is directly apportioned to the lower limb by the gluteus maximus, whereas deceleration of lower limb segments is actively achieved from soleus and gastrocnemius concentric actions. They act to powerfully accelerate the foot into plantar flexion, which creates a pedal reaction force that accelerates the crank and intersegmental forces that concomitantly decelerate the thigh and shank. Mechanical energy consequently decreases and flows distally generating additional W_{EXT} at the pedal (Neptune et al., 2000). Likewise, in water, arm muscles might act not only to produce hydrodynamic forces directly, but also corresponding intersegmental forces that decelerate the upper limb segments, eventually leading to an energy flow towards the extremity and extra W_{EXT} production. Perhaps cocontraction at the biceps and triceps brachii that was previously found to stiffen the elbow joint (Lauer et al., 2013) plays an essential role in that task.

Our findings encourages a reexamination of the energy cascade of aquatic locomotion (i.e., the successive steps of energy conversion from the metabolic energy consumed to the mechanical energy that generates thrust (Daniel, 1991)), which improperly partitions W_{TOT} into some that goes independently to moving the fluid W_{EXT} and some to moving appendages W_{INT}. We propose that moving appendages be regarded as a step of energy exchange with the environment rather than a separate energy loss, and that measures of W_{INT} be abandoned (Fig. 8–3). With regard to bird flight, Pennycuick had long advocated this view although he was lacking the tools to test it, advancing that the work to oscillate the wing was unnecessary because it was in principle already counted in the work transmitted to the air (Pennycuick, 2008; 1968). Practically, a precise 'dissection' of the mechanical determinants of aquatic locomotion energy cost makes the respective efficiencies more reliable indicators of swimming performance (Fish, 1993). Hydraulic

efficiency $W_{EXT}/(W_{INT}+W_{EXT})$ now becomes meaningless. Mechanical efficiency W_{TOT}/E_M and propelling efficiency W_D/W_{TOT} might have been respectively inflated and underestimated when accounting for a virtual W_{INT} cost. Conceptually, this has important consequences for the analysis of the levels at which energy wastage occurs (Minetti, 2004). Potential swimming improvements may arise from a better understanding of how to optimize the energy transfer between the water and the appendages, rather than from simply attempting to reduce inertial cost. We anticipate that musculoskeletal modeling of aquatic activities, which at present has never been carried out, will further enhance our understanding of causal relationships between individual muscle forces and segment energetics.

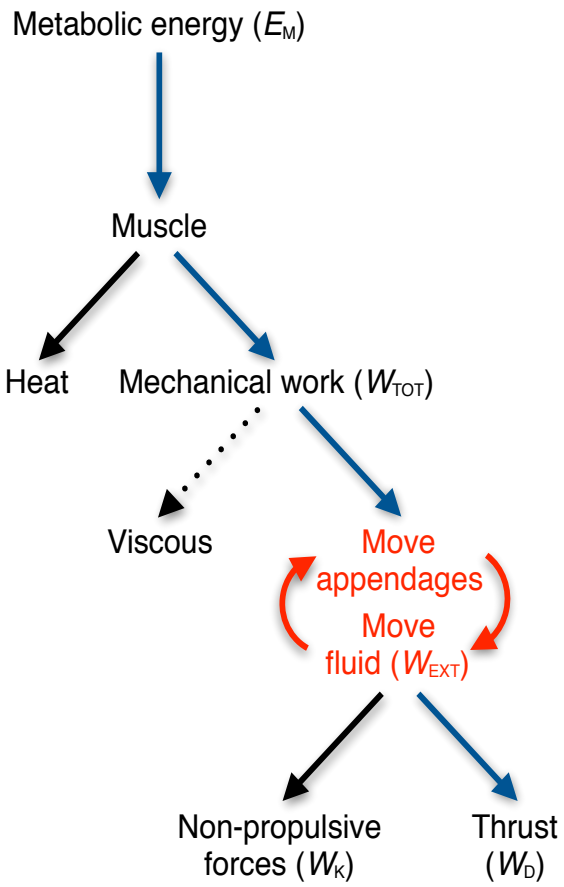

Figure 8–3. A revisited energy cascade of aquatic locomotion. Metabolic energy is successively converted into mechanical work and, ultimately, thrust. At each bifurcation, only a fraction of the energy flows towards a desirable destination (blue arrows) while the remainder is lost in unwanted effects (black arrows). The viscous work (i.e., the energy dissipated to overcome friction and viscosity in various anatomical structures) is indicated by a dotted arrow because it is challenging, if not impossible, to evaluate. A mechanical cost of imparting kinetic energy to the appendages (W_{int}) is no longer regarded as a separate energy loss; it is now an integral part of the work done on the fluid (W_{ext}) and thus vanishes. This new interaction between the water and the appendages marked in red is complex (see Results and discussion), and further insight might be gained in the future via muscle-driven forward dynamics simulations.

9 Shoulder joint load during slow underwater rehabilitation exercises

Mechanical load on the shoulder during slow underwater exercises has only been indirectly assessed via electromyographical measurements. Yet, this is insufficient to understand all the clinical implications. For the first time, we sought to evaluate through a novel integrative approach the effects of environment (water vs air) and body position (supine vs sitting) on shoulder load during scapular plane arm elevation and lowering performed at 30°/s. 18 participants' upper bodies were scanned and virtually animated within unsteady numerical fluid flow simulations to compute hydrodynamic forces. Together with weight, buoyancy and segment inertial parameters, these were fed into an inverse dynamics model to obtain net shoulder moments, power and work. Water provided a considerable three- to fourfold shoulder load reduction. Regardless of body position, shoulder flexors and extensors were the dominant musculature; in contrast, internal/external rotators and adductors/abductors had little to no net mechanical outcome. Compared to exercising supine, sitting more than halved the work done at the shoulder during arm elevation. This is likely advantageous in very early rehabilitation stages to restore joint mobility at very low effort. Shoulder power was constantly positive when sitting, whereas it was alternately negative and positive when supine. Scapular plane exercises when sitting were therefore purely concentric, whereas they required rapid pre-stretch followed by concentric force production when supine. This novel numerical procedure lays the foundations of a more advanced evaluation of joint load in water.

9.1. Introduction

Rotator cuff disorders, regarded as the principal cause of shoulder pain and upper extremity disability, rank among the most common musculoskeletal conditions. In France, about 128 surgical operations on average have been performed daily for the past 3 years (ATIH, 2017). Protecting the postoperative shoulder from excessive load is vital, particularly early in the rehabilitation process. In that context, aquatic therapy provides formidable potential benefits. Thanks to buoyancy, the upward thrust that counteracts the action of gravity, water offers near-weightlessness exercise conditions. This unique physical property significantly accelerates the restoration of shoulder flexion range of motion as early as three weeks post surgery (Brady et al., 2008). Furthermore, water is very viscous and thus highly dampening. Resistance rapidly decays upon cessation of movement, which is thought to dramatically reduce the risk of reinjury (Prins and Cutner, 1999).

The latest American Society of Shoulder and Elbow Therapists' consensus promotes the use of slow (30°/s) aquatic scapular plane movements to initiate aquatic therapy (Thigpen et al., 2016). The guideline is based on the observation that, at that speed, the electromyographical (EMG) activity of the deltoid and rotator cuff muscles was on average ~2–5× lower in water than on land (Castillo-Lozano et al., 2014; Kelly et al., 2000). Assuming load was proportional to muscle activity, the authors concluded that slow underwater shoulder exercises were likely safe enough for early active mobilization. However, EMG recordings only offer insight into individual muscle activation level and are poor indicators of the mechanical load on the musculoskeletal system (Winby et al., 2013; Zajac et al., 2002).

Internal load is best estimated noninvasively from inverse dynamics (van den Bogert, 1994). On land, the procedure requires the knowledge of segment inertial properties, linear and angular accelerations, as well as the ground reaction force. Eventually, it yields mechanical quantities that are superior to EMG in their capacity to analyze how muscle groups meet task mechanical requirements. Joint moments, for example, identify the dominant musculature during the observed motion (Desroches et al., 2010a), and can,

under different conditions, be representative of muscle force production and ligament loading (Kristianslund et al., 2014b). The calculation of joint work, on the other hand, provides a reasonable evaluation of the actual work produced by muscles during slow movement (Sasaki et al., 2009). As such, it is a more objective and meaningful criterion of internal loading than EMG. Remarkably, inverse dynamics also has the potential to unveil the type of dynamic muscle action through the computation of joint power (Robertson and Winter, 1980). Nonetheless, a thorough inverse dynamics analysis of shoulder loading in water has never been reported. Unlike on land, accurate measurements of the hydrodynamic forces acting upon the entire upper limb surface and their respective points of force application are needed—this makes the procedure very complex and one of the major challenge of aquatic therapy (Biscarini and Cerulli, 2007).

We recently developed a new methodology coupling inverse dynamics with numerical fluid flow simulations to calculate instantaneous internal loading (Lauer et al., 2016). Armed with these new tools, it is also now possible, in addition to the quantities described above, to dissect the mechanical effects of buoyancy, weight, and water resistance. It is believed that modulating the action of buoyancy on the upper limb possibly influences the work done at the shoulder (Thein and Brody, 2000). This hypothesis is best viewed from a simple mechanical analysis of identical movements performed in two different positions (Fig. 9–1). When sitting, buoyancy assists scapular plane arm elevation and resists arm lowering. On the other hand, buoyancy alternates between both roles when supine, temporarily assisting then resisting motion. However, the extent to which changes in body position alter shoulder load, and whether this may compromise therapy success, must be clarified.

We therefore sought to evaluate the shoulder mechanical demands of scapular plane movements performed at 30°/s in water and on land, while supine and sitting. Based on past EMG findings, we expected load in water to be roughly within 20–50% that on land. Furthermore, we hypothesized that varying body position would cause substantial changes in task mechanical demands, reflected by marked alterations in shoulder moments, power and work. Specifically, we predicted that elevation and lowering of the arm would require respectively less and more work when sitting compared to supine.

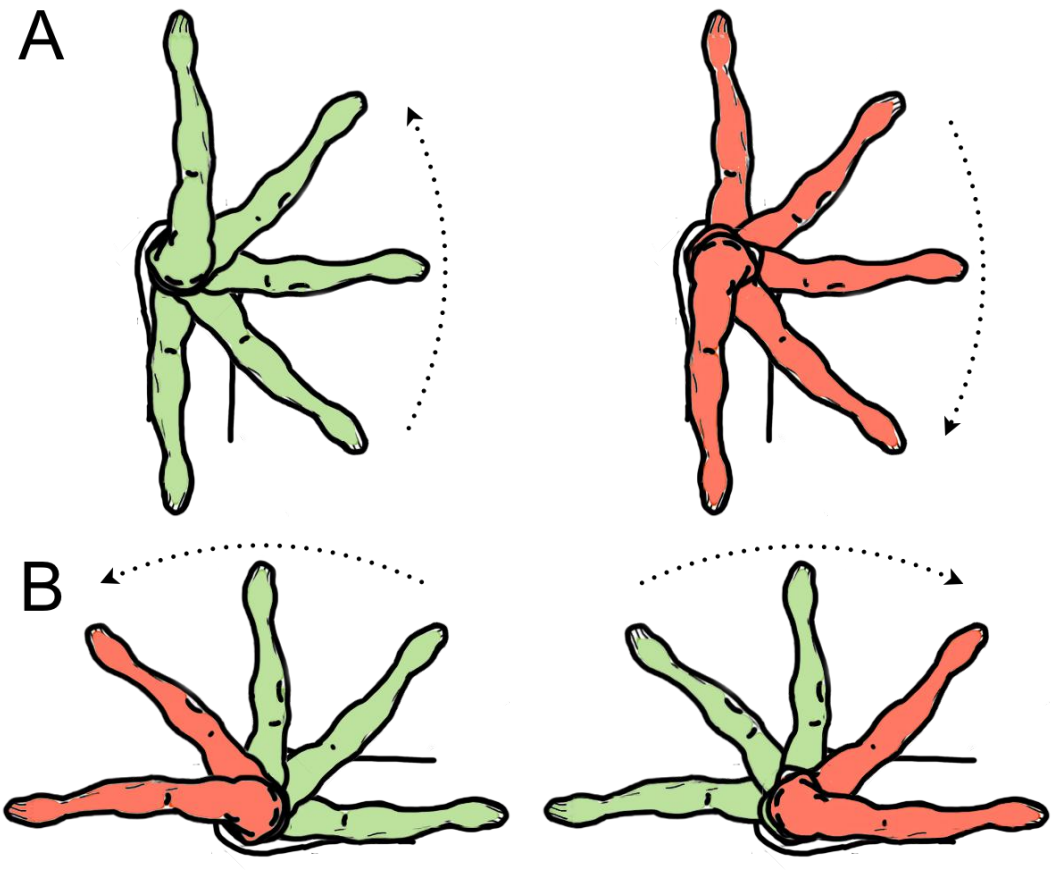

Figure 9–1. Action of buoyancy on the upper limb. Buoyancy either fully assists (green) or resists (red) arm motion when sitting (A). It alternates both roles when supine (B), assisting or resisting motion only temporarily. Dotted arrows indicate direction of movement.

9.2. Material and methods

9.2.1. Participants and numerical procedure

Eighteen adults (Table 9–1), free from upper extremity injury or pain, provided written informed consent to participate in the study. Sample size was determined a priori, based on effect size from a pilot study comparing total mechanical work between positions (d=0.83, N=5). Power analysis (G*Power 3; (Faul et al., 2007) revealed that 18 participants were needed to detect similar effects using two-tailed, paired t-tests with 90% power and 5% type I error rate. Procedures were approved by the University of Porto ethics committee.

Table 9-1. Participant demographics. *N*: number of subjects. BMI: body mass index.

Gender	*N*	Age (years)		Height (m)		Mass (kg)		BMI (kg·m^{-2})	
		Mean	SD	Mean	SD	Mean	SD	Mean	SD
Female	7	30.8	9.6	1.63	0.06	58.1	9.3	21.8	3.2
Male	11	33.1	9.0	1.80	0.09	76.5	13.2	23.6	2.7

Participants' upper bodies were scanned with a Mephisto 3D scanner (4DDynamics, Antwerp, Belgium). Virtual geometries were then edited and converted into computer-aided design models prior to import into ANSYS® Fluent® Release 14.5 CFD software (ANSYS, Inc., Canonsburg, PA, USA). Six anatomical landmarks (suprasternal notch, left and right anterior superior iliac spines, right glenohumeral joint center, medial and lateral epicondyles of the humerus) were located (see Fig. 9–2) to construct thorax and upper arm coordinate systems. Glenohumeral joint center location was experimentally determined in a separate instance according to the procedure described in (Lempereur et al., 2010). For that purpose, four additional markers placed distally on the upper arm were tracked while participants moved their upper limb in all dimensions. This yielded a set of vectors rotating over time, from which the glenohumeral joint center was reconstructed using Gamage and Lasenby's least squares algorithm (Gamage and Lasenby, 2002).

Scapular plane arm elevation and lowering were numerically simulated. Motion was identical in all participants to eliminate inter-individual variability in kinematics and account for variability in morphology. The upper limb was animated relative to the thorax at 30°/s in the scapular plane by injecting a triangle wave of period 12 s and ranging between 0 and π in Fluent via our dynamic mesh algorithm. The surface of the virtual models was meshed with ~40,000 millimeter-scale triangular faces onto which Fluent built-in flow solver computed pressure and shear stress at each time step.

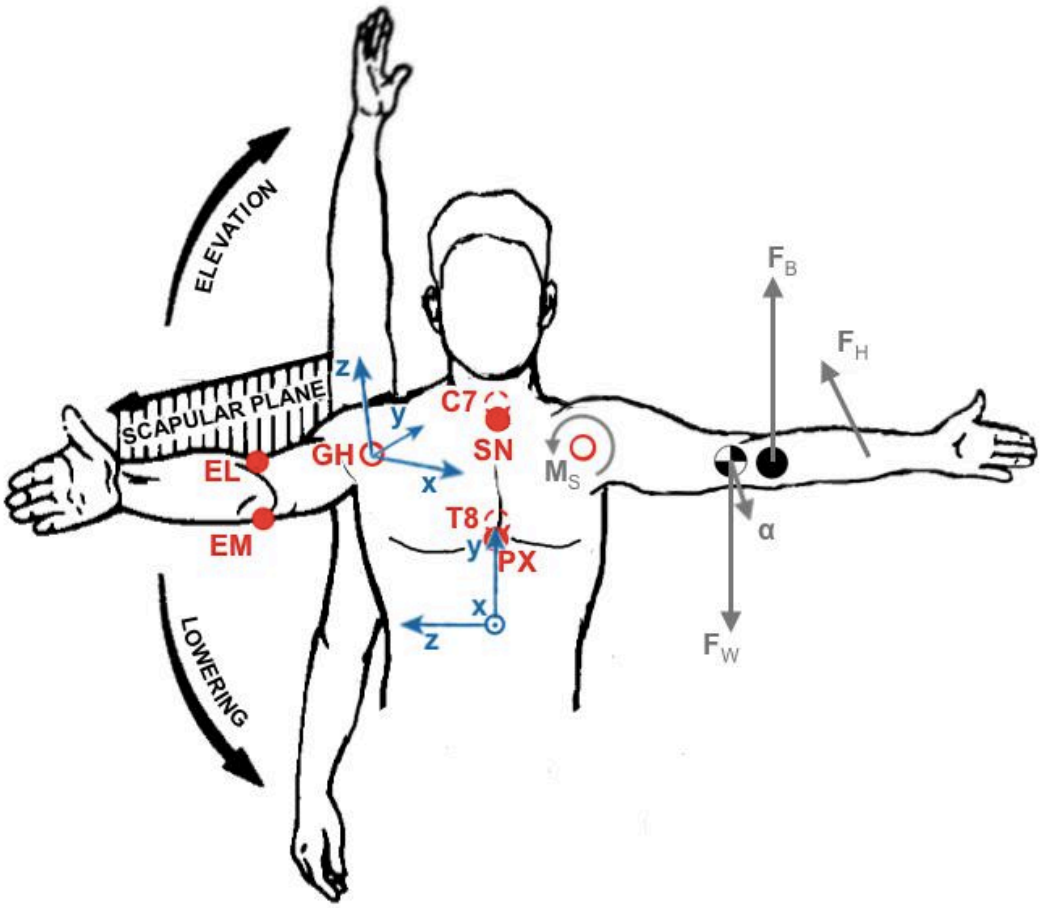

Figure 9–2. Schema of the kinematics and inverse dynamics models. Continuous upper limb elevation and lowering were simulated in the scapular plane, set at an angle of 30° with the sagittal plane. The anatomical landmarks marked in red (EL: lateral epicondyle; EM: medial epicondyle; GH: glenohumeral joint center; SN: suprasternal notch; PX: xiphoid process; plus C7 and T8) were used to construct the upper limb and thorax right-handed coordinate systems (in blue). The latter is purposely represented at its wrong origin for readability. The external forces (weight, buoyancy, hydrodynamic force; Fw, Fb, Fh) are denoted in gray. The resultant shoulder moment Ms, calculated as the sum of the three other moments of force (Mw, Mb, Mh), is the value of interest here.

9.2.2. Inverse dynamics modeling

Net shoulder moment calculations were based on Euler's second law of motion for rigid body dynamics, the general form of which is:

$$\mathbf{M}_S = I\boldsymbol{\alpha} - \mathbf{M}_W - \mathbf{M}_B - \mathbf{M}_H, \tag{8.1}$$

where $\mathbf{M}_S$ is the resultant moment at the shoulder; I, the moments of inertia of the upper limb; $\boldsymbol{\alpha}$, its angular acceleration; $\mathbf{M}_W$, $\mathbf{M}_B$, and $\mathbf{M}_H$, the moments of weight, buoyancy and hydrodynamic force about the glenohumeral joint center, computed as follows:

$$\mathbf{M}_{\mathrm{W}} = \mathbf{r}_{\mathrm{COM}} \times \mathbf{F}_{\mathrm{W}}, \tag{8.2}$$

$$\mathbf{M}_{\mathrm{B}} = \mathbf{r}_{\mathrm{COB}} \times \mathbf{F}_{\mathrm{B}}, \tag{8.3}$$

$$\mathbf{M}_{\mathrm{H}} = \sum_{i=1}^{n} \mathbf{r}_i \times \mathbf{F}_{\mathrm{H},i}, \tag{8.4}$$

where $\mathbf{r}_{\mathrm{COM}}$ is the position vector of the upper limb's center of mass (relative to the glenohumeral joint center); $\mathbf{F}_{\mathrm{W}}$, the upper limb's weight vector; $\mathbf{r}_{\mathrm{COB}}$, the position vector of the upper limb's center of buoyancy; $\mathbf{F}_{\mathrm{B}}$, the buoyant force vector; $\mathbf{r}_i$, the position vector of the centroid of face *i* at the surface of the upper limb virtual geometry; and $\mathbf{F}_{\mathrm{H},i}$, the sum of pressure and friction acting on the face *i*. Upper limb buoyancy and center of buoyancy location were obtained from virtual model volume. Upper limb mass, center of mass location and moments of inertia were estimated from scaling equations based on subject anthropometry (Dumas et al., 2007a). In order to simulate the sitting position, weight and buoyancy vectors were rotated by 90°. The interested reader is referred to (Lauer et al., 2016) for further details regarding numerical settings.

Shoulder moments were described in a non-orthogonal joint coordinate system to get a more coherent anatomical and clinical understanding of joint dynamics (M. Gagnon et al., 2001; Schache and Baker, 2007), and normalized to body weight times arm length (%BW·AL; (Hof, 1996)). By convention, positive joint moments were mechanical actions of flexion, adduction and internal rotation of the shoulder.

9.2.3. Mechanical joint power and work computation

Instantaneous shoulder joint power was readily obtained by dot product of net shoulder moment and shoulder angular velocity vectors, and normalized to participants' body mass. Partitioning the instantaneous power into individual components related to hydrodynamic force, weight and buoyancy was computed likewise. The positive $W^{+}_{\mathrm{E/L}}$ and negative mechanical work $W^{-}_{\mathrm{E/L}}$ delivered at the shoulder joint during arm elevation and lowering in the scapular plane were computed as follows: power time series were individually integrated with respect to time over discrete periods of positive and negative power pertaining to arm elevation and lowering (see Fig. 9–3 for illustration), yielding $W^{+}_{\mathrm{E/L}}$ and $W^{-}_{\mathrm{E/L}}$ done by each force acting upon the upper limb during the corresponding

phases. To assess the load during the same movement performed on land, $W^{+}_{E/L}$ and $W^{-}_{E/L}$ were recomputed once the contributions of hydrodynamic force and buoyancy subtracted.

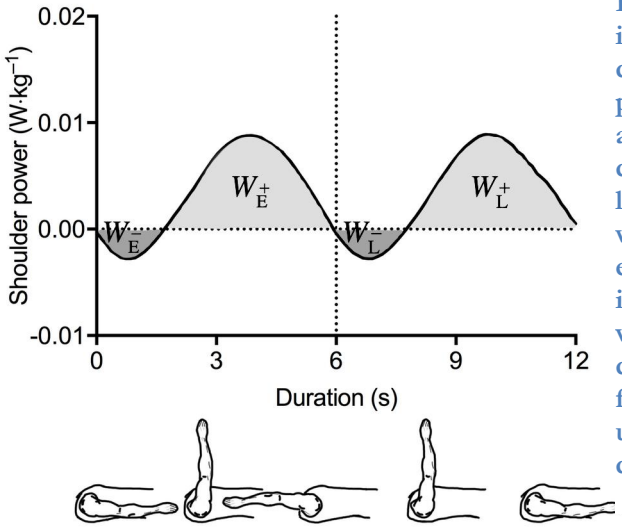

Figure 9–3: Illustrative plot of instantaneous shoulder joint power during one complete cycle. Individual periods of negative (dark gray areas) and positive work (light gray areas) done at the shoulder are respectively labeled W^{+} and W^{-}. Mechanical work values are computed separately for elevation (W_e) and lowering (W_l) by integration of the power time series with respect to time. The vertical dotted line indicates the transition from elevation to lowering of the upper limb, as exemplified by the drawing.

9.2.4. Statistical analysis

Statistical analysis was done in STATA 13 (StataCorp, Inc., College Station, TX, USA), and the significance level set at 0.05. Assumption of normality was checked for all variables with the Shapiro–Wilk test prior to analysis. Means, standard deviations and 95% confidence intervals were computed. Existence of significant differences in peak moment and mechanical work between exercising positions were tested with Student's paired *t*-tests. No tests were run on power profiles since only their shape and polarity were of interest.

9.3. Results

Positive mechanical work done at the shoulder was 32.4% (95% CI [29.2, 35.6]) and 25.0% [22.8, 27.2] that when performing the same movement on land, supine and sitting respectively. Arm elevation was less demanding sitting than supine (0.012±0.018 vs 0.027±0.012 J·kg^{-1}, p=0.034; Fig. 9–4), whereas no differences were noted during arm

lowering (0.038±0.018 vs 0.027±0.012 J·kg^{-1}, p=0.062). Significantly less work was done when supine compared to sitting against buoyancy (0.092±0.026 vs 0.227±0.045 J·kg^{-1}, p<0.001) and weight (0.081±0.015 vs 0.215±0.034 J·kg^{-1}, p<0.001). Work done against water resistance (0.028±0.010 J·kg^{-1}) was unchanged by body position. Overall, little negative mechanical work was done at the shoulder (<0.0009 J·kg^{-1}, or <4% of the positive mechanical work done).

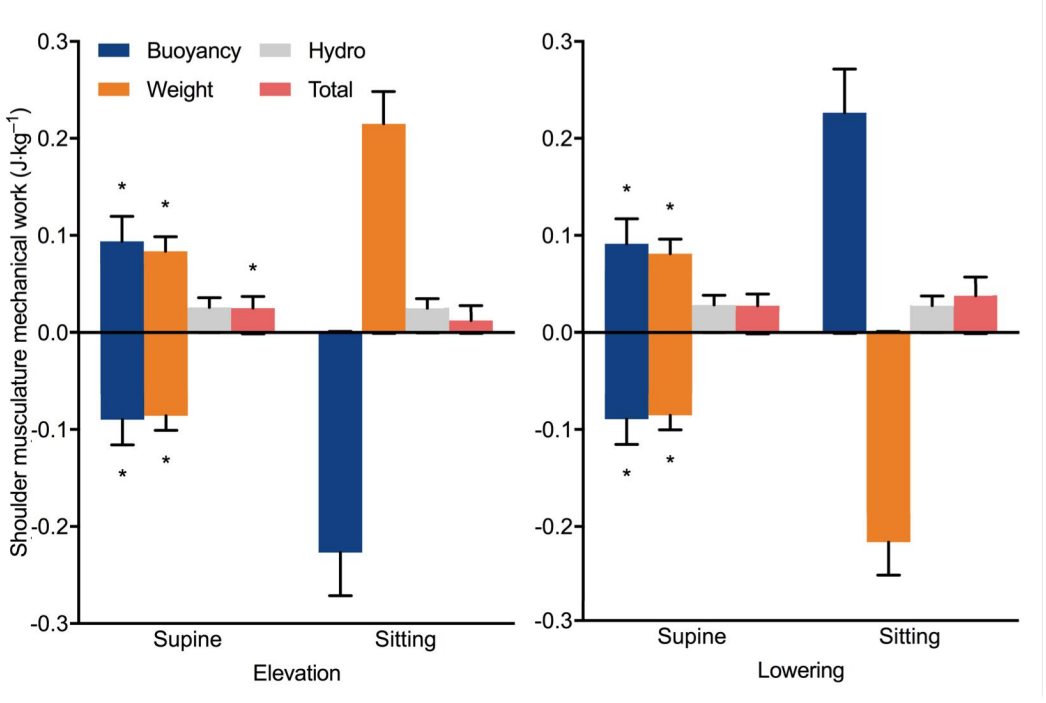

Figure 9–4. Average mechanical work done during aquatic scapular plane arm elevation (left panel) and lowering (right panel). Work has been further broken down into individual components related to external forces (buoyancy, weight, and hydrodynamic force). Data are means ± s.d. * Significantly different (p<0.05) from the value in sitting position.

Net shoulder moments about the axes of internal/external rotation and adduction/abduction were negligible in both positions. However, marked differences were observed about the axis of flexion/extension. Supine exhibited alternation of extension–flexion–extension moments, whereas sitting revealed a flattened flexion moment pattern during arm elevation (Fig. 9–5, first row). Symmetric profiles were seen for moments of weight and buoyancy, although the latter were higher in magnitude. Regardless of body position, moments of hydrodynamic force were null when the arm was either along the thigh or elevated along the head (0 or 180°), and peaked towards the middle of arm elevation and lowering. Means and 95% confidence intervals for moment peaks are displayed in Table 9–2. Buoyancy and weight moment peaks were significantly

higher in magnitude when supine about the axis of adduction/abduction (p<0.001). Net shoulder moment peaks were significantly higher when lying supine about flexion/extension and adduction/abduction during arm elevation only (p<0.001).

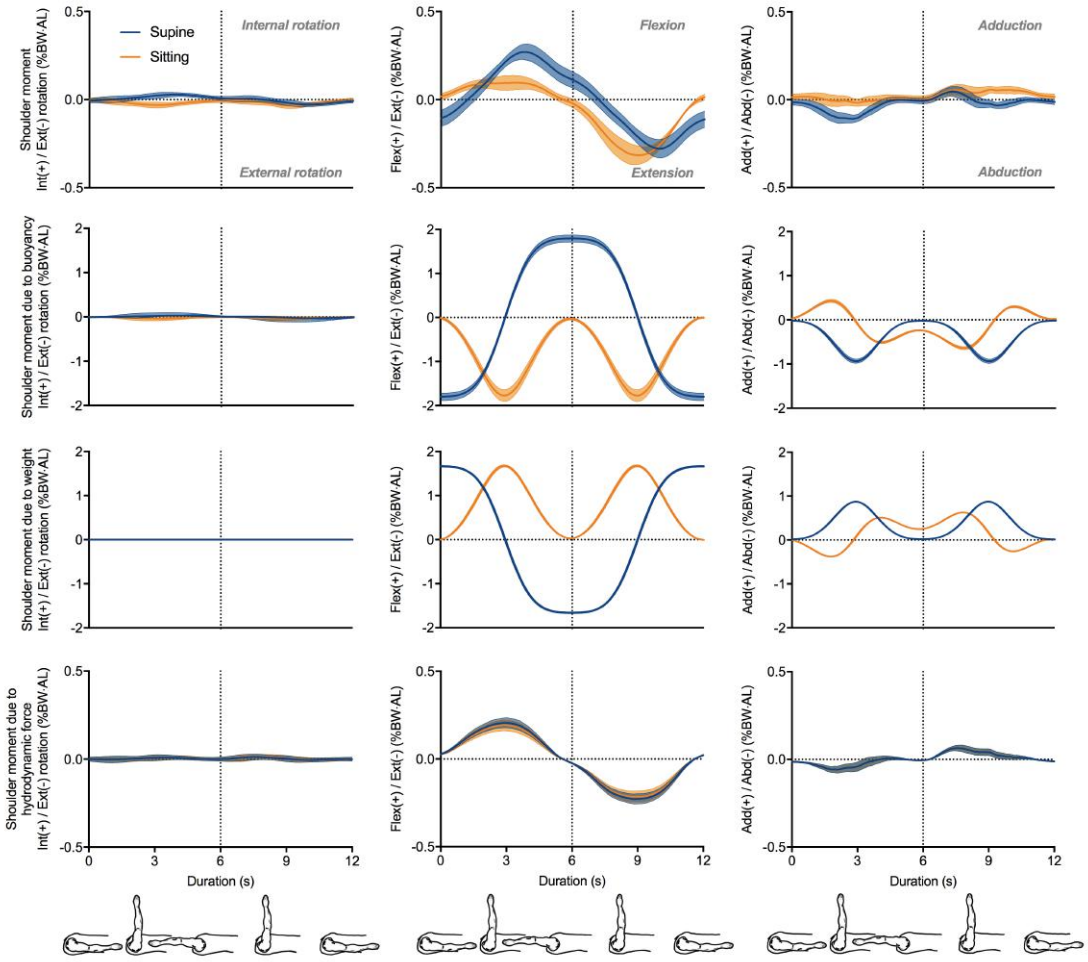

Figure 9–5. Net shoulder joint moment (top row) and moments of external forces (three bottom rows) about internal/external rotation, flexion/extension, and adduction/abduction axes. The vertical dotted line indicates the transition from scapular plane abduction to adduction. Blue and orange traces respectively denote supine and sitting positions. Data are presented as means (thick lines) and 95% confidence bands (filled area). Note that top and bottom graphs were scaled down for better readability.

Table 9-2. Means and 95% confidence intervals for moment peaks. $M_{s,peak}$, $M_{b,peak}$, $M_{w,peak}$, and $M_{h,peak}$ are peak values for net shoulder moment, and moments of buoyancy, weight, and hydrodynamic force. Peaks were identified during arm elevation and lowering about each rotation axis: internal/external rotation, flexion/extension, and adduction/abduction axes. Shaded rows indicate significant differences ($p<0.05$) between performing supine and sitting.

		Elevation				Lowering			
Variable		Supine		Sitting		Supine		Sitting	
$\mathbf{M}_{S,peak}$		mean	95% CI	mean	95% CI	mean	95% CI	mean	95% CI
	Int(+) / Ext(-)	0.03	[0.02, 0.04]	–0.02	[–0.01, –0.03]	–0.01	[–0.01, –0.02]	–0.01	[–0.01, –0.02]
	Flex(+) / Ext(-)	0.27	[0.23, 0.31]	0.10	[0.06, 0.14]	–0.28	[–0.23, –0.33]	–0.32	[–0.26, –0.38]
	Add(+) / Abd(-)	–0.11	[–0.09, –0.13]	0.02	[0.01, 0.04]	0.05	[0.02, 0.08]	0.05	[0.02, 0.09]
$\mathbf{M}_{P,peak}$									
	Int(+) / Ext(-)	0.02	[0.01, 0.02]	–0.02	[–0.01, –0.02]	–0.02	[–0.01, –0.03]	–0.02	[–0.01, –0.03]
	Flex(+) / Ext(-)	±1.80	[±1.72, ±1.88]	–1.77	[–1.64, –1.90]	±1.80	[±1.72, ±1.88]	–1.77	[–1.64, –1.90]
	Add(+) / Abd(-)	–0.94	[–0.89, –0.99]	0.43	[0.40, 0.46]	–0.94	[–0.89, –0.99]	–0.64	[–0.61, –0.67]
$\mathbf{M}_{W,peak}$									
	Int(+) / Ext(-)	0	0	0	0	0	0	0	0
	Flex(+) / Ext(-)	±1.67	[±1.65, ±1.69]	1.67	[1.65, 1.69]	±1.67	[±1.65, ±1.69]	1.67	[1.65, 1.69]
	Add(+) / Abd(-)	0.87	[0.86, 0.88]	0.51	[0.50, 0.52]	0.87	[0.86, 0.88]	0.63	[0.62, 0.64]
$\mathbf{M}_{H,peak}$									
	Int(+) / Ext(-)	0.01	[0.00, 0.02]	0.01	[0.00, 0.02]	0.01	[0.00, 0.02]	0.01	[0.00, 0.02]
	Flex(+) / Ext(-)	0.21	[0.18, 0.23]	0.21	[0.18, 0.23]	–0.23	[–0.20, –0.26]	–0.23	[–0.20, –0.26]
	Add(+) / Abd(-)	–0.06	[–0.04, –0.08]	–0.06	[–0.04, –0.08]	0.06	[0.05, 0.08]	0.06	[0.05, 0.08]

Shoulder mechanical power output differed between the two exercising positions (Fig. 9–6). When supine, both scapular plane elevation and lowering required successively short period (~1.2 s) of negative power and longer period (~4.8 s) of positive power, peaking at 0.01 $W \cdot kg^{-1}$ towards 30 and 80% of the full motion. Conversely, when sitting, levels of power were 3× lower during elevation (0.003 $W \cdot kg^{-1}$), and slightly higher during lowering (0.012 $W \cdot kg^{-1}$). Total power was further partitioned into individual components related to buoyancy, weight, and hydrodynamic forces. Buoyancy and weight peak power was lower supine than sitting (0.05 vs 0.08 $W \cdot kg^{-1}$ and 0.04 vs 0.07 $W \cdot kg^{-1}$, respectively). Patterns changed sign twice as frequently supine compared to sitting, whereas profiles of hydrodynamic force power were identical between positions.

9.4. Discussion

9.4.1. Water reduces load on the shoulder by up to 75%

For the first time, this study reports a quantification of the mechanical demands on the shoulder of underwater scapular plane exercises. We observed a considerable three- to fourfold work reduction at the shoulder compared to the same movement on land, supporting our first hypothesis. This is strong mechanical evidence encouraging the early implementation of aquatic therapy during rehabilitation. EMG studies previously reached the same conclusion (Castillo-Lozano et al., 2014; Kelly et al., 2000), although the actual diminution of shoulder load could not be accurately evaluated. The protective nature of the aquatic environment was solely inferred from the observation that activity of the deltoid and rotator cuff muscles was less in water than on land.

The knowledge of joint work presents additional advantages. Unlike a given level of muscle activity, which may correspond to different load (Tax et al., 1990), joint work offers a robust measure of task mechanical demands (Winter, 2005). Furthermore, since mechanical work necessitates metabolic energy to be performed, it can be used as a physiological marker of intensity across a large variety of exercises. For example, considering the maximum mechanical work output observed during arm elevation (0.027

J·kg^{-1}, hence 1.9 J for an average 70-kg subject) and a conservative muscle efficiency of 0.25 (expected from the thermodynamics of muscle contraction; (Woledge et al., 1985)), we predict a metabolic cost of 7.6 J and metabolic work rate of 1.3 W. This is about 28× less than the energy needed to wash dishes (Jetté et al., 1990)!

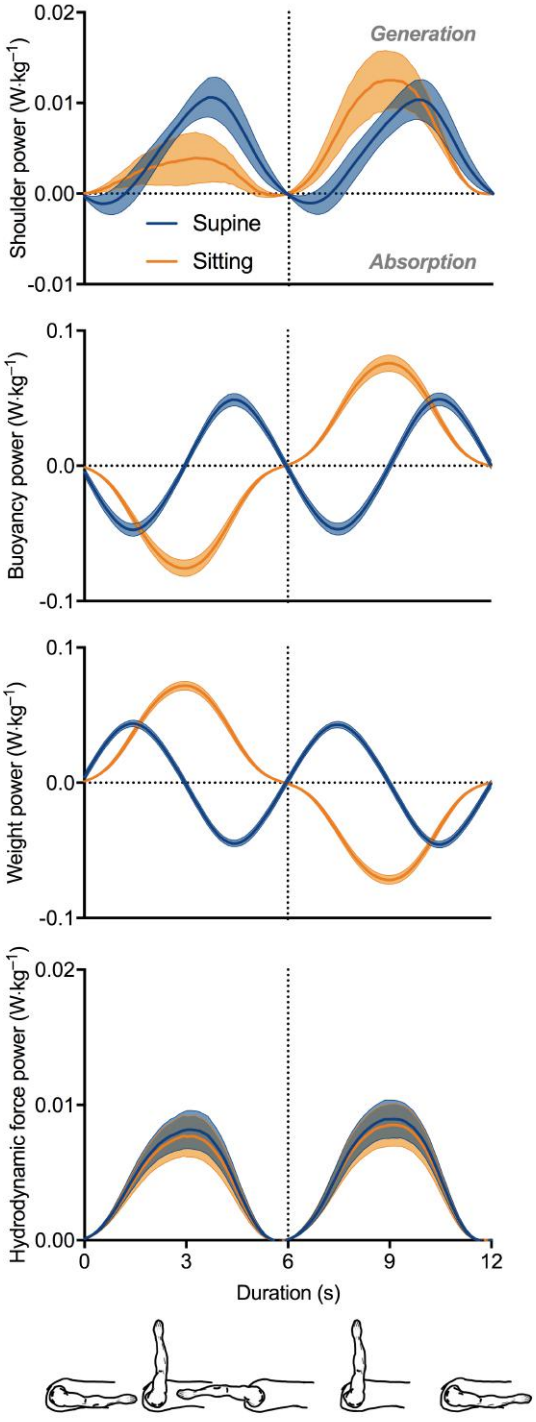

Figure 9–6. Instantaneous power of shoulder musculature and external forces plotted against one cycle. Positive/negative power reflects production/absorption of mechanical energy through concentric/eccentric muscle action. See Figure 9–5 for color legend. Note that top and bottom graphs were plotted on different scales for better readability.

9.4.2. Shoulder load during arm elevation can more than double when supine

Our second hypothesis was only partially supported by our data. Although the mechanical work during arm elevation performed sitting was less than half the work when supine, no differences were noted between positions during arm lowering. Thus, buoyancy alone fails to explain changes in shoulder load. This invalidates our straightforward analysis presented in Introduction (Fig. 9–1), and rather suggests that a more subtle interaction occurs between all external forces. Simply considering buoyancy while disregarding weight and hydrodynamic forces to make an educated guess about movement mechanics and clinical implications is potentially misleading (Prins and Cutner, 1999; Thein and Brody, 2000; Vo et al., 2013). Furthermore, substantial alteration in shoulder load may compromise therapy success. While exercising sitting may prove beneficial in very early rehabilitation stages of a weakened shoulder to restore joint mobility at low effort, mechanical solicitation might very well be too light to elicit active strength gain later on. Inversely, exercising supine seems more likely to be profitable at intermediate rehabilitation stages since task mechanical requirements were overall higher.

9.4.3. EMG improperly identifies the prime movers

Net shoulder moments were ~3–6× higher about the flexion/extension axis than about the adduction/abduction axis, and very low to null about the internal/external rotation axis. Polarity of the net joint moment reflects the dominant muscle group during the observed motion (Winter, 2005). Shoulder flexors and extensors therefore prevailed during elevation and lowering of the arm in the scapular plane; in contrast, internal/external rotators and adductors/abductors had little to no net mechanical outcome. This is consistent with reports of high activation levels (relative to the other muscles studied) of the pectoralis major and anterior deltoid, and silent subscapularis and posterior deltoid (Castillo-Lozano et al., 2014; Kelly et al., 2000). Surprisingly though, Kelly et al. had found that the first and third most recruited muscles were the supraspinatus and infraspinatus (Kelly et al., 2000), which respectively act as shoulder abductor and external rotator. The solution to this paradox likely lies in the dual action of the pectoralis major: as it raises the arm, it also produces an undesired adduction

moment component that must be counteracted by other muscles in order to provide joint stability (Veeger and van der Helm, 2007). Two important consequences follow. First, EMG improperly identifies the prime movers. Second, inverse dynamics does inform about shoulder load but gives little insight into individual muscle function, particularly those cocontracting. Examining individual muscle contributions to total mechanical demands in water would require very elaborate musculoskeletal models, which is a step we are currently exploring.

9.4.4. Body position determines muscle contraction type

Shoulder power was alternately negative (shortly after movement reversal) and positive when supine, whereas it was constantly positive when sitting. Robertson and Winter postulated that a positive/negative joint power reflects the production/absorption of mechanical energy through concentric/eccentric contractions (Robertson and Winter, 1980). Recently, the reliability of joint power analysis in proximal muscle groups with relatively short tendons (such as at the shoulder) has gained experimental support (Cronin et al., 2013). This is important because the identification of muscle contraction type is not easily accessible in vivo on land, and even less so in water. Scapular plane exercises when sitting were therefore purely concentric, whereas they required rapid pre-stretch followed by concentric force production when supine.

In fast (>300°/s) underwater knee exercises, eccentric contraction was found to result from interaction between the moving limb and accelerated masses of water (Pöyhönen et al., 2001a). Here, this cannot be the case; energy absorption would have occurred before movement reversal to slow the upper limb down, which, in addition, is likely unnecessary at 30°/s. Inspection of moment and power traces reveal that energy absorption is rather due to interaction between a high moment of buoyancy tending to pull the arm upward and a very small moment of hydrodynamic force. Most importantly, this means that eccentric contraction can be elicited at 10× slower speeds without buoyant devices, simply by appropriately timing the mechanical actions of buoyancy and water resistance.

9.4.5. Inter-individual differences in buoyancy has the most notable effect on shoulder load

Individuals with varying body composition and shape naturally show different floating ability and resistance to movement. Very lean individuals may have upper limbs that sink. Furthermore, tall individuals generally have longer segments, hence larger surface area in contact with water. By eliminating inter-individual variability in kinematics, our study design allowed us to isolate the effect of variability in morphology on shoulder load. Although body fat was not measured, our sample was representative of healthy and overweight individuals based on BMI in the range 19–30. Judging from standard deviations of mechanical work when sitting, variability in shoulder load had more to do with inter-individual differences in upper limb buoyancy (s=0.045) than hydrodynamic force (s=0.010). Therefore, care should be taken in extrapolating our findings to underweight or obese patients as we can reasonably expect marked changes in kinetic patterns.

One could argue that our conclusions tightly depend on the accuracy with which we evaluated body segment inertial parameters. Yet, we are confident that more expensive techniques (such as MRI) would not have yielded significant improvements for the following reasons. We used the most complete and practical study to date (Dumas et al., 2007a)—unifying two extensive data sets on living subjects (McConville et al., 1980; Young et al., 1983) corrected to relax ambiguous assumptions related to center of mass location, inertia tensor, and anatomical coordinate systems— that is expected to provide accurate segment parameters estimates for a ~30 years old population. This is unlike anthropometric data extracted from measurement on cadavers, where errors may reach 40% (Cappozzo and Berme, 1990) because of limited accuracy due to technical and ethical constraints, small sample sizes, different measurement techniques, and variation in segment boundaries. Moreover, Pearsall and Costigan (Pearsall and Costigan, 1999) conducted inverse dynamics analysis of walking subjects while repeatedly varying segment parameters in the range ±40% over nine increments. Although significant, changes in kinetic measures were less than 1% of subject's body weight. Even extreme variations of 40% only represented small magnitude changes in absolute terms, and were thus of little consequence to joint kinetics. However, segment mass, moments of inertia, and center of mass location were altered independently. Isolated changes are artificial

since a change in a single parameter would likely be met by change in another. Pamiès-Vilà et al. (Pàmies-Vilà et al., 2012) provided additional evidence that inverse dynamics was less sensitive to uncertainty in body segment inertial parameters than it was to noise in ground reaction forces and kinematics data. A thousand statistical simulations (emulating realistic error distribution around ±15% maximum perturbation) revealed that the relative root mean square error in lower limb joint torques during walking did not exceed 6% on average, with segment mass and center of mass location being the most sensitive parameters. Last, although inverse dynamics modeling of arm movements are influenced by the choice of segment inertial parameters to a greater extent than gait analysis because of moments of inertia are lower (Piovesan et al., 2011), upper limb segments in water behave as if they were heavier because of complex hydrodynamic interactions (Lauer et al., 2015). Consequently, the uncertainty associated with estimating segment inertial parameters is likely much less critical than possibly expected on the basis of experiments conducted on land.

9.4.6. Sensitivity to joint center location

Moments of external forces are computed about joint centers, the locations of which are difficult to measure in vivo. Yet, very accurate knowledge of the point about which two segments move relative to one another is crucial. Holden and Stanhope (Holden and Stanhope, 1998) showed that, despite low effect of variation in knee joint center location (±10 mm) on knee moment patterns at normal walking speeds, it can change the sign of the moment at very slow speeds when moment magnitude is small, hence biased joint moment interpretation. In other words, knee joint moment could not be confidently interpreted as representing either a predominantly flexor or extensor strategy because the sign of the moment might be different if joint location were to slightly vary. This is critical especially in clinical studies, where motion is generally slow. Delp and Maloney (Delp and Maloney, 1993) sought to quantify the effects of hip center displacements in a volume of 64 cm^3 on maximum isometric joint moments of hip abductors, adductors, flexors, and extensors. Moment-generating capacities of these muscle groups were found to be very sensitive to hip center location, observing changes of up to 50%. Stagni et al. (Stagni et al., 2000) complemented Delp and Maloney's analysis by quantifying how ±30 mm mislocation errors propagated to hip and knee joint moments expressed in joint

coordinate systems. The largest error (22% into flexion/extension component) occurred at the hip when the hip center was mislocated along the anterior-posterior axis. They advise that hip center location estimation methods minimizing anterior-posterior error be preferred. By contrast, data regarding the influence of glenohumeral joint center mislocation on upper limb inverse dynamics outcome do not exist. Nonetheless, Lempereur et al. (Lempereur et al., 2010) reported that the smallest distance error between the actual joint center obtained through medical imaging and a functional method (Gamage and Lasenby, 2002) was ~11±8 mm. The effect of shoulder center mislocation on joint kinetics is likely relatively low, in the light of Holden and Stanhope's findings on knee errors in the range ±10 mm.

9.4.7. Summary

- For the first time, we calculated shoulder mechanical load during slow aquatic scapular plane exercises.
- These were ~3–4× easier in water than on land.
- Body position dramatically alters shoulder load. Exercising sitting is relevant in very early rehabilitation stages to restore joint mobility at low mechanical solicitation. Exercising supine is restricted to more advanced rehabilitation stages since the mechanical load is overall higher.
- Scapular plane exercises when sitting were purely concentric, whereas they required rapid pre-stretch followed by concentric force production when supine. Eccentric contraction can therefore be elicited at slow speed without buoyant devices.
- This novel numerical procedure lays the foundations of a more advanced evaluation of joint load in water.

10 Shoulder joint dynamics during aquatic scapular plane exercises

Aquatic exercises are widely implemented into rehabilitation programs. However, both evaluating their mechanical demands on the musculoskeletal system and designing protocols to provide progressive loading are difficult tasks. This study reports for the first time shoulder joint kinetics and dynamics during underwater scaptions performed at speeds ranging from 22.5 to 90°/s. Net joint moments projected onto anatomical axes of rotation, joint power, and joint work were calculated in 18 participants through a novel approach coupling numerical fluid flow simulations and inverse dynamics. Joint dynamics was revealed from the 3D angle between the joint moment and angular velocity vectors, identifying three main functions—propulsion, stabilization, and resistance. Speeds <30°/s necessitated little to no power at all, whereas peaks about 0.20 $W \cdot kg^{-1}$ were seen at 90°/s. As speed increased, peak moments were up to 61× higher at 90 than at 22.5°/s, (1.82±0.12%BW·AL vs 0.03±0.01%BW·AL, P<0.038). This was done at the expense of a substantial decrease in the joint moment contribution to joint stability though, which goes against the intuition that greater stabilization is required to protect the shoulder from increasing loads. Slow scaptions (<30°/s) are advantageous for joint mobility gain at low mechanical solicitation, whereas the intensity at 90°/s is high enough to stimulate muscular endurance improvements. Simple predictive equations of shoulder mechanical loading are provided. They allow for easy design of progressive protocols, either for the postoperative shoulder or the conditioning of athlete targeting very specific intensity regions. They also reveal how sensitive load is to exercising speed, to the point that it is urgent to clearly define and control task instructions not to place the shoulder at risk.

10.1. Introduction

Aquatic therapy is a widespread modality used in early stages of shoulder rehabilitation to accelerate recovery. Yet, optimal, gradual planning of aquatic exercises is a difficult task (Colado et al., 2008; Pöyhönen et al., 2001a). Current guidelines are inferred from electromyographical (EMG) recordings of shoulder girdle muscles (Thigpen et al., 2016). Kelly et al. (Kelly et al., 2000) consistently measured lower normalized integrated EMG when performing slow to medium speed (<45°/s) underwater scaption compared to on land, whereas similar activation levels were observed between media at a speed of 90°/s. This unequivocal result led the authors to conclude that 90°/s was the threshold at which aquatic exercises turn from assisted—and *safe*—to resisted. More recently, that critical speed was reevaluated to be closer to 45°/s (Castillo-Lozano et al., 2014). The prescription of aquatic exercises remains largely uncertain.

Monitoring exercise intensity through comparison of in-water and on-land EMG is questionable. First, muscle activity inadequately estimates joint load (Winby et al., 2013). Second, the relation between EMG and muscle force is highly nonlinear (Zajac, 1989), complicating the interpretation of task mechanical requirements. Third, EMG measurements are very sensitive to experimental conditions (Veneziano et al., 2006). Last, EMG amplitude inevitably decreases at body immersion (Pöyhönen and Avela, 2002). Thus, a same level of muscle activity in water and on land might not correspond at all to the same mechanical demand. Some authors rather adopted simplified approaches centered on hydrodynamics to estimate water resistance and establish staged rehabilitation programs (Pöyhönen et al., 2001a; 2002; Tsourlou et al., 2006). For example, the first authors manually determined the leg frontal area A throughout the movement and, together with hydrodynamic coefficients C_D calculated experimentally, estimated the drag D according to the equation: $D = \frac{1}{2}\rho C_D A v^2$, with ρ, the water density and v, the velocity of the moving segment. Although this method does offer a more direct evaluation of exercise intensity, it does not capture the complexity of the fluid flow field in the vicinity of the moving limb. Furthermore, if applied at the upper limb, it likely results in a significant underestimation of the actual hydrodynamic force as lift—a major force component at the hand (Takagi et al., 2013)—is disregarded.

To noninvasively estimate the actual mechanical demands of aquatic exercises, a novel approach integrating numerical fluid flow simulations with inverse dynamics has recently been developed (Lauer et al., 2016). Pressure and shear stress distributions are integrated over the surface of the upper limb, allowing hydrodynamic forces and centers of pressure to be resolved at very high accuracy. In turn, mechanical parameters (e.g., net joint moments of force, power and work) that inform about the load on the musculoskeletal system and the way it adapts to accommodate varying mechanical demands are accessible (Lauer et al., 2017). In addition, these data constitute the basis from which to examine joint dynamics and the motor control strategy underlying the observed motion. Computing the 3D angle between the vectors of the joint moment and the angular velocity, Desroches et al. could identify the mechanical configuration the shoulder was in during manual wheelchair propulsion (Desroches et al., 2010b). The shoulder turned out to be mainly stabilized, which, although suboptimal from the viewpoint of mechanical efficiency, is favorable to maintain joint integrity. Yet, because of simultaneous periods of stabilization and force production, shoulder muscles (the rotator cuff, particularly) are believed to tire faster, which possibly accentuates the risk of shoulder injury. Their elegant approach nicely complements inverse dynamics and sheds light onto shoulder pathomechanics.

An in-depth evaluation of shoulder loading could inform aquatic rehabilitation protocol design. This is essential to understand all clinical implications and optimize treatment effectiveness. For the first time, we computed shoulder kinetics and dynamics during underwater scaptions performed at speeds ranging from 22.5 to 90°/s. We predicted that the previous EMG studies failed to identify the point at which exercises become more demanding in water than on land given that EMG measurements are unreliable indicators of a task's mechanical demands. Furthermore, because of its ball-and-socket nature and the need to provide active stabilization, we hypothesized that the shoulder would be mainly stabilized, more so at high speeds to protect the shoulder against increasing load.

10.2. Material and methods

10.2.1. Participants and numerical procedure

Eighteen volunteers (7 women: 30.8±9.6 years, 1.63±0.06 m, 58.1±9.3 kg, 21.8±3.2 BMI; 11 men: 33.1±9.0 years, 1.80±0.09 m, 76.5±13.2 kg, 23.6±2.7 BMI) provided written informed consent to participate in the study. Their upper bodies were scanned with a Mephisto 3D scanner (4DDynamics, Antwerp, Belgium). Virtual geometries were edited and converted into computer-aided design models prior to import into ANSYS® Fluent® Release 14.5 computational fluid dynamics software (ANSYS, Inc., Canonsburg, PA, USA). Seven anatomical landmarks (C7, T8, suprasternal notch, xiphoid process, right glenohumeral joint center, medial and lateral epicondyles of the humerus) were located in order to construct the thorax and upper arm coordinate systems (Wu et al., 2005). The glenohumeral joint center was determined from the least squares approach proposed by Gamage and Lasenby (Gamage and Lasenby, 2002), since this method yields the most accurate and reliable results when compared to the actual anatomical joint center obtained through medical imaging (Lempereur et al., 2013).

Scaptions at 22.5, 30, 45, and 90°/s were numerically simulated in Fluent. Upper limb models were animated with triangle waves of period 16, 12, 8, and 4 s and ranging between 0 and π in a plane oriented 30° relative to the sagittal plane. The flexible body part at the shoulder was smoothly deformed by means of our dynamic mesh algorithm to preserve mesh quality and ensure simulation convergence. The surface of the virtual models was meshed with ~40000 millimeter-scale triangular facets onto which Fluent flow solver evaluated instantaneous pressure and shear stress. The resultant hydrodynamic force was then obtained through integration over the upper limb surface.

10.2.2. Net shoulder moments, mechanical work and power computation

Weight $\mathbf{F}_w$, buoyancy $\mathbf{F}_b$, and hydrodynamic force $\mathbf{F}_{h,i}$ acting onto element i, as well as their respective points of application $\mathbf{r}_{com}$, $\mathbf{r}_{cob}$, $\mathbf{r}_i$ in the local coordinate system, were substituted in the following equation to solve for the net shoulder joint moment $\mathbf{M}_s$:

$$\mathbf{M}_S = I\boldsymbol{\alpha} - \underbrace{\mathbf{r}_{COM} \times \mathbf{F}_W}_{\mathbf{M}_W} - \underbrace{\mathbf{r}_{COB} \times \mathbf{F}_B}_{\mathbf{M}_B} - \underbrace{\sum_{i=1}^{n} \mathbf{r}_i \times \mathbf{F}_{H,i}}_{\mathbf{M}_H}, \quad (10.1)$$

with I, the moments of inertia of the upper limb and $\boldsymbol{\alpha}$, its angular acceleration. Upper limb volume (hence, Archimedes' thrust and buoyancy) and center of buoyancy location were obtained from the virtual model; upper limb mass, center of mass location and moments of inertia were estimated from scaling equations based on subject anthropometry (Dumas et al., 2007a). Net shoulder moments were projected on a non-orthogonal joint coordinate system so that they correspond to the load that muscles and ligaments must resist about each individual axis (Kristianslund et al., 2014b), and normalized to body weight times arm length (%BW·AL; (Hof, 1996)).

Instantaneous shoulder joint power was calculated as the dot product of the net shoulder moment and shoulder angular velocity vectors, and normalized to body mass. Power time series were individually integrated with respect to time over discrete periods of positive power, yielding the positive mechanical work W^+_{water} done by the shoulder musculature during a scaption. W^+_{water} was recomputed once drag and buoyancy moments subtracted to assess the positive mechanical work W^+_{land} done if the same movement were to be performed on land. The mechanical load in the water was expressed as a fraction of the load on land as follows: $W_{rel} = 100 \times \frac{W^+_{water}}{W^+_{land}}$. A value of 100% therefore indicates that an equal amount of work should theoretically be apportioned in both physical environments. Values below and above this threshold reflect load reduction and amplification, respectively.

10.2.3. Interpretation of mechanical power in 3D

Negative, null, or positive power is traditionally associated with eccentric, isometric and concentric muscle actions (Robertson and Winter, 1980). However, unlike joint moment, joint power cannot simply be decomposed into three components along the three axes of a coordinate system, as power is a scalar quantity (Dumas and Chèze, 2008). Consequently, mechanical power does not readily inform about joint dynamics, nor does it indicate the proportion of the joint moment contributing to the movement (Samson et

al., 2009). For ease of interpretation, Dumas and Cheze (Dumas and Chèze, 2008) proposed the computation of the 3D angle $\theta_{M\omega}$ between the joint moment $\mathbf{M}$ and the joint angular velocity $\boldsymbol{\omega}$ according to:

$$\theta_{M\omega} = \tan^{-1}\left(\frac{||\mathbf{M}\times\boldsymbol{\omega}||}{\mathbf{M}\cdot\boldsymbol{\omega}}\right). \quad (10.2)$$

Equation 2 returns an angle in the range [0–180°]. Recalling that joint power P equals:

$$P = ||\mathbf{M}||\,||\boldsymbol{\omega}||\cos\theta_{M\omega}, \quad (10.3)$$

Dumas and Cheze (Dumas and Chèze, 2008) identified three angular intervals of interest. When $\theta_{M\omega}$ is in the interval 0–60° (i.e., $\cos\theta_{M\omega}>0.5$), it follows from Equation 3 that more than 50% of the joint moment contributes to positive joint power: the joint is in a propulsion configuration. When $\theta_{M\omega}$ is in the interval 60–120° (i.e., $|\cos\theta_{M\omega}|<0.5$), less than 50% of the joint moment contributes to either positive or negative power: the joint is in a stabilization configuration. Finally, when $\theta_{M\omega}$ is in the interval 120–180° (i.e., $\cos\theta_{M\omega}<-0.5$), more than 50% of the joint moment contributes to negative joint power: the joint is in a resistance configuration. It can be noted that for a given set of $\mathbf{M}$ and $\boldsymbol{\omega}$, P is maximal only when both vectors are aligned ($\theta_{M\omega}=0$ or 180°); i.e., when 100% of the mechanical action at the joint translates into movement.

10.2.4. Statistical analysis

All variables were checked for normality with the Shapiro–Wilk test. Group means, standard error of the means, and 95% confidence intervals were computed. Prior to ANOVA, sphericity was verified using the Bartlett's test. One-way repeated measures ANOVAs were used to detect any main effect of angular velocity on shoulder peak moments and mechanical work. Provided that a significant effect was found, post hoc pairwise comparisons using Tukey's HSD were conducted. Omega squared ω^2 were computed to provide an unbiased estimate of effect size (Levine and Hullett, 2002). A ω^2 less than 0.06 was classified as small, 0.07–0.14 as moderate, and >0.14 as large (J. Cohen, 1988). Statistical tests were run in R 3.4.0 (https://www.R-project.org/), with a level of significance of 0.05.

10.3. Results

10.3.1. Curve fitting and predictive equations of shoulder mechanical work

Positive mechanical work done on land during scapular plane exercises was a linear function of subject's body mass (r^2=0.93, P<0.001; Fig. 10–1A). Data of shoulder mechanical load expressed as a fraction of that on land were almost perfectly modeled by second-degree polynomial fits (r^2=0.99, P<0.001; Fig. 10–1B). A one-way repeated measures ANOVA revealed a significant main effect of the angular velocity on shoulder mechanical work (F=276.65, P<0.001, ω^2=0.96). Post-hoc pairwise comparisons indicated that mechanical work was significantly higher at 45 and 90°/s than at the previous speeds (P<0.0013). Exercising in water became mechanically harder than on land at 85°/s.

10.3.2. Shoulder joint kinetics

Moments about the axes of internal/external rotation and adduction/abduction were very low to null (<0.5%BW·AL), whereas moments about the flexion/extension axis were much higher (Fig. 10–2). Angular velocity had a main effect on peak flexion moments (F=74.72, P<0.001, ω^2=0.83). Peak flexion moments significantly increased from 0.03±0.01%BW·AL up to 1.82±0.12%BW·AL at 90°/s (P<0.038; Fig. 10–3). Shoulder mechanical power, the dot product of net joint moment and angular velocity vectors, is plotted in Fig. 10–4A. Power was close to null (<0.001 W·kg^{-1}) at 22.5°/s and positive at higher speeds, with peaks slightly above 0.20 W·kg^{-1} at 90°/s.

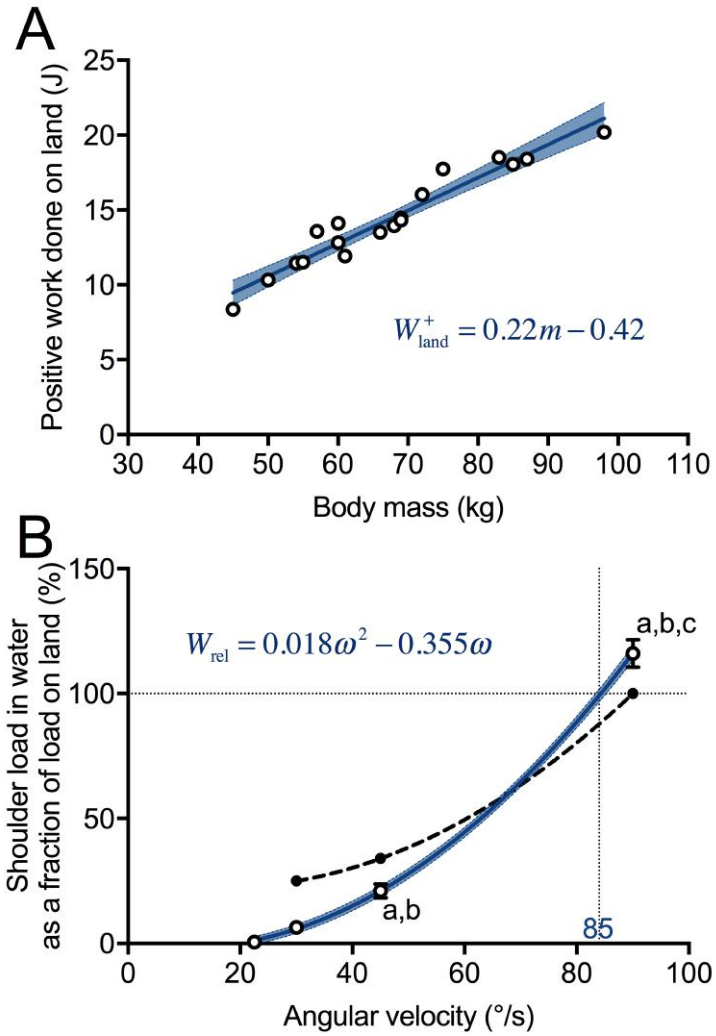

Figure 10–1. (A) Mechanical work produced during scaption on land against subject's body mass. The positive work done can be accurately predicted by a linear regression (r^2=0.93, P<0.0001). (B) Plot of the shoulder load in water expressed as a fraction of the load during the same movement performed on land versus angular velocity. A second-degree polynomial fit perfectly modeled the data (r^2=0.99, P<0.0001). The dashed black trend was extrapolated from EMG data in (Kelly et al., 2000). Points at 30 and 45°/s were taken as the ratio between their underwater and dry EMG measurements. The horizontal dotted line denotes the threshold at which the shoulder musculature produced an equal amount of work regardless of the medium; values below and above respectively reflect load reduction and load amplification. The vertical dotted line at ω = 85°/s marks the speed at which exercising in water became mechanically harder than on land. Blue areas are 95% confidence bands. [a,b,c] Significantly higher than very slow, slow and medium speeds.

10.3.3. Shoulder joint dynamics

Notable differences in joint function were apparent thanks to the computation of the 3D angle $\theta_{M\omega}$ between the vectors of joint moment and angular velocity (Fig. 10–4B). At 22.5°/s, resistance and stabilization configurations respectively occupied 41 and 59% of the scaption duration, as displayed by the frequency plot (Fig. 10–4C). Distributions shifted to the left as speed increased. That is, the shoulder joint became stabilized at 30°/s, and mainly driven at 45 and 90°/s during >90% of the scaption, with the joint moment contributing to 87% of the positive power ($\theta_{M\omega}$=135°).

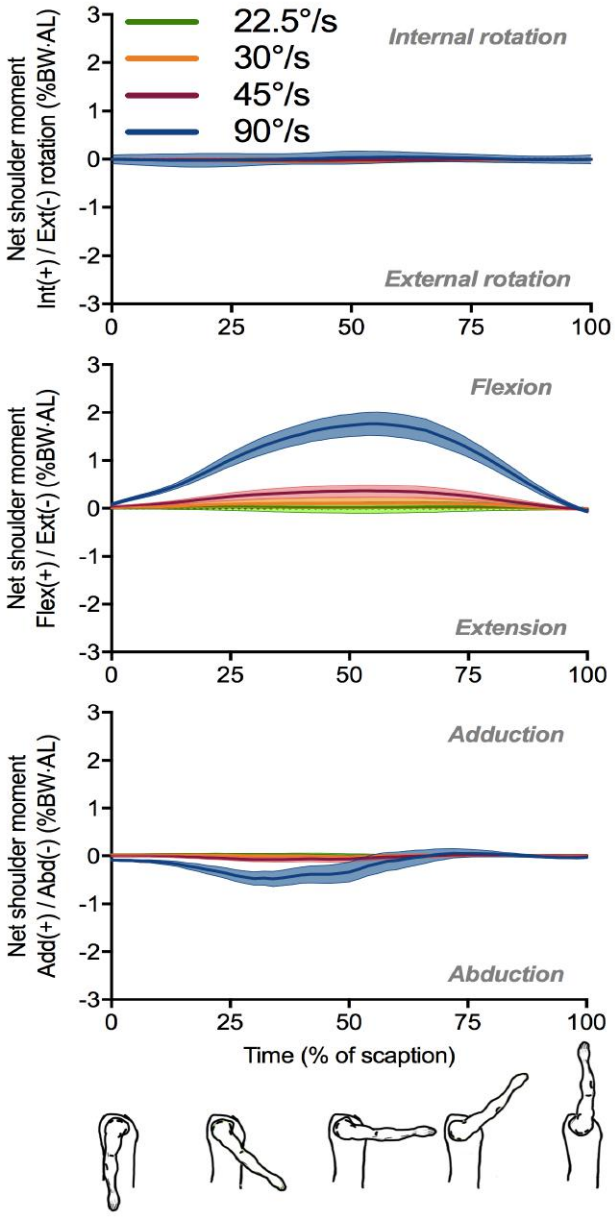

Figure 10–2. Net shoulder joint moment as a function of time when performing at 22.5, 30, 45 and 90°/s. Moments were projected on a non-orthogonal coordinate system so that joint moment components correspond to the load that muscles and ligaments must resist about the axes of internal/external rotation (top), flexion/extension (middle), and adduction/abduction (bottom). Data are presented as means (thick lines) and 95% confidence bands (filled area).

10.4. Discussion

This is the first study to report a thorough inverse dynamics analysis of the upper limb during an exercise done in water. Joint moments and joint work prove essential and unequalled quantities in the evaluation of a task's mechanical demands and in the perspective of informed rehabilitation protocol design. Additionally, joint power and the 3D angle $\theta_{M\omega}$ shed a new light onto joint dynamics and a potentially harmful tradeoff between joint stabilization and force production towards medium to high speeds.

10.4.1. Mechanical demands of underwater scaption

We found scaption to become more demanding in water than on land at a speed of 85°/s. This is close to the estimation of 90°/s made by Kelly et al. (Kelly et al., 2000) from EMG recordings of shoulder muscles, hence invalidating our first hypothesis. Nonetheless, Castillo-Lozano et al. more recently predicted a much lower threshold of 45°/s (Castillo-Lozano et al., 2014). They had proposed, accordingly, a rehabilitation protocol whereby exercises were implemented at that speed indifferently in water or on land, although we predict shoulder musculature to apportion 5× more work on land. The divergence in trends in Fig. 10–1 further challenges the soundness of the rationale behind the assessment of a task's mechanical requirements based on EMG alone. On the contrary, the computation of joint work provides a robust criterion of an exercise demand on the musculoskeletal system and, as such, is a great candidate to avoid premature conclusions and inform clinical decision-making process.

Shoulder joint work scaled with the square of angular velocity. As a result, the first is markedly altered with subtle changes in the latter. As a matter of fact, just a 10% increase in angular velocity would result in a ~25% increase in joint load. This urges the need to check movement speed with the greatest care when prescribing aquatic exercises. Practitioners might resort to the use of wearable aquatic accelerometers and audio-biofeedback, or blinking lights such as those providing swimming pace, to finely control speed and correct deviations in real time.

10.4.2. Joint moments and shoulder loading

Net shoulder moments of flexion/extension were largely dominant while exercising in the scapular plane. Shoulder flexors and extensors were therefore the muscle groups contributing the most to task mechanical demands, regardless of speed. Very low to null moments of internal/external rotation and adduction/abduction support the idea that exercising in the scapular plane is mechanically advantageous. Peak flexion moments measured here at 22.5°/s were equivalent to <1% of the maximum isokinetic concentric torque of flexion in untrained, healthy individuals (Mayer et al., 1994), whereas they reached ~20–25% at 90°/s. According to ACSM's guidelines for exercise prescription (Garber et al., 2011), this intensity is sufficient to improve muscular endurance in adults, and power in older adults. Exercises at that speed are therefore highly discouraged in frail patients and during initial stages of aquatic therapy. Inferior speeds must be favored for early mobilization at low mechanical solicitation and joint mobility gain.

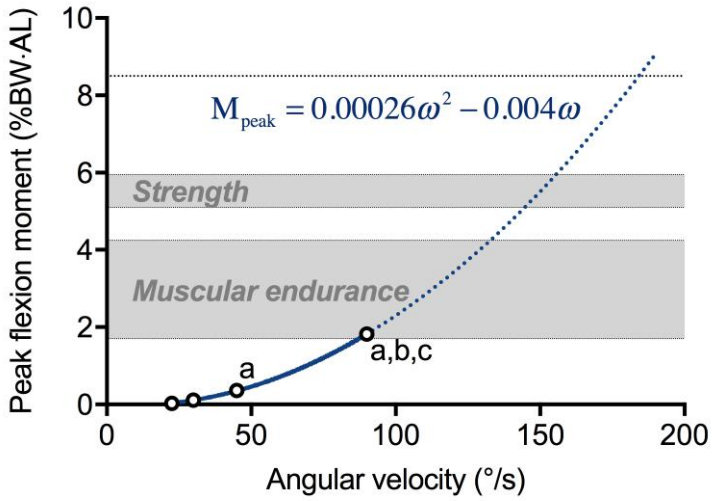

Figure 10–3. Normalized peak flexion moment as a function of angular velocity. The quadratic curve fit (r^2=0.99, P<0.0001) is represented by the solid blue line. Peak moments were extrapolated beyond 90°/s (dotted blue line). The horizontal dotted line represents the maximal isokinetic flexion moment in a population of 32 healthy, untrained men (Mayer et al., 1994). We used an average acromion-to-fingertip distance of 0.70 m to normalize their results. For illustration purposes, intensity regions promoting improvements in muscular endurance (20–50% of the maximum) and strength (60–70%) were shaded in grey (according to (Garber et al., 2011)). [a,b,c] Significantly higher than very slow, slow and medium speeds.

Our predictive equation is relevant to the framework of aquatic resistance training. In contrast to the freshly operated patient for whom indirect kinetic evaluation from data in

the literature is necessary, a healthy individual's maximal moments can be directly measured with an isokinetic dynamometer. This way, intensity regions are individualized. Consider a subject (mass *m*: 70 kg; arm length AL: 0.70 m) tested with a maximal shoulder flexion moment M_{max} of 50 N·m. One wants to predict the speed at which he needs to move his arm in the water to promote improvements in strength (target intensity of 70% of his maximal capacity). The necessary variables can now be substituted into the following equation to solve for ω:

$$\omega = \frac{0.004 + \sqrt{0.000106 \frac{M_{max} \cdot target}{m \cdot AL}}}{0.00052}, \quad (10.4)$$

which yields a required training speed of 175°/s. Naturally, graded therapeutic exercises can be planned following the same procedure, with great control over the exercise intensity. For example, if one were to design a protocol for the postoperative shoulder whereby loading smoothly increases from 2% of the maximum value (42 N·m) reported in Mayer et al. (Mayer et al., 1994) to 10% by increment of 2, one would readily come up with the required speeds of 34, 44, 53, 60, and 66°/s. Unlike EMG, the peaks of moments projected onto the axes of a non-orthogonal joint coordinate system correspond to the maximal instantaneous load that muscles and ligaments must resist. Thus, in addition to the mechanical work produced by the shoulder musculature, peak moment is a second ideal candidate to inform rehabilitation protocol design, predict dose-response relationships, establish safety thresholds, and share and compare aquatic rehabilitation protocols.

10.4.3. Shoulder joint dynamics

Shoulder joint power was positive at all speeds but the slowest, indicating that scaptions were either fully passive or eliciting concentric muscle actions. However, the examination of joint moments and mechanical power alone is not sufficient to investigate the extent to which the net mechanical action of all structures crossing the joint induces movement. It may very well be that a great part of it translates into joint stabilization because of how vectors are oriented in space, which is invisible on moment or power curves. The calculation of the 3D angle $\theta_{M\omega}$ between the joint moment and the joint angular velocity

vectors addresses such issue, and directly reflects the proportion of the joint moment that goes into either driving or stabilizing the joint.

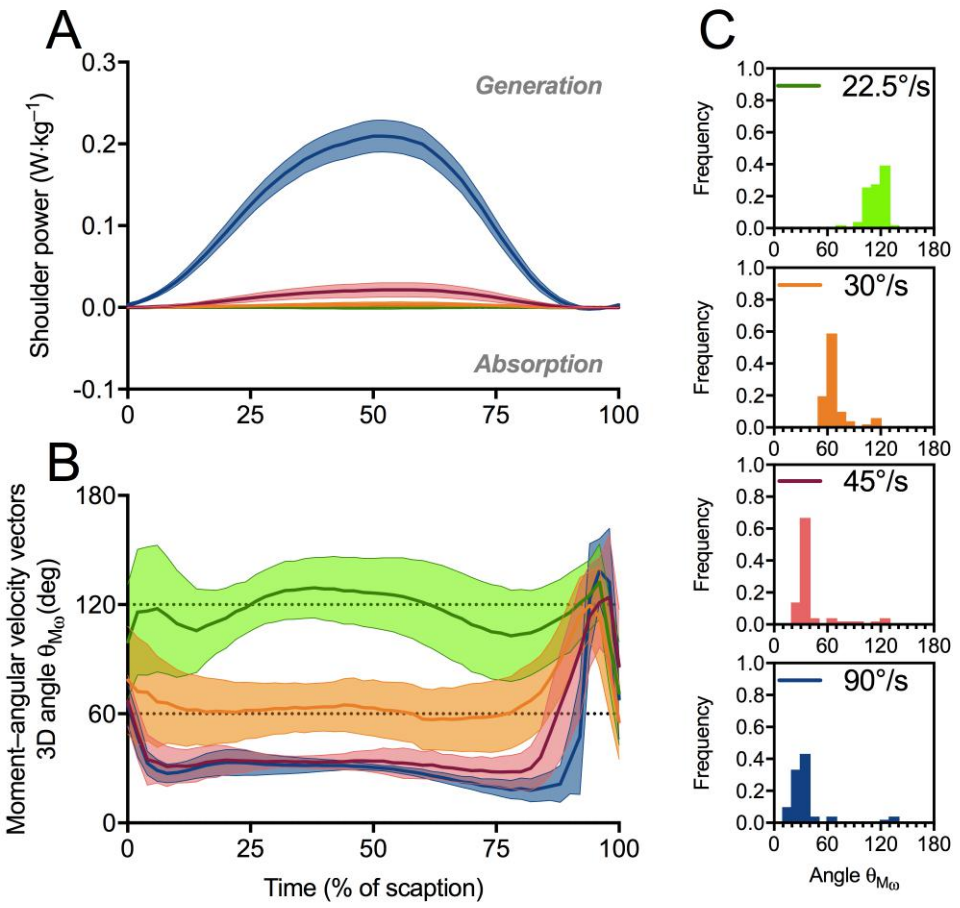

Figure 10–4. (A) Instantaneous shoulder joint power at four speeds. The absorption of energy through eccentric contraction (negative power) was insignificant, in contrast to the generation of energy through concentric contraction (positive power). (B) Instantaneous 3D angle $\theta_{M\omega}$ between the net shoulder moment and angular velocity vectors. Three joint configurations are identified: propulsion in the range 0–60°; stabilization in the range 60–120°; resistance in the range 120–180°. The closer the angle is to 0 and 180°, the more the joint is driven; i.e., the higher the proportion of the joint moment that contributes to the power. (C) Frequency plots representing the distribution of the 3D angle values. As speed increases, there is a marked shift from stabilization to propulsion. Bins are 10 degrees wide. All bar heights sum to 1.

Regardless of the exercising speed, $\theta_{M\omega}$ was bounded between 30 and 135°. Consequently, the shoulder was never fully driven (i.e., $\theta_{M\omega}$ never reached 0 or 180°). This seems to be a general principle of human motion (Desroches et al., 2010b; Dumas and Chèze, 2008; Samson et al., 2009) that is produced by a redundant musculoskeletal system. The shoulder, particularly, is a very complex structure. Each muscle will not only generate joint moments to meet external forces, but also considerable undesired joint

moment components, which must in turn be compensated by other muscles (Veeger and van der Helm, 2007), such that a fraction of the net joint moment is inevitably apportioned to other than pure motor-like actions.

One such action is to ensure joint stability. Yet, the shoulder was in a stabilization configuration only at speeds <30°/s. As speed increased, periods of stabilization were greatly reduced, ultimately representing <10% of the cycle duration at 90°/s. In other words, shoulder moment contribution to joint stability diminished toward the highest speed, which is counter-intuitive given the inherently unstable ball and socket nature of the shoulder joint (Lugo et al., 2008; Veeger and van der Helm, 2007). We therefore rejected our second hypothesis. Hydrodynamic force increases dramatically at high speeds, hence its dominating action in the plane of movement must necessarily be balanced by a greater fraction of joint moment that is directed perpendicular to that plane; i.e., closer to angular velocity vector alignment. This tradeoff between stability and production of force might however be harmful, as stabilization is crucial to preserve joint integrity (Lugo et al., 2008). We therefore propose that speeds >30°/s be avoided in patients with unstable shoulders regardless of tissue healing stage.

10.4.4. Conclusion

Examining aquatic movement under the light of inverse dynamics offers unprecedented insight into its mechanics. Despite its apparent simplicity, underwater scaption reveals very complex dynamics at the shoulder joint. Low speeds must be favored for joint mobility gain at low mechanical solicitation. As speed increases, intensity becomes likely sufficient to stimulate muscle function enhancement, though at the expense of decreased moment contribution to joint stability. This tradeoff between stability and production of force might however be harmful and warrants cautious prescription. Shoulder mechanical loading proves highly sensitive to exercising speed, to the point that it is urgent to clearly define and control task instructions not to place the shoulder at risk. This novel numerical approach paves the way towards a more rigorous approach to aquatic rehabilitation protocol design and a deeper understanding of the associated clinical implications.

11 General discussion and conclusion

11.1. Summary of core contributions

The present thesis was aimed at developing novel numerical tools allowing the use of inverse dynamics and the assessment of joint mechanics and internal load during movements performed in water. We began by implementing algorithms derived from computer graphics to realistically animate virtual models for unsteady numerical fluid flow simulations (Chapter 6). This was the absolute precondition before conducting an inverse dynamics analysis and gain access to otherwise inaccessible kinetic quantities. The accuracy of hydrodynamic force computation was very high, yielding errors <2% between the calculated impulse and the impulse that had to be theoretically imparted by the arms on the water to produce sufficient lift. Joint resultant forces were about 5% of subject's body weight, which is similar to the internal load during walking in shallow water (Orselli and Duarte, 2011). This also corresponded to a 2–7-fold reduction in shoulder loading with respect to dry-land upper limb activities (such as slow walking with crutches [~35% (Slavens et al., 2010)] or wheelchair locomotion [~10% (Gil-Agudo et al., 2010)]). We provided the first quantitative mechanical evidence for the benefits of upper limb aquatic therapy on weakened musculoskeletal system. Moreover, we observed both a proximo-distal and disto-proximal sequencing of joint moment peaks within a cycle. The first is a fundamental motor control strategy of healthy biological systems to produce power, whereas the second had surprisingly never been observed at the upper limb before. During on-land locomotion, a disto-proximal organization of moment peaks may function as a strategy of stiffness regulation to provide a distal, compliant interface with the environment and facilitate energy absorption by larger proximal muscles

(Nichols et al., 2016). We hypothesized that aquatic environment instability may be sensed distally at the hand and forearm, and that perhaps the disto-proximal sequencing of peak net joint moments contributes to damp the perturbations. We established through this study a significant departure from what had been published in the literature, estimating for the first time joint kinetics in water, and paving the way towards new insights into 'competitive' and 'therapeutic' aquatic movement mechanics.

Armed with that new tool, we answered fundamental questions regarding the way the human musculoskeletal system accommodated increasing mechanical demands in water (Chapter 7). Such tasks, unlike level terrestrial locomotion, required net positive work to be continuously apportioned by the upper limbs to replace the energy lost against the dissipative load of the water. Muscles crossing the shoulder and elbow apportioned >97% of the upper limb total work, consistent with the proximo-distal gradient of work performance in the limbs of terrestrial animals for which evolutionary pressures favored work modulation by large muscle masses located proximally (Biewener and Daley, 2007). However, no proximal redistribution of work was observed across a threefold increase in load. Surprisingly, it had only been observed previously on land during tasks necessitating no net work. This suggested that a task's mechanical requirements are a rather poor predictor of the strategy employed to meet them, and perhaps complex human movements are controlled modularly regardless of physical environment and moving limb. Modularity in motor control has gained increasing support in the past ten years after its first demonstration in frog hindlimb movements (Tresch et al., 1999), and is believed to originate from ancestral neural networks of command (Lacquaniti et al., 2013). EMG recordings would have been required to test the assumption that modules were more and more activated, resulting in proportional increases in mechanical work at all joints. We had also found very negligible negative joint power (<3.5% of the total generated power), indicating little to no dissipation or storage of energy in anatomical structures. In line with previous modeling studies of animal musculoskeletal system, we brought convincing evidence against the usefulness of elastic mechanisms in aquatic locomotion, such that performance is directly limited by the maximal work and power theoretically available from muscle mass alone. At maximal effort though, joint work and power were found to be up to 8 times less than the estimated capacity of rapidly contracting striated muscle (Weis-Fogh and Alexander, 1977), suggesting a severe

limitation to human upper limb performance in water likely due to poor morphological design.

Understanding how power is produced at a joint level would not offer a complete kinetic picture without deeper insight into the complex interaction between the water and one's arm. In Chapter 8, we challenged the longstanding idea that internal and external works were two independent mechanical costs in water. Specifically, total mechanical work had traditionally been computed as the sum of the external work done on water and the internal work to accelerate and the appendages relative to the body center of mass, in water just as on land. Yet, several studies argued against such definition on land because, despite the irrefutable existence of a metabolic equivalent of internal work, both mechanical costs are intimately linked to each other. In other words, part of the internal work results in the production of external work too. Although challenged once, this idea had never been strictly tested in water. Thanks to inverse dynamics and unsteady fluid flow simulations, all the required power time series could be computed to investigate the transfers of energy from the muscles to the limb, and from the limb to the water. Internal work measures, based on kinematics and the calculation of segmental mechanical energies, were found not to be correlated with the work done in excess of the external work. Furthermore, segment deceleration was not associated with negative joint power as imagined by David Winter back in 1979, but rather actively achieved by muscle concentric action and the transfer of energy to the water. In other words, production of external power was not simply achieved by accelerating the upper limb as commonly understood; kinetic energy from active deceleration as well was reconverted into significant amount of work imparted to the water. We imagined a potential mechanism analog to cycling in order to explain how energy may flow towards the extremity. Although purely hypothetical at that stage, muscles might act not only to produce forces on the water but also corresponding joint reaction forces decelerating upper limb segments, eventually leading to distal energy flow and extra work production. Concluding that internal work was an integral part of external work, strong arguments against the view traditionally adopted in the fields of energetics and biomechanics of aquatic locomotion were provided. A revision of the energy cascade was proposed, suggesting that traditional measures of internal work should be abandoned.

We extended the richness of inverse dynamics to aquatic rehabilitation. This was partly motivated by requests from healthcare professionals who acknowledge the fact that assessing joint load was crucially needed to guide their practice. As a very first step in that direction, we chose to provide a full picture of shoulder kinetics during scapular plane aquatic exercises performed at 30°/s (Chapter 9). Exercising in water was found to be ~4× less demanding than on land at the same speed, yet changing body position could sensibly alter shoulder mechanical demands. During arm elevation, shoulder load more than doubled when supine vs sitting, whereas no differences were seen during arm lowering. This suggested that considering buoyancy action alone to make an educated guess about shoulder loading is misleading, and more complex interaction between all external forces must be taken into account. When sitting, exercises were achieved through purely concentric muscle actions whereas eccentric contractions likely occurred when supine, unveiling unprecedented insight into muscle function in water. This also meant that short eccentric contractions could in principle be achieved in water without the use buoyant devices. In addition, shoulder flexors and extensors were prime movers, unlike previous EMG findings identifying rotator cuff muscles as the most activated; hence EMG is hardly reliable to predict the most highly loaded muscle groups.

Yet, therapeutic aquatic exercises are part of a continuum of exercises that span the entire rehabilitation process. Therefore, the way load can be manipulated and what are the associated clinical implications is just equally important. In Chapter 10, we examined the extent to which varying exercising speed altered shoulder mechanical demands. Mechanical work done at the shoulder increased quadratically with speed: as a result, a subtle 10% increase in speed yielded a ~20% increase in load. Straightforward predictive equations were devised to provide clinicians with a simple access to shoulder load estimation, so that aquatic exercise intensity can easily be expressed relative to its equivalent on a dynamometer. The analysis of joint dynamics revealed a counter-intuitive mechanical behavior as exercising speed increased, where the contribution of shoulder moment to joint stability significantly diminished at the expense of improved force production. This unsuspected trade-off might be harmful, and asks for an update of the established guidelines. Together, these two last studies demonstrated that empirical approaches cannot hold, and encouraged a more scientifically based examination of aquatic rehabilitation exercises.

11.2. Future work

Overall, this thesis aspired to be a collection of pioneering works exploring aquatic movement mechanics under a new light. As the use of inverse dynamics in water will grow, a systematic evaluation of the potential source of errors and their associated effect on inverse dynamics outcome will be necessary. However, we do believe it is too early for sensitivity analyses, and acceptance towards numerical simulations must be gained first. Things have previously gone through a similar 'cycle' on land. If we disregard the pioneering work from Elftman (Elftman, 1939) and consider only the works from Morrison (Morrison, 1970) or Winter and colleagues in the 1970s (Quanbury et al., 1975; Winter et al., 1976) as those that initiated the adoption of inverse dynamics in many laboratories, that is still a ~20-year lag before the first attempts to understand individual modeling uncertainties (e.g., Holden and Stanhope, 1998; McCaw and DeVita, 1995; Pearsall and Costigan, 1999), and ~30 years before comprehensive reports (e.g., Riemer et al., 2008). We will be working on a 6 DOF validation of our simulations; that is, using only front crawl kinematics and no prescribed flow velocity at the inlet of the computation domain, forces will be computed through CFD and instantly fed into the balance equation to update center of mass kinematics (in a manner conceptually akin to (Richards, 2008)). We believe that a comparison of predicted swimming speed with experimental data is the ultimate accuracy test and will help spot model failure.

Inverse dynamics was demonstrated to provide answers to fundamental issues of aquatic biomechanics, but it raises just as many new questions (mainly left unanswered because of inevitable modeling limitations) that will only find answers with musculoskeletal modeling. One of them is the issue of joint force *stricto sensu*. More realistic estimates of joint loading require the knowledge of muscle forces. Indeed, they are acknowledged to produce knee joint loading over 3× body weight during human gait (Taylor et al., 2004). Muscle forces computation was first approached through simplified model of the knee (e.g., Schipplein and Andriacchi, 1991). Yet, we now know that muscles located at different joints (the gluteus maximus and soleus) also significantly contribute to knee contact force through their contributions to the ground reaction forces (Sasaki and Neptune, 2010). Furthermore, upper limb geometry, and the shoulder particularly is highly complex (van der Helm, 1994). Dissecting what truly happens at the shoulder

beyond the simplified thoracohumeral joint require musculoskeletal models. They are mandatory to overcome the kinematic incompatibility between the real anatomy of the system and its virtual analog. Now that the necessary inputs can be computed through inverse dynamics (principally, hydrodynamic forces, the respective centers of pressure, and net joint moments), we will explore this possibility with OpenSim and a novel, advanced biomechanical model of the scapulothoracic joint that has just recently been published (Seth et al., 2016). This simulation framework augurs very well for our understanding of upper limb pathologies (notably swimmer's shoulder etiology) and the clinical implications of current aquatic rehabilitation protocols on rotator cuff musculature. Additionally, it can elucidate the fundamental principles of muscle coordination, evaluate the loading of individual anatomical structures, identify the sources of abnormal movement identified, etc. (Seth et al., 2011).

Fluent is a commercial software solution requiring a user license. This is not quite compatible with OpenSim and the idea of having a freely available pipeline. We will envisage two solutions to turn our research open to a wider audience. A Fluent server session could be accessed through a remote console, and allow a researcher to benefit from our coupled CFD and inverse dynamics code. Fluent technical documentation however warns that only one client connection to the remote machine at a time is supported. Alternatively, the entire workflow could be ported in C++ to OpenFOAM, which is, as its name suggests, an open source CFD package. It possesses an incredible amount of features, and would perfectly fit in that open-to-all perspective. It is much less user-friendly than Fluent though, and the learning curve is steeper. But that is surely a fair price to pay to foster the research activities on aquatic locomotion biomechanics.

11.3. Perspectives

Recalling what inverse dynamics has brought to our understanding of terrestrial locomotion mechanics since its very early use, it is exciting to imagine what is left to be discovered with respect to movements in water. Perhaps an effort towards markerless motion capture may prove valuable to popularize the present analysis to various field measurements, either competitive events or tracking several patients simultaneously in balneotherapy pools. Algorithms for markerless motion analysis had first been developed

in the context of the biomechanical analysis of human gait by Corazza et al. (Corazza et al., 2006), based on the concept of 'visual hull' (first described twelve years earlier) that approximates the volume occupied by an object. Lower limb joint and shoulder 3D kinematics were in good agreement with true kinematics (slightly less so about thigh and shank internal/external rotation because of the high degree of axial symmetry makes them noise-sensitive; mean errors of ~5). There are important advantages to markerless motion capture. First, skin motion artifact is severely reduced since few hundreds points per segment are tracked, naturally averaging noise across the segment. Second, a lesser amount of time is devoted to subject preparation, which also eliminates inter-operator variability due to different marker placement. Their original algorithm was patented in 2010. To further validate the system for clinical applications, Ceseracciu et al. (Ceseracciu et al., 2014) critically examined the performance of markerless and marker-based technologies simultaneously. Best results were found at the knee along flexion–extension, with an average RMS error of ~12 deg, corresponding to ~18% of knee range of motion. Estimates along the internal–external rotation dimension, particularly at the hip, showed however very large errors: ~90% at the ankle, up to ~130% at the hip. The authors concluded that the level of accuracy and robustness is still insufficient for use in clinical studies, warranting additional work to improve system accuracy. The same team had refined this technology for the motion analysis of swimmers (Ceseracciu et al., 2011), which conveniently deals with the restricted space available for cameras in small pools. The presence of bubbles around the arms complicated the kinematical reconstruction of arm pose in some subjects. RMS errors at the wrist were of the order of ~5±2 cm, and propagated proximally to the shoulder, with exacerbated errors of up to 14 cm along the antero-posterior dimension. This was due to 'phantom volumes' close to the surface being attributed as pertaining to the subject. While underwater markerless analysis is promising for the study of gross swimming technique, errors this large are critical for the identification of joint centers, and prevent, for the time being, its use jointly with inverse dynamics.

Because of water physical properties, shoulder load was found to increase steeply with (the square of) movement speed. This urges the need to control movement speed with the greatest care, possibly through the development of devices providing visual or auditory bio-feedback to the patient for instantaneous movement correction. Similar devices had been used in swimming to improve propulsion, by providing real time

auditory feedback about pressure at the palm of the hand and intracycle speed fluctuations (e.g., Chollet et al., 1988; 1992; Svec, 1982). It can easily be imagined that, with the advent of in-water inertial measurement units, patients could be similarly informed about the speed at which they move their arms, which would provide greater control over task instructions. Technological development is not only limited to such devices. In silico investigations of joint load also provides a framework for parametric studies testing the influence of varying the positioning of resistive or buoyant devices. As a matter of fact, we have seen that the moment exerted by a force about an axis of rotation, more than the force itself, dictates the mechanical requirements of a task. Therefore, the distance at which a device is positioned relative to the joint center has the highest impact on shoulder loading. There is definitely large room for improvement, and deepening our understanding of aquatic movement mechanics is expected to drastically reshape the way aquatic rehabilitation protocols are designed nowadays.

It is well documented that muscle activity recordings amazingly complement inverse dynamics analysis. For the specific purpose of investigating strategies of power modulation, for example, EMG data could tell us whether the observed changes in net joint moments resulted from the recruitment of different, synergistic muscles, or whether the same muscles were recruited at different intensities. Inverse dynamics is limited to an idealized representation of the structures crossing a joint, and thus does not inform us about what occurs at the muscle level. As discussed in our second study, EMG measurements ease our interpretation of muscle function. This is very true for biarticular muscles, the action of which may be confounded by net joint moment during inverse dynamics analysis. For instance, net ankle joint moment was found to decrease during single-leg squat at 24 vs 16° decline angle, whereas integrated EMG of the gastrocnemius concomitantly increased (Richards et al., 2008). This was due to the dual action of the gastrocnemius in the control of the anterior translation of the knee, which is not apparent at the ankle moment. Erroneous clinical conclusions (i.e., lesser mechanical effort at the ankle) may be drawn in such cases. On top of that, EMG has the potential to unveil muscle synergies, and relate to fundamental biomechanical tasks and how these are achieved under various conditions. During walking, for example, there is compelling evidence for a link between control modules and specific biomechanical subtasks (i.e., body support, forward propulsion, leg swing; Allen and Neptune, 2012). Such an analysis would allow us to distinguish muscle contributions to "useful", "wasted" propulsion, and

balance during swimming, with the ultimate goal of understanding how the execution of these biomechanical subtasks is altered with pain, load, fatigue, or expertise.

In the era of large datasets and sophisticated statistical analyses, biomechanical knowledge is expected to advance at increasingly faster rate (Ferber et al., 2016). This trend is accompanied by the rapid expansion of supercomputers, and the quest for providing clinicians with almost instantaneous feedbacks. In that context, numerical fluid flow simulations do not get even close to that 'real time' goal because of the extreme amount of computational power required. A question then arises: what are the levels at which substantial speed gain can be achieved without compromising solution accuracy? Perhaps the great resolution offered by scans is not needed, and an upper limb may be more practically modeled as geometrical shapes that could be meshed using coarser grids. An intermediate step would be to collect subject's anthropometrics and create a virtual, realistic character with the corresponding dimensions (e.g., by using MakeHuman free software solution). Accuracy of these simplified approaches could be evaluated on the basis of limb hydrodynamic coefficients and net joint torque to examine whether errors propagate and to what extent. Bypassing the need for an expensive 3D body scanner setup and the cumbersome geometry preprocessing would entail a significant reduction in the overall processing time.

In addition to geometric simplification, perhaps most gain can be achieved by approximating the fluid flow rather than attempting its accurate resolution. A very recent work presented at the International Conference on Knowledge Discovery and Data Mining 2016 achieved a significant step in that direction (Guo et al., 2016). The authors reported the use of a data-driven surrogate model based on convolutional neural networks to predict a 3D non-uniform steady laminar flow (Re = 20). This technique comes from supervised machine learning, and proved successful and very memory-efficient in geometry representation learning and per-pixel prediction in images. In short, their model builds a geometrical representation of a given shape from a signed distance function sampled on a Cartesian grid. Velocity fields on the same grid were computed through CFD. The neural networks were trained with a set of geometrical primitives and the corresponding flow fields (channel dimension: 32×32×32, N = 400,000). Results were obtained two orders of magnitude faster than traditional CFD solvers, with difference between the predicted velocity field and the one generated

through CFD of <3% on average. This is very promising for the prediction of higher Reynolds number flows, as those around human upper limbs. We can imagine a similar machine learning architecture predicting the pressure at a subset of points on a body surface, hence the hydrodynamic forces and inputs to inverse dynamics analysis.

References

Agence Technique de l'Information sur l'Hospitalisation. URL http://www.atih.sante.fr (accessed 5.8.17).

Aguinaldo, A.L., Chambers, H., 2009. Correlation of throwing mechanics with elbow valgus load in adult baseball pitchers. Am J Sports Med 37, 2043–2048.

AIAA, 1998. Guide for the Verification and Validation of Computational Fluid Dynamics Simulations G-077-1998. American Institute of Aeronautics and Astronautics, Reston, VA.

Aleshinsky, S.Y., 1986a. An energy 'sources' and "fractions" approach to the mechanical energy expenditure problem--I. Basic concepts, description of the model, analysis of a one-link system movement. J Biomech 19, 287–293.

Aleshinsky, S.Y., 1986b. An energy 'sources' and "fractions" approach to the mechanical energy expenditure problem--II. Movement of the multi-link chain model. J Biomech 19, 295–300.

Alexa, M., 2002. Linear combination of transformations. ACM Transactions on Graphics (TOG) 21, 380–387.

Alexander, R.M., 2002. Tendon elasticity and muscle function. Comp. Biochem. Physiol., Part A Mol. Integr. Physiol. 133, 1001–1011.

Alexander, R.M., 1997. Optimum muscle design for oscillatory movements. J. Theor. Biol. 184, 253–259.

Allen, J.L., Neptune, R.R., 2012. Three-dimensional modular control of human walking. J Biomech 45, 2157–2163.

Anderson, E.J., McGillis, W.R., Grosenbaugh, M.A., 2001. The boundary layer of swimming fish. J Exp Biol 204, 81–102.

Anderson, J.D., 2009. Governing Equations of Fluid Dynamics, in: Wendt, J.F. (Ed.), Computational Fluid Dynamics, Computational Fluid Dynamics. Springer Berlin Heidelberg, Berlin, Heidelberg, pp. 15–51.

Anderson, J.D., 2005. Ludwig Prandtl's Boundary Layer. Physics Today 58, 42–48.

Anjyo, K., Lewis, J.P., Pighin, 2014. Scattered data interpolation for computer graphics 1–69.

ANSYS, Inc, 2012. ANSYS Fluent Release 14.5, Help System, ANSYS Fluent User's Guide.

Arellano, R., 1999. Vortices and Propulsion, in: Sanders, R.H., Linsten, J. (Eds.), Applied Proceedings of the XVII International Symposium on Biomechanics in Sports: Swimming. School of Biomedical and Sports Science, Edith Cowan University, Perth, Western Australia, pp. 53–65.

Arnold, A.S., Lee, D.V., Biewener, A.A., 2013. Modulation of joint moments and work in the goat hindlimb with locomotor speed and surface grade. J Exp Biol 216, 2201–2212.

Astley, H.C., Roberts, T.J., 2012. Evidence for a vertebrate catapult: elastic energy storage in the plantaris tendon during frog jumping. Biol. Lett. 8, 386–389.

Audu, M.L., Kirsch, R.F., Triolo, R.J., 2007. Experimental verification of a computational technique for determining ground reactions in human bipedal stance. J Biomech 40, 1115–1124.

Azevedo, L.F., Costa-Pereira, A., Mendonça, L., Dias, C.C., Castro-Lopes, J.M., 2016. The economic impact of chronic pain: a nationwide population-based cost-of-illness study in Portugal. Eur J Health Econ 17, 87–98.

Badler, N.I., Morris, M.A., 1982. Modelling flexible articulated objects. Proc. Computer

Graphics' 82.
Bahr, R., Krosshaug, T., 2005. Understanding injury mechanisms: a key component of preventing injuries in sport. Br J Sports Med 39, 324–329.
Baran, I., Popovic, J., 2007. Automatic rigging and animation of 3D characters. ACM Transactions on Graphics (TOG) 26, 72.
Baratta, R., Solomonow, M., Zhou, B.H., Letson, D., Chuinard, R., D'Ambrosia, R., 1988. Muscular coactivation. The role of the antagonist musculature in maintaining knee stability. Am J Sports Med 16, 113–122.
Bardina, J.E., Huang, P.G., Coakley, T.J., 1997. Turbulence modeling validation, testing, and development (No. 110446). Moffett Field, CA.
Bates, D., Mächler, M., Bolker, B., Walker, S., 2015. Fitting Linear Mixed-Effects Models Using lme4. Journal of Statistical Software 67, 1–48.
Beaumont, F., Popa, C., Liger Belair, G., Polidori, G., 2014. Numerical modeling of bubble-induced flow patterns in champagne glasses. Int J Numer Method H 24, 563–578.
Belkin, M., Sun, J., Wang, Y., 2008. Discrete laplace operator on meshed surfaces. Proceedings of the 24th annual Symposium on Computational Geometry 278–287.
Belli, A., Kyröläinen, H., Komi, P.V., 2002. Moment and power of lower limb joints in running. Int J Sports Med 23, 136–141.
Berger, M.A., de Groot, G., Hollander, A.P., 1995. Hydrodynamic drag and lift forces on human hand/arm models. J Biomech 28, 125–133.
Berger, M.A., Hollander, A.P., de Groot, G., 1999. Determining propulsive force in front crawl swimming: a comparison of two methods. J Sports Sci 17, 97–105.
Biewener, A., Corning, W., Tobalske, B., 1998. In vivo pectoralis muscle force-length behavior during level flight in pigeons (Columba livia). J Exp Biol 201 (Pt 24), 3293–3307.
Biewener, A.A., 2016. Locomotion as an emergent property of muscle contractile dynamics. J Exp Biol 219, 285–294.
Biewener, A.A., 2011. Muscle function in avian flight: achieving power and control. Philos. Trans. R. Soc. Lond., B, Biol. Sci. 366, 1496–1506.
Biewener, A.A., 2006. Patterns of mechanical energy change in tetrapod gait: pendula, springs and work. J. Exp. Zoolog. Part A Comp. Exp. Biol. 305, 899–911.
Biewener, A.A., 1990. Biomechanics of mammalian terrestrial locomotion. Science 250, 1097–1103.
Biewener, A.A., Blickhan, R., Perry, A.K., Heglund, N.C., Taylor, C.R., 1988. Muscle forces during locomotion in kangaroo rats: force platform and tendon buckle measurements compared. J Exp Biol 137, 191–205.
Biewener, A.A., Daley, M.A., 2007. Unsteady locomotion: integrating muscle function with whole body dynamics and neuromuscular control. J Exp Biol 210, 2949–2960.
Bilinauskaite, M., Mantha, V.R., Rouboa, A.I., Ziliukas, P., Silva, A.J., 2013. Computational Fluid Dynamics Study of Swimmer's Hand Velocity, Orientation, and Shape: Contributions to Hydrodynamics. BioMed Research International 2013, 14.
Biscarini, A., Cerulli, G., 2007. Modeling of the knee joint load in rehabilitative knee extension exercises under water. J Biomech 40, 345–355. doi:10.1016/j.jbiomech.2005.12.018
Bixler, B., Pease, D.L., Fairhurst, F., 2007. The accuracy of computational fluid dynamics analysis of the passive drag of a male swimmer. Sports Biomech 6, 81–98.
Bixler, B., Riewald, S., 2002. Analysis of a swimmer's hand and arm in steady flow conditions using computational fluid dynamics. J Biomech 35, 713–717.
Bixler, B., Schloder, M., 1996. Computational Fluid Dynamics: An Analytical Tool for the 21st Century Swimming Scientist. J Swim Res 11, 4–22.

Blake, R.W., 1979. The Mechanics of Labriform Locomotion I. Labriform Locomotion in the Angelfish (Pterophyllum Eimekei): An Analysis of the Power Stroke. J Exp Biol 82, 255–271.
Blazek, J., 2005. Principles of Solution of the Governing Equations, in: Computational Fluid Dynamics: Principles and Applications, Computational Fluid Dynamics: Principles and Applications (Second Edition). Elsevier Science, Oxford, pp. 29–75.
Borelli, G.A., 1680. De Motu Animalium... Opus Posthumum. Angeli Bernabo, Rome.
Brady, B., Redfern, J., MacDougal, G., Williams, J., 2008. The addition of aquatic therapy to rehabilitation following surgical rotator cuff repair: a feasibility study. Physiother Res Int 13, 153–161.
Braune, W., Fischer, O., 1895. Der Gang des Menschen, I. Teil: Versuche an unbelasteten und belasteten Menschen. Abhandlungen der Königlich Sächsischen Gesellschaft der Wissenschaften Mathematisch-physische Classe 21, 153–322.
Buczek, F.L., Kepple, T.M., Siegel, K.L., Stanhope, S.J., 1994. Translational and rotational joint power terms in a six degree-of-freedom model of the normal ankle complex. J Biomech 27, 1447–1457.
Büchler, P., Ramaniraka, N.A., Rakotomanana, L.R., Iannotti, J.P., Farron, A., 2002. A finite element model of the shoulder: application to the comparison of normal and osteoarthritic joints. Clin Biomech (Bristol, Avon) 17, 630–639.
Cappozzo, A., Berme, N., 1990. Subject-specific segment inertial parameter determination—a survey of current methods, in: Berme, N., Cappozzo, A. (Eds.), Biomechanics of Human Movement, Applications in Rehabilitation, Sports and Ergonomics. Bertec Corporation, Worthington, OH, pp. 179–185.
Cappozzo, A., Croce, Della, U., Leardini, A., Chiari, L., 2005. Human movement analysis using stereophotogrammetry. Part 1: theoretical background. Gait Posture 21, 186–196.
Castillo-Lozano, R., Cuesta-Vargas, A., Gabel, C.P., 2014. Analysis of arm elevation muscle activity through different movement planes and speeds during in-water and dry-land exercise. J Shoulder Elbow Surg 23, 159–165.
Caty, V., Aujouannet, Y., Hintzy, F., Bonifazi, M., Clarys, J.P., Rouard, A.H., 2007. Wrist stabilisation and forearm muscle coactivation during freestyle swimming. Journal of Electromyography and Kinesiology 17, 285–291.
Cavagna, G.A., 1975. Force platforms as ergometers. J Appl Physiol 39, 174–179.
Cavagna, G.A., Franzetti, P., 1986. The determinants of the step frequency in walking in humans. J Physiol 373, 235–242.
Cavagna, G.A., Heglund, N.C., Taylor, C.R., 1977. Mechanical work in terrestrial locomotion: two basic mechanisms for minimizing energy expenditure. Am J Physiol 233, R243–61.
Cavagna, G.A., Kaneko, M., 1977. Mechanical work and efficiency in level walking and running. J Physiol 268, 467–481.
Ceseracciu, E., Sawacha, Z., Cobelli, C., 2014. Comparison of markerless and marker-based motion capture technologies through simultaneous data collection during gait: proof of concept. PLoS ONE 9, e87640.
Ceseracciu, E., Sawacha, Z., Fantozzi, S., Cortesi, M., Gatta, G., Corazza, S., Cobelli, C., 2011. Markerless analysis of front crawl swimming. J Biomech 44, 2236–2242.
Chen, I.H., Kuo, K.N., Andriacchi, T.P., 1997. The influence of walking speed on mechanical joint power during gait. Gait & Posture 6, 171–176.
Chollet, D., Madani, M., Micallef, J.P., 1992. Effects of two types of biomechanical bio-feedback on crawl performance, in: MacLaren, D., Reilly, T., Lees, A. (Eds.), Biomechanics and Medicine in Swimming, Swimming Science VI. E& FN SPON, London, pp. 57–62.

Chollet, D., Micallef, J.P., Rabischong, P., 1988. Biomechanical signals for external biofeedback to improve swimming techniques, in: Ungerechts, B.E., Wilke, K., Reischle, K. (Eds.), Swimming Science V. Human Kinetics Publishers Inc., Champaign, IL, pp. 389–396.

Clark, B.D., Fish, F.E., 1994. Scaling of the locomotory apparatus and paddling rhythm in swimming mallard ducklings (Anas platyrhynchos): Test of a resonance model. J Exp Zool 270, 245–254.

Cleather, D.J., Goodwin, J.E., Bull, A.M.J., 2011. An optimization approach to inverse dynamics provides insight as to the function of the biarticular muscles during vertical jumping. Ann Biomed Eng 39, 147–160.

Cohen, J., 1988. Statistical Power Analysis for the Behavioral Sciences. L. Erlbaum Associates.

Cohen, R.C.Z., Cleary, P.W., Mason, B.R., 2012. Simulations of dolphin kick swimming using smoothed particle hydrodynamics. Hum Mov Sci 31, 604–619.

Cohen, R.C.Z., Cleary, P.W., Mason, B.R., Pease, D.L., 2015. The Role of the Hand During Freestyle Swimming. J Biomech Eng 137, 111007.

Colado, J.C., Tella, V., Triplett, N.T., 2008. A method for monitoring intensity during aquatic resistance exercises. J Strength Cond Res 22, 2045–2049.

Collins, S.H., Wiggin, M.B., Sawicki, G.S., 2015. Reducing the energy cost of human walking using an unpowered exoskeleton. Nature 522, 212–215.

Colwin, C.M., 1985. Essential fluid dynamics of swimming propulsion. ASCA Newsletter 4, 22–27.

Corazza, S., Mündermann, L., Chaudhari, A.M., Demattio, T., Cobelli, C., Andriacchi, T.P., 2006. A markerless motion capture system to study musculoskeletal biomechanics: visual hull and simulated annealing approach. Ann Biomed Eng 34, 1019–1029.

Costa, L., Mantha, V.R., Silva, A.J., Fernandes, R.J., Marinho, D.A., Vilas-Boas, J.P., Machado, L., Rouboa, A., 2015. Computational fluid dynamics vs. inverse dynamics methods to determine passive drag in two breaststroke glide positions. J Biomech 48, 2221–2226.

Counsilman, J.E., 1970. The application of Bernoulli's principle to human propulsion in water. Indiana University Publications, Bloomington, IN.

Cronin, N.J., Prilutsky, B.I., Lichtwark, G.A., Maas, H., 2013. Does ankle joint power reflect type of muscle action of soleus and gastrocnemius during walking in cats and humans? J Biomech 46, 1383–1386.

Crowninshield, R.D., Brand, R.A., 1981. The prediction of forces in joint structures; distribution of intersegmental resultants. Exerc Sport Sci Rev 9, 159–181.

d'Avella, A., Saltiel, P., Bizzi, E., 2003. Combinations of muscle synergies in the construction of a natural motor behavior. Nat Neurosci 6, 300–308.

Daanen, H.A.M., Brunsman, M.A., Robinette, K.M., 1997. Reducing movement artifacts in whole body scanning, in:. Presented at the Proceedings. International Conference on Recent Advances in 3-D Digital Imaging and Modeling, Ottawa, Ont, pp. 262–265.

Dabiri, J.O., 2005. On the estimation of swimming and flying forces from wake measurements. J Exp Biol 208, 3519–3532.

Dabnichki, P., Avital, E., 2006. Influence of the postion of crew members on aerodynamics performance of two-man bobsleigh. J Biomech 39, 2733–2742.

Daley, M.A., Felix, G., Biewener, A.A., 2007. Running stability is enhanced by a proximo-distal gradient in joint neuromechanical control. J Exp Biol 210, 383–394.

Daly, D., Lambeck, J., 2007. New trends in adapted swimming, in: Arellano, R., Sanchez, A.J., Navarro, F., Morales, E., Lopez, G. (Eds.), Swimming Science I. Editorial

Universidad de Granada, Granada, pp. 7–18.
Daniel, T.L., 1991. Efficiency in aquatic locomotion: limitations from single cells to animals, in: Blake, R.W. (Ed.), Efficiency and Economy in Animal Physiology. Cambridge University Press, Cambridge, UK, pp. 83–96.
de Leva, P., 1993. Joint force terminology. A reply to Hinrichs' message. [WWW Document]. Biomch-l.isbweb.org. URL http://biomch-l.isbweb.org/threads/1315-Joint-force-terminology-A-reply-to-Hinrichs-message (accessed 4.17).
Defraeye, T., Blocken, B., Koninckx, E., Hespel, P., Carmeliet, J., 2010a. Aerodynamic study of different cyclist positions: CFD analysis and full-scale wind-tunnel tests. J Biomech 43, 1262–1268.
Defraeye, T., Blocken, B., Koninckx, E., Hespel, P., Carmeliet, J., 2010b. Computational fluid dynamics analysis of cyclist aerodynamics: performance of different turbulence-modelling and boundary-layer modelling approaches. J Biomech 43, 2281–2287.
Delp, S.L., Maloney, W., 1993. Effects of hip center location on the moment-generating capacity of the muscles. J Biomech 26, 485–499.
Desbrun, M., Meyer, M., der, P.S.2., Barr, A.H., 1999. Implicit fairing of irregular meshes using diffusion and curvature flow 317–324.
Desroches, G., Chèze, L., Dumas, R., 2010a. Expression of joint moment in the joint coordinate system. J Biomech Eng 132, 114503.
Desroches, G., Dumas, R., Pradon, D., Vaslin, P., Lepoutre, F.-X., Chèze, L., 2010b. Upper limb joint dynamics during manual wheelchair propulsion. Clin Biomech (Bristol, Avon) 25, 299–306.
Detrembleur, C., Dierick, F., Stoquart, G., Chantraine, F., Lejeune, T., 2003. Energy cost, mechanical work, and efficiency of hemiparetic walking. Gait Posture 18, 47–55.
di Prampero, P.E., Pendergast, D.R., Wilson, D.W., Rennie, D.W., 1974. Energetics of swimming in man. J Appl Physiol 37, 1–5.
Dickinson, M.H., 1996. Unsteady Mechanisms of Force Generation in Aquatic and Aerial Locomotion. Amer Zool 36, 537–554.
Diebel, J., 2006. Representing Attitude: Euler Angles, Unit Quaternions, and Rotation Vectors, Matrix. Stanford University, Stanford, CA.
Dionne, O., de Lasa, M., 2014. Geodesic Binding for Degenerate Character Geometry Using Sparse Voxelization. IEEE Trans Vis Comput Graph 20, 1367–1378.
Dipaola, M., Pavan, E.E., Cattaneo, A., Frazzitta, G., Pezzoli, G., Cavallari, P., Frigo, C.A., Isaias, I.U., 2016. Mechanical Energy Recovery during Walking in Patients with Parkinson Disease. PLoS ONE 11, e0156420.
Dominguez-Castells, R., Izquierdo, M., Arellano, R., 2013. An updated protocol to assess arm swimming power in front crawl. Int J Sports Med 34, 324–329.
Doriot, N., Chèze, L., 2004. A three-dimensional kinematic and dynamic study of the lower limb during the stance phase of gait using an homogeneous matrix approach. IEEE Trans Biomed Eng 51, 21–27.
Douros, I., Dekker, L., Buxton, B.F., 1999. Reconstruction of the surface of the human body from 3D scanner data using B-splines, in: Nurre, J.H., Corner, B.D. (Eds.). Presented at the Electronic Imaging '99, SPIE, San Jose, CA, pp. 234–245.
Drucker, E., Lauder, G., 1999. Locomotor forces on a swimming fish: three-dimensional vortex wake dynamics quantified using digital particle image velocimetry. J Exp Biol 202, 2393–2412.
Dumas, R., Aissaoui, R., de Guise, J.A., 2004. A 3D generic inverse dynamic method using wrench notation and quaternion algebra. Comput Methods Biomech Biomed Engin 7, 159–166.
Dumas, R., Chèze, L., 2008. Hip and knee joints are more stabilized than driven during the stance phase of gait: an analysis of the 3D angle between joint moment and joint

angular velocity. Gait Posture 28, 243–250.
Dumas, R., Chèze, L., 2007. 3D inverse dynamics in non-orthonormal segment coordinate system. Med Biol Eng Comput 45, 315–322.
Dumas, R., Chèze, L., Frossard, L., 2009. Loading applied on prosthetic knee of transfemoral amputee: comparison of inverse dynamics and direct measurements. Gait Posture 30, 560–562.
Dumas, R., Chèze, L., Verriest, J.-P., 2007a. Adjustments to McConville et al. and Young et al. body segment inertial parameters. J Biomech 40, 543–553.
Dumas, R., Nicol, E., Chèze, L., 2007b. Influence of the 3D inverse dynamic method on the joint forces and moments during gait. J Biomech Eng 129, 786–790.
Dumas, R., Nicol, E., Chèze, L., 2006. Influence of perturbated gait data on four 3D inverse dynamic methods. 9th Symposium on 3D Analysis of Human Movement, Valenciennes, France, July (pp. 28–30).
Dumont, K., Stijnen, J.M.A., Vierendeels, J., van de Vosse, F.N., Verdonck, P.R., 2004. Validation of a fluid-structure interaction model of a heart valve using the dynamic mesh method in fluent. Comput Methods Biomech Biomed Engin 7, 139–146.
Duncan, J.A., Kowalk, D.L., Vaughan, C.L., 1997. Six degree of freedom joint power in stair climbing. Gait & Posture 5, 204–210.
Dupont, P., 1990. Friction Modeling in Dynamic Robot Simulation, in: Proceedings., 1990 IEEE International Conference on Robotics and Automation. Cincinnati, OH, pp. 1370–1376.
Elftman, H., 1939. Forces and energy changes in the leg during walking. Am J Physiol 125, 339–356.
Elftman, H., 1938. THE MEASUREMENT OF THE EXTERNAL FORCE IN WALKING. Science 88, 152–153.
Falconer, K., Winter, D.A., 1985. Quantitative assessment of co-contraction at the ankle joint in walking. Electromyogr Clin Neurophysiol 25, 135–149.
Farley, C.T., Ferris, D.P., 1998. Biomechanics of walking and running: centre of mass movements to muscle action. Exerc Sport Sci Rev 26, 253–285.
Farris, D.J., Sawicki, G.S., 2012. The mechanics and energetics of human walking and running: a joint level perspective. Journal of The Royal Society Interface 9, 110–118.
Faul, F., Erdfelder, E., Lang, A.-G., Buchner, A., 2007. G*Power 3: a flexible statistical power analysis program for the social, behavioral, and biomedical sciences. Behav Res Methods 39, 175–191.
Fenn, W.O., 1930. Frictional and kinetic factors in the work of sprint running. Am J Physiol 92, 583–611.
Ferber, R., Osis, S.T., Hicks, J.L., Delp, S.L., 2016. Gait biomechanics in the era of data science. J Biomech 49, 3759–3761.
Ferziger, J.H., Peric, M., 2002. Turbulent Flows, in: Computational Methods for Fluid Dynamics. Springer-Verlag Berlin Heidelberg, Berlin, pp. 265–307.
Fish, F.E., 1993. Influence of hydrodynamic design and propulsive mode on mammalian swimming energetics. Aust J Zool 42, 79–101.
Fish, F.E., 1984. Mechanics, power output and efficiency of the swimming muskrat (Ondatra zibethicus). J Exp Biol 110, 183–201.
Fish, F.E., Legac, P., Williams, T.M., Wei, T., 2014. Measurement of hydrodynamic force generation by swimming dolphins using bubble DPIV. J Exp Biol 217, 252–260.
Fluit, R., Andersen, M.S., Kolk, S., Verdonschot, N., Koopman, H.F.J.M., 2014. Prediction of ground reaction forces and moments during various activities of daily living. J Biomech 47, 2321–2329.
Formenti, F., Ardigò, L.P., Minetti, A.E., 2005. Human locomotion on snow: determinants of economy and speed of skiing across the ages. Proc Biol Sci 272, 1561–1569.

Formosa, D.P., Mason, B.R., Burkett, B.J., 2010. Measuring Active Drag within the Different Phases of Front Crawl Swimming, in: Kjendlie, P.-L., Stallman, R.K., Cabri, J. (Eds.), Biomechanics and Medicine in Swimming XI. Norwegian School of Sport Sciences, Oslo, Norway, pp. 82–84.
Fornalski, S., Gupta, R., Lee, T.Q., 2003. Anatomy and biomechanics of the elbow joint. Tech Hand Up Extrem Surg 7, 168–178.
Fukashiro, S., Komi, P.V., Järvinen, M., Miyashita, M., 1993. Comparison between the directly measured achilles tendon force and the tendon force calculated from the ankle joint moment during vertical jumps. Clin Biomech (Bristol, Avon) 8, 25–30.
Gagnon, M., Desjardins, P., Larrivé, A., 2001. Joint coordinate systems of axes for coherence in reporting kinematic and kinetic data. Clinical Biomechanics 16, 349–350.
Gal, J.M., Blake, R.W., 1988. Biomechanics of frog swimming: II. Mechanics of the limb-beat cycle in Hymenochirus Boettgeri. J Exp Biol 138, 413–429.
Gamage, S.S.H.U., Lasenby, J., 2002. New least squares solutions for estimating the average centre of rotation and the axis of rotation. J Biomech 35, 87–93.
Garber, C.E., Blissmer, B., Deschenes, M.R., Franklin, B.A., Lamonte, M.J., Lee, I.-M., Nieman, D.C., Swain, D.P., American College of Sports Medicine, 2011. American College of Sports Medicine position stand. Quantity and quality of exercise for developing and maintaining cardiorespiratory, musculoskeletal, and neuromotor fitness in apparently healthy adults: guidance for prescribing exercise. Med Sci Sports Exerc. 43, 1334–1359
Gil-Agudo, A., Del Ama-Espinosa, A., Pérez-Rizo, E., Pérez-Nombela, S., Pablo Rodríguez-Rodríguez, L., 2010. Upper limb joint kinetics during manual wheelchair propulsion in patients with different levels of spinal cord injury. J Biomech 43, 2508–2515.
Gottlieb, G.L., 1994. The generation of the efferent command and the importance of joint compliance in fast elbow movements. Exp Brain Res 97, 545–550.
Gourgoulis, V., Aggeloussis, N., Kasimatis, P., Vezos, N., Boli, A., Mavromatis, G., 2008a. Reconstruction accuracy in underwater three-dimensional kinematic analysis. J Sci Med Sport 11, 90–95.
Gourgoulis, V., Aggeloussis, N., Vezos, N., Kasimatis, P., Antoniou, P., Mavromatis, G., 2008b. Estimation of hand forces and propelling efficiency during front crawl swimming with hand paddles. J Biomech 41, 208–215.
Gourgoulis, V., Boli, A., Aggeloussis, N., Antoniou, P., Toubekis, A., Mavromatis, G., 2015. The influence of the hand's acceleration and the relative contribution of drag and lift forces in front crawl swimming. J Sports Sci 33, 696–712.
Gouveia, M., Augusto, M., 2011. Custos indirectos da dor crónica em Portugal (Indirect costs of chronic pain in Portugal). Revista Portuguesa de Saúde Pública 29, 100–107.
Gray, J., 1936. Studies in Animal Locomotion. VI. The propulsive powers of the dolphin. J Exp Biol 13, 192–199.
Gribble, P.L., Mullin, L.I., Cothros, N., Mattar, A., 2003. Role of cocontraction in arm movement accuracy. J Neurophysiol 89, 2396–2405.
Griffin, T.M., Kram, R., 2000. Penguin waddling is not wasteful. Nature 408, 929–929.
Guo, X., Li, W., Iorio, F., 2016. Convolutional Neural Networks for Steady Flow Approximation. Proceedings of the 22nd ACM SIGKDD International Conference on Knowledge Discovery and Data Mining, 481–490.
Hall, J., Swinkels, A., Briddon, J., McCabe, C.S., 2008. Does aquatic exercise relieve pain in adults with neurologic or musculoskeletal disease? A systematic review and meta-analysis of randomized controlled trials. Arch Phys Med Rehabil 89, 873–883.
Hanlon, M., Kearney, P., Condell, J., 2012. Kinematic variability in running: a caution regarding use of the spanning set measure. J Appl Biomech 28, 99–104.

Hansen, A.H., Childress, D.S., Miff, S.C., Gard, S.A., Mesplay, K.P., 2004. The human ankle during walking: implications for design of biomimetic ankle prostheses. J Biomech 37, 1467–1474.
Harlow, F.H., 2004. Fluid dynamics in Group T-3 Los Alamos National Laboratory: (LA-UR-03-3852). J Comput Phys 195, 414–433.
Hatton, L., 1997. The T-experiments: errors in scientific software, in: Boisvert, R.F. (Ed.), Quality of Numerical Software: Assessment and Enhancement, Quality of Numerical Software: Assessment and Enhancement. Springer US, Boston, MA, pp. 12–31.
Hatze, H., 2002. The fundamental problem of myoskeletal inverse dynamics and its implications. J Biomech 35, 109–115.
Havriluk, R., 2007. Variability in measurement of swimming forces: a meta-analysis of passive and active drag. Res Q Exerc Sport 78, 32–39.
Heglund, N.C., Willems, P.A., Penta, M., Cavagna, G.A., 1995. Energy-saving gait mechanics with head-supported loads. Nature 375, 52–54.
Heiderscheit, B.C., Chumanov, E.S., Michalski, M.P., Wille, C.M., Ryan, M.B., 2011. Effects of step rate manipulation on joint mechanics during running. Med Sci Sports Exerc 43, 296–302.
Hirashima, M., Kudo, K., Ohtsuki, T., 2007. A new non-orthogonal decomposition method to determine effective torques for three-dimensional joint rotation. J Biomech 40, 871–882.
Hirsch, C., 2007. Introduction: An Initial Guide to CFD and to this Volume, in: Numerical Computation of Internal and External Flows, Numerical Computation of Internal and External Flows. Butterworth-Heinemann, Oxford, pp. 1–20.
Hochstein, S., Blickhan, R., 2011. Vortex re-capturing and kinematics in human underwater undulatory swimming. Hum Mov Sci 30, 998–1007.
Hoerner, S.F., 1965. Fluid-dynamic Drag, 2nd ed. Published by the author, Midland Park, NJ.
Hof, A.L., 1996. Scaling gait data to body size. Gait Posture 4, 222–223.
Hoi, Y., Meng, H., Woodward, S.H., Bendok, B.R., Hanel, R.A., Guterman, L.R., Hopkins, L.N., 2004. Effects of arterial geometry on aneurysm growth: three-dimensional computational fluid dynamics study. J. Neurosurg. 101, 676–681.
Holden, J., Stanhope, S., 1998. The effect of variation in knee center location estimates on net knee joint moments. Gait Posture 7, 1–6.
Hollander, A.P., de Groot, G., van Ingen Schenau, G.J., Toussaint, H.M., De Best, H., Peeters, W., Meulemans, A., Schreurs, A.W., 1986. Measurement of active drag during crawl arm stroke swimming. J Sports Sci 4, 21–30.
Hollerbach, M.J., Flash, T., 1982. Dynamic interactions between limb segments during planar arm movement. Biol Cybern 44, 67–77.
Holzbaur, K.R.S., Murray, W.M., Gold, G.E., Delp, S.L., 2007. Upper limb muscle volumes in adult subjects. J Biomech 40, 742–749.
Hortobágyi, T., Solnik, S., Gruber, A., Rider, P., Steinweg, K., Helseth, J., DeVita, P., 2009. Interaction between age and gait velocity in the amplitude and timing of antagonist muscle coactivation. Gait Posture 29, 558–564.
Hutchinson, E.B., Riley, P.O., Krebs, D.E., 1994. A dynamic analysis of the joint forces and torques during rising from a chair. IEEE Trans Rehabil Eng 2, 49–56.
Iino, Y., Kojima, T., 2012. Validity of the Top-Down Approach of Inverse Dynamics Analysis in Fast and Large Rotational Trunk Movements 28, 420–430.
Jacobson, A., 2013. Algorithms and Interfaces for Real-Time Deformation of 2D and 3D Shapes. ETH, Zurich, Switzerland.
Jacobson, A., Baran, I., Popovic, J., Sorkine, O., 2011. Bounded biharmonic weights for

real-time deformation. ACM Transactions on Graphics (TOG) 30, 1–8.
Jacobson, A., Deng, Z., Kavan, L., Lewis, J.P., 2014. Skinning: real-time shape deformation. ACM, Vancouver, Canada.
Jacobson, A., Sorkine, O., 2011. Stretchable and Twistable Bones for Skeletal Shape Deformation. ACM Transactions on Graphics (TOG) 30, 1–8.
Jetté, M., Sidney, K., Blümchen, G., 1990. Metabolic equivalents (METS) in exercise testing, exercise prescription, and evaluation of functional capacity. Clin Cardiol 13, 555–565.
Jones, E.M., Fjeld, P., 2011. Gimbal Angles, Gimbal Lock, and a Fourth Gimbal for Christmas [WWW Document]. http://www.hq.nasa.gov/alsj/gimbals.html. URL (accessed 11.8.16).
Karduna, A.R., McClure, P.W., Michener, L.A., 2000. Scapular kinematics: effects of altering the Euler angle sequence of rotations. J Biomech 33, 1063–1068.
Kautz, S.A., Hull, M.L., Neptune, R.R., 1994. A comparison of muscular mechanical energy expenditure and internal work in cycling. J Biomech 27, 1459–1467.
Kautz, S.A., Neptune, R.R., 2002. Biomechanical determinants of pedaling energetics: internal and external work are not independent. Exerc Sport Sci Rev 30, 159–165.
Kavan, L., Collins, S., O'Sullivan, C., 2009. Automatic linearization of nonlinear skinning. Proceedings of I3D '09, pp. 49–56.
Kavan, L., Collins, S., Zára, J., O'Sullivan, C., 2008. Geometric skinning with approximate dual quaternion blending. ACM Transactions on Graphics (TOG) 27, 105–123.
Kavan, L., Collins, S., Zára, J., O'Sullivan, C., 2007. Skinning with dual quaternions. Proceedings of I3D '07, pp. 39–46. ACM, Seattle, Washington.
Kavan, L., Sorkine, O., 2012. Elasticity-inspired deformers for character articulation. ACM Transactions on Graphics (TOG) 31, 1–8.
Kelly, B.T., Roskin, L.A., Kirkendall, D.T., Speer, K.P., 2000. Shoulder muscle activation during aquatic and dry land exercises in nonimpaired subjects. J Orthop Sports Phys Ther 30, 204–210.
Ketcham, C.J., Dounskaia, N.V., Stelmach, G.E., 2004. Multijoint movement control: the importance of interactive torques. Prog. Brain Res. 143, 207–218.
Keys, M., 2010. Establishing Computational Fluid Dynamics models for swimming technique assessment. Perth, Australia.
Kingma, I., de Looze, M.P., Toussaint, H.M., Klijnsma, H.G., Bruijnen, T.B.M., 1996. Validation of a full body 3-D dynamic linked segment model. Human Movement Science 15, 833–860.
Kline, S.J., Reynolds, W.C., Schraub, F.A., Runstadler, P.W., 1967. The structure of turbulent boundary layers. Journal of Fluid Mechanics 30, 741–773.
Kolmogorov, S.V., Duplishcheva, O.A., 1992. Active drag, useful mechanical power output and hydrodynamic force coefficient in different swimming strokes at maximal velocity. J Biomech 25, 311–318.
Kristianslund, E., Bahr, R., Krosshaug, T., 2011. Kinematics and kinetics of an accidental lateral ankle sprain. J Biomech 44, 2576–2578.
Kristianslund, E., Faul, O., Bahr, R., Myklebust, G., Krosshaug, T., 2014a. Sidestep cutting technique and knee abduction loading: implications for ACL prevention exercises. Br J Sports Med 48, 779–783.
Kristianslund, E., Krosshaug, T., Mok, K.-M., McLean, S., van den Bogert, A.J., 2014b. Expressing the joint moments of drop jumps and sidestep cutting in different reference frames--does it matter? J Biomech 47, 193–199.
Kudo, S., Yanai, T., Wilson, B., Takagi, H., Vennell, R., 2008. Prediction of fluid forces acting on a hand model in unsteady flow conditions. J Biomech 41, 1131–1136.

Lacquaniti, F., Ivanenko, Y.P., d'Avella, A., Zelik, K.E., Zago, M., 2013. Evolutionary and developmental modules. Front Comput Neurosci 7, 61.

Lacquaniti, F., Ivanenko, Y.P., Zago, M., 2012. Patterned control of human locomotion. J Physiol 590, 2189–2199.

Landahl, M.T., Mollo-Christensen, E., 1992. Turbulence and Random Process in Fluid Mechanics, 2nd ed. Cambridge University Press, New York, NY.

Larivière, C., Gagnon, D., 1998. Comparison between two dynamic methods to estimate triaxial net reaction moments at the L5/S1 joint during lifting. Clin Biomech (Bristol, Avon) 13, 36–47.

Latash, M.L., Zatsiorsky, V.M., 2015. Biomechanics and Motor Control: Defining Central Concepts. Academic Press, London, UK.

Lauder, Dabnichki, P., Bartlett, R.M., 2001. Improved accuracy and reliability of sweepback angle, pitch angle and hand velocity calculations in swimming. J Biomech 34, 31–39.

Lauder, G.V., Drucker, E.G., 2002. Forces, fishes, and fluids: hydrodynamic mechanisms of aquatic locomotion. News Physiol. Sci. 17, 235–240.

Lauder, M.A., Dabnichki, P., 2005. Estimating propulsive forces—sink or swim? J Biomech 38, 1984–1990.

Lauer, J., Figueiredo, P., Vilas-Boas, J.P., Fernandes, R.J., Rouard, A.H., 2013. Phase-dependence of elbow muscle coactivation in front crawl swimming. J Electromyogr Kinesiol 23, 820–825.

Lauer, J., Olstad, B.H., Minetti, A.E., Kjendlie, P.-L., Rouard, A.H., 2015. Breaststroke swimmers moderate internal work increases toward the highest stroke frequencies. J Biomech 48, 3012–3016.

Lauer, J., Rouard, A.H., Vilas-Boas, J.P., 2017. Modulation of upper limb joint work and power during sculling while ballasted with varying loads. J Exp Biol 220, 1729–1736.

Lauer, J., Rouard, A.H., Vilas-Boas, J.P., 2016. Upper limb joint forces and moments during underwater cyclical movements. J Biomech 49, 3355–3361.

Launder, B.E., Spalding, D.B., 1974. The numerical computation of turbulent flows. Computer Methods in Applied Mechanics and Engineering 3, 269–289.

Lecrivain, G., Payton, C.J., Slaouti, A., Kennedy, I., 2010. Effect of body roll amplitude and arm rotation speed on propulsion of arm amputee swimmers. J Biomech 43, 1111–1117.

Lecrivain, G., Slaouti, A., Payton, C.J., Kennedy, I., 2008. Using reverse engineering and computational fluid dynamics to investigate a lower arm amputee swimmer's performance. J Biomech 41, 2855–2859.

Lee, J., Ashdoon, S.P., 2005. Upper body surface change analysis using 3-D body scanner. J Korean Soc Cloth Textiles 29, 1595–1607.

Legnani, G., Casolo, F., Righettini, P., Zappa, B., 1996. A homogeneous matrix approach to 3D kinematics and dynamics — I. Theory. Mech. Mach. Theory 31, 573–587.

Lejeune, T.M., Willems, P.A., Heglund, N.C., 1998. Mechanics and energetics of human locomotion on sand. J Exp Biol 201, 2071–2080.

Lempereur, M., Brochard, S., Rémy-Néris, O., 2013. Repeatability assessment of functional methods to estimate the glenohumeral joint centre. Comput Methods Biomech Biomed Engin 16, 6–11.

Lempereur, M., Leboeuf, F., Brochard, S., Rousset, J., Burdin, V., Rémy-Néris, O., 2010. In vivo estimation of the glenohumeral joint centre by functional methods: accuracy and repeatability assessment. J Biomech 43, 370–374. doi:10.1016/j.jbiomech.2009.09.029

Levi, Z., Levin, D., 2014. Shape Deformation via Interior RBF. IEEE Trans Vis Comput Graph 20, 1062–1075.

Levine, T.R., Hullett, C.R., 2002. Eta Squared, Partial Eta Squared, and Misreporting of Effect Size in Communication Research. Human Communication Research 28, 612–625.
Lewis, J.P., Cordner, M., Fong, N., 2000. Pose space deformation: a unified approach to shape interpolation and skeleton-driven deformation, in:. Presented at the Proceedings of the 27th annual conference on Computer graphics and interactive techniques, ACM Press/Addison-Wesley Publishing Co., pp. 165–172.
Liao, J.C., Beal, D.N., Lauder, G.V., Triantafyllou, M.S., 2003. Fish exploiting vortices decrease muscle activity. Science 302, 1566–1569.
Lighthill, M.J., 1971. Large-amplitude elongate-body theory of fish locomotion. Proc. R. Soc. Lond. B 179, 125–138.
Lipfert, S.W., Günther, M., Renjewski, D., Seyfarth, A., 2014. Impulsive ankle push-off powers leg swing in human walking. J Exp Biol 217, 1218–1228.
Liu, H., Wassersug, R., Kawachi, K., 1997. The three-dimensional hydrodynamics of tadpole locomotion. J Exp Biol 200, 2807–2819.
Loebbecke, von, A., Mittal, R., 2012. Comparative analysis of thrust production for distinct arm-pull styles in competitive swimming. J Biomech Eng 134, 074501.
Loebbecke, von, A., Mittal, R., Fish, F.E., Mark, R., 2009a. Propulsive efficiency of the underwater dolphin kick in humans. J Biomech Eng 131, 054504.
Loebbecke, von, A., Mittal, R., Mark, R., Hahn, J., 2009b. A computational method for analysis of underwater dolphin kick hydrodynamics in human swimming. Sports Biomech 8, 60–77.
Loetz, C., Reischle, K., Schmitt, G., 1988. The evaluation of highly skilled swimmers via quantitative and qualitative analysis, in: Ungerechts, B.E., Wilke, K., Reischle, K. (Eds.), Swimming Science V. Human Kinetics Publishers Inc., Champaign, IL, pp. 361–367.
Lorente, S., Cetkin, E., Bello-Ochende, T., Meyer, J.P., Bejan, A., 2012. The constructal-law physics of why swimmers must spread their fingers and toes. J. Theor. Biol. 308, 141–146.
Lugo, R., Kung, P., Ma, C.B., 2008. Shoulder biomechanics. Eur J Radiol 68, 16–24.
Magnenat-Thalmann, N., re, R.L.2., Thalmann, D., 1988. Joint-dependent local deformations for hand animation and object grasping 26–33.
Marinho, D.A., Barbosa, T.M., Reis, V.M., Kjendlie, P.L., Alves, F.B., Vilas-Boas, J.P., Machado, L., Silva, A.J., Rouboa, A.I., 2010. Swimming propulsion forces are enhanced by a small finger spread. J Appl Biomech 26, 87–92.
Marinho, D.A., Silva, A.J., Reis, V.M., Barbosa, T.M., Vilas-Boas, J.P., Alves, F.B., Machado, L., Rouboa, A.I., 2011. Three-dimensional CFD analysis of the hand and forearm in swimming. J Appl Biomech 27, 74–80.
Marshall, R.N., Elliott, B.C., 2000. Long-axis rotation: the missing link in proximal-to-distal segmental sequencing. J Sports Sci 18, 247–254. doi:10.1080/026404100364983
Martens, J., Figueiredo, P., Daly, D., 2015. Electromyography in the four competitive swimming strokes: a systematic review. J Electromyogr Kinesiol 25, 273–291.
Matsuuchi, K., Miwa, T., Nomura, T., Sakakibara, J., Shintani, H., Ungerechts, B.E., 2009. Unsteady flow field around a human hand and propulsive force in swimming. J Biomech 42, 42–47.
Mayer, F., Horstmann, T., Röcker, K., Heitkamp, H.C., Dickhuth, H.H., 1994. Normal values of isokinetic maximum strength, the strength/velocity curve, and the angle at peak torque of all degrees of freedom in the shoulder. Int J Sports Med 15 Suppl 1, S19–25.
McCaw, S.T., DeVita, P., 1995. Errors in alignment of center of pressure and foot

coordinates affect predicted lower extremity torques. J Biomech 28, 985–988.
McConville, J.T., Clauser, C.E., Churchill, T.D., Cuzzi, J., Kaleps, I., 1980. Anthropometric Relationships of Body and Body Segment Moments of Inertia (No. AFAMRL-TR-80-119). Wright-Patterson AFB, OH.
McGibbon, C.A., Krebs, D.E., Puniello, M.S., 2001. Mechanical energy analysis identifies compensatory strategies in disabled elders' gait. J Biomech 34, 481–490.
McGowan, C.P., Neptune, R.R., Clark, D.J., Kautz, S.A., 2010. Modular control of human walking: Adaptations to altered mechanical demands. J Biomech 43, 412–419.
Meile, W., Reisenberger, E., Mayer, M., Schmölzer, B., Müller, W., Brenn, G., 2006. Aerodynamics of ski jumping: experiments and CFD simulations. Exp Fluids 41, 949–964.
Menter, F.R., 1992. Improved Two-Equation *k*–**ω** Turbulence Models for Aerodynamic Flows (No. 103975). Moffett Field, CA.
Merry, B., Marais, P., Gain, J., 2006. Normal transformations for articulated models 134.
Meyer, M., Desbrun, M., Schröder, P., Barr, A.H., 2003. Discrete Differential-Geometry Operators for Triangulated 2-Manifolds, in: Visualization and Mathematics III, Mathematics and Visualization. Springer Berlin Heidelberg, Berlin, Heidelberg, pp. 35–57.
Minetti, A.E., 2011. Bioenergetics and biomechanics of cycling: the role of 'internal work'. Eur J Appl Physiol 111, 323–329.
Minetti, A.E., 2004. Passive tools for enhancing muscle-driven motion and locomotion. J Exp Biol 207, 1265–1272.
Minetti, A.E., 1998. The biomechanics of skipping gaits: a third locomotion paradigm? Proc Biol Sci 265, 1227–1235.
Minetti, A.E., Ardigò, L.P., Saibene, F., 1994a. The transition between walking and running in humans: metabolic and mechanical aspects at different gradients. Acta Physiol Scand 150, 315–323.
Minetti, A.E., Ardigò, L.P., Saibene, F., 1994b. Mechanical determinants of the minimum energy cost of gradient running in humans. J Exp Biol 195, 211–225.
Minetti, A.E., Ardigò, L.P., Saibene, F., 1993. Mechanical determinants of gradient walking energetics in man. J Physiol 472, 725–735.
Minetti, A.E., Machtsiras, G., Masters, J.C., 2009. The optimum finger spacing in human swimming. J Biomech 42, 2188–2190.
Mittal, R., Iaccarino, G., 2005. Immersed boundary methods. Annu. Rev. Fluid Mech. 37, 239–261.
Monaghan, J.J., 2012. Smoothed Particle Hydrodynamics and Its Diverse Applications. Annu. Rev. Fluid Mech. 44, 323–346.
Morrison, J.B., 1970. The mechanics of muscle function in locomotion. J Biomech 3, 431–451.
Morrow, M.M.B., Hurd, W.J., Kaufman, K.R., An, K.-N., 2009. Upper-limb joint kinetics expression during wheelchair propulsion. J Rehabil Res Dev 46, 939–944.
Nagura, T., Dyrby, C.O., Alexander, E.J., Andriacchi, T.P., 2002. Mechanical loads at the knee joint during deep flexion. J. Orthop. Res. 20, 881–886.
Nakashima, M., 2007. Mechanical Study of Standard Six Beat Front Crawl Swimming by Using Swimming Human Simulation Model TI . Journal of Fluid Science and Technology 2, 290–301.
Nakashima, M., Hasegawa, T., Kamiya, S., Takagi, H., 2013. Musculoskeletal Simulation of the Breaststroke. Journal of Biomechanical Science and Engineering 8, 152–163.
Nakashima, M., MAEDA, S., Miwa, T., ICHIKAWA, H., 2012. Optimizing Simulation of the Arm Stroke in Crawl Swimming Considering Muscle Strength Characteristics

of Athlete Swimmers TI . Journal of Biomechanical Science and Engineering 7, 102–117.
Nakashima, M., Motegi, Y., 2007. Development of a full-body musculo-skeletal simulator for swimming, in:. Tainan, Taiwan, pp. 59–60.
Nakashima, M., SATOU, K., MIURA, Y., 2007. Development of Swimming Human Simulation Model Considering Rigid Body Dynamics and Unsteady Fluid Force for Whole Body TI . Journal of Fluid Science and Technology 2, 56–67.
Nealen, A., Igarashi, T., Sorkine, O., Alexa, M., 2006. Laplacian mesh optimization 381–389.
Neptune, R.R., Kautz, S.A., Zajac, F.E., 2000. Muscle contributions to specific biomechanical functions do not change in forward versus backward pedaling. J Biomech 33, 155–164.
Neptune, R.R., McGowan, C.P., Kautz, S.A., 2009. Forward dynamics simulations provide insight into muscle mechanical work during human locomotion. Exerc Sport Sci Rev 37, 203–210.
Neptune, R.R., Sasaki, K., Kautz, S.A., 2008. The effect of walking speed on muscle function and mechanical energetics. Gait & Posture 28, 135–143.
Neptune, R.R., van den Bogert, A.J., 1998. Standard mechanical energy analyses do not correlate with muscle work in cycling. J Biomech 31, 239–245.
Neviaser, R.J., Neviaser, T.J., 1992. Reoperation for failed rotator cuff repair: Analysis of fifty cases. J Shoulder Elbow Surg 1, 283–286.
Newman, J.N., 1977. Marine Hydrodynamics. The MIT Press, Cambridge, MA.
Nichols, T.R., Bunderson, N.E., Lyle, M.A., 2016. Neural Regulation of Limb Mechanics: Insights from the Organization of Proprioceptive Circuits, in: Prilutsky, B.I., Edwards, D.H. (Eds.), Neuromechanical Modeling of Posture and Locomotion, Neuromechanical Modeling of Posture and Locomotion. Springer New York, New York, NY, pp. 69–102.
Nordin, M., Frankel, V.H., 2012. Basic Biomechanics of the Musculoskeletal System, 4 ed. Lippincott Williams & Wilkins, Philadelphia, PA.
Orselli, M.I.V., Duarte, M., 2011. Joint forces and torques when walking in shallow water. J Biomech 44, 1170–1175.
Osu, R., Franklin, D.W., Kato, H., Gomi, H., Domen, K., Yoshioka, T., Kawato, M., 2002. Short- and long-term changes in joint co-contraction associated with motor learning as revealed from surface EMG. J Neurophysiol 88, 991–1004.
Pabst, D.A., 1996. Springs in swimming animals. Amer Zool 36, 723–735.
Pai, Y.-C., Hay, J.G., 1988. A Hydrodynamic Study of the Oscillation Motion in Swimming. International Journal of Sport Biomechanics 4, 21–37.
Patankar, S., 1980. Numerical Heat Transfer and Fluid Flow. CRC Press.
Paul, J.P., 1976. Force actions transmitted by joints in the human body. Proc. R. Soc. Lond., B, Biol. Sci. 192, 163–172.
Pàmies-Vilà, R., Font-Llagunes, J.M., Cuadrado, J., Alonso, F.J., 2012. Analysis of different uncertainties in the inverse dynamic analysis of human gait. Mechanism and Machine Theory 58, 153–164.
Pearsall, D.J., Costigan, P.A., 1999. The effect of segment parameter error on gait analysis results. Gait Posture 9, 173–183.
Pellegrini, B., Zoppirolli, C., Bortolan, L., Zamparo, P., Schena, F., 2014. Gait models and mechanical energy in three cross-country skiing techniques. J Exp Biol 217, 3910–3918. doi:10.1242/jeb.106740
Pendergast, D.R., di Prampero, P.E., Craig, A.B., Wilson, D.R., Rennie, D.W., 1977. Quantitative analysis of the front crawl in men and women. J Appl Physiol Respir Environ Exerc Physiol 43, 475–479.

Pendergast, D.R., Zamparo, P., di Prampero, P.E., Capelli, C., Cerretelli, P., Termin, A.C., Craig, A.B., Bushnell, D., Paschke, D., Mollendorf, J.C., 2003. Energy balance of human locomotion in water. Eur J Appl Physiol 90, 377–386.

Peng, J., Dabiri, J.O., Madden, P.G., Lauder, G.V., 2007. Non-invasive measurement of instantaneous forces during aquatic locomotion: a case study of the bluegill sunfish pectoral fin. J Exp Biol 210, 685–698.

Pennycuick, C.J., 2008. Mechanics of Level Flight, in: Modelling the Flying Bird, Modelling the Flying Bird. Academic Press, Burlington, MA, pp. 37–78.

Pennycuick, C.J., 1968. Power requirements for horizontal flight in the pigeon *Columba livia*. J Exp Biol 49, 527–555.

Peplowski, M.M., Marsh, R.L., 1997. Work and power output in the hindlimb muscles of Cuban tree frogs Osteopilus septentrionalis during jumping. J Exp Biol 200, 2861–2870.

Persyn, U., Colman, V., 1997. Flow visualisation and propulsion in undulated swimming techniques. Técnicas simultâneas e ondulatórias Desafios contemporâneos em natação.

Peskin, C.S., 1982. The Fluid Dynamics of Heart Valves: Experimental, Theoretical, and Computational Methods. Annu. Rev. Fluid Mech. 14, 235–259.

Phadke, V., Braman, J.P., LaPrade, R.F., Ludewig, P.M., 2011. Comparison of glenohumeral motion using different rotation sequences. J Biomech 44, 700–705.

Piovesan, D., Pierobon, A., Dizio, P., Lackner, J.R., 2011. Comparative analysis of methods for estimating arm segment parameters and joint torques from inverse dynamics. J Biomech Eng 133, 031003.

Pittler, M.H., Karagülle, M.Z., Karagülle, M., Ernst, E., 2006. Spa therapy and balneotherapy for treating low back pain: meta-analysis of randomized trials. Rheumatology (Oxford, England) 45, 880–884.

Plamondon, A., Gagnon, M., Desjardins, P., 1996. Validation of two 3-D segment models to calculate the net reaction forces and moments at the L(5)/S(1) joint in lifting. Clin Biomech (Bristol, Avon) 11, 101–110.

Poitout, D.G., 2016. Biomechanics and Biomaterials in Orthopedics. Springer-Verlag London.

Pope, S., 2000. Turbulent Flows. Cambridge University Press, New York, NY.

Pöyhönen, T., Avela, J., 2002. Effect of head-out water immersion on neuromuscular function of the plantarflexor muscles. Aviat Space Environ Med 73, 1215–1218.

Pöyhönen, T., Keskinen, K.L., Kyröläinen, H., Hautala, A., Savolainen, J., Mälkiä, E., 2001a. Neuromuscular function during therapeutic knee exercise under water and on dry land. Arch Phys Med Rehabil 82, 1446–1452.

Pöyhönen, T., Kyröläinen, H., Keskinen, K.L., Hautala, A., Savolainen, J., Mälkiä, E., 2001b. Electromyographic and kinematic analysis of therapeutic knee exercises under water. Clin Biomech (Bristol, Avon) 16, 496–504.

Pöyhönen, T., Sipilä, S., Keskinen, K.L., Hautala, A., Savolainen, J., Mälkiä, E., 2002. Effects of aquatic resistance training on neuromuscular performance in healthy women. Med Sci Sports Exerc 34, 2103–2109.

Prilutsky, B.I., Petrova, L.N., Raitsin, L.M., 1996. Comparison of mechanical energy expenditure of joint moments and muscle forces during human locomotion. J Biomech 29, 405–415.

Prins, J., Cutner, D., 1999. Aquatic therapy in the rehabilitation of athletic injuries. Clin Sports Med 18, 447–461.

Putnam, C.A., 1993. Sequential motions of body segments in striking and throwing skills: descriptions and explanations. J Biomech 26 Suppl 1, 125–135.

Qiao, M., Jindrich, D.L., 2016. Leg joint function during walking acceleration and

deceleration. J Biomech 49, 66–72.
Quanbury, A.O., Winter, D.A., Reimer, G.D., 1975. Instantaneous power and power flow in body segments during walking. J. Human Movement Studies 1, 59–67.
R Core Team, n.d. R: A Language and Environment for Statistical Computing.
Rayner, J.M.V., 1985. Linear relations in biomechanics: the statistics of scaling functions. J Zool 206, 415–439.
Reed, M., Manary, M.A., Schneider, L.W., 1999. Methods for measuring and representing automobile occupant posture (No. 1999-01-0959). SAE Technical Paper.
Reid, M., Elliott, B., Alderson, J., 2007. Shoulder joint loading in the high performance flat and kick tennis serves. Br J Sports Med 41, 884–9– discussion 889.
Ribak, G., Swallow, J.G., Jones, D.R., 2010. Drag-based "hovering" in ducks: the hydrodynamics and energetic cost of bottom feeding. PLoS ONE 5, e12565.
Richards, C.T., 2008. The kinematic determinants of anuran swimming performance: an inverse and forward dynamics approach. J Exp Biol 211, 3181–3194.
Richards, C.T., Sawicki, G.S., 2012. Elastic recoil can either amplify or attenuate muscle-tendon power, depending on inertial vs. fluid dynamic loading. J. Theor. Biol. 313, 68–78.
Richards, J., Thewlis, D., Selfe, J., Cunningham, A., Hayes, C., 2008. A biomechanical investigation of a single-limb squat: implications for lower extremity rehabilitation exercise. J Athl Train 43, 477–482.
Riddick, R.C., Kuo, A.D., 2016. Soft tissues store and return mechanical energy in human running. J Biomech 49, 436–441.
Riemer, R., Hsiao-Wecksler, E.T., Zhang, X., 2008. Uncertainties in inverse dynamics solutions: a comprehensive analysis and an application to gait. Gait Posture 27, 578–588.
Risberg, M.A., Moksnes, H., Storevold, A., Holm, I., Snyder-Mackler, L., 2009. Rehabilitation after anterior cruciate ligament injury influence joint loading during walking but not hopping. Br J Sports Med 43, 423–428.
Roach, N.T., Venkadesan, M., Rainbow, M.J., Lieberman, D.E., 2013. Elastic energy storage in the shoulder and the evolution of high-speed throwing in Homo. Nature 498, 483–486.
Roberts, T.J., Belliveau, R.A., 2005. Sources of mechanical power for uphill running in humans. J Exp Biol 208, 1963–1970.
Roberts, T.J., Scales, J.A., 2004. Adjusting muscle function to demand: joint work during acceleration in wild turkeys. J Exp Biol 207, 4165–4174.
Robertson, A.M.B., Biewener, A.A., 2012. Muscle function during takeoff and landing flight in the pigeon (Columba livia). J Exp Biol 215, 4104–4114.
Robertson, D.G.E., Winter, D.A., 1980. Mechanical energy generation, absorption and transfer amongst segments during walking. J Biomech 13, 845–854.
Rodi, W., Ferziger, J.H., Breuer, M., Pourquiée, M., 1997. Status of Large Eddy Simulation: Results of a Workshop. J. Fluids Eng. 119, 248–262.
Rouard, A.H., Clarys, J.P., 1995. Cocontraction in the elbow and shoulder muscles during rapid cyclic movements in an aquatic environment. J Electromyogr Kinesiol 5, 177–183.
Rouboa, A.I., Silva, A.J., Leal, L., Rocha, J., Alves, F.B., 2006. The effect of swimmer's hand/forearm acceleration on propulsive forces generation using computational fluid dynamics. J Biomech 39, 1239–1248.
Samson, W., Desroches, G., Chèze, L., Dumas, R., 2009. 3D joint dynamics analysis of healthy children's gait. J Biomech 42, 2447–2453.
Sanders, R.H., 1999. Hydrodynamic Characteristics of a Swimmer's Hand. J Appl Biomech 15, 3–26.
Sasaki, K., Neptune, R.R., 2010. Individual muscle contributions to the axial knee joint

contact force during normal walking. J Biomech 43, 2780–2784.
Sasaki, K., Sasaki, K., Neptune, R.R., Kautz, S.A., 2009. The relationships between muscle, external, internal and joint mechanical work during normal walking. J Exp Biol 212, 738–744.
Sawicki, G.S., Ferris, D.P., 2009. Mechanics and energetics of incline walking with robotic ankle exoskeletons. J Exp Biol 212, 32–41.
Sawicki, G.S., Ferris, D.P., 2008. Mechanics and energetics of level walking with powered ankle exoskeletons. J Exp Biol 211, 1402–1413.
Sawicki, G.S., Lewis, C.L., Ferris, D.P., 2009. It pays to have a spring in your step. Exerc Sport Sci Rev 37, 130–138.
Sawicki, G.S., Robertson, B.D., Azizi, E., Roberts, T.J., 2015. Timing matters: tuning the mechanics of a muscle-tendon unit by adjusting stimulation phase during cyclic contractions. J Exp Biol 218, 3150–3159.
Schache, A.G., Baker, R., 2007. On the expression of joint moments during gait. Gait Posture 25, 440–452.
Schache, A.G., Blanch, P.D., Dorn, T.W., Brown, N.A.T., Rosemond, D., Pandy, M.G., 2011. Effect of running speed on lower limb joint kinetics. Med Sci Sports Exerc 43, 1260–1271.
Schache, A.G., Brown, N.A.T., Pandy, M.G., 2015. Modulation of work and power by the human lower-limb joints with increasing steady-state locomotion speed. J Exp Biol 218, 2472–2481.
Schepens, B., Bastien, G.J., Heglund, N.C., Willems, P.A., 2004. Mechanical work and muscular efficiency in walking children. J Exp Biol 207, 587–596.
Schipplein, O.D., Andriacchi, T.P., 1991. Interaction between active and passive knee stabilizers during level walking. J. Orthop. Res. 9, 113–119.
Schleihauf, R.E., 1979. A hydrodynamic analysis of swimming propulsion, in: Terauds, J., Bedingfield, E.W. (Eds.), Swimming III. University Park Press, Baltimore, pp. 70–109.
Schollmeier, G., Uhthoff, H.K., Sarkar, K., Fukuhara, K., 1994. Effects of immobilization on the capsule of the canine glenohumeral joint. A structural functional study. Clin. Orthop. Relat. Res. 304, 37–42.
Sell, T.C., Ferris, C.M., Abt, J.P., Tsai, Y.-S., Myers, J.B., Fu, F.H., Lephart, S.M., 2007. Predictors of proximal tibia anterior shear force during a vertical stop-jump. J. Orthop. Res. 25, 1589–1597.
Senk, M., Chèze, L., 2006. Rotation sequence as an important factor in shoulder kinematics. Clin Biomech (Bristol, Avon) 21 Suppl 1, S3–8.
Seth, A., Matias, R., Veloso, A.P., Delp, S.L., 2016. A Biomechanical Model of the Scapulothoracic Joint to Accurately Capture Scapular Kinematics during Shoulder Movements. PLoS ONE 11, e0141028.
Seth, A., Sherman, M., Reinbolt, J.A., Delp, S.L., 2011. OpenSim: a musculoskeletal modeling and simulation framework for in silico investigations and exchange. Procedia IUTAM 2, 212–232.
Shepard, D., 1968. A two-dimensional interpolation function for irregularly-spaced data 517–524.
Silva, M.P.T., Ambrósio, J.A.C., Pereira, M.S., 1997. Biomechanical Model with Joint Resistance for Impact Simulation. Multibody System Dynamics 1, 65–84.
Silvia, C.E., 1970. Manual and Lesson Plans for Basic Swimming, Water Stunts, Life Saving, Springboard Diving, Skin and Scuba Diving. Privately published by the author, Springfield, MA.
Skals, S., Jung, M.K., Damsgaard, M., Andersen, M.S., 2016. Prediction of ground reaction forces and moments during sports-related movements. Multibody System

Dynamics 1–21.
Slavens, B.A., Bhagchandani, N., Wang, M., Smith, P.A., Harris, G.F., 2011. An upper extremity inverse dynamics model for pediatric Lofstrand crutch-assisted gait. J Biomech 44, 2162–2167.
Slavens, B.A., Sturm, P.F., Harris, G.F., 2010. Upper extremity inverse dynamics model for crutch-assisted gait assessment. J Biomech 43, 2026–2031.
Sreenivasan, K.R., 1989. The turbulent boundary layer, in: Gad-el-Hak, M. (Ed.), Frontiers in Experimental Fluid Mechanics, Frontiers in Experimental Fluid Mechanics. Springer Berlin Heidelberg, Berlin, Heidelberg, pp. 159–209.
Stagni, R., Leardini, A., Cappozzo, A., Grazia Benedetti, M., Cappello, A., 2000. Effects of hip joint centre mislocation on gait analysis results. J Biomech 33, 1479–1487.
Stamhuis, E., Videler, J., van Duren, L., Müller, U., 2002. Applying digital particle image velocimetry to animal-generated flows: Traps, hurdles and cures in mapping steady and unsteady flows in Re regimes between 10–2 and 105. Experiments in Fluids 33, 801–813.
Stamhuis, E.J., Nauwelaerts, S., 2005. Propulsive force calculations in swimming frogs. II. Application of a vortex ring model to DPIV data. J Exp Biol 208, 1445–1451.
Stephenson, R., 1994. DIVING ENERGETICS IN LESSER SCAUP (AYTHYTA AFFINIS, EYTON). J Exp Biol 190, 155–178.
Sutherland, D.H., Cooper, L., Daniel, D., 1980. The role of the ankle plantar flexors in normal walking. J Bone Joint Surg Am 62, 354–363.
Svec, O.J., 1982. Biofeedback for pulling efficiency. Swimming Technique 19, 38–40,42,45–46.
Swaine, I.L., 2000. Arm and leg power output in swimmers during simulated swimming. Med Sci Sports Exerc 32, 1288–1292.
Takagi, H., Nakashima, M., Ozaki, T., Matsuuchi, K., 2013. Unsteady hydrodynamic forces acting on a robotic hand and its flow field. J Biomech 46, 1825–1832.
Takagi, H., Nakashima, M., Sato, Y., Matsuuchi, K., Sanders, R.H., 2016. Numerical and experimental investigations of human swimming motions. J Sports Sci 34, 1564–1580.
Takagi, H., Shimada, S., Miwa, T., Kudo, S., Sanders, R., Matsuuchi, K., 2014. Unsteady hydrodynamic forces acting on a hand and its flow field during sculling motion. Hum Mov Sci 38, 133–142.
Takagi, H., Wilson, B., 1999. Calculating hydrodynamic force by using pressure differences in swimming, in: Keskinen, K.L., Komi, P.V., Hollander, A.P. (Eds.), Biomechanics and Medicine in Swimming VIII. University of Jyväskylä, Jyväskylä, Finland, pp. 101–106.
Takahashi, K.Z., Horne, J.R., Stanhope, S.J., 2015. Comparison of mechanical energy profiles of passive and active below-knee prostheses: a case study. Prosthet Orthot Int 39, 150–156.
Tax, A.A., Denier van der Gon, J.J., Erkelens, C.J., 1990. Differences in coordination of elbow flexor muscles in force tasks and in movement tasks. Exp Brain Res 81, 567–572.
Taylor, W.R., Heller, M.O., Bergmann, G., Duda, G.N., 2004. Tibio-femoral loading during human gait and stair climbing. J. Orthop. Res. 22, 625–632.
Teixeira-Salmela, L.F., Nadeau, S., Milot, M.-H., Gravel, D., Requião, L.F., 2008. Effects of cadence on energy generation and absorption at lower extremity joints during gait. Clin Biomech (Bristol, Avon) 23, 769–778.
Thayer, A.M., 1994. Hand pressures as predictors of resultant and propulsive hand forces in swimming. J Biomech 27, 598.
Thein, J.M., Brody, L.T., 2000. Aquatic-based rehabilitation and training for the shoulder.

J Athl Train 35, 382–389.
Thigpen, C.A., Shaffer, M.A., Gaunt, B.W., Leggin, B.G., Williams, G.R., Wilcox, R.B., 2016. The American Society of Shoulder and Elbow Therapists' consensus statement on rehabilitation following arthroscopic rotator cuff repair. J Shoulder Elbow Surg 25, 521–535.
Thoroughman, K.A., Shadmehr, R., 1999. Electromyographic correlates of learning an internal model of reaching movements. J Neurosci 19, 8573–8588.
Tikuisis, P., Meunier, P., Jubenville, C.E., 2001. Human body surface area: measurement and prediction using three dimensional body scans. Eur J Appl Physiol 85, 264–271.
Topka, H., Konczak, J., Schneider, K., Boose, A., Dichgans, J., 1998. Multijoint arm movements in cerebellar ataxia: abnormal control of movement dynamics. Exp Brain Res 119, 493–503.
Toussaint, H.M., Beelen, A., Rodenburg, A., Sargeant, A.J., de Groot, G., Hollander, A.P., van Ingen Schenau, G.J., 1988. Propelling efficiency of front-crawl swimming. J Appl Physiol 65, 2506–2512.
Toussaint, H.M., Knops, W., de Groot, G., Hollander, A.P., 1990. The mechanical efficiency of front crawl swimming. Med Sci Sports Exerc 22, 402–408.
Toussaint, H.M., Roos, P.E., Kolmogorov, S.V., 2004. The determination of drag in front crawl swimming. J Biomech 37, 1655–1663.
Toussaint, H.M., van den Berg, C., Beek, W.J., 2002. "Pumped-up propulsion" during front crawl swimming. Med Sci Sports Exerc 34, 314–319.
Tresch, M.C., Saltiel, P., Bizzi, E., 1999. The construction of movement by the spinal cord. Nat Neurosci 2, 162–167.
Tsourlou, T., Benik, A., Dipla, K., Zafeiridis, A., Kellis, S., 2006. The effects of a twenty-four-week aquatic training program on muscular strength performance in healthy elderly women. J Strength Cond Res 20, 811–818.
Tsunokawa, T., Nakashima, M., Takagi, H., 2015. Use of pressure distribution analysis to estimate fluid forces around a foot during breaststroke kicking. Sports Engineering 18, 149–156.
Urwin, M., Symmons, D., Allison, T., Brammah, T., Busby, H., Roxby, M., Simmons, A., Williams, G., 1998. Estimating the burden of musculoskeletal disorders in the community: the comparative prevalence of symptoms at different anatomical sites, and the relation to social deprivation. Ann. Rheum. Dis. 57, 649–655.
Vaillant, R., Barthe, L., Guennebaud, G., Cani, M.-P., Rohmer, D., Wyvill, B., Gourmel, O., Paulin, M., 2013. Implicit skinning: real-time skin deformation with contact modeling. ACM Transactions on Graphics (TOG) 32, 1–12.
Vaillant, R., Guennebaud, G., Barthe, L., Wyvill, B., Cani, M.-P., 2014. Robust iso-surface tracking for interactive character skinning. ACM Transactions on Graphics (TOG) 33, 1–11.
van den Bogert, A.J., 1994. Analysis and simulation of mechanical loads on the human musculoskeletal system: a methodological overview. Exerc Sport Sci Rev 22, 23–51.
van den Bogert, A.J., Su, A., 2008. A weighted least squares method for inverse dynamic analysis. Comput Methods Biomech Biomed Engin 11, 3–9.
van der Helm, F.C., 1994. Analysis of the kinematic and dynamic behavior of the shoulder mechanism. J Biomech 27, 527–550.
van Ingen Schenau, G.J., Cavanagh, P.R., 1990. Power equations in endurance sports. J Biomech 23, 865–881.
van Ingen Schenau, G.J., van Woensel, W.W., Boots, P.J., Snackers, R.W., de Groot, G., 1990. Determination and interpretation of mechanical power in human movement: application to ergometer cycling. Eur J Appl Physiol Occup Physiol 61, 11–19.
Veeger, H.E.J., van der Helm, F.C.T., 2007. Shoulder function: the perfect compromise

between mobility and stability. J Biomech 40, 2119–2129.
Veneziano, W.H., da Rocha, A.F., Gonçalves, C.A., Pena, A.G., Carmo, J.C., Nascimento, F.A.O., Rainoldi, A., 2006. Confounding factors in water EMG recordings: an approach to a definitive standard. Med Biol Eng Comput 44, 348–351.
Versteeg, H., Malalasekra, W., 2007a. Implementation of boundary conditions, in: An Introduction to Computational Fluid Dynamics: the Finite Volume Method. Pearson, Harlow, England, pp. 267–284.
Versteeg, H., Malalasekra, W., 2007b. Errors and uncertainty in CFD modelling, in: An Introduction to Computational Fluid Dynamics: the Finite Volume Method Approach. Pearson, Harlow, England, pp. 285–303.
Vilas-Boas, J.P., Ramos, R.J., Fernandes, R.J., Silva, A.J., Rouboa, A.I., Machado, L., Barbosa, T.M., Marinho, D.A., 2015. Hydrodynamic Analysis of Different Finger Positions in Swimming: A Computational Fluid Dynamics Approach. Journal of Applied Biomechanics 31, 48–55.
Vo, A., Zhou, H., Dumont, G., Fogerty, S., Rosso, C., Li, X., 2013. Physical Therapy and Rehabilitation after Rotator Cuff Repair: A Review of Current Concepts. Int J Phys Med Rehabil 1, 142.
Vogel, S., Feder, N., 1966. Visualization of Low-speed Flow using Suspended Plastic Particles. Nature 209, 186–187.
Wang, J., Gallagher, D., Thornton, J.C., Yu, W., Horlick, M., Pi-Sunyer, F.X., 2006. Validation of a 3-dimensional photonic scanner for the measurement of body volumes, dimensions, and percentage body fat. Am. J. Clin. Nutr. 83, 809–816.
Wang, X.C., Phillips, C., 2002. Multi-weight enveloping: least-squares approximation techniques for skin animation. Proceedings of ACM SIGGRAPH '02, pp. 129–138.
Wardetzky, M., 2008. Convergence of the Cotangent Formula: An Overview, in: Discrete Differential Geometry, Oberwolfach Seminars. Birkhäuser Basel, Basel, pp. 275–286.
Wardetzky, M., Mathur, S., lberer, F.K.2., Grinspun, E., 2007. Discrete laplace operators: no free lunch. Symposium on Geometry processing, pp. 33–37.
Weber, W., Weber, E., 1992. Mechanics of the Human Walking Apparatus. Springer-Verlag, New York, NY.
Wei, T., Mark, R., Hutchison, S., 2014. The fluid dynamics of competitive swimming. Annu. Rev. Fluid Mech. 46, 547–565.
Weinberg, S.M., Scott, N.M., Neiswanger, K., Brandon, C.A., Marazita, M.L., 2004. Digital three-dimensional photogrammetry: evaluation of anthropometric precision and accuracy using a Genex 3D camera system. Cleft Palate Craniofac. J. 41, 507–518.
Weis-Fogh, T., Alexander, R.M., 1977. The sustained power output from striated muscle, in: Pedley, T.J. (Ed.), Scale Effects in Animal Locomotion. Academic Press, London, pp. 511–525.
Wilcox, D.C., 2006. Turbulence Modeling for CFD, 3rd ed. DCW Industries, La Cañada, CA.
Wilcox, D.C., 1988. Reassessment of the scale-determining equation for advanced turbulence models. AIAA J 26, 1299–1310.
Willems, P.A., Cavagna, G.A., Heglund, N.C., 1995. External, internal and total work in human locomotion. J Exp Biol 198, 379–393.
Willert, C.E., Gharib, M., 1991. Digital particle image velocimetry. Exp Fluids 10, 181–193.
Winby, C.R., Gerus, P., Kirk, T.B., Lloyd, D.G., 2013. Correlation between EMG-based co-activation measures and medial and lateral compartment loads of the knee during gait. Clin Biomech (Bristol, Avon) 28, 1014–1019.

Winter, D.A., 2005. Biomechanics and Motor Control of Human Movement, 3rd ed. John Wiley & Sons, Hoboken, NJ.
Winter, D.A., 1983. Energy generation and absorption at the ankle and knee during fast, natural, and slow cadences. Clin. Orthop. Relat. Res. 147–154.
Winter, D.A., 1979. A new definition of mechanical work done in human movement. J Appl Physiol 46, 79–83.
Winter, D.A., 1978. Calculation and interpretation of mechanical energy of movement. Exerc Sport Sci Rev 6, 183–201.
Winter, D.A., Ishac, M.G., 1994. Interpretation of 3D moments-of-force during gait. J Biomech 27, 818.
Winter, D.A., Quanbury, A.O., Reimer, G.D., 1976. Analysis of instantaneous energy of normal gait. J Biomech 9, 253–257.
Winters, J.M., Woo, S.L.-Y., 2012. Multiple Muscle Systems. Springer-Verlag, New York, NY.
Woledge, R.C., Curtin, N.A., Homsher, E., 1985. Energetic Aspects of Muscle Contraction. Academic Press, Orlando, FL.
Woltring, H.J., 1994. 3-D attitude representation of human joints: a standardization proposal. J Biomech 27, 1399–1414.
Wood, T.C., 1979. A Fluid Dynamic Analysis of the Propulsive Potential of the Hand and Forearm in Swimming, in: Terauds, J., Bedingfield, E.W. (Eds.), Swimming III. Baltimore University Park Press, Baltimore, pp. 62–69.
Wu, G., Siegler, S., Allard, P., Kirtley, C., Leardini, A., Rosenbaum, D., Whittle, M., D'Lima, D.D., Cristofolini, L., Witte, H., Schmid, O., Stokes, I., Biomechanics, S.A.T.C.O.T.I.S.O., 2002. ISB recommendation on definitions of joint coordinate system of various joints for the reporting of human joint motion--part I: ankle, hip, and spine. International Society of Biomechanics. J Biomech 35, 543–548.
Wu, G., van der Helm, F.C.T., Veeger, H.E.J.D., Makhsous, M., Van Roy, P., Anglin, C., Nagels, J., Karduna, A.R., McQuade, K.J., Wang, X., Werner, F.W., Buchholz, B., Biomechanics, I.S.O., 2005. ISB recommendation on definitions of joint coordinate systems of various joints for the reporting of human joint motion--Part II: shoulder, elbow, wrist and hand. J Biomech 38, 981–992.
Xu, G., 2004. Discrete Laplace–Beltrami operators and their convergence. Geometric Modeling and Processing 2004 21, 767–784.
Yang, X., Zhang, J.J., 2006. Stretch It - Realistic Smooth Skinning, in:. Presented at the International Conference on Computer Graphics, Imaging and Visualisation (CGIV'06) IS - SN - VO - VL -, Sydney, pp. 323–328.
Yang, X.S., Zhang, J.J., 2005. Realistic Skeleton Driven Skin Deformation, in: Gervasi, O., Gavrilova, M.L., Kumar, V., Laganà, A., Lee, H.P., Mun, Y., Taniar, D., Tan, C.J.K. (Eds.), Computational Science and Its Applications – ICCSA 2005: International Conference, Singapore, May 9-12, 2005, Proceedings, Part III, Computational Science and Its Applications – ICCSA 2005: International Conference, Singapore, May 9-12, 2005, Proceedings, Part III. Springer Berlin Heidelberg, Berlin, Heidelberg, pp. 1109–1118. doi:10.1007/11424857_119
Young, J., Walker, S.M., Bomphrey, R.J., Taylor, G.K., Thomas, A.L.R., 2009. Details of insect wing design and deformation enhance aerodynamic function and flight efficiency. Science 325, 1549–1552.
Young, J.W., Chandler, R.F., Snow, C.C., Robinette, K.M., Zehner, G.F., Lofberg, M.S., 1983. Anthropometric and mass distribution characteristics of the adults female (No. FA-AM-83-16). Oklahoma City, Oklahoma.
Yu, C.-Y., Lo, Y.-H., Chiou, W.-K., 2003. The 3D scanner for measuring body surface area: a simplified calculation in the Chinese adult. Appl Ergon 34, 273–278.

Zack, T.I., Claverie, T., Patek, S.N., 2009. Elastic energy storage in the mantis shrimp's fast predatory strike. J Exp Biol 212, 4002–4009.
Zaïdi, H., Fohanno, S., Taïar, R., Polidori, G., 2010. Turbulence model choice for the calculation of drag forces when using the CFD method. J Biomech 43, 405–411.
Zaïdi, H., Taïar, R., Fohanno, S., Polidori, G., 2008. Analysis of the effect of swimmer's head position on swimming performance using computational fluid dynamics. J Biomech 41, 1350–1358.
Zajac, F.E., 1989. Muscle and tendon: properties, models, scaling, and application to biomechanics and motor control. Crit Rev Biomed Eng 17, 359–411.
Zajac, F.E., Neptune, R.R., Kautz, S.A., 2002. Biomechanics and muscle coordination of human walking. Part I: introduction to concepts, power transfer, dynamics and simulations. Gait Posture 16, 215–232.
Zamparo, P., Gatta, G., Pendergast, D.R., Capelli, C., 2009. Active and passive drag: the role of trunk incline. Eur J Appl Physiol 106, 195–205.
Zamparo, P., Pendergast, D.R., Mollendorf, J.C., Termin, A.C., Minetti, A.E., 2005. An energy balance of front crawl. Eur J Appl Physiol 94, 134–144.
Zamparo, P., Pendergast, D.R., Termin, A.C., Minetti, A.E., 2006. Economy and efficiency of swimming at the surface with fins of different size and stiffness. Eur J Appl Physiol 96, 459–470.
Zamparo, P., Pendergast, D.R., Termin, B., Minetti, A.E., 2002. How fins affect the economy and efficiency of human swimming. J Exp Biol 205, 2665–2676.
Zamparo, P., Swaine, I.L., 2012. Mechanical and propelling efficiency in swimming derived from exercise using a laboratory-based whole-body swimming ergometer. J Appl Physiol 113, 584–594.
Zatsiorsky, V.M., 1998. Can total work be computed as a sum of the 'external' and "internal" work? J Biomech 31, 191–193.
Zatsiorsky, V.M., Prilutsky, B.I., 2012. Biomechanics of Skeletal Muscles. Human Kinetics, Champaign, IL.
Zelik, K.E., Kuo, A.D., 2010. Human walking isn't all hard work: evidence of soft tissue contributions to energy dissipation and return. J Exp Biol 213, 4257–4264.
Zelik, K.E., Takahashi, K.Z., Sawicki, G.S., 2015. Six degree-of-freedom analysis of hip, knee, ankle and foot provides updated understanding of biomechanical work during human walking. J Exp Biol 218, 876–886.
Zhang, Y., Ahn, P.B., Fitzpatrick, D.C., Heiner, A.D., Poggie, R.A., Brown, T.D., 1999. Interfacial frictional behavior: cancellous bone, cortical bone, and a novel porous tantalum biomaterial. J. Musculoskelet. Res. 03, 245–251.
Zikanov, O., 2010. Conducting CFD Analysis, in: Essential Computational Fluid Dynamics. John Wiley & Sons, Hoboken, NJ, pp. 280–295.